DESIGN AND CONTROL OF A 6-DEGREE-OF-FREEDOM LEVITATED

POSITIONER WITH HIGH PRECISION

A Dissertation

by

TIEJUN HU

Submitted to the Office of Graduate Studies of
Texas A&M University
in partial fulfillment of the requirements for the degree of

DOCTOR OF PHILOSOPHY

May 2005

Major Subject: Mechanical Engineering

DESIGN AND CONTROL OF A 6-DEGREE-OF-FREEDOM LEVITATED

POSITIONER WITH HIGH PRECISION

A Dissertation

by

TIEJUN HU

Submitted to Texas A&M University
in partial fulfillment of the requirements
for the degree of

DOCTOR OF PHILOSOPHY

Approved as to style and content by:

Won-jong Kim (Chair of Committee)	Suhada Jayasuriya (Member)
Alexander Parlos (Member)	Hamid A. Toliyat (Member)
Dennis O'Neal (Head of Department)	

May 2005

Major Subject: Mechanical Engineering

ABSTRACT

Design and Control of a 6-Degree-of-Freedom Levitated Positioner with High Precision.

(May 2005)

Tiejun Hu, B.S., Tsinghua University, China;

M.S., Tsinghua University, China

Chair of Advisory Committee: Dr. Won-jong Kim

This dissertation presents a high-precision positioner with a novel superimposed concentrated-field permanent-magnet matrix. This extended-range multi-axis positioner can generate all 6-DOF (degree-of-freedom) motions with only a single moving part. It is actuated by three planar levitation motors, which are attached on the bottom of the moving part. Three aerostatic bearings are used to provide the suspension force against the gravity for the system. The dynamic model of the system is developed and analyzed. And several control techniques including SISO (single input and single output) and MIMO (multi inputs and multi outputs) controls are discussed in the dissertation. The positioner demonstrates a position resolution of 20 nm and position noise of 10 nm rms in x and y and 15 nm rms in z. The angular resolution around the x-, y-, and z-axes is in sub-microradian order. The planar travel range is 160 mm × 160 mm, and the maximum velocity achieved is 0.5 m/s at a 5-m/s^2 acceleration, which can enhance the throughput in precision manufacturing. Various experimental results are presented in this dissertation to demonstrate the positioner's capability of accurately tracking any planar trajectories. Those experimental results verified the potential utility of this 6-DOF high-precision positioner in precision manufacturing and factory automation.

To my parents,

who brought my life into the world;

to my family,

who always shared my failures and happiness;

and to my wife,

forever.

ACKNOWLEDGMENTS

I would like to express my deep gratitude to my thesis advisor Dr. Won-jong Kim for his consistently invaluable advice, financial support, encouragement, and especially for my research guidance. It was he who gave me that valuable opportunity to study in the US and offered me the privilege to be his first doctoral student. I admire his competence throughout electrical and mechanical engineering disciplines. His earnest attitude to science and diligence to research will always be remembered and modeled by me.

I would especially like to thank Prof. Dianfang He who was my B.S. and M.S. advisor in Tsinghua University, China. I cannot forget those years we spent together in research and projects. His critical guidance both in science and life for me will benefit me forever. His voice and spirit will always live in my memory.

I would like to offer my great thanks to Profs. Jayasuriya, Parlos, and Toliyat for serving as my advisory committee members. I appreciated their time, advice, and consideration in my doctoral program. Without their contributions, this dissertation simply could not have developed as it did.

I extend my sincere thanks to Mr. Nikhil Bhat who was a former student of Dr. Won-jong Kim. He contributed to the mechanical design and fabrication of some important parts, such as the concentrated-field magnet matrix base plate, and the moving platen.

Finally, I can never thank enough for my parents Mr. Haitao Hu and Mrs. Zhanyu Deng for their love and encouragement. I always owe my wife, Song Liu, a lot for her support and understanding. She has always been a smart consultant of mine in my life and work.

The work in this dissertation is an important part of a two-year project supported by Texas Advanced Technology Program under Grant No. 000512-0225-2001.

TABLE OF CONTENTS

LIST OF FIGURES

LIST OF TABLES

CHAPTER I

INTRODUCTION

1.1 High-Precision Motion-Control Technology

With the rapid development of material science and advanced manufacturing, high-precision (nanometer- or micrometer- scale) motion control technology is used in industry more frequently than ever. The birth of nanotechnology at the beginning of last century accelerated the application of high-precision motion control technology in industry. Some key challenges such as nano-manipulation require to control and fabricate nano-scale objects in very high precision. The related instruments, such as scanning tunneling microscopes (STMs), which have already become a common interface for many manipulation systems [1−3], also heavily rely on the high-precision motion control technology. Besides, the nano-scale assembling technique which requires ultra high-precision motion control is still in infancy in the nanotechnology field.

In microelectronic manufacturing in the semiconductor industry, high-precision motion control is very critical. One example is the photolithography in wafer fabrications (FABs). As it can be seen from Fig. 1-1, in this process, a wafer coated with a light-sensitive photoresist is transported to the exposure field by a wafer stage which has a high-resolution positioning capability in several different directions. The wafer stage, which can be also called the step-and-repeat aligner or stepper, is critical equipment for photolithography. The wafer stage will align and expose successive reticle which has the die patterns by stepping from one exposure site to

This dissertation follows the style and format of the *IEEE/ASME Transactions on Mechatronics*.

another on the resist-coated wafer surface. The industry has converted to the step-and-scan system for deep ultraviolet (DUV) light source system called step-and-scan technology [6]. The accuracy of the position for each die has a significant effect on the critical dimension (CD). So the precision motion control is very important in the current and future deep-submicron lithography technology.

Besides shrinking feature size and demanding overlay accuracy, transitioning the wafer size to 300 mm in diameter and beyond will introduce significant design challenges in microelectronics manufacturing and material handling automation. For example, an unprocessed 300-mm wafer is more than twice as heavy as a 200-mm wafer (125 g vs. 56 g). Thus, the mass of twenty-five 300-mm wafers along with their film frame and cassette will be over 13.5 kg, which will double the mass of the cassette of twenty-five 200-mm wafers currently being used [4]. It will introduce significant changes in wafer dicing, mounting, die-attach machines, pod door openers, stockers, and handling robots, increasing foot prints, and force and power requirements. And the traditional wafer handling systems mainly consist of pneumatic, hydraulic, and mechanical/electromechanical devices [5]. Such systems are complicated and expensive to produce, and it takes much time and cost to repair and maintain them. Those conventional wafer handling technologies for 200-mm wafers may not be able to meet the new specifications and many technical challenges of this transition to 300-mm wafers. Therefore, reliable low-cost positioning for precision manufacturing processes requiring clean room, extreme-temperature, or vacuum environments is key for microelectronics manufacturing, packaging, machine tool, and high-precision inspection industries. In this thesis, a novel high-precision 6-degree-of-freedom (DOF) positioner is presented as a potential future wafer stage in semiconductor manufacturing industry.

UV light source

Shutter

Shutter is closed during focus
and alignment and removed
during wafer exposure

Alignment laser

Reticle (may contain one or
more dies in the reticle field)

Projection lens (reduces the size
of reticle field for presentation to
the wafer surface)

Single field exposure, includes:
focus, align, expose, step, and
repeat process

Wafer stage controls
position of wafer in
X, Y, Z, θ

Fig. 1-1 Illustration of photolithography process in wafer fabrications (after [6])

1.2   Stage Technology

With high-accuracy positioning capabilities for sophisticated photolithographic processes, wafer stages have been used to manufacture integrated circuits (ICs) via fully automated control for many years [7]. According to the semiconductor industry association's (SIA) annual report published in 2004, the 193-nm photolithography technology is now under commercialization [8]. Like other strategic equipment, high precision wafer steppers, whose motion is mainly confined in the *x-y* plane must be available at least two years before the production ramps up. As a result, the high-precision positioner being used in a wafer stepper in semiconductor manufacturing faces new challenges. The wafer stage in photolithography process

usually has three basic purposes, all of which should meet critical specifications for accuracy and repeatability [6]:

- Focus and align the wafer surface to the quartz plate reticle containing the circuit patterns.

- Reproduce a high-resolution reticle image on the wafer through exposure of photoresist.

- Produce an adequate quantity of acceptable wafers per unit time to meet production requirements.

In order to meet these requirements, the research on the stage technology never stopped since the beginning of semiconductor industry. The crossed-axis type as shown in Fig. 1-2 (a), where a stage for one axis stacks on top of another is one of the most common design concepts. This design usually has two or three moving parts driven by stepper motors and ball screws. Each actuator takes care of one DOF. And many of those conceptual designs use ball or roller bearings for guidance and suspension. Some sophisticated systems may use aerostatic bearings to eliminate the friction. Another traditional design for the positioning system is called gantry type which is shown in Fig. 1-2 (b). This gantry-type configuration usually has a bridgelike framework which spans a distance between two motors at the end. For applications which do not require high positioning resolution such as scanners and plotters, stepper motors are frequently used. Either crossed-axis-type or gantry-type positioners do not have the capability to generate rotary motion. If rotational motion is needed, one or more independent mechanical devices and actuators should be added. Those additional apparatuses usually make the whole positioning system more complicated and bulkier, and lead to complex dynamics, which makes it difficult to control the whole system [9−11].

(a)

(b)

Fig. 1-2   Configurations of (*a*) crossed-axis and (*b*) gantry type positioning system (photo courtesy of Aerotech, Inc.)

There are three different motors commonly used in the positioning system in the past years. They are DC motors, synchronous motors, and induction motors. The DC motors have brushes, and a mechanical commutator is necessary. The field magnetomotive force (mmf) and armature mmf are maintained orthogonal to each other, and the axis for the armature mmf is fixed in space. As a result, a DC motor has a simple decoupled system and it can be easily controlled. Before the advent of microcomputers, DC motors were the most common type used for motion control purpose. The main drawback for a DC motor used in high-precision positioning system is the wear in the brush. The wear particles excluded the DC motors from the applications in clean-room manufacturing.

The steady-state speed of a synchronous motor is proportional to the electrical frequency in the armature excitation. The rotor spins at the same speed as the rotating armature magnetic field. The spin speed of the motor is not affected by the load, which affects the torque angle. The torque angle is defined by the phase difference between the mmf of the field winding and the resultant air-gap magnetic flux per pole. The traditional synchronous motors normally have two excitations for magnetic field sources: one for the rotor and the other for the stator are with many windings. This makes the structure of a wound-field synchronous motor complicated. Moreover, the power consumption due to the current in the rotor may bring thermal expansion to the positioner which will reduce the accuracy.

Now the induction motor is often used as an actuator in maglev-train propulsion. However, this kind of motor is seldom used in high-precision positioning system. First of all, the heat generated by the induced current can cause thermal expansion of the rotor, which is problematic in high-precision control applications [12]. Second, the induced current can be generated only by the speed difference, there will be no magnetic force if there is no relative motion between the excitation field wave and the stage. Third, the speed characteristic of

induction motors is complicated and nonlinear, modeling and control of such a motor for precision positioning system is difficult. Furthermore, since the angular position of the rotor magnetic axis is unknown, vector control or field oriented control is necessary [12].

The traditional rotary motors can hardly be used in a high-precision positioning system alone although they can be used as actuators for low-precision coarse motions. The high-precision positioning capability is often achieved by piezoelectric or voice-coil actuators. One reason is that additional mechanical system, such as rack and pinions or ball screws, is needed to convert rotary motions from those servo motors into planar motions. The backlash due to the mechanical tolerance introduced by the transmission system is a significant obstacle to achieve high precision. The other reason is the bearings used in the rotary motors and the positioning systems are typically mechanical contact bearings such as angular ball bearings, antithrust bearings, and barrel bearings [13]. Those bearings have frictions between the balls and the surface. Due to these inherent frictions, those traditional positioners are limited to applications requiring repeatability on the order of 0.5 to 0.1 μm [13]. To achieve high-precision positioning, those mechanical bearings must be replaced by non-friction air bearings or magnetic bearings [14]. Piezoelectric motors and voice-coil motors are two of the most promising motors used in the high-precision positioning system.

1.2.1   Piezoelectric Motors

Piezoelectric motors use a piezoelectric ceramic element to produce ultrasonic vibrations of an appropriate type in a stator structure. The elliptical movements of the stator are converted into the movement of a slider pressed into frictional contact with the stator [13]. The consequent movement may either be rotational or linear depending on the design of the structure. According to the number of ceramic layers, piezoelectric motors can be classified as single layer motor,

two-layer motor, and multi-layer motors. Single layer piezoelectric motors typically offer one degree of freedom, such as in linear stages. However, the multi-layers motor can provide more complex positioning factors by combining several layers in different way. Rotating piezoelectric motors are commonly used in sub-micrometric positioning devices. Large mechanical torque can be achieved by combining several of these rotational units [15].

(a)   (b)
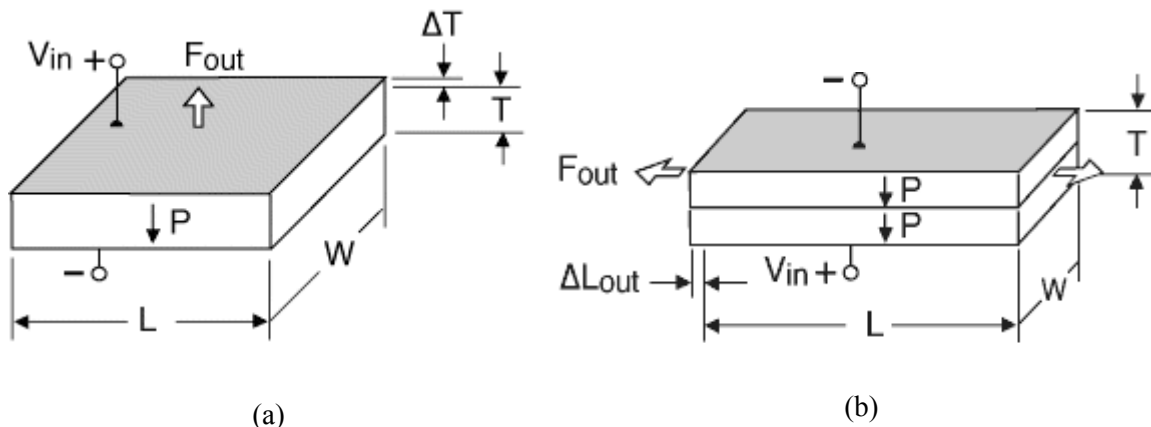
Fig. 1-3 Working principle of (*a*) one layer and (*b*) two layers piezoelectric motor [16]

The working principle of the piezoelectric motors is simple. It can be illustrated in Fig. 1-3. Suppose there is an electrical field V_{in} which has the same polarity and orientation as the original polarization field P of a sheet of piezoceramic with the thickness of T. When this electrical field is applied across the piezoceramic sheet, the sheet expands ΔT in the thickness or "longitudinal" direction (i.e., along the axis of polarization) and contracts in the transverse direction (perpendicular to the axis of polarization). Thus it will generate corresponding driving force F_{out} in the expanding direction. When the electrical field is reversed, the motions are reversed.

Fig. 1-3 (b) illustrates the working principle of a 2-layer piezoelectric motor. A 2-layer element behaves similar to a single layer when both layers expand (or contract) together. If an electric field is applied which makes the element thinner, extension along the length and width

happens. Typically, only motion along one axis is utilized. Usually the extending motion is on the order of micrometers to tens of micrometers, and the driving force is on the order of tens to hundreds of newtons [16].

Piezoelectric motors have been in industrial use for years, but have not been popular due to what was perceived as an exorbitant cost of production and use. Those piezoelectric motors do have some disadvantages. These disadvantages include the need for high voltage, high frequency power sources and the possibility of wear at the rotor / stator interface, which tends to shorten service life [17]. Most of all, because of the deformation of the material is limited by the property of the ceramics, the maximum displacement generated by a piezoelectronic motor is always limited to the order of hundreds of micrometers. So for the application which needs both long travel range and high precision positioning, piezoelectric motor can be only cooperatively used with another positioning system which can provide longer travel range with low positioning resolution.

1.2.2 Voice-Coil Motors

Voice-coil motors (VCM), offer the speed, efficiency, and accuracy modern industries need. Because voice-coil motors are direct drive, they generate no backlash or positioning problems. Additionally, voice coils eliminate losses attributed to gear heads, which typically operate at only 60 to 70% efficiencies [18]. These losses, which usually show up as heat dissipation, are expensive. Voice-coil motors were originally used in loudspeakers but these non-commutated devices can now be widely found in linear and rotary-motion devices such as hard disk drive (HDD), camera focus systems, and high-precision linear positioner which require linear force or torque and high acceleration (50 g or more) or high-frequency actuation (20 to 400 Hz).

The name of "voice-coil" comes from the original application of this motor as a speaker invented by Alexander Graham Bell in 1876. In speakers, the magnet is cylindrical north-south pole in-out (or top-bottom of the cylinder) and the coil goes north-to-south pole (or top-bottom of an inner cylinder). Changing the amplitude and polarity of the current in the coil causes an in-out force that 'plays' the diaphragm on the speaker. The spring tension on the diaphragm keeps the voice coil actuator centered when no current is applied. The working principle can be illustrated in Fig. 1-4.

(a)

(b)
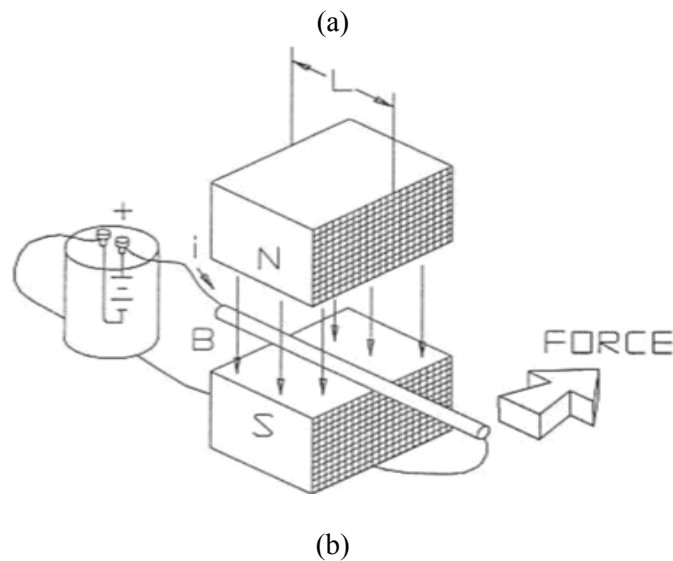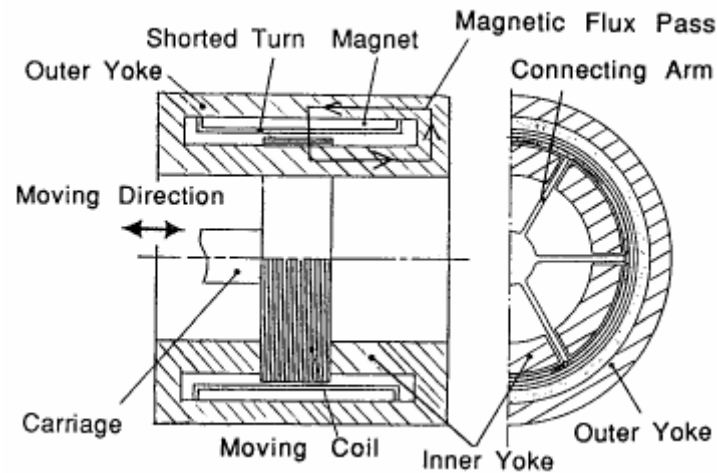
Fig. 1-4 (*a*) cross-sectional view of VCM and (*b*) its working principle[19]

Fig. 1-4 (a) shows a cross sectional view of a typical voice coil motor. It can be seen in the figure, there is a permanent radial distributed magnetic field, whose magnetic flux density is B, inside the motor. When there is a current i flowing in the moving voice coil, a magnetic force, whose direction is at right angles to both the direction of current and magnetic field, will be generated by Lorentz force law with interaction of the magnetic field and the current in the voice coil.

Compared with the piezoelectric motor, voice coil motor has a much larger operating range and less natural frequency [20]. As a result, the voice coil motor and piezoelectric transducer are often used together as a dual-actuator system in many industry applications [21−27]. A typical application is in the computer hard disk drive (HDD) manufacturing. Fig. 1-5 shows the servo system of a typical computer hard disk drive.
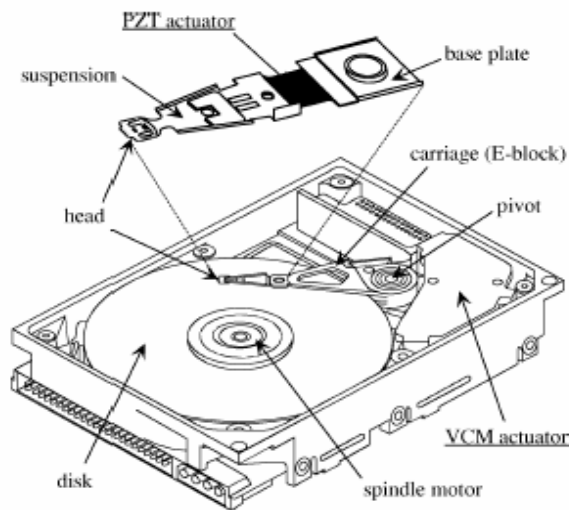
Fig. 1-5 Schematic diagram of a hard disk drive with dual actuator servo system [20]

There the voice coil motor, which has large operating range and low natural frequency, is used as the first coarse positioning stage actuator and a push-pull-type piezoelectric transducer (PZT), which has a small operating range and a high natural frequency, is used as the second

stage actuator for fine positioning purpose [28−31]. Since in most cases, only the sum of two different PZT actuator's and VCM actuator's output, i.e., the position of read/write head is available for the servo controller, the controller design is a big challenge to deal with two different dynamics of actuators.

1.2.3 Planar Motors

Compared with traditional rotary motors, planar motors which can generate two-dimensional motions in a plane are used in precision manufacturing industry more frequently than ever. Since the planar motor can provide dual-axis driving forces, it can easily generate crossed-axis motions without any other additional mechanical devices. It can be expected that a planar motor driving positioner can easily generate any 3 dimensional motions with much simpler and more compact structure.

Based on the previous research on the planar motors [32], the structure of planar motor can be mainly categorized as variable-reluctance type, permanent-magnet matrix type, and induction type [33−38]. A variable-reluctance type planar motor has many salient teeth on its rotor surface. The rotor has a tendency to align for geometry with minimum air-gap reluctance so that the whole motor stays at the minimum magnetic energy status [39−43]. It is unnecessary to use feedback control to get relatively low precision of a fraction of tooth pitch. A typical example of variable-reluctance type planar motor is the Sawyer motor which has frequently been used in industry without explicit position feedback [44].

Keeping pace with advances in permanent-magnet materials in the last decades, another type of planar motor, i. e. the permanent-magnet matrix planar motor was developed, which uses permanent magnet matrix as sources of magnetic field intensity and windings for current density. The driving force for motion is generated by controlling the current in the windings. The planar

positioning concepts using permanent magnet matrix were presented by Asakawa [45] and Ebihara and Watada [46]. Another planar motion system, which led to the SVGL Micrascan system, was designed by Buckley, et al. [47]. It has two unipolar permanent-magnet planar motors to generate major two-dimensional motions and rotation about the normal to the stage. Much progress in precision planar motors based on the permanent-magnet matrix type and the variable reluctance type have been recently reported [48−52]. The development and research on induction planar motors have a long way to go to make this kind of planar motor be used in real world precision industry.

In the following sub sections, the variable reluctance (VR) type and permanent magnet matrix type planar motor will be discussed in detail due to their wide applications in the planar motion control.

Sawyer Motor

The sawyer motor is the first VR-type planar motor. It has been widely used in industry such as wafer probing and automated assembly for long time. The motor is made by conceptually superimposing two orthogonal linear variable reluctance motors. As it can be seen from Fig. 1-6, the motor consists of housing with four symmetrically mounted linear motors. In the base plate as shown in Fig. 1-6 (b), there are many square protrusions (teeth) which are used to generate magnet flux density. The motor floats on a steel waffle platen by air bearings (at a nominal air gap of 20 μm) and has two translational degrees of freedom (DOF) along with a rotational DOF about the *z*-axis. Those aerostatic bearing pads are used to cancel the attraction force and the gravity load acting on the platen. The original sawyer motor was operated in open loop, since the resolution it can achieve at that time was enough for those relatively low resolution applications. For precision motion control with a particular emphasis on wafer stepper stages, Hinds and Nocito [53] and Pelta [54] improved the original version of the Sawyer motor.

14

Furthermore, the closed-loop control of Sawyer motors has recently received attention in the literature [55−60].
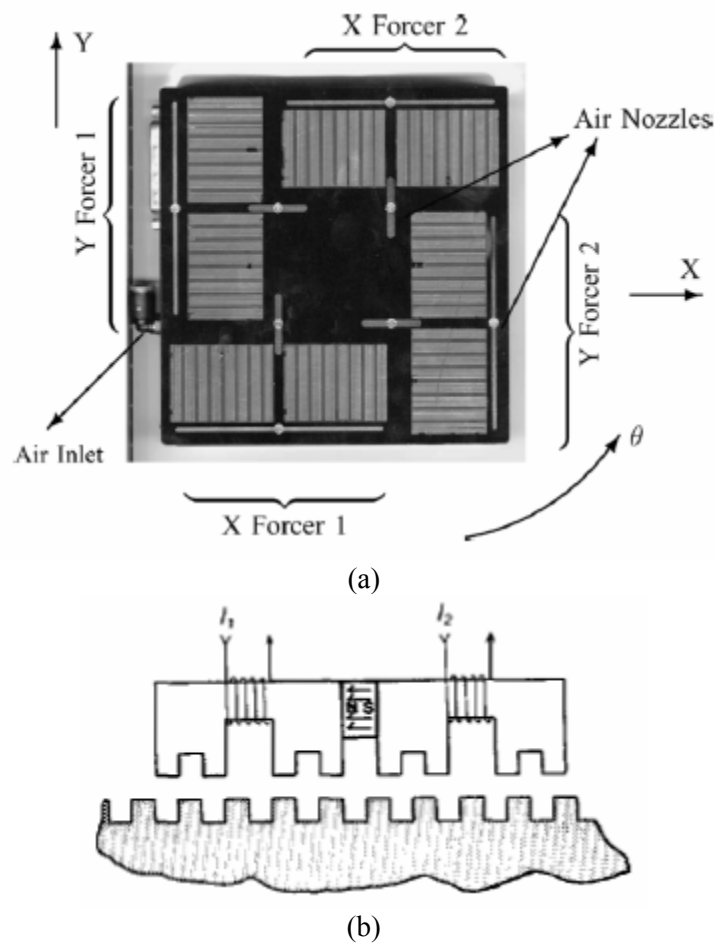
Fig. 1-6 (*a*) Bottom view of Sawyer motor and (*b*) its working principle [61]

The sawyer motor was commercialized by Northern Magnetics and Megamation. However, there are some drawbacks in the sawyer motor: (1) According to Northern Magnetics the 2-phase full-step size is as coarse as 250 μm with a possibility of reduction by microstepping. (2) The Sawyer motor needs tight air gap less than 25 μm, so it requires ultra-fine surface finish of the motor surfaces. (3) Its position repeatability is only as good as 5 μm. (4) In addition to large cogging force, attractive force of one model is as large as 1800 N [62]. (5) When it is

operated in open-loop, they can miss steps, have long settling time of 100−200 ms, and degraded performance due to the possible loss of synchronization between motor and platen teeth. (6) Typically the Sawyer motor has about ten times stronger attraction force than lateral force. The vertical motions can not be controlled at high resolution with the presence of aerostatic bearings. Megamation's *x-y* stage has been used in an IBM printed circuit board assembly line, and its accuracy specification is about 25 μm [63].

Permanent Magnet Matrix Planar Motor

The design concept of Sawyer motor inspired the design of Asakawa and Chitayat in magnet matrix planar motor. Instead of using a large number of iron protrusions in the base plate, they use many permanent-magnet cubes which form the checker-board-like stator in the base plate. The rotor usually carries windings with it. When there is current flowing in those windings, the magnet force will be generated in the specific magnet field provided by those permanent magnet matrices. Since the design of windings are quite similar and well developed the main difference in planar motors lies in the design concept of permanent magnet matrix. There are two papers [64−65] discussing the design of the magnet matrix.

Asakawa was the first person that proposed the permanent magnet arrays for planar motor [66]. Fig. 1-7 (a) shows the structure of Asakawa magnet matrix. It is the direct superposition of two orthogonal conventional one-dimensional magnet arrays. The blank square space denotes non-magnetic material. Besides those magnet matrices presented in the figure, there are four coils on the platen to interact with the magnets. However, the magnet packing density in Asakawa's magnet matrix is half of that in the one-axis driving linear motor [67]. In addition, the available forces are varied with the relative position between the coils and the magnet matrix, and they are nonlinear with position. Chitayat improved the packing density of

the magnets by assembling the magnets in diagonal direction. His magnet matrix is much more compact than Asakawa's design.

(a)   (b)
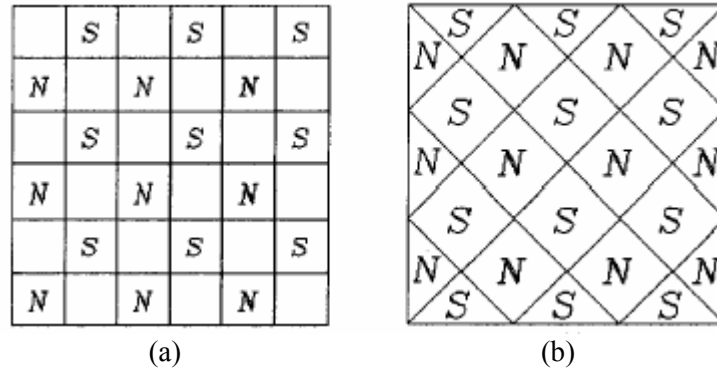
Fig. 1-7 Permanent magnet matrix (*a*) Asakawa and (*b*) Chitayat (after [67])

1.3   Proposed 6-DOF High-Precision Positioner

Fig. 1-8 shows the novel concentrated-field magnet matrix that produces the constant magnetic field for actuation. Compared with other magnet matrices, this magnet matrix is produced by the superimposition of two orthogonal Halbach arrays resulting in the plane view shown in Fig. 1-8. The detailed analysis of this magnet matrix will be given in Chapter III. Based on this magnet matrix, the prototype multi-dimensional positioner is designed and fabricated whose picture and perspective view are shown in Fig. 1-9.

This multi-dimensional positioner as an synchronous permanent magnet planar motor (SPMPM) presented in this thesis overcomes all these shortcomings of the established Sawyer motor and traditional permanent magnet planar motor technology, and can generate all fine and coarse motions with only one levitated moving part required for wafer processing.

Fig. 1-8 Conceptual superimposition of two orthogonal Halbach magnet arrays to produce a concentrated-field magnet matrix [68].

This prototype achieved a 20-nm positioning resolution and 160×160 mm travel range without requiring additional primary coarse-motion or secondary fine-motion stages. It employs a novel superimposed concentrated-field double-axis magnet matrix patented by one of the authors. to improve the positioner's force capability by a factor of $\sqrt{2}$ [68]. It does not require excessive surface finish, and its cogging force is less than a fraction of a newton without strong attractive force.

(a)

(b)
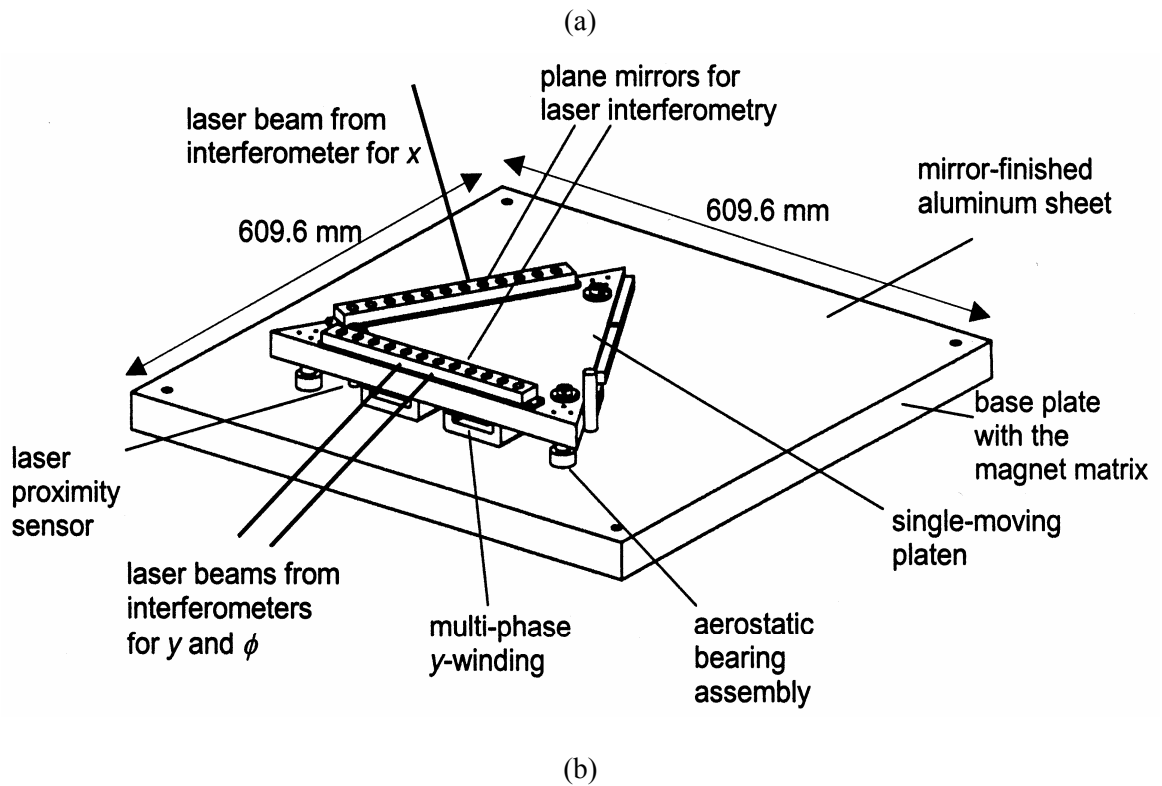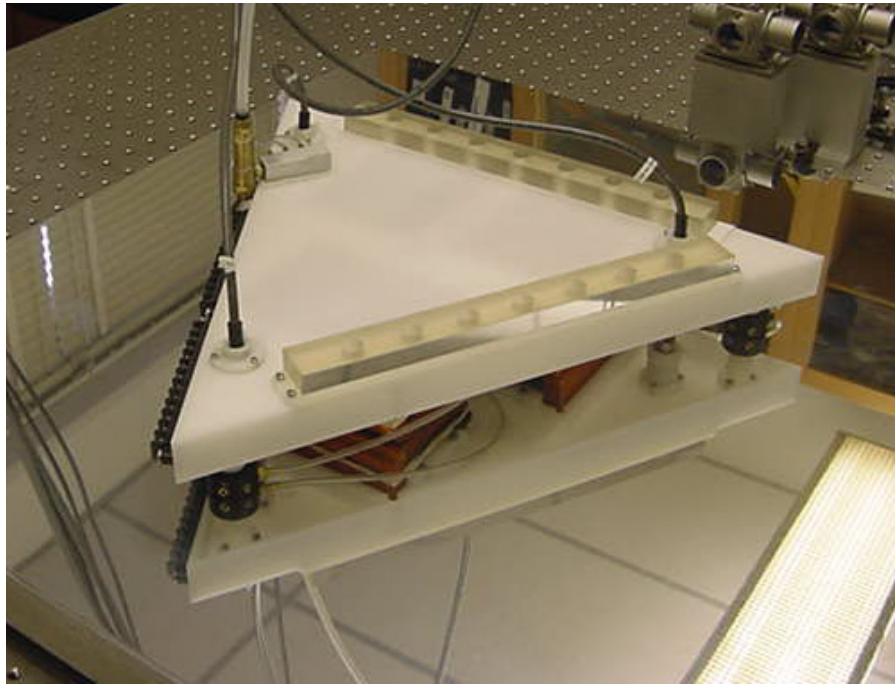
Fig. 1-9 (*a*) Picture of the six-degree-of-freedom positioner with high resolution. (*b*) Perspective view of the positioning system.

This positioning technology has potential to satisfy the dynamic performance specifications necessary for next-generation deep-submicron semiconductor manufacturing equipment with significant advantages: (1) A non-contact stage requires no lubricants, does not generate wear particles, is non-contaminating, and thus is highly suited for clean-room environments. (2) Footprint is reduced by superimposing multiple linear motors into one unified actuation system. (3) One moving part can be designed to have high natural frequencies compared with prevailing multi-element stages with complex dynamics. (4) By eliminating complicated mechanical elements, the fabrication cost is reduced and the reliability is increased. Therefore, the development of extended-range 6-DOF high-precision motion generation technology holds promise for future semiconductor manufacturing and factory automation applications.

1.4   Dissertation Overview

This dissertation consists of seven chapters: introduction, mechanical design and assembly, electromagnetic design, dynamic analysis and modeling, control system design and implementation, multivariable control system design and implementation, and conclusions and future work.

Chapter I of the thesis first provides a literature review of the precision motion control technology and its application in precision engineering. Then an overview of the stage technology which is often used in the precision engineering is given. Some widely used actuators in precision motion control, such as piezoelectric motor (PZT), voice coil motor (VCM), variable reluctance motor (VRM), and synchronous permanent magnetic planar motor (SPMPM) are discussed.

Chapter II presents the mechanical design and assembly of the positioning system. The detailed mechanical design procedure and assembly is discussed in this chapter. Chapter III focuses on the electromechanical analysis of the permanent-magnet planar motor. The design concept for the platen and the magnet matrix is determined. A full analysis of the permanent-magnet matrix is covered in the chapter. This chapter also introduced the sensor system and DSP control system. Some critical issues in low-level bus programming such as byte swapping, data format change are also discussed in the chapter.

Chapter IV concentrated on the dynamic analysis and modeling of the system. The dynamics of the system is analyzed using Newton's second law. Then both the decoupled model and the state-space model were developed by using linearization near the operating point. To eliminate nonlinearity in the dynamics, *DQ* decomposition is used in developing the model. Some system parameters are also identified.

Chapter V and chapter VI are control system design and implementation for the system. Chapter V mainly used the classical control algorithm to achieve the precision motion objective. Chapter VI employed multivariable control methodology to control the system. Both of the two chapters include detailed design procedures and experimental results.

In the last chapter, conclusions of the thesis and future work about the positioning system are given. Appendices include mechanical design drawings, real-time control codes, and Matlab files.

1.5   Dissertation Contributions

The dissertation presents the design, construction, and control of a novel integrated 6-DOF high-precision positioning system consisting of a novel superimposed concentrated-field double-axis magnet matrix with a triangular single-moving platen. It has only a single moving

platen with a 5.91-kg mass, and is based on a patented concentrated-field magnet matrix with dimensions of 304.8 mm × 304.8 mm × 12.7 mm. The moving platen carries the multi-phase windings, and the concentrated-field magnet matrix was assembled in the stationary base plate.

Specific contributions of this thesis include: (1) Design and construction of the mechanical system and electrical instrumentation of the multidimensional high-precision positioning system, (2) Analysis and development of the primary dynamic model of the positioning system, (3) Design and implement digital control system which includes both classical single input and single output (SISO) control and advanced multi-input-and-multi-output (MIMO) control methodologies, (4) Experimental verification of nanometer and sub-micrometer level planar position control. Hopefully, this thesis can be a good practical reference in the design and control of permanent-magnet planar motor.

CHAPTER II

ELECTROMAGNETIC DESIGN

In this chapter, detailed electromagnetic design procedure and working principles are discussed. A novel patented concentrated-field magnet matrix based on the Halbach magnet array is first presented. Then the electromagnetic analysis of this magnet matrix is carried out. The digital control structure based on a digital signal processor (DSP) and its hardware setup are also covered.

2.1   Design and Fabrication of Concentrated Magnet Matrix

2.1.1   Halbach Magnet Array

In magnet arrays used for conventional permanent-magnet linear motors, there exists two-sided field if no iron backing is used. In usual cases with the winding on one side of the array, half of the field is wasted. A type of magnet array which provides a magnetic field concentrated on one side of the array was first proposed by Halbach for use in undulators and particle accelerators [69]. The Halbach magnet array has the remarkable property of primarily single-sided field pattern. This type of magnet array differs from conventional arrays in that each adjacent magnet segment is rotated around an axis perpendicular to the direction in which the array extends by a predetermined angle, for instance 90˚ or 45˚. As shown in Fig. 2-1, one spatial pitch of such a Halbach array consists of four blocks of magnets with magnetization rotated by 90° in each successive block. Such a linear Halbach array has $\sqrt{2}$ times stronger field than that

of a conventional ironless magnet array with the same volume, thereby doubling the power efficiency of the linear motor or reducing magnet mass. Such an array was also studied by Marinescu, et al. [70], where it is represented by a two dimensional multiple field expansion via complex variable theory. Abele, et al. [71] represented the magnet array in spherical harmonics and calculated its coefficients. Leupold, et al. suggested a free-electron laser with a pair of permanent-magnet wigglers with a Halbach array [72].

2.1.2   Concentrated-Field Magnet Matrix

Fig. 2-1 shows the novel concentrated-field magnet matrix that produces the constant magnetic field for actuation [73]. This magnet matrix can be produced by the superimposition of two orthogonal Halbach arrays [74] resulting in the plane view shown in Fig. 2-1. In Fig. 2-1 (b), magnet blocks with an arrow have $1/\sqrt{2}$ remanence of the magnets noted with North (N) and South (S) poles, since they correspond to the vector addition of two orthogonal vectors rather than parallel vectors. Shaded blocks with solid arrows tip up at 45° whereas shaded blocks with hollow arrows tip down at 45°. Magnetic field cancellation occurs in the blank squares. The Halbach array has a stronger fundamental field by a factor of $\sqrt{2}$. This will also be the case with the two-dimensional magnet matrices, since the magnetic fields obey linear superposition. By using such an array higher power efficiency can be achieved than those which utilize conventional magnetization patterns. This innovative magnet matrix will play a key role in the development of the unified motion generation technology. As mentioned earlier the magnet matrix in the positioner is present in the stationary base plate. The number of pitches on the magnet matrix determines the travel range of the positioner. In the prototype design the whole

magnet matrix has 6 pitches in the *x*- and *y*-directions, respectively, to have a 160 mm × 160 mm planar travel range.
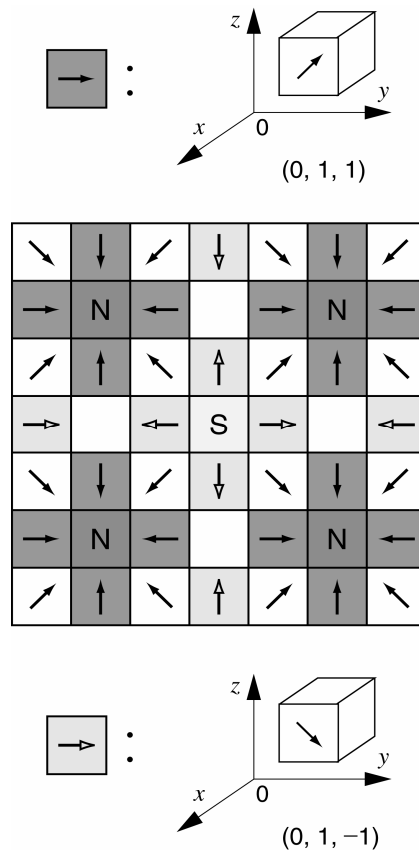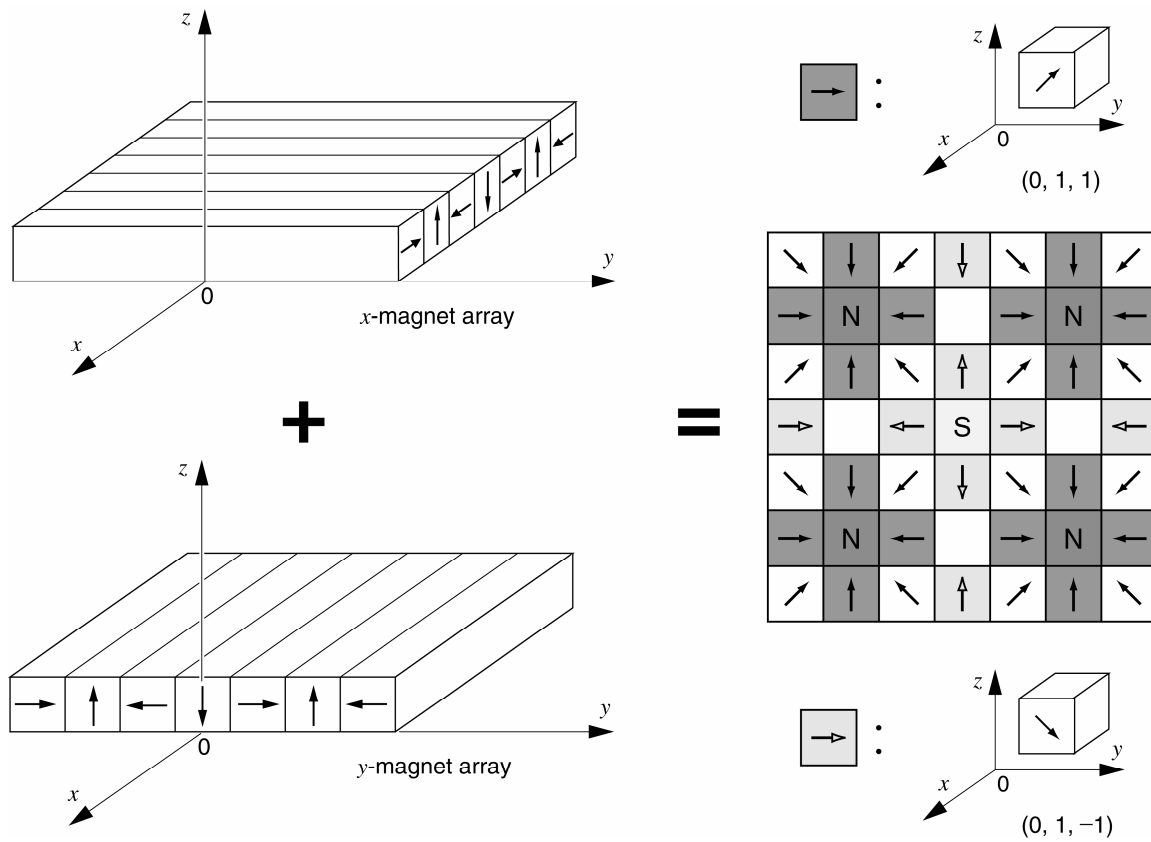

Fig. 2-1 (*a*) Conceptual superimposition of the two orthogonal Halbach magnet arrays to produce a concentrated-field magnet matrix. (*b*) Top view of the concentrated-field magnet matrix. In the current prototype positioner, there are 24 × 24 individual magnet pieces in the matrix.

2.1.3 Magnet Specifications

Various magnetic materials like alnicos, ferrites, samarium-cobalt, neodymium-iron-boron (NdFeB) are available. Alnicos have low coercivity, ferrites have low remanence, and samarium magnets are expensive [75]. Therefore NdFeB material was considered to be the most

suitable material for the concentrated-field magnet matrix. However, since NdFeB material corrodes easily, proper coating is required for any application. One of the coating methods, nickel coating, proved to be inappropriate for adhesion of epoxy. Phenolic resin coating was considered most appropriate for this application, as epoxy adheres to it very well. The magnet matrix used has two kinds of magnets. One is a strong magnet with 90˚ magnetization. NdFeB50 material was chosen for the strong magnet which has a residual flux density of 1.43 T. The other magnet used was a weak magnet with magnetization in 45˚. NdFeB30 with a residual flux density of 1.10 T was chosen as the material for the weaker magnets. Both the weak magnets and strong magnets were of dimensions 0.5 × 0.5 × 0.5" with a dimensional tolerance ±0.002". To distinguish the two magnets from each other, we had specified two chamfers on the weaker magnet and one chamfer on the stronger magnet as shown in Fig. 2-2. The magnets were purchased from Magstar Technologies.
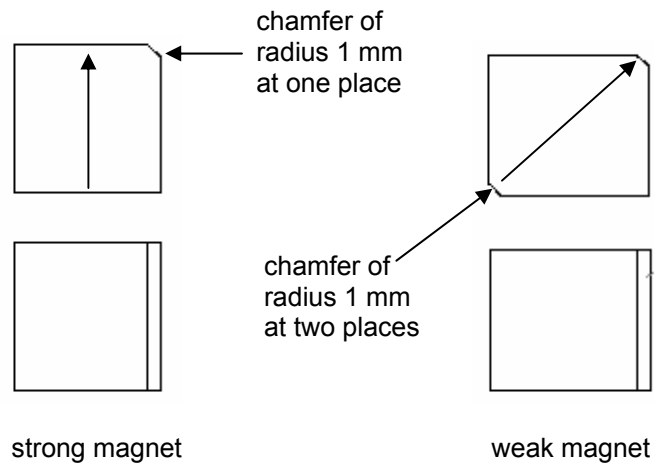
Fig. 2-2 Magnet specifications [after Bhat]

2.1.4   Fabrication of the Concentrated-Field Magnet Matrix

The design and fabrication of the concentrated field magnet matrix was based on Dr. Won-jong Kim's US patent [68, 74]. One of Dr. Kim's former students, Nikhil Bhat, supervised and helped fabricate the concentrated-field magnet matrix and the base plate. The magnet matrix consisted of a total of 432 weak magnets, 72 strong magnets and 72 aluminum spacers of dimensions $0.5 \times 0.5 \times 0.5$" with a dimensional tolerance of ±0.002". To glue the magnets together, PC-7 epoxy was chosen as it adheres very well to the phenolic resin coating. Gluing of the magnet array was a significant challenge, as the magnets during gluing have to be held at all the faces to prevent them from either flipping or coming out of the matrix. The magnet matrix was present in an aluminum base plate of $24 \times 24 \times 1.5$". It contained a pocket of $12.125 \times 12.125 \times 0.540$" for the magnet matrix. The epoxy thickness between the magnets was 0.010". Fig. 2-3 shows the magnet assembly in its preliminary stage.
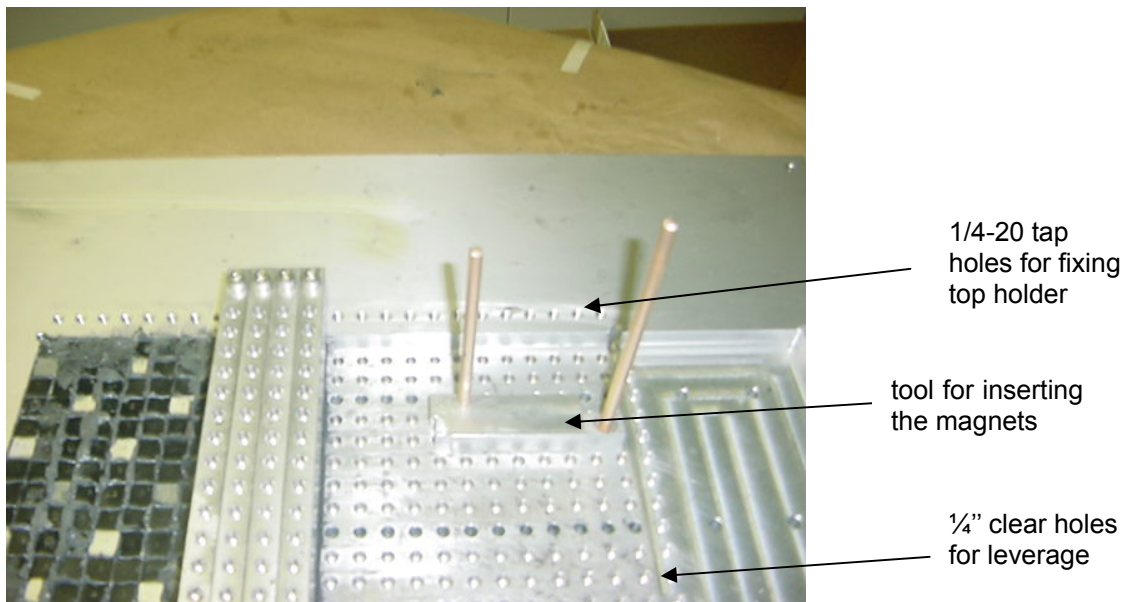
Fig. 2-3 Assembly process of the magnets [after Bhat]

For assembly, 1/4-20 tap holes were made on the base plate at 24 places on each side to fix the top holder of the magnets. Then ¼" clearance holes of depth 0.5" were made in the pocket at 576 places at distances of 0.5" from each other such that each hole is exactly at the center of each magnet. These were made to give leverage to the tool, which was designed to push the magnets next to each other in the matrix. During the assembly, initially the top holder was sprayed with E408 Dry Film Mold Release by Stoner, so that the epoxy does not stick to the top holder while gluing the magnets. Then the top holder was fixed in place over the row being assembled. It consisted of 24 brass set screws at a distance of 0.5" from each other, such that when the magnet was placed, the set screw over that particular magnet was tightened, preventing the magnet from moving. Then the orientation of the magnet was fixed using the pole finder manufactured by Walker Scientific Corporation. To give the epoxy a very good surface for gluing, the magnet coating was very lighted roughed using fine sandpaper. After sanding the magnet, the required layer of epoxy was applied, and the magnet was placed in the tool, and pushed into the correct location using the tool. The tool to push the magnet was the result of experience with pushing the magnet in by hand. Initially when the assembly of magnets was started, we tried to push the magnets in by hand, but the magnetic force was very strong and it took a lot of effort in pushing in the magnets by hand. So this tool was designed. As shown in Fig. 2-4, it consisted of a channel of dimensions $2.544 \times 0.510 \times 0.513$" with a plunger behind it having a hole for providing the leverage for pushing the magnet. The channel prevented the magnet from flipping. As mentioned earlier the magnet with the correct orientation was placed in the channel then the locating rod was used to locate the position where the magnet was to be inserted. After that the plunger was used with the locating rod to push the magnet into its correct position. After the magnet was positioned correctly the top holder set screw was brought down

and tightened lightly to prevent the magnet from moving. This process was repeated for 24 magnets in a single row.

brass rod for leverage

brass locating rod

aluminium plunger
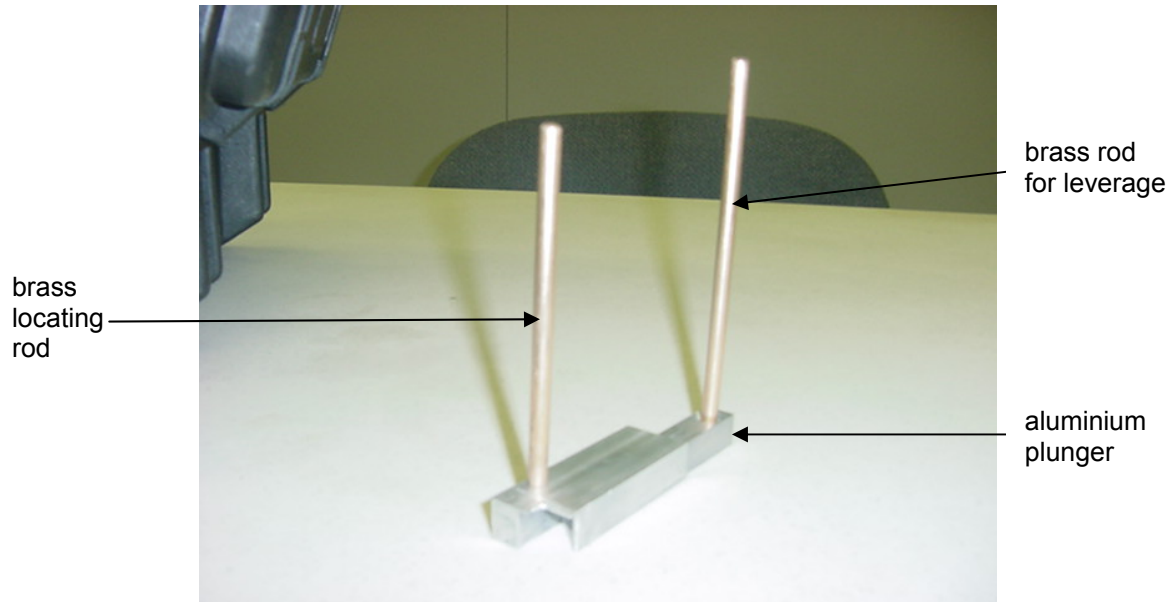
Fig. 2-4 Tools for inserting the magnets into the correct position [after Bhat]

After the completion of one row, all the set screws in the holder were reexamined to ascertain that equal amount of force was applied to each magnet. The top holder was kept in this position for 24 hours to allow the epoxy to cure completely. Then next row was assembled using a similar method with a new top holder. In one single day we were able to assemble 4 rows. After 4 rows were assembled, a teflon block was placed next to the last row. Then an aluminum block was placed next to the teflon block and two clamps were used to clamp the entire assembly. A teflon block was used because epoxy does not stick to the teflon block. Fig. 2-5 (a) shows the magnet matrix after completion of four rows and (b) shows the completed concentrated-field magnet matrix.
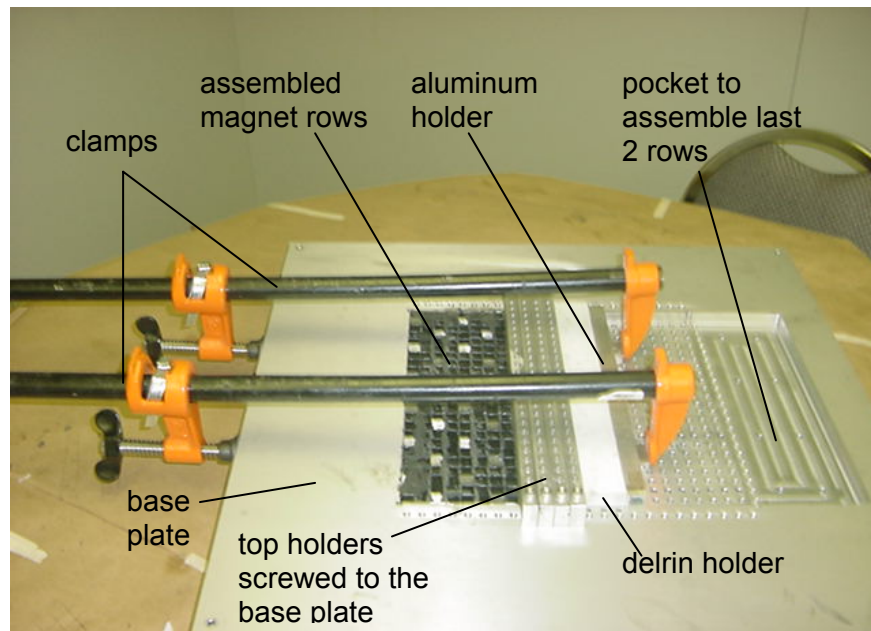
(a)
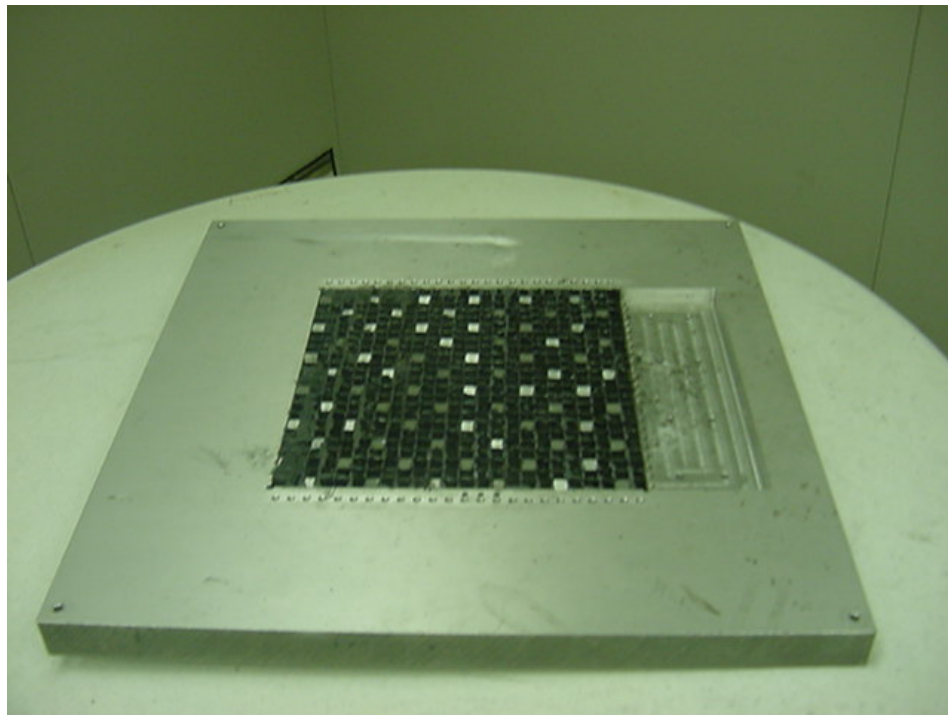
(b)

Fig. 2-5 (*a*) Magnet matrix after the completion of one set of four rows. (*b*) Completed concentrated-field magnet matrix.

2.1.5   Fabrication of the Base Plate

After the entire magnet matrix was assembled in the base plate, the pocket which was opened in the base plate for facilitating the assembly of the last two rows, was closed by tightly fitting an aluminum block of the exact same dimension of the pocket as can be seen in Fig. 2-6 (a). The block had four ¼-20 tap holes at the bottom. So four ¼-20 screws were used to fix the block into the base plate. During the assembly of the magnets some excessive epoxy which was squeezed out between the magnets and formed high points on the matrix which can be seen in Fig. 2-6 (a). To remove this excess epoxy, a very sharp razor blade was used. Air bearings, which are critical in providing the levitation for the positioner, require a very good surface finish of ±20 μm. To achieve this over the whole magnet matrix was a big challenge. Initially the gap between the surface of magnet matrix and the base plate was calculated after measuring thickness of the aluminum base plate and the magnet matrix by using a CMM. Then, a 0.050"-thick layer of epoxy was spread over the whole magnet matrix as shown in Fig. 2-6 (b).

As it can be seen in Fig. 2-7 that, after the epoxy was cured, the base plate was mounted over a big chuck of a lathe, and by using a long facing tool, the surface was faced and 0.030" of material was removed. So the thickness of epoxy over the magnet matrix became 0.020". After the finishing was completed, the entire surface was flat. The epoxy after machining has small pores as we had anticipated. So to get the good finished surface of known thickness for the optimum performance of the air bearings, mirror finished aluminum sheet with surface roughness of 0.1 μm dimensions 24 × 24 × 0.040" bought from MacMaster is placed over the entire base plate. Although the eddy current damping effect produced between the aluminum sheet and the base plate prevented it from moving, several adhesive tapes were used to fix the sheet to the base plate to prevent the aluminum sheet from warping.
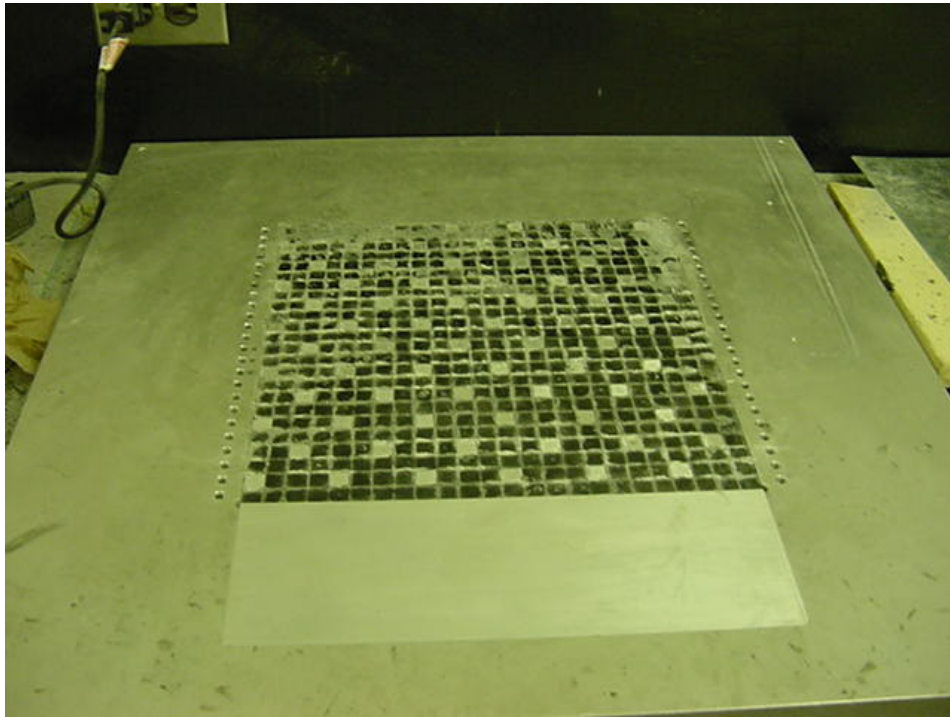
(a)
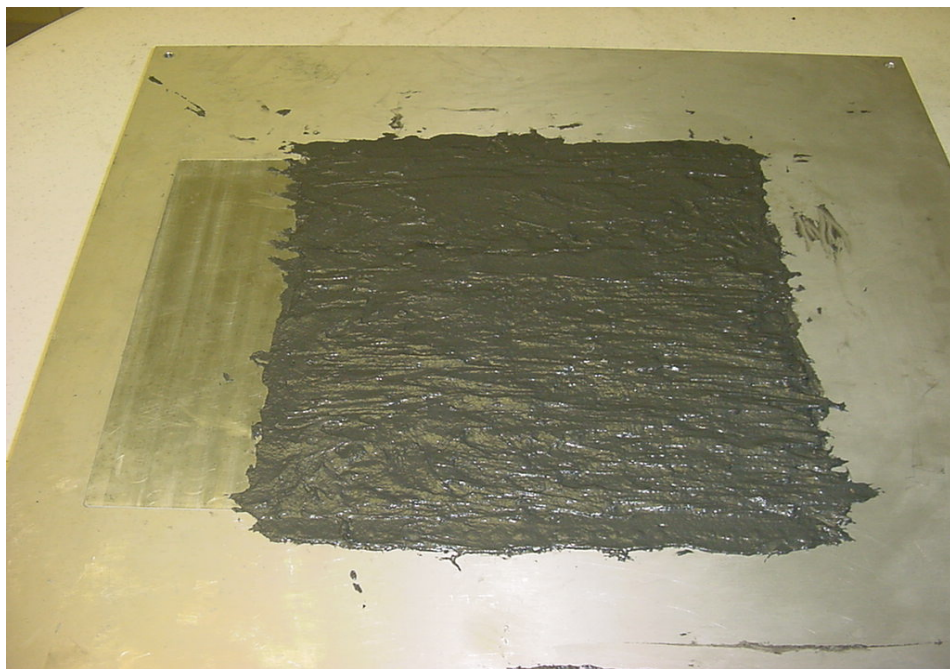
(b)

Fig. 2-6 (*a*) Magnet matrix base plate after closing the pocket. (*b*) 0.05'' thick layer of epoxy covered magnet matrix. [after Bhat]

(a)

(b)

Fig. 2-7 (*a*) Large-chuck lathe. (*b*) Picture of the unfinished base plate with epoxy layer mounted on the big chuck lathe with long facing tool. (*c*) The base plate is under facing and the excessive epoxy was faced off.
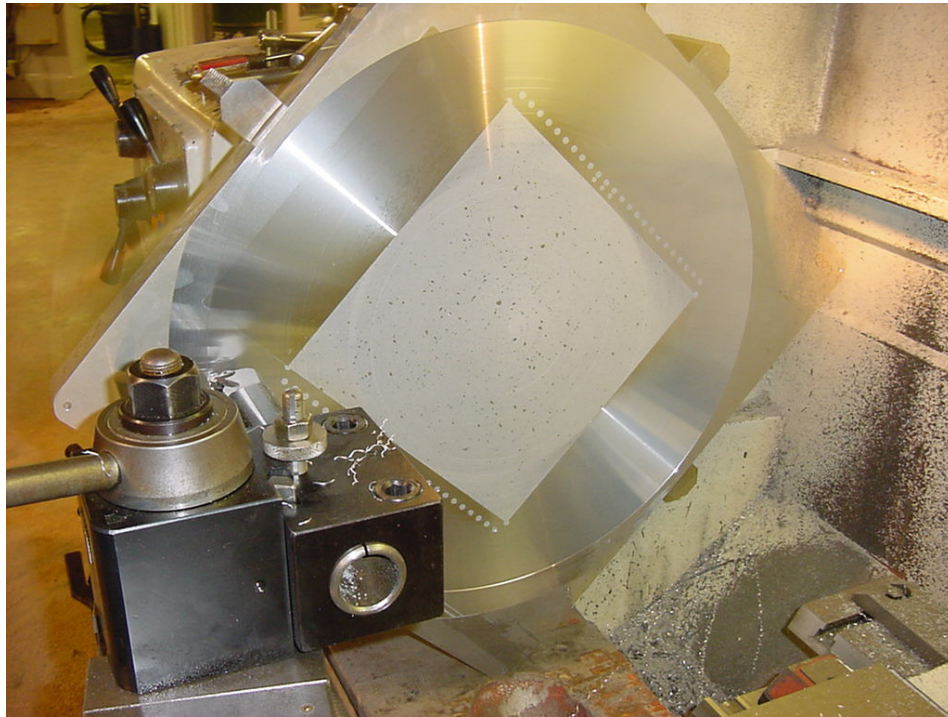
(c)

Fig. 2-7 continued

2.2   Design and Assembly of the 3-Phase Planar Motor

2.2.1   Motor Windings

The planar motor consists of coil windings. There are at least four types of windings for planar motor: (1) single-layer winding, (2) double-layer winding, (3) triangular winding, and (4) wrap-around winding which is termed as a Gramme-type winding. Gramme-type winding was found to be the most suitable for the positoner [76].

Fig. 2-8 shows the shape and dimensions of the stator winding which is 0.3345" thick. Twelve windings are stacked side by side to form one planar motor. Each of the three phases consists of four such windings in series. One such winding has three hundred and five turns with

AWG#24 heat bondable wire (diameter of 0.0213"). To maintain a good flatness of the bottom surface, the leads of each winding are soldered inside of the motor, and also at the short sides of the windings.
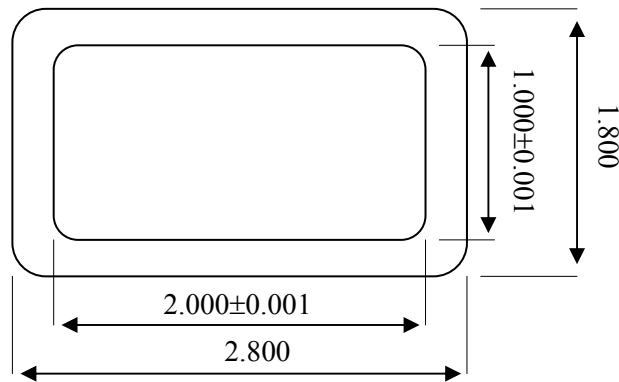
Fig. 2-8 Dimensions of the motor winding

Determining winding parameters such as, thickness of wire, number of layers, number of turns, along with the peak phase current and terminal voltage required a lot of design iterations. The final winding specifications were as follows: according to the wire specifications AWG#24 has resistivity of 0.02567Ω/ft. The resistance of one winding was measured to be 5 Ω, which matched the calculated value. The number of turns is 305. The cross sectional area of one winding was 8.6534×10^{-5} m^2. A preliminary force calculation indicated that at a nominal current density of 2×10^6 A/m^2 the force generated by the three motors would be sufficient to meet the requirements. At this current density the current flowing through the wire was calculated to be 0.5674 A. As there are 4 windings per phase the resistance per phase was found out to be 20 Ω. So the nominal terminal voltage per phase was calculated to be 11.348 V, which is reasonable.

2.2.2   Motor Assembly

Three delrin cores were designed to attach the windings to the moving part. All the windings were stacked into the delrin cores side by side. The connection of those windings was critical to the planar motor. The assembly of the windings was done as follows. First the first winding *A* was slid onto the core and moved to the farthest end. The windings were placed in such a way that the flat surface of the windings will face the base plate. Then the winding B was slide next to *A*. Then the winding *C* was slid. When the winding *A'* was slid, *A* and *A'* were soldered from inside and a heat-shrinkable tubing was placed on top to insulate the leads. Similarly windings *B'* and *C'* are placed and connected to windings *B* and *C* respectively. This whole process completes assembling one pitch. In a similar way the second pitch is assembled. Then the outside leads of *A'*, *B'* and *C'* of the first pitch are soldered to the outside leads of *A'*, *B'* and *C'* of the second pitch. After all the windings were stacked and soldered together in such a pattern, four screws were used for each motor to press the core tightly onto the bottom surface of the moving part. This completes the assembly of the planar motor, which is shown in the following Fig. 2-9. The flatness of the three planar motor is critical to the magnet force generated by those planar motors. A flat granite table was used as a criteria plane to measure the flatness of the planar motors. Several standard-thickness shims made by 3M were inserted in the pockets which accommodated the windings to adjust the flatness of the planar motors. Finally, the roughness of the whole surface of the planar motor was achieved to be 0.1 mm.
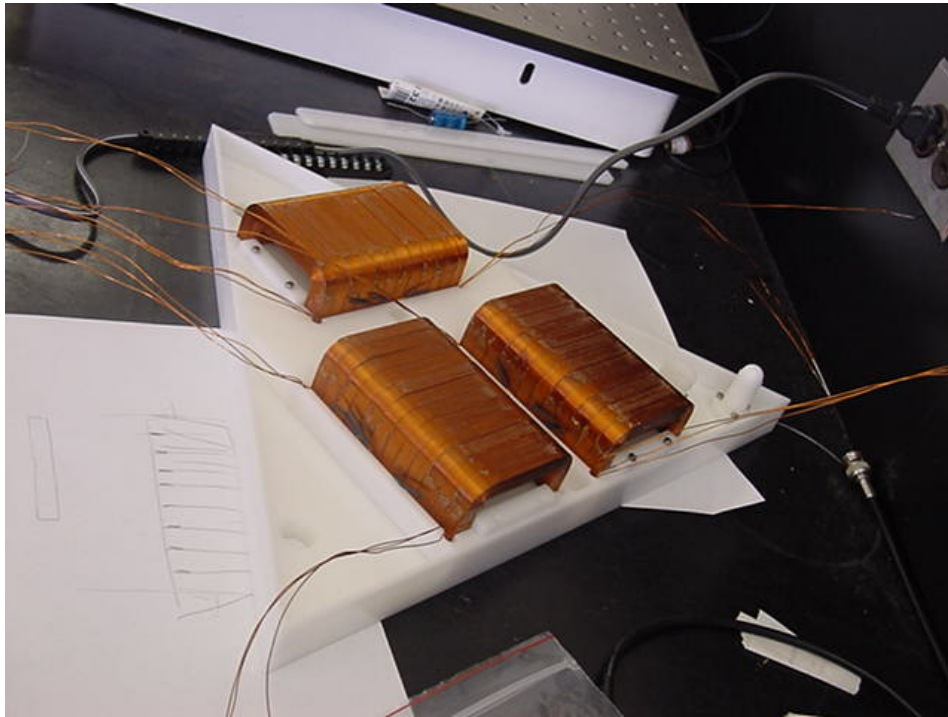
Fig. 2-9 Planar motors are under assembly. (The inner leads of the windings are soldered inside the windings and outer leads are connected in the side of the windings to make a flat bottom plane for the planar motors.)

2.2.3   Working Principle of the Multi-Dimensional Positioner

In Fig. 2-10 (a), on the bottom surface of the single moving part, namely the platen, is attached a two-dimensional superimposed concentrated-field magnet matrix. The stator currents flow in orthogonally interwoven multi-phase *x*- and *y*-windings. The stator current in the *x*- and *y*-windings generate air-gap magnetic field traveling in the *x*- and *y*-directions, respectively. Consequently, the *x*- and *y*-stator currents interact only with the corresponding *x*- and *y*-magnet array component. Fig. 2-11 shows the working principle of this technology. For visualization purpose, the windings were replaced with the sinusoidal waves of the magnetic field generated by the multi-phase stator currents.
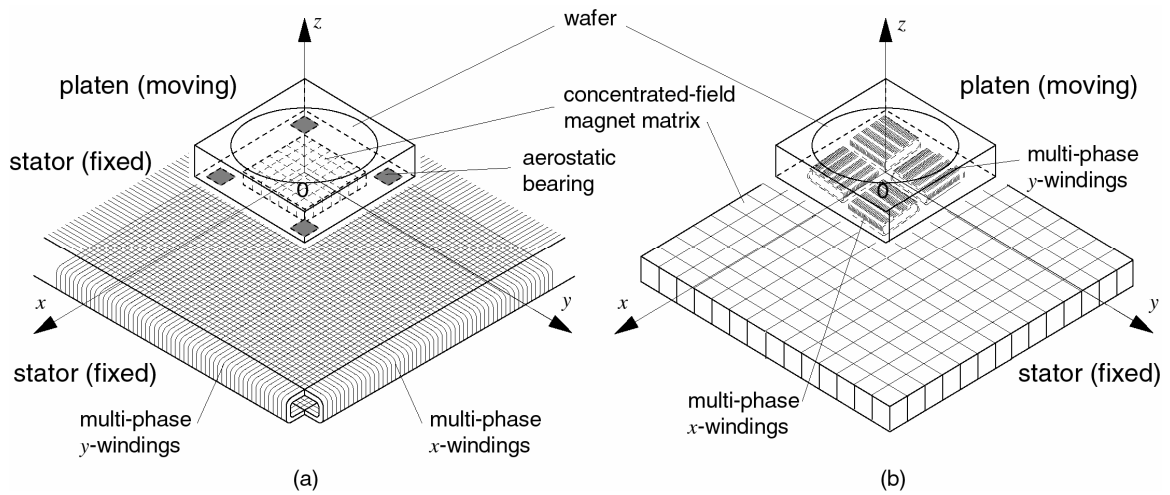
Fig. 2-10 Perspective views of integrated multi-dimensional positioner concepts. (*a*) Moving-magnet-stationary-winding design. (*b*) Moving-winding-stationary-magnet design. [after Dr. Won-jong Kim]
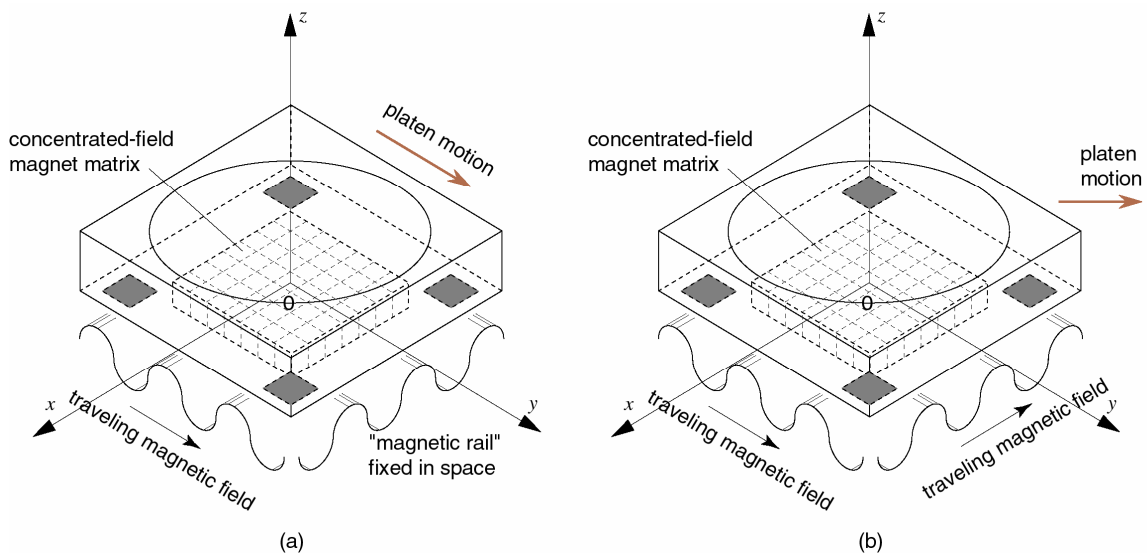
Fig. 2-11   Working principle of the integrated multidimensional positioning technology. (*a*) *y*-directional motion generation. (*b*) Diagonal motion generation. [after Dr. Won-jong Kim]

In Fig. 2-11 (a), the windings in the *y*-direction generated sinusoidal magnetic field. At the same time the magnetic field generated by the *x*-windings is stationary (without commutation)

and serves as a "magnetic rail." As a result, the platen can move continuously in the y-direction and does not move in the x-direction. In part (b), both the x- and the y-windings generate the sinusoidal magnetic field, such that diagonal motion can be generated by controlling the phase currents in the x- and y-windings, independently.

On the other hand, another positioner concept shown in Fig. 2-10 (b) carries the windings that energize the actuation system on the platen. Since only half the power consumed by the windings can be used to generate the magnet force, put more windings in the stationary base plate will consume more power which will require much more powerful power amplifiers for the system. Three winding sets instead of four are decided to be accommodated in the platen, as the four winding sets shown in Fig. 2-10 (b) are redundant to generate 6-DOF motions.

2.3   Design of Power Amplifiers

Power amplifiers supply current to the planar motor. They are important elements in positioning systems. Since three 3-phase planar motors were used in the multi-dimensional system, nine-channel power amplifiers were needed to control the individual phase current in each planar motor. As for a planar motor, the magnetic suspension and drive force was primarily determined by the current flowing in the windings, the power amplifier should provide appropriate current for the planar motors corresponding to the voltage command from those D/A converters. If the dynamics of the power amplifier circuit including the winding is fast enough, compared with the mechanical dynamics of the system, the power amplifier dynamics can be simply ignored in the control loop. Then, the power amplifier can be regarded as a controlled current source for the planar motors.

2.3.1 Power OP Amp

Among many power OP Amps, PA12A by Apex[1] was proven to be a good linear power OP Amp in our previous experience. It matches or exceeds the required current and voltage swings and has a decent voltage slew rate. Fig. 2-12 shows the picture of PA12A power OP amplifier.
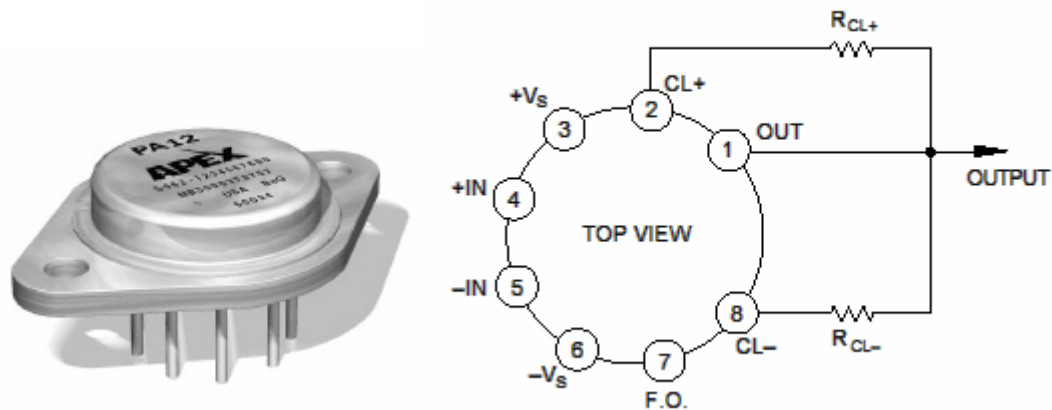
Fig. 2-12 Picture of power OP Amp PA12A and its external connections. [After Apex PA12]

It has the following specifications [Apex PA12 data sheet].

- Wide supply range: ±10 V to ±50 V

- High output current: up to ±15 A peak

- Low thermal resistance: 1.4 ˚C/W

- Power dissipation: 125 W

---

[1] Apex Microtechnology Corp., 5980 N. Shannon Road, Tucson, Arizona 85741

As these power OP Amps may output large current to the planar motor, heat sinks which were provided by Thermalloy were used to lower the temperature of those OP Amps. For safe operation, the output current was limited to 2.0 A by a fuse.

2.3.2   Power Supplies

In order to prevent any electrical noise from going into the system, a linear power supply was chosen to provide power for the power amplifier circuits. It was proved that linear power supply was more desirable for high precision applications. Take the ripple errors of linear and switching power supply as an example, the ripple errors of linear power supplies were 5 mV but those of switching power supplies were typically 150 mV.

Considering the power capacity of the system, two LZS-250-3 power[2] supplies were used. It has the followings specifications.

- Output voltage range: 18.0 – 29.4 V

- Output current (@ 40 ˚C): 12.5 A

- Ripple and noise (@ 20 MHz bandwidth): 100 mV (pk-pk)

The current and voltage ratings of the power supply were determined by the power OP Amp ratings and maximum output current to the planar motors. Since the maximum current that will flow in each phase is 1.3 A, the maximum input current should be larger than $1.3 \times 9 = 11.7$ A (the planar motors altogether have 9 phases). It can be seen that the LZS-250-3 satisfies the maximum current requirement for the system.

---

[2] Lambda Americas, 3055 Del Sol Blvd, San Diego, CA 92154

One HDC-15 power supply purchased from Lambda Americas Inc., was used to supply power to the operational amplifiers (TL072). This power supply has dual output voltage of 15 V and current of 3.4 A.

2.3.3 Power Amplifier Circuit

The power amplifier is shown in Fig. 2-13. This circuit consists of three main parts: differential amplifier, feedback amplifier, and power booster. The differential amplifier blocks common-mode input signals from the D/A converter and it also serves as a low pass. The accuracy of those resistors R_1, R_2, R_3, and R_4 in differential amplifier was critical to realize the function of the differential amplifier. The selected resistors all had an accuracy of 10 ± 0.001 kΩ. A feedback amplifier was designed to stabilize the current control loop.

In the power booster part, R_{10} with resistance of 1 Ω was used as a current sensor to measure the current flowing through the winding of planar motor in realtime. That is because the feedback gain resistor R_7 (1.3 kΩ) had a much larger resistance than R_{10} almost all the phase current through the winding flows through the sensing resistor. Since the resistance of R_{10} is 1 Ω, the numerical value of voltage across R_{10} was equal to the numerical value of phase current. Then this value was feedback to the second TL072 OP Amp, which serves as a proportional-integral (PI).
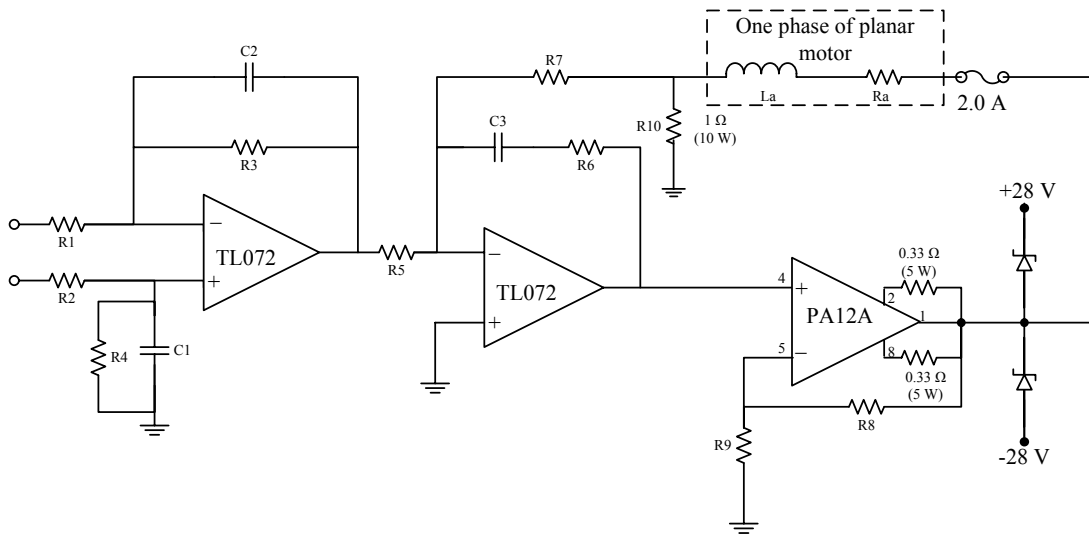
Fig. 2-13 Power amplifier circuit

By Laplace transform, the transfer function of each subsystem can be derived. The whole system can be presented in the following block diagram in s domain as shown in Fig. 2-14. Here the V_i is the differential input voltage to the system and V_o is the corresponding output voltage to the windings. Special attention must be paid for the transfer function of $\dfrac{1}{1 + R_1 C_1 s}$, since it is based on the fact of $R_1 = R_2 = R_3 = R_4$.
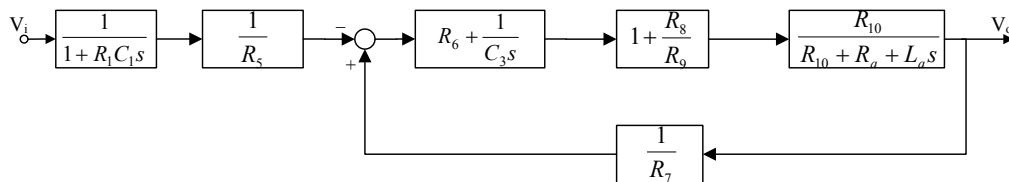
Fig. 2-14 Transfer function block diagram of power amplifier system
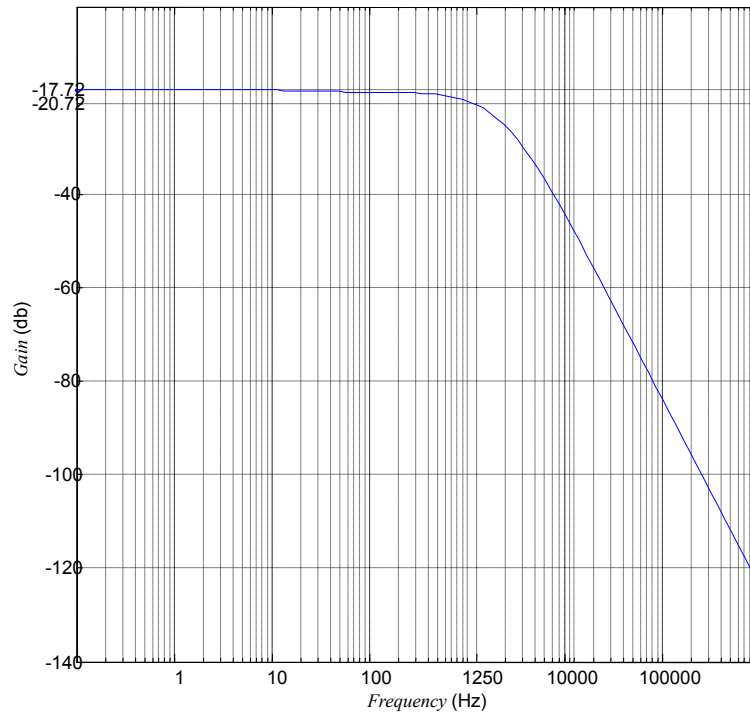
Fig. 2-15 Frequency response of power amplifier

The element parameters in the power amplifier circuits were designed as following: $R_1 = R_2 = R_3 = R_4 = R_5 = R_8 = R_9 = 10$ kΩ, $= R_6 = 82$ kΩ, $= R_7 = 1.3$ kΩ, $= R_{10} = 1\Omega$, $C_1 = C_2 = C_3 = 0.01$ μF, Ra = 19.44 Ω, La = 15.26 mH. As a result, the amplifier closed-loop bandwidth was 1.3 kHz, which can be seen from Fig. 2-15. Considering that the mechanical dynamics and overall control bandwidth will not exceed 100 Hz, the dynamics of the power amplifier can be ignored.

After the power amplifiers were built, they were tested to demonstrate its capability of supplying required current to the planar motors. In this test, the power amplifiers were connected to a single winding, which has a resistance of 4.98 Ω. The input of the power amplifier was connect to the digital/analog (D/A) converters output. The power amplifier was supposed to

output ± 1.3 A current corresponding to the D/A converters output of ± 10 V. The testing results were shown in Table 2.1.

Table 2.1 Power amplifier and D/A converters test results

Board/Channel		0x000	0x400	0x800	0xc00	0xfff
1-1	V (V)	-10	-5.02	N/A	5.02	10
UP	I (A)	-1.278	-0.640	0	0.639	1.276
1-2	V (V)	-10.1	-5.03	N/A	5.01	10
DOWN	I (A)	1.29	0.639	-0.004	-0.646	-1.287
2-1	V (V)	-10.1	-5.05	N/A	5.04	10
UP	I (A)	-1.29	-0.649	-0.005	0.639	1.281
2-2	V (V)	-10.1	-5.06	N/A	4.99	9.99
DOWN	I (A)	1.291	0.644	-0.004	-0.653	-1.3
3-1	V (V)	-10.0	-5.02	N/A	5.07	10.1
UP	I (A)	-1.285	-0.646	-0.005	0.635	1.274
3-2	V (V)	-9.98	-4.97	N/A	5.09	10.1
DOWN	I (A)	1.300	0.65	-0.002	-0.654	-1.305
4-1	V (V)	-10	-5.01	N/A	5.04	10.01
UP	I (A)	-1.258	-0.645	-0.004	0.637	1.277
4-2	V (V)	-10.1	-5.02	N/A	5.04	10.0
DOWN	I (A)	1.282	0.64	-0.005	-0.649	-1.291
5-1	V (V)	-10	-5	N/A	5.07	10.1
UP	I (A)	-1.284	-0.646	-0.005	0.634	1.273
5-2	V (V)	-10.0	-5.01	N/A	5.04	10.0
DOWN	I (A)	1.293	0.646	-0.002	-0.651	-1.298

2.4   Instrumentation Structure

Fig. 2-16 shows a schematic diagram of the instrumentation structure of the multidimensional positioning system. The Pentek 4284 board with a TMS320C40 DSP is employed for the real-time digital control of the system. Sampling of position data, control variable calculation, and real-time control take place in an interrupt service routine (ISR). A VMEbus (Versa Module Eurocard bus) based PC (VMIC 7751), 3 laser-axis boards (Agilent

10897B) and a DATEL[3] DVME-622 D/A converter board are on the VME chassis along with the

DSP board. The VME PC is used to compile the C codes and downloads the executable file to

the DSP and to transfer the commands in real time via user interface during the system operation.

This communication between the DSP and the VME PC is established via a dual-port memory

on the Pentek 4284 board.
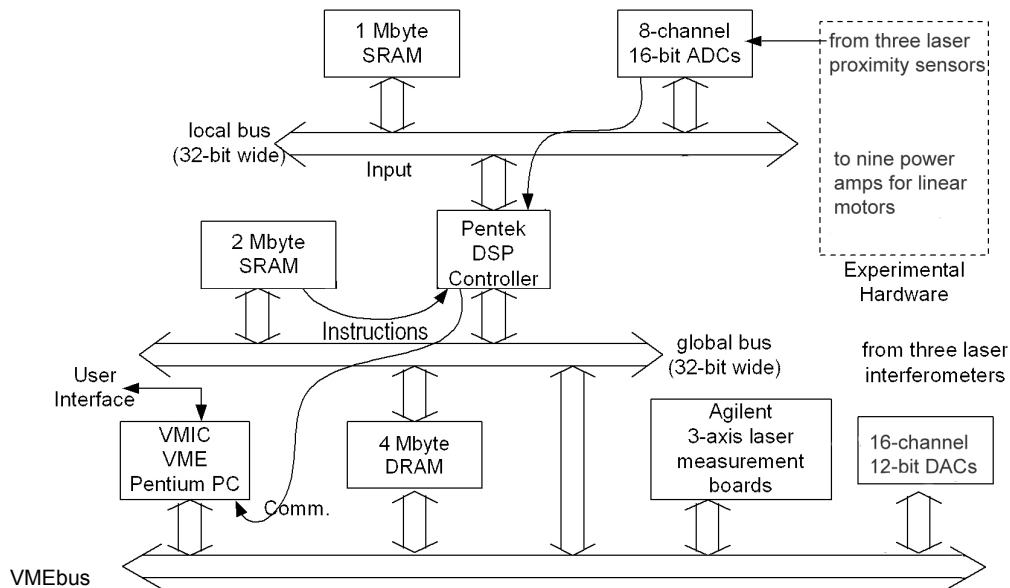
Fig. 2-16 Schematic diagram of the instrumentation structure

The laser interferometer system consists of a laser head, three laser interferometers,

beam benders, beam splitters, receivers, plane mirrors, and laser-axis boards. An Agilent laser

head (HP 5517D) is the 632.99 nm HeNe laser source with the 0.5-m/s maximum slew rate for

plane-mirror interferometer. The beam power output is 180 μW ~ 1 mW. Fig. 2-17 (a) shows the

photograph of the laser head.

---

[3] DATEL, Inc., 11 Cabot Blvd., Mansfield, Massachusetts 02048

<div align="center">(a)   (b)</div>
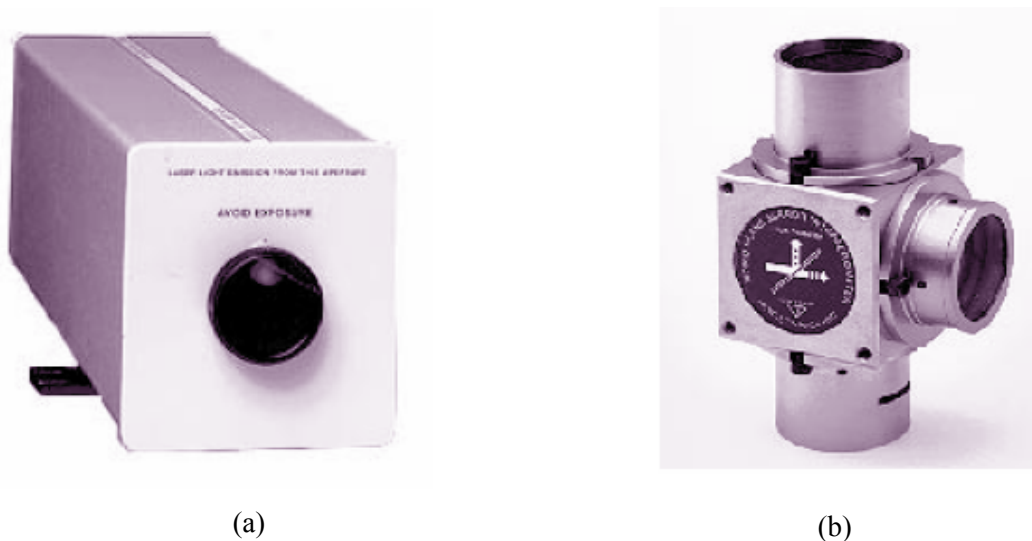
Fig. 2-17 Picture of (*a*) HP 5517D laser head. (*b*) HP 10706B laser interferometer [After optics and laser head data sheet of Aiglent Corp.]

As shown in Fig. 2-17 (b), the three interferometers (HP 10706B) can give the 3-DOF position information (translation in *x*, *y*, and yawn) of the platen at a position resolution of 0.6 nm. Digital 35-bit-position and 24-bit-velocity data are available directly from the laser-axis boards (HP 10897B) at a refresh rate of 10 MHz. Three laser distance sensors (Nanogage 100) are used for position feedback in the vertical mode (translation in *z*, pitch, and roll). The sensors were made of nonmagnetic body, and their response is independent of the magnetic field in which they will operate. They work on the principle of optical triangulation. Their linear measuring range is 100 μm and resolution is 15 nm. They had a bandwidth of 100 kHz. Fig. 2-18 shows the picture of those instruments.
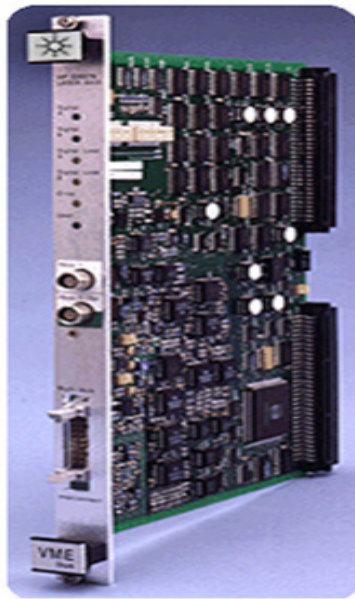
<div align="center">(a)   (b)</div>

Fig. 2-18   Photographs of (*a*) HP 10897B VME bus laser-axis board. (*b*) Nanogage 100 laser distance sensor [After HP 10897 manual and Nanogage 100 datasheet].

These distance sensors pass the 3 vertical-axis position measurements to a data-acquisition board through first-order *RC* anti-aliasing filters with a cut-off frequency of 1 kHz. The data-acquisition system contains 8 channels of 16-bit analog-to-digital converters (ADCs) (Pentek 6102) and 16 channels of 12-bit digital-to-analog converters (DACs) (Datel DVME-622) with the input and output voltage swings of ± 5 V and ± 10 V, respectively. The ADC board communicates with the DSP via the MIXbus while the DAC board, via the VME bus. Nine DAC channels are used to give the control outputs to the 9 transconductance amplifiers. Then, these amplifiers flow commanded currents through the linear motor winding sets to generate the actuation forces.

2.5   Anti-Aliasing Filter and Voltage Clamp Circuit Design

In order to prevent aliasing by sampling, an anti-aliasing filter was designed and implemented right after the output signal of those distance sensors. The anti-aliasing filter is basically a first order low-pass analog filter with a cut-off frequency of 1 kHz. Fig. 2-19 shows the designed circuit.
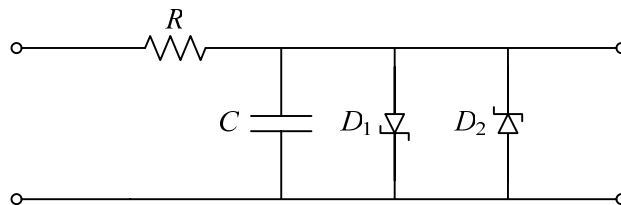
Fig. 2-19 Anti-aliasing filter with voltage clamp circuit

In Fig. 2-19, the resistor R and capacitor C were designed to be 10 kΩ and 0.015 µF, respectively. This low-pass filter was proven in Fig. 2-20 to have a cut-off frequency of about 1 kHz. There are two clamping diodes D_1 and D_2 in the anti-aliasing filter circuit. These two clamping diodes were used to clamp the output voltage of the laser distance sensors to the range of ±5 V, which was the input swing of A/D converters. The clamping circuits were necessary to protect the A/D converters from over-voltage, because when the laser distance sensors went of their measuring range, their output voltage was within ±10 V which may blow out the A/D input channels.
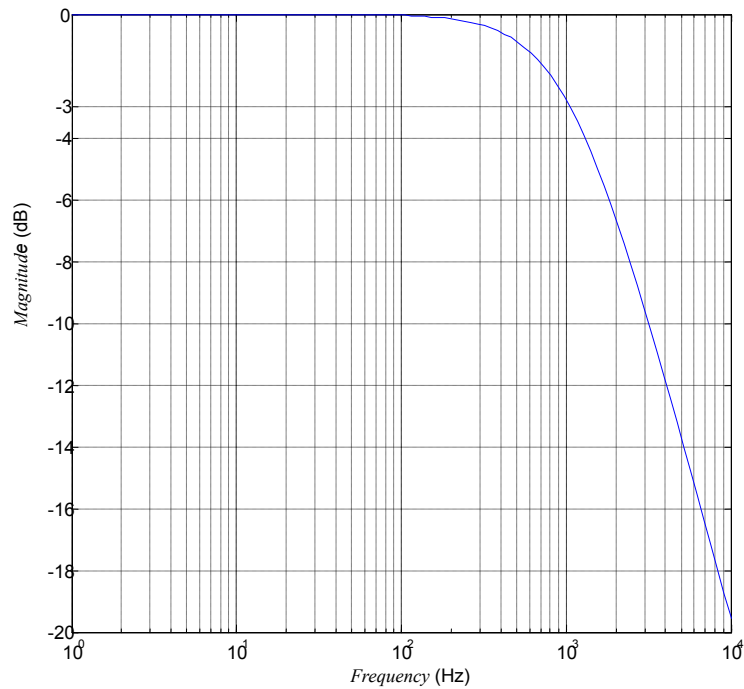
Fig. 2-20 Frequency response of anti-aliasing filter

2.6   Control Structure

2.6.1   Configuration of Control Hardware

Fig. 2-17 shows a detailed hardware schematic diagram of the control structure of the 6-DOF high precision-positioning system, which illustrates how the control and sensor signals go into and out of the DSP. All the sensors and interface circuits are already introduced in previous sections. And the Pentek 4284 board with a TMS320C40 DSP is used to perform the real-time digital control of the system. A VersaModule Eurocard (VME) personal computer is used to compile the C codes and transfer the executable file to the DSP.

```
┌─────────────────┐        ┌──────────────────────────────────┐
│   9-Channel     │◄───────│                                  │
│   12-bit DACs   │        │        DSP (TMS320C40)           │
└─────────────────┘        └──────────────────────────────────┘
        │                      ▲                      ▲
        ▼                      │                      │
┌─────────────────┐  ┌──────────────────┐  ┌──────────────────┐
│ 9-Channel Power │  │ Laser-Axis Boards│  │   3-Channel      │
│   Amplifier     │  │                  │  │   16-bit ADCs    │
└─────────────────┘  └──────────────────┘  └──────────────────┘
        │                      ▲                      ▲
        ▼                      │                      │
┌─────────────────┐  ┌──────────────────┐            │
│                 │─►│ Laser Interferom-│            │
│   6-DOF High    │  │ eters and        │            │
│   Precision     │  │ Receivers        │            │
│   Positioner    │  └──────────────────┘            │
│                 │  ┌──────────────────┐  ┌──────────────────┐
│                 │─►│ Laser Distance   │─►│  Anti-Aliasing   │
│                 │  │ Sensors          │  │    Filters       │
└─────────────────┘  └──────────────────┘  └──────────────────┘
```
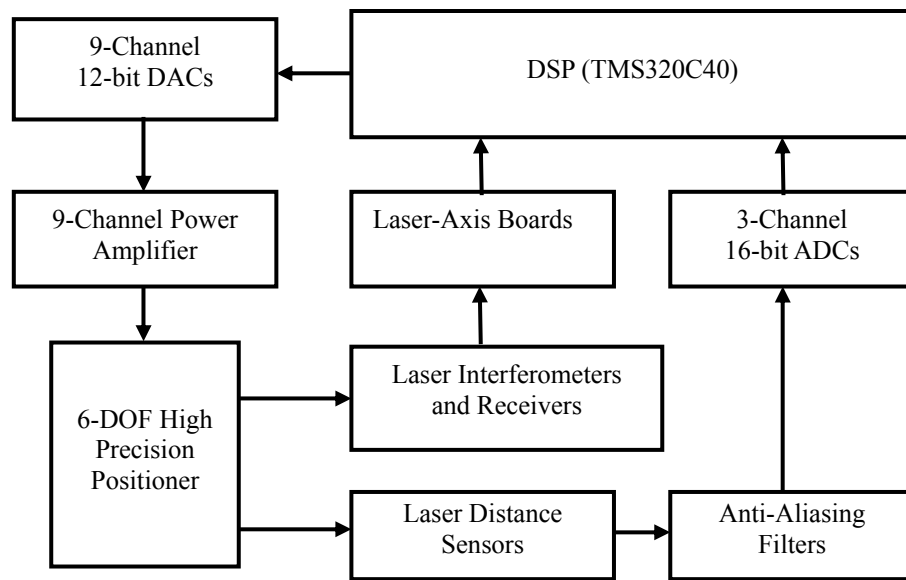
Fig. 2-21 Diagram of the control structure

An interrupt service routine (ISR) we developed, which processes all the position measurement data and computes the control outputs for the positioner, runs on the DSP at a sampling frequency of 5 kHz. Once the control outputs are calculated, they are sent to a 9-channel power amplifier through 12-bit digital-to-analog converters (DACs). Then this amplifier supplies commanded 9 independent phase currents through the planar motor winding sets to generate the actuation forces.

2.6.2   Control Software

The control software includes two parts. One is the VME PC-based user interface which runs on the VME PC to build a real-time interface between the operator and the DSP. The other is the DSP-based real-time control routine which runs on the DSP and performs the real-time control for the high-precision positioner according to the command from the operator and real-time sensing information. The communication between those two programs was achieved by the dual-port DRAM located in Pentek 4284 DSP board. Most of the original software development

was done by Jie Gu, one of Dr. Won-jong Kim's former students. The control software especially

the user interface used here is a modification of Jie Gu's work.
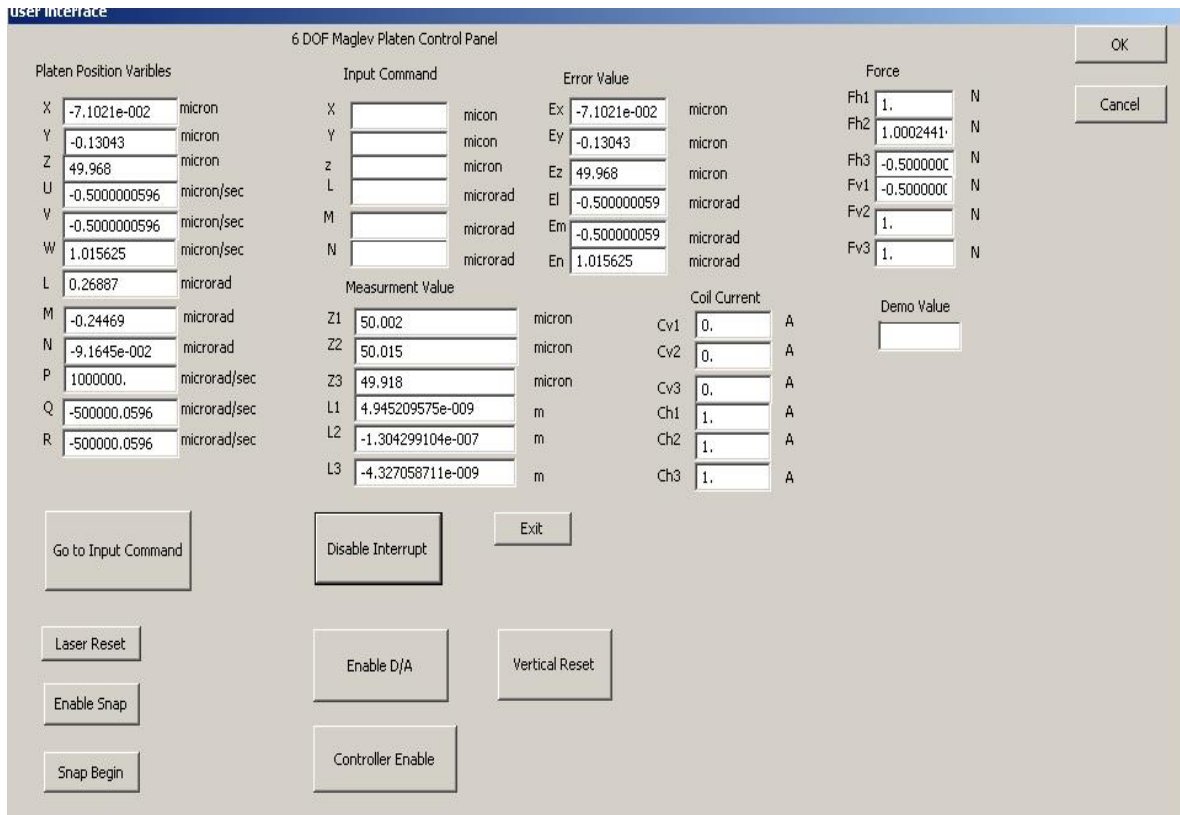
Fig. 2-22 User interface of the high-precision multidimensional positioning system

Fig. 2-22 showed the user interface (control panel) of the system. The user interface

routine was developed on the VMIC VME PC by Visual C++.net. The user can use following

functions from the user interface:

(1) Send user's commands to the DSP. These commands include step commands in all

axes, demonstration commands of different motions for the positioner, and system

initial commands for initializing DSP, A/D and D/A boards, and sensors.

(2) Display the whole system's status in real time. This information let the operator know whether the system runs properly. All the measurement values from the laser interferometers and laser distance sensors will be displayed on the screen in realtime.

(3) Snap and save data into the computer for further use. As mentioned earlier, the DSP communicates with VME PC via a 4-Mbyte dual-port dynamic random access memory (DRAM). In the real-time control routine, DSP will snap all the position information in the DRAM if there is a snap command sent from user interface. After the DSP saved all the data in the DRAM, the user interface routine will read all the data from DRAM and write them into the hard disk of VME PC with the file format of "data.txt."

Some commands and register variables were defined to allocate the physical position in the DRAM. The configuration of memory allocation for the command, and data is shown in Table 2.2.

The TMS320C30/C40 C compiler makes all the data be of 32-bit wide, so that there is no difference among short, int, and long data types. Since the minimum separable address is 32-bit apart, the 320C40's byte size is also 32 bits. However, since the VMEbus uses a byte of 8 bits, a conversion from the address on the VMEbus to the TMS320C40 address is needed when the DSP accesses VMEbus-based modules such as the laser axis boards and the D/A board. Eq. (2.1) shows the conversion formula from VMEbus address to the DSP address.

$$\text{TMS320C40 address} = \frac{\text{VMEbus address}}{4} + 0\text{xb0000000} \qquad (2.1)$$

The real-time control routine running on the DSP was originally edited and compiled in the VME PC by Texas Instrument (TI) TMS320C3x/4x code composer. This code composer is running under the Windows 2000 environment. C language resource codes were first developed

by us. Then they were compiled and built into the executive ASM language for the DSP by the code composer. If no errors were found in the codes, the code composer will download those

Table 2.2 Memory map in the dual-port DRAM

Data Type and Capacity	Detailed Data Type	DSP Address
Commands	PC Command	0x80000000
(0x80000000~0x8000000F)	Snap Command	0x80000001
	Position Command	0x80000002~0x80000007
Control variables and flags	PC_Command_Acknowledge	0x80000010
(0x80000010~0x8000001F)	Snap_Command_Acknowledge	0x80000011
	Interrupt Count	0x80000012
Real-time position and	Platen Position	0x80000020~0x80000025
velocity variable	Platen Velocity	0x80000026~0x8000002B
(0x80000020~0x8000004F)	Measurement Value	0x80000030~0x80000035
	Current	0x80000036~0x8000002B
	Force	0x80000040~0x80000045
Snapped data	$x, y, z, \theta, \varphi, \psi, \dot{x}, \dot{y}, \dot{\psi}$	0x80100000~0x801FFFFF
(0x80100000~0x801FFFFF)		

executive files to the DSP. Since data transfer between VME 8-bit-width bus and the Intel Pentium III processor on the VME PC, there is a byte-ordering problem. In big-endian architectures, the leftmost bytes are most significant. On the other hand, in little-endian the rightmost bytes are most significant. Byte swapping must be done whenever there is a data communication between those two different byte ordering convention systems. SwiftNet which

is a commercial software designed by Pentek can automatically perform the byte swapping. Thus SwiftNet was always running on the background when the DSP is operated.

The whole real-time control routine was developed in the C language. It can be divided into three parts:

(1) main.c is the main body of the whole control routine. This routine initializes all the variables and constants. And it calls several functions to initialize and set up all the input/output (I/O) devices. It also writes real-time information such as position, velocity, and sensors' readings to the dual-port DRAM. When all the initialization and setup were completed, the routine keeps checking the command status from the user interface.

(2) dsp_command.c routine is called by main.c in every looping time to check the command status from the VME PC. Once any command was set by the user, the "dsp_command" routine calls the corresponding functions.

(3) cint_01.c routine was designed as an ISR. The interrupt signal is generated by the programmable Intel 82C54 clock timer counter chip embedded in the Pentek 4284 board. The chip accurately generates 5000 interrupt signals per second. A real-time digital controller was implemented in this routine. In each sampling period, cint_01 reads the sensors and extracts the position information.

Fig. 2-23 (a), (b), and (c) shows a flowchart of these routines. To save space, the flowcharts only illustrate the key processes of each routine. The complete routines are listed in Appendix of this dissertation.
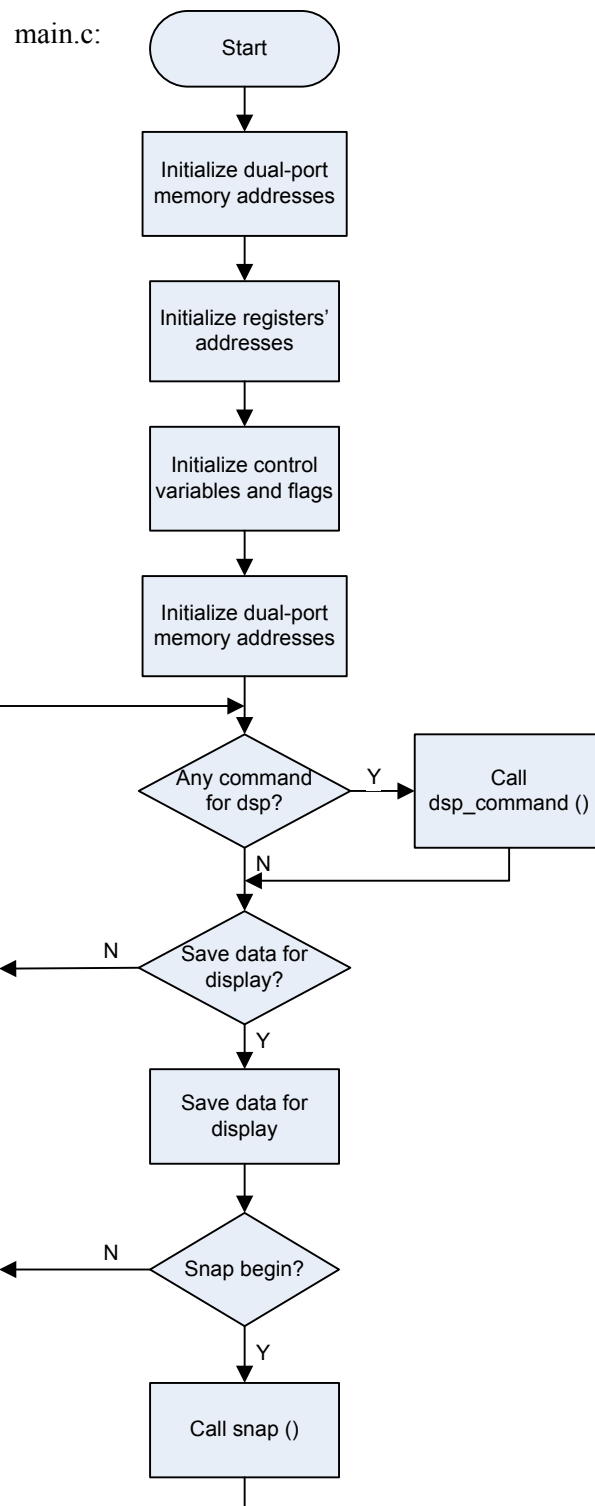
main.c:

(a)

Fig. 2-23 Flowcharts of (*a*) main.c, (*b*) dsp_command.c, and (*c*) cint_01.c

dsp_commmand.c:
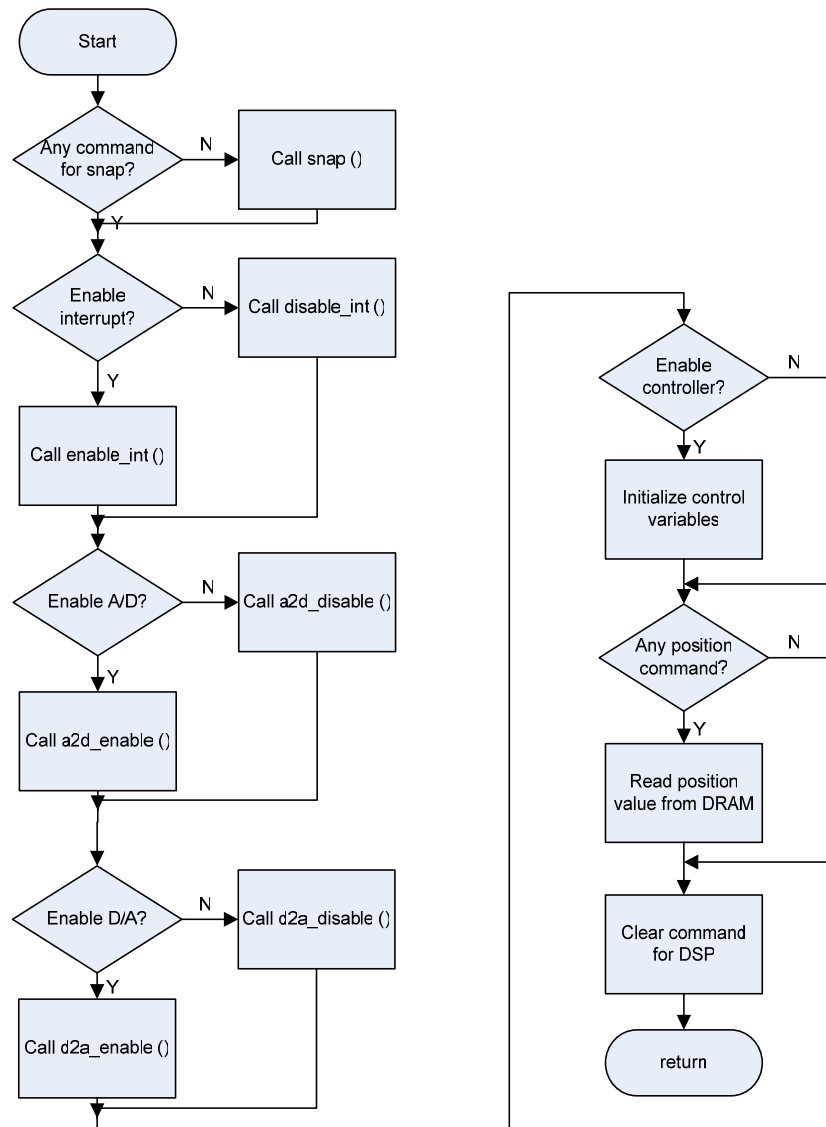
(b)

Fig. 2-23 continued
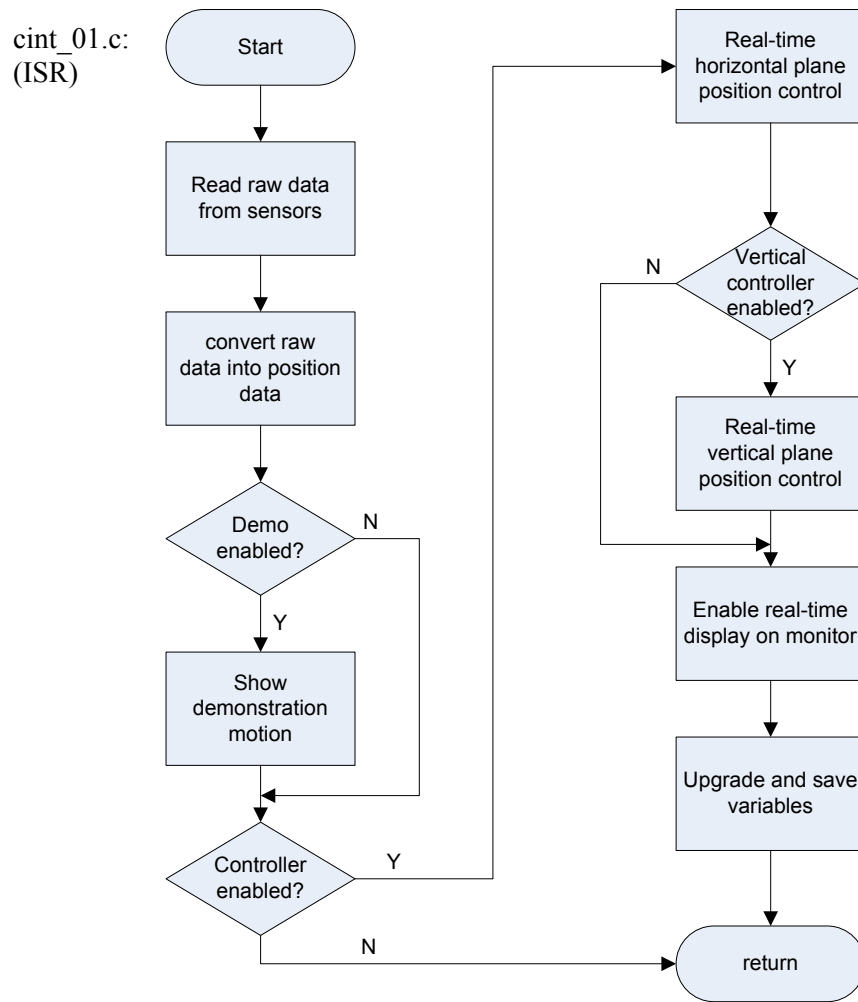
(c)

Fig. 2-23 continued

CHAPTER III

MECHANICAL DESIGN AND ASSEMBLY

In this chapter, the detailed mechanical design of the whole positioner is first explored. The design process of the main parts in the positioner is also explained. With the mechanical fabricated, the assembly process is then illustrated. Mr. Nikhil Bhat, a former student of Dr. Won-jong Kim did most of the mechanical design and help assembly of the positioner.

3.1   Design Considerations

3.1.1   Dynamic Performance Goals

This positioner is supposed to have a capability of both coarse motion and nanoscale positioning resolution. In other words, the positioner should have a long travel range in the horizontal mode and at the same time have a nanometer-level positioning capability. In order to satisfy the requirements in industry, the positioner should also have high precision positioning capability in the vertical mode. The travel range in the vertical direction was within hundreds of micrometers.   And the dynamic response of the positioner should be fast enough to meet the ever-increasing product efficiency in industry. Since the main application of this positioner will be in the precision manufacturing industry, power consumption of the system should be as small as possible to meet the thermal stability requirement.

The specific performance values of the positioner were shown as following:

- Horizontal mode travel range: 200 × 200 mm

- Horizontal angular range (yaw): ±500 µrad

- Vertical mode travel range: ± 100µm

- Vertical mode angular range (pitch and roll): ± 200µrad

- Linear positioning speed capability: 500 mm/s

- Linear positioning acceleration capability: 1 g (= 10 m/s^2)

- 3-σ position noise:

    x, y: 20 nm

    z: 100 nm

    θ (rotation around x), φ (rotation around y), ψ (rotation around z): 0.5 µrad

The single-moving-part design concept presented in this thesis is different from the conventional design in high precision positioning system, which is either a crossed-axis type or gantry type. The only moving part can be designed in a compact structure and has good dynamic properties for precision control. Furthermore, the single light-weight moving part can reduce the power consumption of the system.

3.1.2   Selection of Actuators

The actuators should have the capability of generating 6-DOF forces for the positioner. There are many choices for the actuators. The variable-reluctance motor has inevitable cogging and attraction forces. It is thus difficult to get high-precision position control. The resolution of such a stepper motor is limited by its minimum step, which is usually much bigger than 1 µm.

The multi-dimensional positioner as an SPMPM presented in this thesis overcomes all these shortcomings of the established Sawyer motor technology, and can generate all fine and coarse motions with only a single levitated moving part required for wafer processing.   It

employs a novel superimposed concentrated-field double-axis magnet matrix patented by Dr. Won-jong Kim. The planar motor used in the positioning system can generate both horizontal as well as vertical forces. Thus, 6-DOF motions can be achieved by flowing proper current in the planar motors. The windings of the planar motor were shown in Fig. 3-1. The planar motor was designed to have 3 phases, and each motor consists of two pitches. The electromagnetic working principle is discussed in Chapter IV.

Fig. 3-1 Windings of planar motor

3.2   Design of the Platen

There are two different ways to accommodate the planar motor in a high precision positioning system. One is having the permanent magnet matrix on the stator. The other is having the windings on the stator. If the windings are stationary, since only the permanent magnet matrix will be attached to the mover, namely the platen, there will be no umbilical cable connecting to the platen. In this way, the unbalanced attraction force between the permanent magnet matrix and the platen can be eliminated if no ferromagnetic material is used on the platen. However, there are some drawbacks in this design. If those windings were fixed in the base plate,

much of total power will be wasted. This is because that only the top surface of the windings can generate magnetic field that will interact with the permanent magnets. The more windings used, the more power will be wasted. Therefore, the moving-magnet design concept will make the moving part (platen) much heavier than moving-winding design concept. And more power will be dissipated to control the positioner. As a result, the moving-winding design concept was used in the mechanical structure design for the postioning system. This design concept can also achieve the objective of 6-DOF motion for the system.

So the platen consists of the planar motor windings, while the magnets are present on the stationery base plate. To achieve maximum acceleration and cheap control for the system, the mass of the platen has to be as small as possible. Several different non-ferromagnetic material such as: copper, aluminum, and Delrin®, can be candidates to make the platen. The mass density of them is 8.94 g/cm³, 2.70 g/cm³, and 1.54 g/cm³ respectively. If the platen was made of Delrin, the total mass of the platen will be reduced by 85% and 43% respectively, compared with copper and aluminum. Meanwhile, all the other mechanical properties of Delrin were comparable to those of aluminum. As a result, Delrin was chosen to be the appropriate material for the platen. The platen was designed in an equilateral triangular shape with dimensions of 15". The motivation for the triangular design was to make the system as compact as possible. Three planar motors were used as the actuators in the system. The working principle will be illustrated in Chapter IV.

Fig. 3-2 shows the perspective views of the positioner. There are two high-precision stick mirrors attached on the top surface of the platen. Those mirrors were used to reflect the laser beams to the interferometers. The air supply distributor was used to supply air to the three aerostatic bearing pads. As in Fig. 3-2 (b), the platen carries three windings and three laser

distance sensors. The currents flow into the windings through the terminal blocks mounted on one side of the triangular platen. Although the platen can be levitated by magnetic forces, three
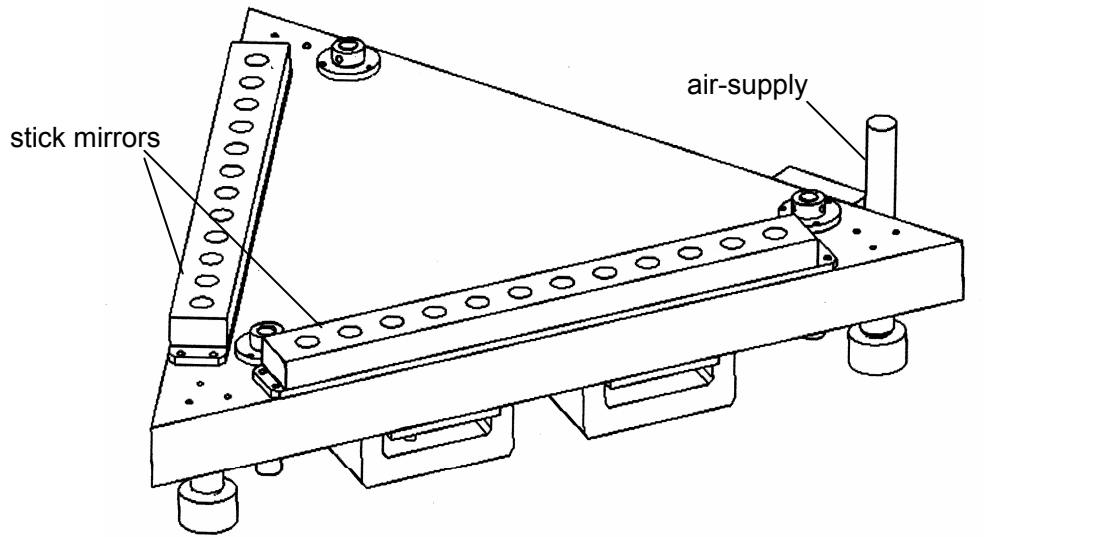
(a)
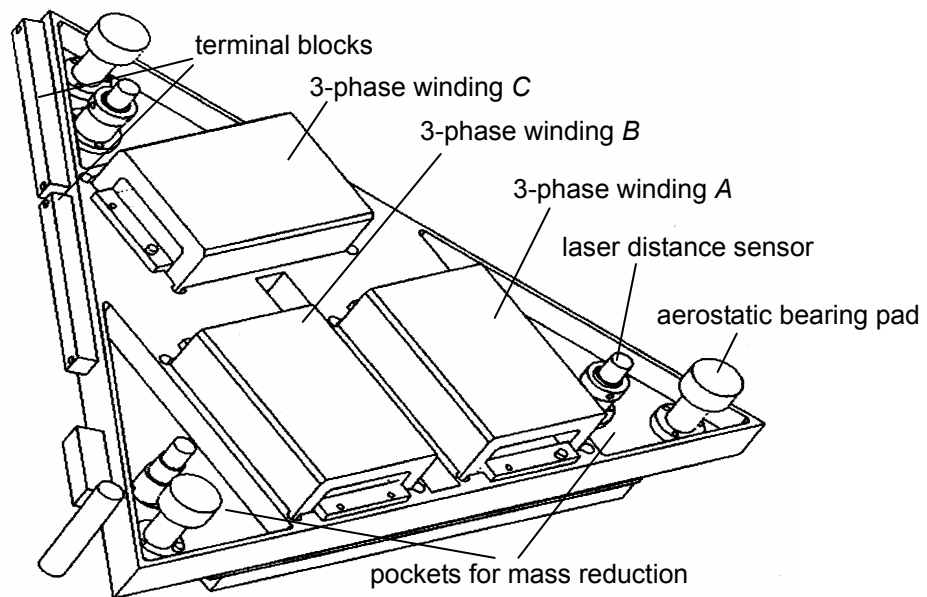
(b)

Fig. 3-2 (*a*) Top and (*b*) bottom views of the platen

aerostatic bearing pads were used to levitate the platen to put most of the power into the dynamics control. By levitating the platen in this way, the vertical force generated by the planar motor can be wholly used to control the motion in vertical direction.

As mentioned earlier in Chapter II the dimension of the coils is $1.8025 \times 2.8580 \times 0.3345$". Twelve coils make one motor, so the overall dimension of one linear motor is $1.8025 \times 2.8580 \times 4.014$". As a result, at the bottom of the platen, three pockets of dimensions $2.959 \times 4.134 \times 0.75$" with a tolerance of ± 0.005" were made to accommodate the planar motor windings. According to the force calculations, the pitch of the system was fixed at 2.007". The distance between the motors was 1 pitch. In order to make the platen have enough strength to bear all the elements, the thickness of the platen was designed to be 1". Three triangular pockets were made to decrease the total mass of the platen.

3.3 Mirror and Mirror Mounting

Fig. 3-3 shows the configuration of the stick mirror and its mount. The length of the mirror is determined by the plane travel range of the platen. And the flatness of the mirror is determined by the positioning resolution of the system. In order to achieve the desired positioning resolution and travel range, two stick mirrors of dimensions $250 \times 25 \times 12$ mm are mounted on the top surface of the platen. Those mirrors made of zerodur with flatness of 31 nm were produced by Bond Optics[4]. To reduce the mass of the mirror, 12 round holes of diameter 9.5 mm were made in the mirror. The mass of one mirror is 177.5 g.

---

[4] Bond Optics, Etna road, Dept. 60H Lebanon, NH 03766
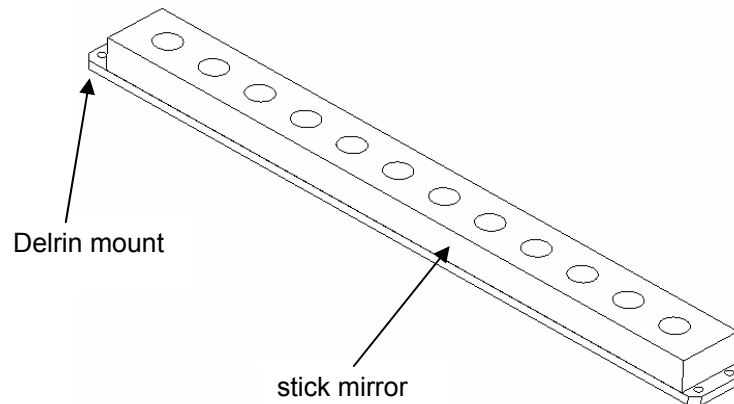
Fig. 3-3 Mirror and its mounts [after Bhat]

A Delrin mount was designed to mount the mirrors. Two 4-40 through round holes were drilled on each side of the mount to fix it to the top of the platen. Double-sided tape by 3M[5] was used to glue the mirror and the mount together. Because the mount is attached by 4-40 screw holes drilled by CNC machine to the platen, once the mirror and mount is parallel in the vertical mode, the mirror will be parallel to one edge of the platen too. To make the mirror and mount parallel in the vertical mode, a granite table was used as a standard surface when sticking them together. After that, the mirror and mount were mounted on the platen by using 4-40 screws.

---

[5] 3M, 3M Center, St. Paul, MN 55144

3.4 Aerostatic Bearing System Design and Assembly

Three aerostatic bearing pads were used to provide levitation to the platen. The model of FP-C-010 produced by Nelson Air Corporation[6] was found to be suitable. The air bearings were made of ceramic and each one could bear a load of 10 kg with the air gap maintained at 25 μm. Fig. 3-4 shows the photo and dimension of the aerostatic pad. These air bearings require approximately 20− 90 psi air supply. Air regulator made by Parker Hannifin[7] was used to regulate the air pressure.
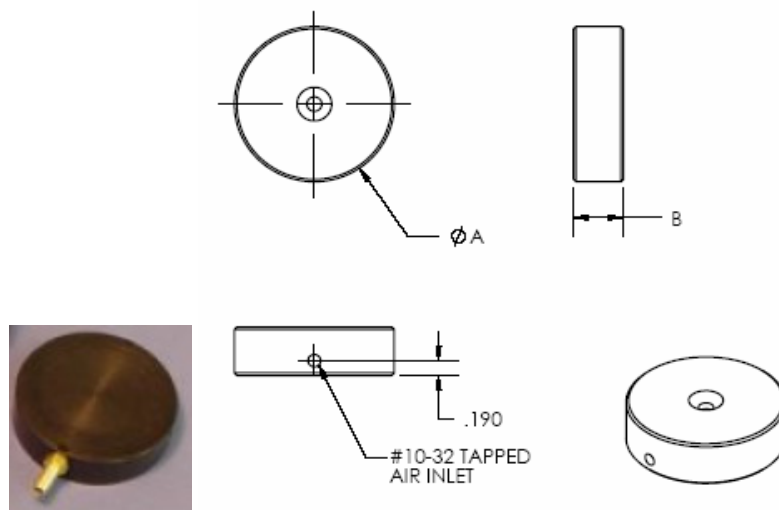
Fig. 3-4 Aerostatic bearing pad [after Nelson Air Corp.]

Delrin mounts were designed to mount the air bearings. A ball joint was designed to connect the pads and mounts. Delrin balls of radius 0.25" were initially used to mount the air bearings onto the air bearing mounts. But it was found that by using 0.25" radius balls, the gap between the motor surface and the base plate surface becomes 0.150". So the Delrin balls were

[6] Nelson Air Corp., 559 Route 13 South, Milford, NH 03055

[7] Parker Hannifin Corp., 2220 Palmer Avenue, Kalamazoo, MI 49001

sanded to a hemi-sphere ball by using fine sandpaper. And their height was reduced to 0.380".

The gap between the motor surface and the bottom surface becomes 0.03" which is 762 μm. Fig.

3-5 shows the assembly procedure of the air bearings. The whole platen sits on the air bearings

through the hemi-sphere. This ball-joint connection design made the adjustment of the height

very flexible.

air bearing mount

Delrin hemi-sphere

air bearing pad
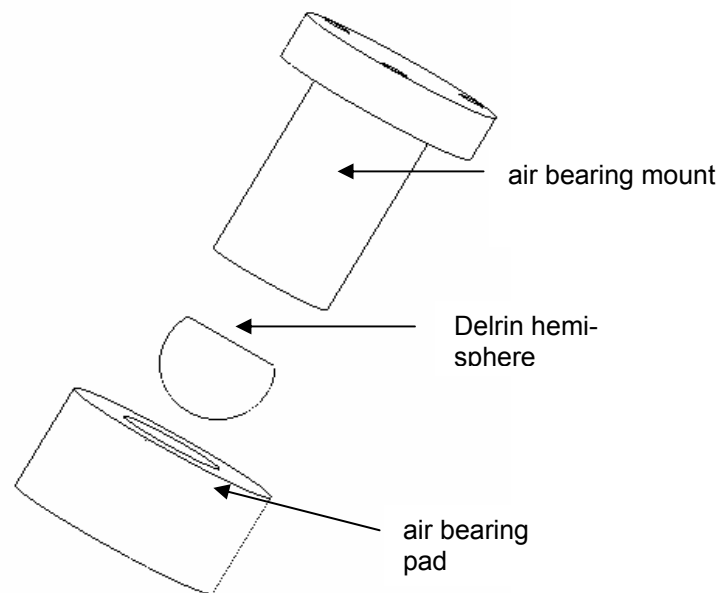
Fig. 3-5 Ball-joint mounts of aerostatic bearing [after Bhat]

3.5   Laser Distance Sensor Assembly

As mentioned in the previous chapter, the gap between the planar motor windings and

the magnetic matrix base plate is monitored by laser distance sensor, Nanogage 100. To mount

the laser distance sensor on the platen, three clearance holes of diameter 0.614 ± 0.001" were

drilled near each corner of the platen. The laser distance sensors were inserted through these

holes from the top of the platen and then were mounted by the top and bottom mounts.

Nanogage 100 requires a standoff distance of 3 mm for operation so the mounting for the sensors was designed in such a way to maintain 3 mm standoff exactly. The perpendicular tolerance of the laser distance sensor was ±0.1 degrees. To meet the specifications, mounts were designed for 2 different places. Fig. 3-6 shows bottom and top mounts for the sensor. The bottom mount had a clearance hole of diameter 0.614 ± 0.001" up to a distance of 0.631 ± 0.001". The sensor has a change in diameter from 0.610" to 0.5", so the mount was designed in such a way that the step in the sensor diameter rests exactly on the notch. And when the sensor fit in, the standoff was 3 mm.

notch where the sensor mounting diameter sits

4-40 set screws at 3 different places to hold the sensor
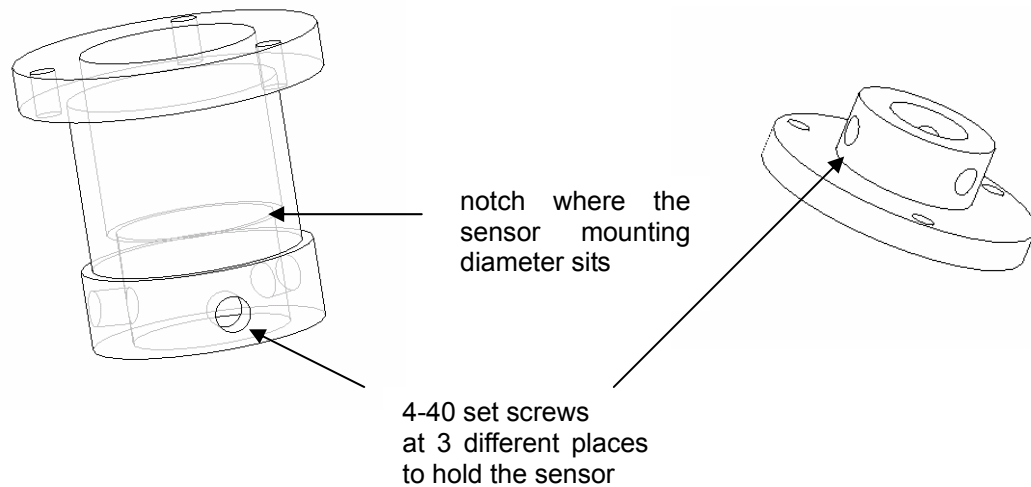
Fig. 3-6 Bottom and top mounts for Nanogage 100 [after Bhat]
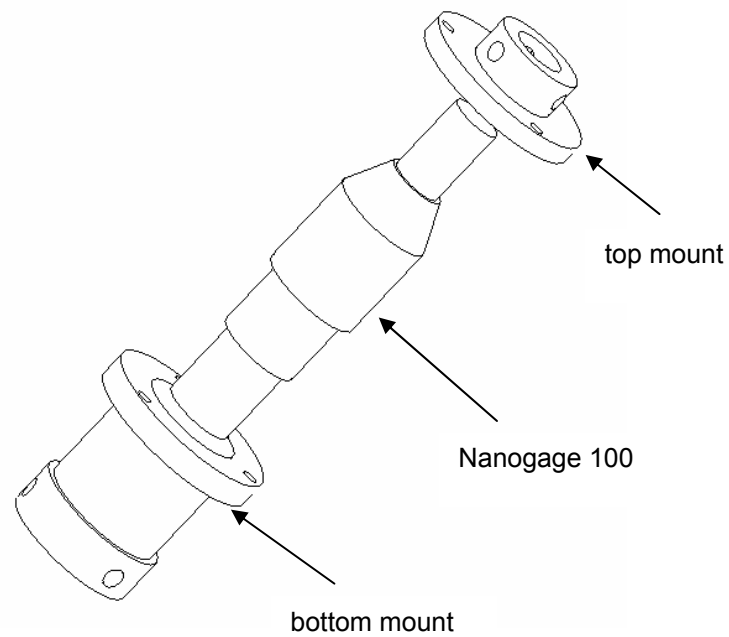
Fig. 3-7 Assembly of Nanogage 100 [after Bhat]

Small variations in the standoff can be adjusted by the three set screws on the mount. The mount was fastened on the bottom of the platen by using three 2-56 screws. To mount the sensor from the top, a Delrin hat as shown in Fig. 3-6 was designed for the sensor. It also had three 4-40 set screws to hold the sensor in its correct position.

The assembly of the sensor system is shown in Fig. 3-7. The top mount was placed in the sensor with the help of sensor's manufacturer. For the purpose of providing a clearer perspective view of the assembly, the platen was omitted in Fig. 3-7. The laser distance sensor was inserted through the platen and was fixed by the bottom and top mounts. The clearance holes of 0.614 ± 0.005" on the platen and bottom mount provide a guide to the sensor to make it perpendicular to the base plate.

3.6   Whole Platen Assembly

To make the three planar motors generate precision force, the gap between those planar motors and the base plate should be the same. In other words, the coplanarity of the bottom surface of the three planar motors should be high. The windings were put in the pocket and fixed by Delrin core in the vertical direction. The pocket was designed to exactly fit the windings so that the windings cannot move in the pocket in the horizontal direction. However, after individual planar motor was assembled on its core, the total length of the motor became 4.014". The dimension of the pocket was 4.134". Thus to get the tight fit of the motor into the pocket, shims of 0.003" thickness were inserted between the individual windings. Shims of thickness 0.045" were inserted between the ends of the coil core and the pocket. Then the motor was placed into the pocket in the platen as shown in the Fig. 3-8.
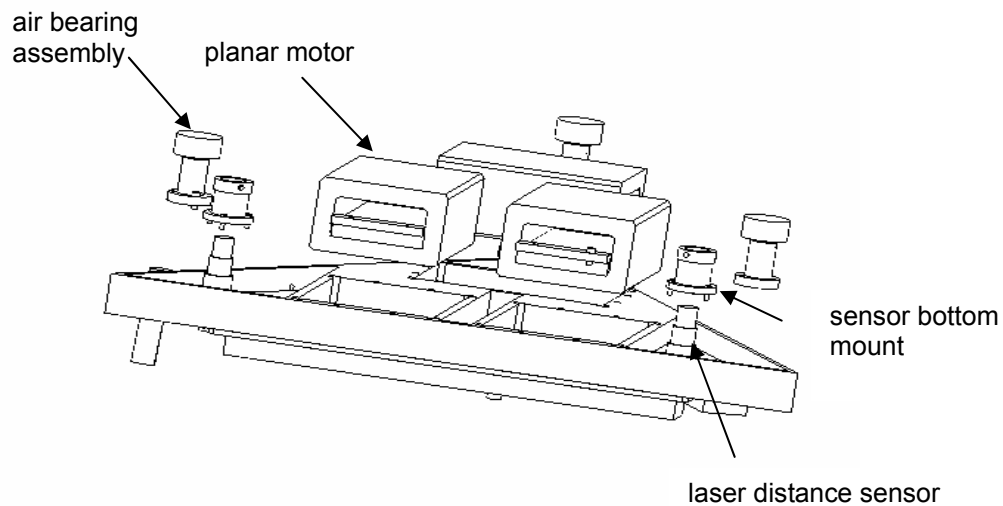
Fig. 3-8 Exploded view of the assembly of the parts at the bottom [after Bhat]

After assembling the motors, the platen was placed on the granite table, the height of individual coils of the three motor surfaces were checked, which face the magnet matrix. The

results were shown in Table 3.1. From the table, it can be seen that motor C is a little bit lower than the other two, so a shim of thickness 0.003" was placed between the winding sets of motor C and the platen to make all the planar motors planar to the granite surface, after trial and error.

Table 3.1 Height measurement results of individual coils

	Motor A (mm)	Motor B (mm)	Motor C (mm)
1	0.000	0.295	0.496
2	0.108	0.374	0.638
3	0.218	0.349	0.710
4	0.121	0.405	0.531
5	0.256	0.418	0.715
6	0.264	0.628	0.645
7	0.252	0.472	0.573
8	0.331	0.544	0.550
9	0.351	0.551	0.710
10	0.461	0.552	0.730
11	0.417	0.543	0.774
12	0.413	0.499	0.628

The three planar motors were pressed on the bottom surface of the pockets in the platen by the Delrin cores. The air bearing pads were mounted on the bottom surface of the platen by using 4-40 screws. Then three laser distance sensors' bottom mounts with 4-40 set screws were also mounted on the bottom surface of the platen by three 2-56 screws. The whole bottom parts assembly process is shown in the Fig. 3-8.

When the assembly of bottom parts in the platen was finished, the platen was flipped over to assemble the top parts such as air distributor for the air bearings, terminal blocks, stick mirrors, and top mounts of the laser distance sensors to the platen. The air distributor used for

supplying air to all the three air bearings was mounted on one of the side walls of the platen by using an adhesive tape. Then the terminal blocks were also mounted on the wall of the platen. The mirror was then mounted on the top of the platen by using 4-40 screws. Fig. 3-9 shows an exploded view of the top parts assembly. As shown in the figure, the laser distance sensors were inserted into three guiding holes and fixed by the top mounts. And the terminal blocks for the signal cables were attached on one side of the platen. All the detailed drawings of those mechanical parts can be found in the appendix *A* of the thesis.
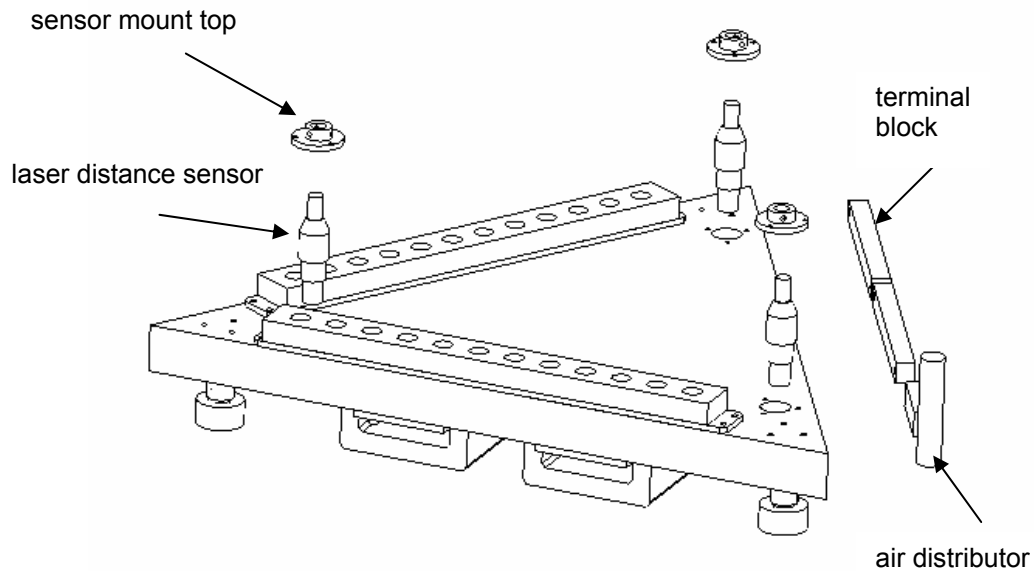
Fig. 3-9 Exploded view of the assembly of the parts at the top [after Bhat]

CHAPTER IV

DYNAMIC ANALYSIS AND MODELING

After the postioner was constructed, dynamic characteristics of the postioner were determined. Moments of inertia were determined by both software and calculation. Other dynamic parameters such as spring constant and damping coefficient of the air bearings were found experimentally. A dynamic model of the system is developed in this chapter.

4.1   Mass and Inertia Tensor of the Platen

The mass of the assembled platen carrying all the sensors and attachments was measured by a precision scale which has a resolution of 0.1 g. The total mass of the assembled platen, which includes three planar motors, two stick mirrors, three laser distance sensors, air distributor, and connection terminals, was measured to be 5.91 kg. So the weight of the platen is 57.92 N. From Chapter II, the total suspension force generated by the three planar motors was 68.60 N. Therefore, compared with the total weight of the platen, it would be possible to levitate the platen magnetically.

The whole assembled model of the positioner was built in Solidworks. With material properties and dimensions assigned to each part of the assembled platen, Solidworks can accurately calculate the center of the mass of the positioner. The coordinates of the mass center is calculated as:

$$CM = [CM_x \ CM_y \ CM_z]^{\mathrm{T}} = [191.8 \ 106.6 \ -1.0]^{\mathrm{T}}$$

in millimeters. And the center of the triangular platen is

$$CG = [CM_x \; CM_y \; CM_z]^{\mathrm{T}} = [190.5 \; 109.9 \; -1.2]^{\mathrm{T}}$$

in millimeters. It can be seen the offset of the platen center of mass is significant in the *x-y* plane compared with that in the vertical mode, due to the location of the three planar motors and two stick mirrors. The mirror was intended to be placed at the center of each side of the platen to get longer travel range in the *x-y* plane. Solidworks defines the right bottom corner as the origin for the mass center calculation. Fig. 4-1 shows the origin and coordinates that Solidworks used to determine the center of the mass of the platen.
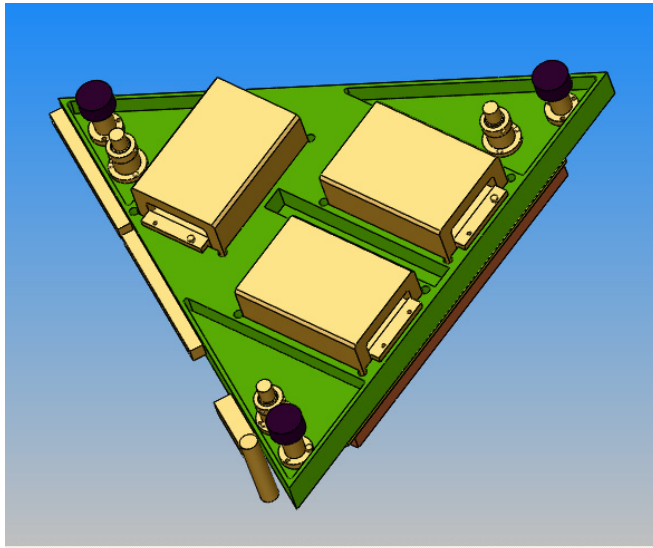
Fig. 4-1 Coordinate system of the model in Solidworks

The intertia matrix at the center of the mass of the platen was calculated by the Solidworks:

$$I = \begin{bmatrix} I_{xx} & -I_{xy} & -I_{xz} \\ -I_{yx} & I_{yy} & -I_{yz} \\ -I_{zx} & -I_{zy} & I_{zz} \end{bmatrix} = \begin{bmatrix} 0.0357 & -0.00120 & -0.000808 \\ -0.00120 & 0.0261 & 0.000263 \\ -0.000808 & 0.000263 & 0.0561 \end{bmatrix} \tag{4.1}$$

in kg-m^2. Where the quantities I_{xx}, I_{yy}, and I_{zz} are known as the moments of inertia of a body about the x, y, and z axes, respectively, and I_{xy}, I_{yz}, I_{zx}, I_{yx}, I_{xz}, and I_{zy} are known as products of inertia. The products of inertia were more than 10 times less than those moments of inertia about the x, y, and z axes, which indicated that the rotational dynamics mainly lie on the x, y, and z axes simplifying the rotational dynamics modeling of the system.

4.2   Decoupled Equations of Motion

In this section, linearized force equations for one planar motor in vertical and horizontal directions are derived. Most of the analysis in this section is based on Dr. Won-jong Kim's Ph. D. thesis in MIT.

4.2.1   Magnetic Force Equation and DQ Decomposition

When the magnetic field solutions of both the stator and the mover were ready, the total magnet field equation can be easily derived by superposition of those two magnet field. Maxwell stress tensor methodology was used to derive the final interact force between the stator and the planar motor. The force equation [77−78] of one planar motor was derived as following:

$$\begin{bmatrix} f_{y\lambda} \\ f_{z\lambda} \end{bmatrix} = \mu_0 M_0 G e^{-\gamma_1 z_0} \begin{bmatrix} \cos\gamma_1 y & \sin\gamma_1 y \\ -\sin\gamma_1 y & \cos\gamma_1 y \end{bmatrix} \begin{bmatrix} J_a \\ J_b \end{bmatrix}, \tag{4.2}$$

where $f_{y\lambda}$ and $f_{z\lambda}$ were the y-directed and z-directed forces per spatial wavelength, respectively. J_a and J_a were the input current density. And $\mu_0 M_0$ was the remanence of the permanent magnets. The constant

$$G = \frac{\sqrt{2}wl^2}{\pi^2}(1 - e^{-\gamma_1 \Gamma})(1 - e^{-\gamma_1 \Delta}), \tag{4.3}$$

contains the effects of the motor geometry; w is the width of one magnet array; Δ is the thickness of magnet array; Γ is the thickness of the winding in planar motor; and γ_1 is the absolute value of the fundamental wave number. z_0 denotes the nominal motor air gap between the bottom surface of the planar motor and the top surface of the magnet matrix. The displacement in the y-direction was denoted by "y" in Eq. (4.2). This planar motor is basically a Lorentz-force-type actuator, since it obeys the Lorentz force law,

$$\boldsymbol{F} = \boldsymbol{J} \times \boldsymbol{B}, \tag{4.4}$$

Since the motor geometric constant G has a unit in m^3, the right hand side of Eq. (4.2) gives the force in N. The force equation of Eq. (4.2) exhibits spatial nonlinearity. The DQ decomposition methodology is used here to partially eliminate the nonlinearity in the model.
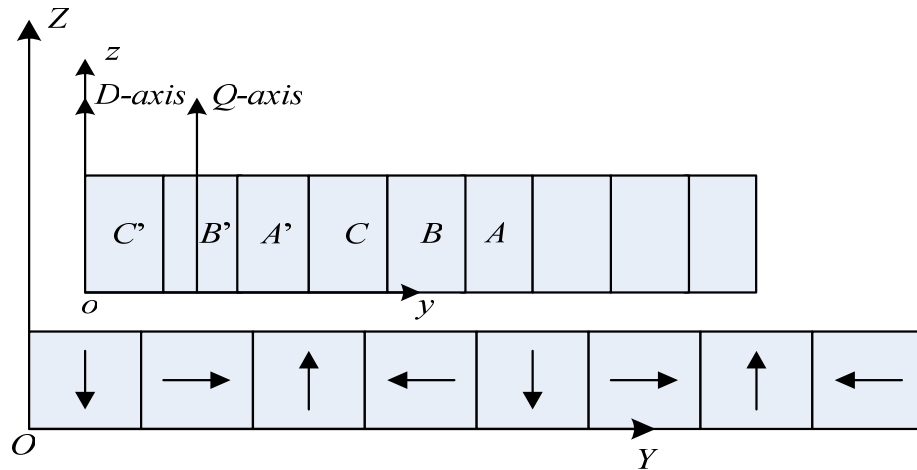
Fig. 4-2 DQ coordinates attached to the platen

The DQ decomposition in conventional rotary machines was originally introduced to separate the stator current component that generates torque [76]. Here, the direct-axis (D-axis) and quadrature-axis (Q-axis) are attached to the mover (positioner) such that they move with the positioner. As a result, the magnetic force equations and commutation described in the DQ frame

do not contain the position dependence with respect to the stator (magnet matrix base plate). So the nonlinearity due to the trigonometric function dependence in the Eq. (4.2) can be eliminated. Conventionally, the D-axis is aligned to the stator magnetic axis and Q-axis was orthogonal to the D-axis with a 90° electrical angle leading shown as in Fig. 4-2. The D-component current does effective work in the vertical direction, the Q-component current generates driving force in the horizontal direction.

The planar motor is designed to generate the suspension force and the drive force. Decoupling these two orthogonal force components was necessary to control the two DOFs independently. As shown in Fig. 4-2, the D-axis is defined as the z'-axis in the DQ coordinates. And the Q-axis leads the D-axis by $l/4$, which is 90° in electrical angle, in the $+y$-direction.

Now the transformation from $[J_a \ J_b]^T$ to $[J_Q \ J_D]^T$ can be built as following:

$$\begin{bmatrix} J_Q \\ J_D \end{bmatrix} = e^{\gamma_1 y \, J} \begin{bmatrix} J_a \\ J_b \end{bmatrix} \quad , \tag{4.5}$$

where $e^{\gamma_1 y J}$ is a transformation matrix given by

$$e^{\gamma_1 y_0 J} = e^{\gamma_1 y \begin{bmatrix} 0 & 1 \\ -1 & 0 \end{bmatrix}} = \begin{bmatrix} \cos \gamma_1 y & \sin \gamma_1 y \\ -\sin \gamma_1 y & \cos \gamma_1 y \end{bmatrix}, \tag{4.6}$$

4.2.2 Linearized Force Equations

The relationship between the total forces $f_{y,z}$ and $f_{(y,z)\lambda}$ that are the forces per spatial wavelength is shown as following.

$$\begin{aligned} f_y &= N_m f_{y\lambda} \\ f_z &= N_m f_{z\lambda} \end{aligned} \quad , \tag{4.7}$$

where N_m was the number of the planar-motor pitches. The relationship between $i_{a,b}$ and $J_{a,b}$ can be derived as:

$$i_a = 2\eta_0 J_a$$
$$i_b = 2\eta_0 J_b,$$
(4.8)

where η_0 denoted the winding turn density in one planar motor and i_a and i_b were the peak

current components in the winding. Plugging Eqs. (4.5) and (4.6) into (4.2), the force equation

of one planar motor can be rewritten as the relationship between total vertical and lateral

forces f_y and f_z and the peak current components i_a and i_b.

$$\begin{bmatrix} f_y \\ f_z \end{bmatrix} = \frac{1}{2}\mu_0 M_0 \eta_0 N_m Ge^{-\gamma_1 z_0} \begin{bmatrix} \cos\gamma_1 y & \sin\gamma_1 y \\ -\sin\gamma_1 y & \cos\gamma_1 y \end{bmatrix} \begin{bmatrix} i_a \\ i_b \end{bmatrix},$$
(4.9)

According to the inverse Blondel-Park transformation, the relationship between the peak

current i_a and i_b and each phase current i_A, i_B, and i_C was shown in Eq. (4.10) [79−81].

$$\begin{bmatrix} i_A \\ i_B \\ i_C \end{bmatrix} = \begin{bmatrix} 1 & 0 \\ \dfrac{1}{2} & \dfrac{\sqrt{3}}{2} \\ -\dfrac{1}{2} & \dfrac{\sqrt{3}}{2} \end{bmatrix} \begin{bmatrix} i_a \\ i_b \end{bmatrix},$$
(4.10)

Then Eq. (4.11) represents the relationship between the phase currents and the magnetic force

as following:

$$\begin{bmatrix} f_y \\ f_z \end{bmatrix} = \frac{1}{2}\mu_0 M_0 \eta_0 N_m Ge^{-\gamma_1 z_0} \begin{bmatrix} \cos\gamma_1 y & \sin\gamma_1 y \\ -\sin\gamma_1 y & \cos\gamma_1 y \end{bmatrix} \begin{bmatrix} \dfrac{2}{3} & -\dfrac{1}{3} & -\dfrac{1}{3} \\ 0 & \dfrac{1}{\sqrt{3}} & -\dfrac{1}{\sqrt{3}} \end{bmatrix} \begin{bmatrix} i_A \\ i_B \\ i_C \end{bmatrix},$$
(4.11)

With the above equation, the magnetic force can be generated by flowing corresponding phase

current in the planar motors.

From Eqs. (4.2) and (4.5) that the magnetic force can be decoupled in the lateral and

vertical components in J_Q (i_Q) and J_D (i_D).

$$f_y = \frac{1}{2}\mu_0 M_0 \eta_0 N_m Ge^{-\gamma_1 z_0} i_Q$$

$$f_z = \frac{1}{2}\mu_0 M_0 \eta_0 N_m Ge^{-\gamma_1 z_0} i_D$$

, (4.12)

The above equations have multiplicative terms of position z_0 and current i_Q or i_D which can be linearized near the operating point by using Taylor series expansion.

$$f_y = f_y(i_{Q0},z_0) + \left.\frac{\partial f_y}{\partial z}\right|_{\substack{i_Q=i_{Q0} \\ z=z_0}} (z-z_0) + \left.\frac{\partial f_y}{\partial i_Q}\right|_{\substack{z=z_0 \\ i_Q=i_{Q0}}} (i_Q - i_{Q0})$$

$$= \frac{1}{2}\mu_0 M_0 \eta_0 N_m Ge^{-\gamma_1 z_0} i_{Q0} - \frac{1}{2}\mu_0 M_0 \eta_0 N_m Ge^{-\gamma_1 z_0} i_{Q0}\gamma_1 (z-z_0) + \frac{1}{2}\mu_0 M_0 \eta_0 N_m Ge^{-\gamma_1 z_0} (i_Q - i_{Q0})$$

, (4.13)

$$f_z = f_z(i_{D0},z_0) + \left.\frac{\partial f_z}{\partial z}\right|_{\substack{i_D=i_{D0} \\ z=z_0}} (z-z_0) + \left.\frac{\partial f_z}{\partial i_D}\right|_{\substack{z=z_0 \\ i_D=i_{D0}}} (i_D - i_{D0})$$

$$= \frac{1}{2}\mu_0 M_0 \eta_0 N_m Ge^{-\gamma_1 z_0} i_{D0} - \frac{1}{2}\mu_0 M_0 \eta_0 N_m Ge^{-\gamma_1 z_0} i_{D0}\gamma_1 (z-z_0) + \frac{1}{2}\mu_0 M_0 \eta_0 N_m Ge^{-\gamma_1 z_0} (i_D - i_{D0})$$

, (4.14)

Let $\tilde{f}_y = f_y - f_y(i_{Q0},z_0), \tilde{z} = z - z_0, \tilde{i}_Q = i_Q - i_{Q0}$, then (4.13) can be rewritten as:

$$\tilde{f}_y = -\frac{1}{2}\mu_0 M_0 \eta_0 N_m Ge^{-\gamma_1 z_0} i_{Q0}\gamma_1 \tilde{z} + \frac{1}{2}\mu_0 M_0 \eta_0 N_m Ge^{-\gamma_1 z_0} \tilde{i}_Q,$$

(4.15)

Let $\tilde{f}_z = f_z - f_z(i_{D0},z_0), \tilde{z} = z - z_0, \tilde{i}_D = i_D - i_{D0}$, then (4.14) can also be rewritten as:

$$\tilde{f}_z = -\frac{1}{2}\mu_0 M_0 \eta_0 N_m Ge^{-\gamma_1 z_0} i_{D0}\gamma_1 \tilde{z} + \frac{1}{2}\mu_0 M_0 \eta_0 N_m Ge^{-\gamma_1 z_0} \tilde{i}_D,$$

(4.16)

where z_0, i_{Q0}, and i_{D0} are corresponding constant values of air gap, i_Q and i_D at equilibrium point. Since the coefficients of $\tilde{z}$, $\tilde{i}_Q$, and $\tilde{i}_D$ were constant, the force equations of (4.15) and (4.16) are linear force equations of one planar motor about $\tilde{z}$, $\tilde{i}_Q$, and $\tilde{i}_D$.

4.3   Dynamic Analysis of System

With the equations of forces generated by planar motors, it is ready to derive the dynamics of the system. To generate motions in any direction, each of the three planar motors

should be responsible for its own contribution for the motion. Basically, any motion is achieved

by all of the three planar motors, which is illustrated in Fig. 4.3. In this figure, the Roman

numeral I, II, and III denotes the planar motor A, B, and C respectively. The coordinate system on

the uper left hand side of the picture, whose origin was located at the mass center of the

positioner (for the purpose of clearly presenting, the origin of the coordinate was placed outside

of the positioner in Fig. 4.3), defined the force and torque direction. Motors A and B can generate

force f_{1y} and f_{2y} in the y-direction respectively. Motor C can generate force f_{3x} in the x-direction.

All the planar motors A, B, and C can also generate magnetic suspension force f_{1z}, f_{2z}, and f_{3z} in

the z-direction.

Fig. 4-3 (b), (c), and (d) illustrated how the positioner generated motion in the horizontal

mode. If the positioner wanted to make a movement in the x-direction, motor C will generate f_{3x}

in the x-direction and at the same time motor A and B will generate a canceling torque τ_z to

balance the torque brought by motor C. Translation in the y-direction can be achieved by motor

A and B. (e), (f), and (g) explained the way to generate motion in the vertical mode. Since all the

planar motors can generate the vertical force, changing the direction and magnitude of those

vertical forces can generate the vertical motion.

The magnitude and direction of magnet force generated by each motor can be

determined by force equations. And the moments about the center of mass can be calculated by

$$\vec{M}_c = \vec{F} \times \vec{L} , \qquad (4.17a)$$

where L was the arm from the center of the planar motor to the corresponding x-, y-, or z-axis,

which can be obtained from the dimensions of the positioner. The positioner can generate any 6-

DOF motion by inputting proper phase currents into these planar motors.
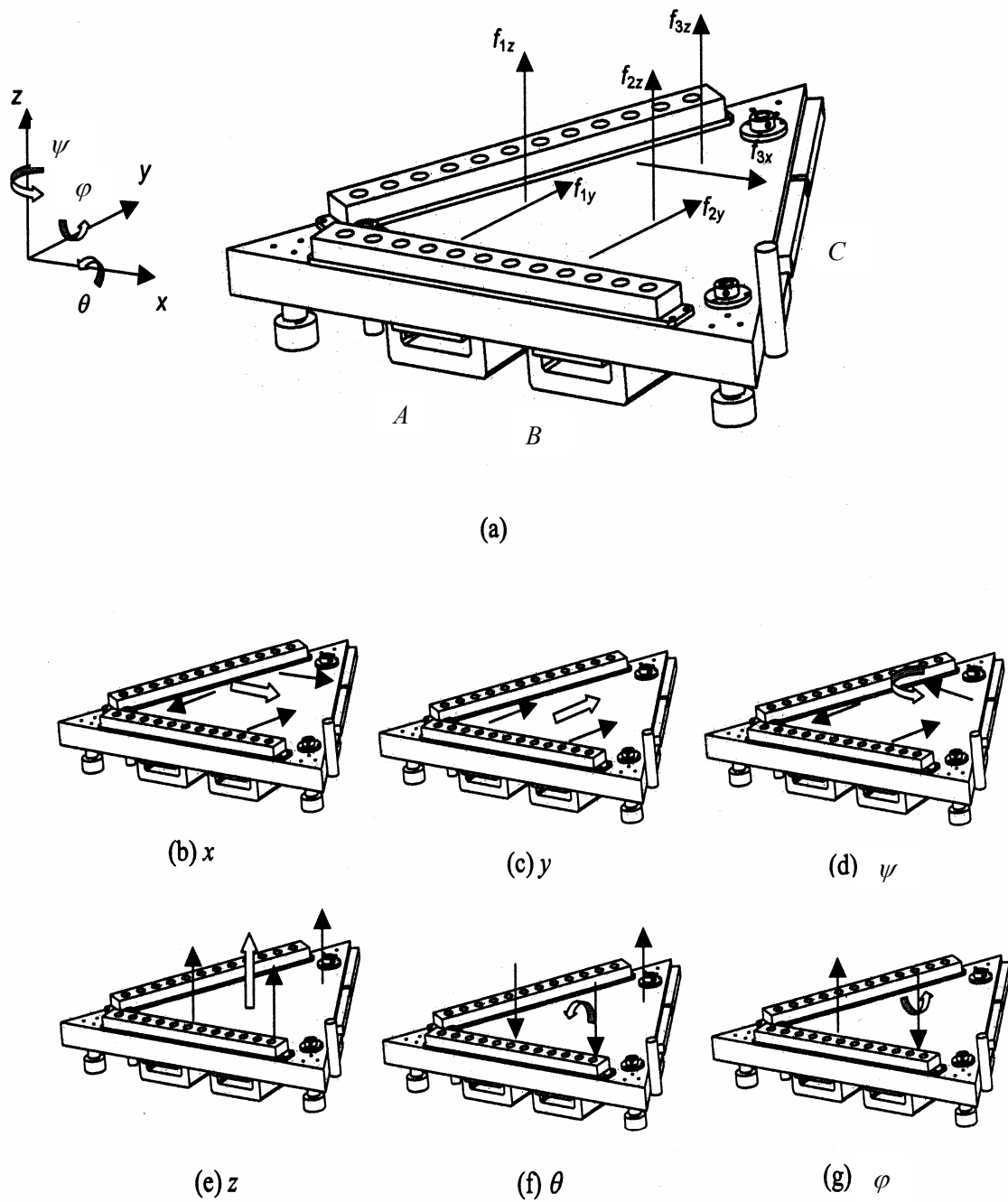
Fig. 4-3 Illustration of generating 6-DOF motions by three planar motors

Since the movement due to the deformation of the positioner is only a minor part of its motion in all 6-DOF motions, the positioner can be regarded as a rigid body [82]. To analyze the

dynamics of the positioner, two sets of coordinate systems were defined for the system. As shown in Fig. 4-4, the *XOY* coordinate system was fixed at the initial position of the positioner which was the center of the mass of the positioner at the beginning. Another coordinate system *xoy*, whose origin was the mass center of the positioner, was attached on the positioner. *XOY* and *xoy* coordinates were overlapped in the beginning. The magnet force generated by the planar motor can be regarded as concentrated force which was applied at the center of each planar motor.
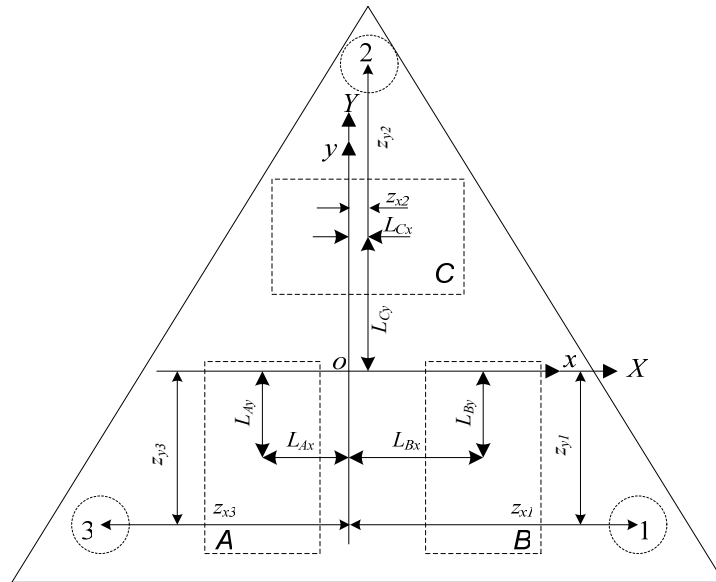
Fig. 4-4 Coordinate systems of the positioner (Top view)

There, $L_{(A, B, C)x}$ denoted the distance from the centers of motors *A*, *B*, and *C* to the *y*-axis respectively. Similarly, $L_{(A, B, C)y}$ denoted the distance to the *x*-axis respectively. The three dash line circles labeled 1, 2, and 3 in counterclockwise sequence were the aerostatic bearing pads. z_x $_{(1,2,3)}$ denote the distance from the center of the air bearing pad to the *x*-axis. $z_{y(1,2,3)}$ means the distance from that to the *y*-axis. The values of those distances are presented in the Fig. 4-1.

Table 4.1 Dimensions of planar motors and air bearings to *xoy* coordinate system

Variable	Value (mm)	Variable	Value (mm)
L_{Ax}	49.7	z_{x1}	147.0
L_{Bx}	52.7	z_{x2}	1.3
L_{Cx}	1.3	z_{x3}	167.0
L_{Ay}	44.8	z_{y1}	88.0
L_{By}	44.8	z_{y2}	175.0
L_{Cy}	84.3	z_{y3}	95.0

Since the displacement in the horizontal mode was measured by three fixed laser interferometers, the displacement was actually already measured in the *XOY* coordinate system. As a result, for the motion in horizontal mode, it is unnecessary to apply any coordinate transformation from the *xoy* system to the *XOY* system. However, the three laser distance sensors were attached on the platen which means those displacements (translation in the *z*-axis, rotation about the *x*- and *y*-axis) were measured in the moving coordinate system *xoy*. To simplify the calculation, a coordinate transformation was carried out to transform all the displacement in the *XOY* coordinate system to the *xoy* coordinate system.

The coordinate system transformation can be divided into three steps: (i) yaw about the *z*-axis, (ii) roll about the *x*-axis, and (iii) pitch about the *y*-axis. The corresponding transformation matrix was:

$$[R_\phi] = \begin{bmatrix} \cos\phi & \sin\phi & 0 \\ -\sin\phi & \cos\phi & 0 \\ 0 & 0 & 1 \end{bmatrix},$$

(4.17)

$$[R_\theta] = \begin{bmatrix} 1 & 0 & 0 \\ 0 & \cos\theta & \sin\theta \\ 0 & -\sin\theta & \cos\theta \end{bmatrix}, \tag{4.18}$$

$$[R_\varphi] = \begin{bmatrix} \cos\varphi & 0 & -\sin\varphi \\ 0 & 1 & 0 \\ \sin\varphi & 0 & \cos\varphi \end{bmatrix}, \tag{4.19}$$

As a result, the overall transformation can be obtained by combining Eqs. (4.17), (4.18), and (4.19), with the result that

$$\begin{bmatrix} x \\ y \\ z \end{bmatrix} = [R] \begin{bmatrix} X \\ Y \\ Z \end{bmatrix}, [R] = [R_\phi][R_\theta][R_\varphi], \tag{4.20}$$

$$\begin{bmatrix} X \\ Y \\ Z \end{bmatrix} = [R^{-1}] \begin{bmatrix} x \\ y \\ z \end{bmatrix}, \tag{4.21}$$

With those coordinate transformation equations, it is ready to develop equations of motion for the system by using Newton's second law as following:

$$\left\{ \begin{matrix} \sum F_x \\ \sum F_y \\ \sum F_z \end{matrix} \right\} = m \left\{ \begin{matrix} a_{ox} \\ a_{oy} \\ a_{oz} \end{matrix} \right\}, \tag{4.22}$$

$$\left\{ \begin{matrix} \sum M_{ox} \\ \sum M_{oy} \\ \sum M_{oz} \end{matrix} \right\} = [I] \left\{ \begin{matrix} \alpha_x \\ \alpha_y \\ \alpha_z \end{matrix} \right\} + \begin{bmatrix} 0 & -\omega_z & \omega_y \\ \omega_z & 0 & -\omega_x \\ -\omega_y & \omega_x & 0 \end{bmatrix} [I] \left\{ \begin{matrix} \omega_x \\ \omega_y \\ \omega_z \end{matrix} \right\}, \tag{4.23}$$

In the foregoing, $\sum F_x$, $\sum F_y$, and $\sum F_z$ are the sums of the external forces acting on the positioner in the three coordinate directions. Similarly, $\sum M_{ox}$, $\sum M_{oy}$, and $\sum M_{oz}$ represent the sum of the moments of the external forces about the coordinate axes whose origin is point O. Here, it

must be emphasized that point O is selected as the center of mass of the positioner to satisfy the moment Eq. (4.23).

Since the positioner is levitated by the air bearings, there is no friction between the positioner and the base plate. As a result, the positioner can be regarded as a pure mass system in the horizontal mode. The equations of motion in the horizontal mode can be presented as

$$m\frac{d^2x}{dt^2} = f_x, \tag{4.24}$$

$$m\frac{d^2y}{dt^2} = f_y, \tag{4.25}$$

$$I_{zz}\frac{d^2\phi}{dt^2} = M_{oz} + (I_{xx} - I_{yy})\omega_x\omega_y, \tag{4.26}$$

Compared with I_{xx}, I_{yy}, and I_{zz}, those products of inertia can be neglected. This equation can be linearized at equilibrium point, where $\omega_x = \omega_y = 0$ rad/s. The linearized equation is presented in Eq. (4.27).

$$I_{zz}\frac{d^2\phi}{dt^2} = M_{oz}, \tag{4.27}$$

In the vertical direction, because of the presence of the air bearings, the system can be modeled as spring-mass-damper system. The same case will happen to the other rotational motion about the x- and y-axis. So the similar methodology can be used to derive equation of motions in those directions.

$$I_{xx}\frac{d^2\theta}{dt^2} = M_{ox} - K_\theta\theta - C_\theta\dot{\theta}, \tag{4.28}$$

$$I_{yy}\frac{d^2\varphi}{dt^2} = M_{oy} - K_\varphi\varphi - C_\varphi\dot{\varphi}, \tag{4.29}$$

$$m\frac{d^2z}{dt^2} = f_z - K_z z - C_z\dot{z}, \tag{4.30}$$

where K_θ, K_φ, and K_z, are spring constants in the vertical mode and C_θ, C_φ, and C_z, are damping ratio coefficients. The spring constant and damping ratio coefficient in the z-axis can be determined by experiment using Hooke's law [83]. Then the whole positioner can be regarded as a stage sitting on three sets of spring as shown in the Fig. 4-5.
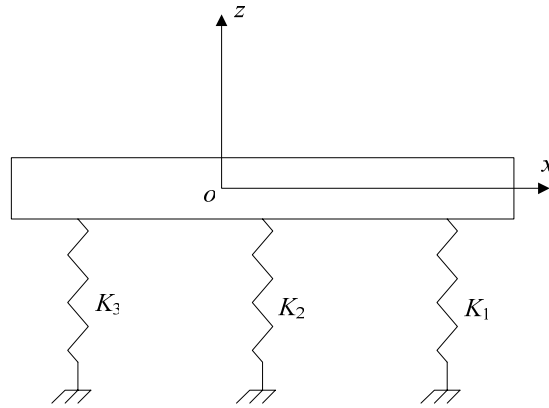
Fig. 4-5 Spring-mass model of the positioner in the vertical mode (side view)

K_1, K_2, and K_3 were the spring constant of the three air bearings 1, 2, and 3. Their value is 1/3 of K_z, which is determined to be 10^6 N/m by experiment. With the distance from the center of the air bearing pads to the x- and y-axis in the xoy coordinate system, which is shown in Fig. 4-4, the rotational spring constant K_θ and K_φ can be determined by the following mathematic manipulations. As shown in Fig. 4-6, suppose the positioner has a rotational angle φ about the y-axis. This angular motion will cause deflection in the three springs.
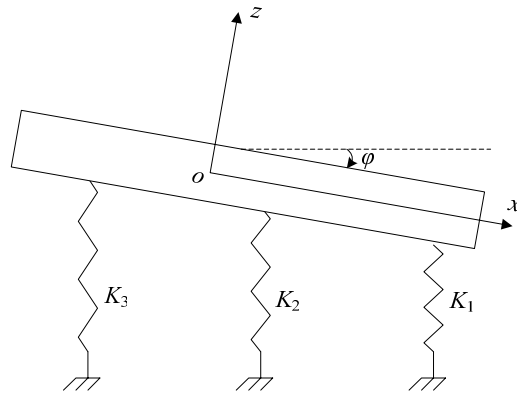
Fig. 4-6 Illustration of rotation about the *y*-axis

Then the displacement of each spring introduced by φ can be determined by the following formula

$$\varphi = \frac{d}{r},$$
(4.31)

where, r is the distance from each spring to the *y*-axis. And d is the length of arc which took place in the intersection point between the spring and the positioner. Since the angel φ is a small angle (on the order of microradians), d can be regarded as the displacement of spring due to the rotational displacement. As a result, the force generated by the spring due to the deformation of spring can be calculated by Hooke's law

$$F = Kd,$$
(4.32)

According to the dimensions shown in Fig. 4-4, the force can be calculated as following

$$
\begin{aligned}
F_1 &= K_1 z_{x1} \varphi \\
F_2 &= K_2 z_{x2} \varphi \quad . \\
F_3 &= -K_3 z_{x3} \varphi
\end{aligned}
$$
(4.33)

Now applying Newton's second law to the moment about the *y*-axis as shown in Eq. (4.34), the moment of equation about the *y*-axis can be developed in Eq. (4.35).

$$\sum M_{oy} = 0, \tag{4.34}$$

$$K_{\varphi}\varphi = K_1 z_{x1}^2 \varphi + K_2 z_{x2}^2 \varphi + K_3 z_{x3}^2 \varphi, \tag{4.35}$$

Plugging K_1, K_2, K_3, z_{x1}, z_{x2}, and z_{x3}, K_{φ} can be calculated as 11653 N-m/rad. A similar formula can be derived for K_{θ} as shown in Eq. (4.36).

$$K_{\theta}\theta = K_1 z_{y1}^2 \theta + K_2 z_{y2}^2 \theta + K_3 z_{y3}^2 \theta, \tag{4.36}$$

And K_{θ} is calculated as 11152 N-m/rad. Those coefficients of damping coefficient C_z, C_{θ}, and C_{φ}, can be experimentally determined by observing the time domain dynamics of the pulse response of the postioner. After those parameters are determined, it is ready to derive the models for the positioner by Laplace transform of Eqs. from (4.24) to (4.30).

$$\frac{x(s)}{f_x(s)} = \frac{1}{ms^2}, \tag{4.37}$$

$$\frac{y(s)}{f_y(s)} = \frac{1}{ms^2}, \tag{4.38}$$

$$\frac{\phi(s)}{M_{oz}(s)} = \frac{1}{I_{zz}s^2}, \tag{4.39}$$

Eqs. (4.37), (4.38), and (4.39) are the dynamic models of the positioner in the horizontal mode. A similar Laplace transform can be applied to these ordinary differential equations (ODE) in the vertical mode. Then the corresponding dynamic model can be developed.

$$\frac{z(s)}{f_z(s)} = \frac{1}{ms^2 + C_z s + K_z}, \tag{4.40}$$

$$\frac{\theta(s)}{M_{ox}(s)} = \frac{1}{I_{xx}s^2 + C_{\theta}s + K_{\theta}}, \tag{4.41}$$

$$\frac{\varphi(s)}{M_{oy}(s)} = \frac{1}{I_{yy}s^2 + C_{\varphi}s + K_{\varphi}}, \tag{4.42}$$

Eqs. (4.37) to (4.42) are the dynamic models of the positioning system. With those equations, proper controllers can be designed to satisfy the dynamic requirement for the system. However, the input to those models is forces and moments instead of phase currents to those planar motors. There exists a force allocation to each motor when some commanded force or moment is generated.

4.4   Force Allocation

As mentioned in last section, force allocation for each planar motor will be discussed in this section. Fig. 4-7 illustrated the force allocation for each planar motor *A*, *B*, and *C* when commanded fore or moment is generated. The relationship of total force or moment applied in center of mass and those generated by actuators can be developed as follows.
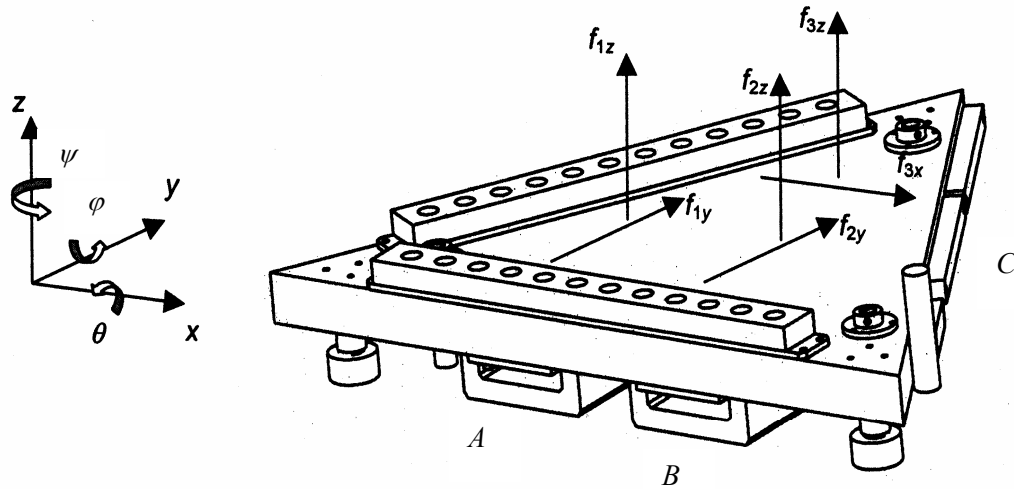
Fig. 4-7 Illustration of force allocation

The force and moment in horizontal mode are first studied. From Fig. 4-7, it can be seen that each force or moment in the horizontal mode can be achieved as follows.

$$f_x = f_{cx},$$

(4.43)

$$f_y = f_{Ay} + f_{By},$$ (4.44)

$$M_{oz} = -L_{Ax}f_{Ay} + L_{Bx}f_{By} - L_{Cy}f_{Cx},$$ (4.45)

As mentioned in section 4.3, these L values are lengths from each actuator to the center of the mass. The above equations can be rewritten as the matrix from.

$$\begin{bmatrix} f_x \\ f_y \\ M_{oz} \end{bmatrix} = \begin{bmatrix} 0 & 0 & 1 \\ 1 & 1 & 0 \\ -L_{Ax} & L_{Bx} & -L_{Cy} \end{bmatrix} \begin{bmatrix} f_{Ay} \\ f_{By} \\ f_{Cx} \end{bmatrix},$$ (4.46)

The relationship from total force or moment to each planar motor force in the horizontal mode can be got by inversing the coefficient matrix.

$$\begin{bmatrix} f_{Ay} \\ f_{By} \\ f_{Cx} \end{bmatrix} = \begin{bmatrix} -\dfrac{L_{Cy}}{L_{Ax}+L_{Bx}} & \dfrac{L_{Bx}}{L_{Ax}+L_{Bx}} & -\dfrac{1}{L_{Ax}+L_{Bx}} \\ \dfrac{L_{Cy}}{L_{Ax}+L_{Bx}} & \dfrac{L_{Ax}}{L_{Ax}+L_{Bx}} & \dfrac{1}{L_{Ax}+L_{Bx}} \\ 1 & 0 & 0 \end{bmatrix} \begin{bmatrix} f_x \\ f_y \\ M_{oz} \end{bmatrix},$$ (4.47)

Plugging those L values shown in the Table 4.1, the above force allocation matrix becomes

$$\begin{bmatrix} f_{Ay} \\ f_{By} \\ f_{Cx} \end{bmatrix} = \begin{bmatrix} -0.82273 & 0.51452 & -9.75956 \\ 0.82273 & 0.48548 & 9.75956 \\ 1 & 0 & 0 \end{bmatrix} \begin{bmatrix} f_x \\ f_y \\ M_{oz} \end{bmatrix},$$ (4.48)

Similarly, according to the Fig. 4-7, in the vertical mode, the total force and moments can be generated by each planar motor as following.

$$f_z = f_{Az} + f_{Bz} + f_{Cz},$$ (4.49)

$$M_{ox} = -f_{Az}L_{Ay} - f_{Bz}L_{By} + f_{Cz}L_{Cy},$$ (4.50)

$$M_{oy} = f_{Az}L_{Ax} - f_{Bz}L_{Bx} - f_{Cz}L_{Cx},$$ (4.51)

The corresponding matrix form is:

$$\begin{bmatrix} f_z \\ M_{ox} \\ M_{oy} \end{bmatrix} = \begin{bmatrix} 1 & 1 & 1 \\ -L_{Ay} & -L_{By} & L_{Cy} \\ L_{Ax} & -L_{Bx} & -L_{Cx} \end{bmatrix} \begin{bmatrix} f_{Az} \\ f_{Bz} \\ f_{Cz} \end{bmatrix}, \tag{4.52}$$

After plugging those L values into the Eq. (4.52), the force allocation in the vertical mode is

$$\begin{bmatrix} f_{Az} \\ f_{Bz} \\ f_{Cz} \end{bmatrix} = \begin{bmatrix} 0.34024 & -3.88602 & 9.75956 \\ 0.31251 & -3.85715 & -9.75956 \\ 0.34725 & 7.74316 & 0 \end{bmatrix} \begin{bmatrix} f_z \\ M_{ox} \\ M_{oy} \end{bmatrix}, \tag{4.53}$$

The Eqs. (4.48) and (4.52) has are a way to allocate the total force or moment to each planar motor which actually made a connection between the commanded force or moment and the forces for each actuator. These relations make it possible to use these models shown in Eqs. (4.37) through (4.42) to design single input and single output (SISO) controllers, which have "force" or "moment" as the outputs to these models. Eqs. (4.37) and (4.42) are force allocations in the horizontal and vertical mode respectively. Here, the reason that divided the force allocation into two independent planes is that there are two steps to make the positioner work from its initial position. So the controllers in the horizontal mode and the vertical mode will not work simultaneously at the beginning.

4.5   State-Space Model of the System

In Section 4.4, the force allocation equations make it possible to design controllers for each decoupled dynamic model of the system (6 models for 6-DOF motions). For such a multi-directional positioning system, there are inevitable coupled dynamics. To study the dynamics, a state-space model based on the real inputs and outputs of the system is necessary to be developed. In this section, the current input and displacement output state-space model will be developed for the advanced controller design, such as LQR, and LQG in the following chapters.

In order to derive the state-space model which has the current input, those dynamics presented in Eqs. (4.24) through (4.30) should be in "current" form. Plugging the force Eq. (4.12), the dynamics can be represented as

$$m\frac{d^2x}{dt^2} = \frac{1}{2}\mu_0 M_0 \eta_0 N_m G e^{-\gamma_1 z_0} i_{CQ},\tag{4.54}$$

$$m\frac{d^2y}{dt^2} = \frac{1}{2}\mu_0 M_0 \eta_0 N_m G e^{-\gamma_1 z_0} (i_{AQ} + i_{BQ}),\tag{4.55}$$

$$I_{zz}\frac{d^2\phi}{dt^2} = \frac{1}{2}\mu_0 M_0 \eta_0 N_m G e^{-\gamma_1 z_0} (-L_{Ax}i_{AQ} + L_{Bx}i_{BQ} - L_{Cy}i_{CQ}),\tag{4.56}$$

The right-hand-side non-linear equations can be linearized about an equilibrium point. Plugging the linearized horizontal force equations from Eq. (4.15), the linearized equation is presented as follows.

$$m\frac{d^2\tilde{x}}{dt^2} = \frac{1}{2}\mu_0 M_0 \eta_0 N_m G e^{-\gamma_1 z_0} \tilde{i}_{CQ},\tag{4.57}$$

$$m\frac{d^2\tilde{y}}{dt^2} = \frac{1}{2}\mu_0 M_0 \eta_0 N_m G e^{-\gamma_1 z_0} (\tilde{i}_{AQ} + \tilde{i}_{BQ}),\tag{4.58}$$

$$I_{zz}\frac{d^2\tilde{\phi}}{dt^2} = \frac{1}{2}\mu_0 M_0 \eta_0 N_m G e^{-\gamma_1 z_0} (-L_{Ax}\tilde{i}_{AQ} + L_{Bx}\tilde{i}_{BQ} - L_{Cy}\tilde{i}_{CQ}),\tag{4.59}$$

Comparing above equations and 4.15, it can be seen that i_{Q0} term is missing. That is because in the equilibrium point all the i_{Q0} terms are zero. The above linearized equations can be presented in standard state-space form. Since the term of $\frac{1}{2}\mu_0 M_0 \eta_0 N_m G e^{-\gamma_1 z_0}$ is a constant, let character C denote that expression in the state-space form. Six states x, y, r, h, u, and v are introduced to represent above equations in state-space form.

$$
\begin{bmatrix} \dot{x} \\ \dot{y} \\ \dot{r} \\ \dot{h} \\ \dot{u} \\ \dot{v} \end{bmatrix} = \begin{bmatrix} 0 & 0 & 0 & 1 & 0 & 0 \\ 0 & 0 & 0 & 0 & 1 & 0 \\ 0 & 0 & 0 & 0 & 0 & 1 \\ 0 & 0 & 0 & 0 & 0 & 0 \\ 0 & 0 & 0 & 0 & 0 & 0 \\ 0 & 0 & 0 & 0 & 0 & 0 \end{bmatrix} \begin{bmatrix} x \\ y \\ r \\ h \\ u \\ v \end{bmatrix} + \begin{bmatrix} 0 & 0 & 0 \\ 0 & 0 & 0 \\ 0 & 0 & 0 \\ 0 & 0 & \dfrac{c}{m} \\ \dfrac{c}{m} & \dfrac{c}{m} & 0 \\ -\dfrac{c}{I_{zz}}L_{Ay} & \dfrac{c}{I_{zz}}L_{By} & -\dfrac{c}{m}L_{Cy} \end{bmatrix} \begin{bmatrix} i_{AQ} \\ i_{BQ} \\ i_{CQ} \end{bmatrix}, \quad (4.60)
$$

$$
Y_1 = \begin{bmatrix} 1 & 0 & 0 & 0 & 0 & 0 \\ 0 & 1 & 0 & 0 & 0 & 0 \\ 0 & 0 & 1 & 0 & 0 & 0 \\ 0 & 0 & 0 & 1 & 0 & 0 \\ 0 & 0 & 0 & 0 & 1 & 0 \\ 0 & 0 & 0 & 0 & 0 & 1 \end{bmatrix} \begin{bmatrix} x \\ y \\ r \\ h \\ u \\ v \end{bmatrix}, \quad (4.61)
$$

The above Eqs. (4.60) and (4.61) are the state-space model of the positioner in the horizontal mode. In Eq. (4.61) Y_1 is used to denote the outputs of interferometers in the horizontal mode. Because the interferometers in the horizontal mode can provide both displacement and velocity information, the output matrix is a 6 by 6 identity matrix.

For the vertical mode motions, the similar methodology of plugging in linearized vertical force equation can be applied to get the linearized equations in the vertical mode.

$$
I_{xx}\frac{d^2\theta}{dt^2} = \frac{1}{2}\mu_0 M_0 \eta_0 N_m G e^{-\gamma_1 z_0}(-L_{Ay}\tilde{i}_{AD} - L_{By}\tilde{i}_{BD} + L_{Cy}\tilde{i}_{CD}) - K_\theta\theta - C_\theta\dot{\theta}, \quad (4.62)
$$

$$
I_{yy}\frac{d^2\varphi}{dt^2} = \frac{1}{2}\mu_0 M_0 \eta_0 N_m G e^{-\gamma_1 z_0}(L_{Ax}\tilde{i}_{AD} - L_{Bx}\tilde{i}_{BD} - L_{Cx}\tilde{i}_{CD}) - K_\varphi\varphi - C_\varphi\dot{\varphi}, \quad (4.63)
$$

$$
m\frac{d^2 z}{dt^2} = \frac{1}{2}\mu_0 M_0 \eta_0 N_m G e^{-\gamma_1 z_0}(\tilde{i}_{AD} + \tilde{i}_{BD} + \tilde{i}_{CD}) - K_z z - C_z\dot{z}, \quad (4.64)
$$

Let C equal to $\dfrac{1}{2}\mu_0 M_0 \eta_0 N_m G e^{-\gamma_1 z_0}$ and introduce z, s, t, p, q, and w as the states of the system. Then the state-space model in the vertical mode can be presented as

$$\begin{bmatrix} \dot{z} \\ \dot{s} \\ \dot{t} \\ \dot{p} \\ \dot{q} \\ \dot{w} \end{bmatrix} = \begin{bmatrix} 0 & 0 & 0 & 1 & 0 & 0 \\ 0 & 0 & 0 & 0 & 1 & 0 \\ 0 & 0 & 0 & 0 & 0 & 1 \\ -\dfrac{K_z}{m} & 0 & 0 & 0 & 0 & 0 \\ 0 & -\dfrac{K_\theta}{I_{xx}} & 0 & 0 & -\dfrac{C_\theta}{I_{xx}} & 0 \\ 0 & 0 & -\dfrac{K_\varphi}{I_{yy}} & 0 & 0 & -\dfrac{C_\varphi}{I_{yy}} \end{bmatrix} \begin{bmatrix} z \\ s \\ t \\ p \\ q \\ w \end{bmatrix} + \begin{bmatrix} 0 & 0 & 0 \\ 0 & 0 & 0 \\ 0 & 0 & 0 \\ \dfrac{c}{m} & \dfrac{c}{m} & \dfrac{c}{m} \\ -\dfrac{c}{I_{xx}}L_{Ay} & -\dfrac{c}{I_{xx}}L_{By} & \dfrac{c}{I_{xx}}L_{Cy} \\ \dfrac{c}{I_{yy}}L_{Ax} & -\dfrac{c}{I_{yy}}L_{Bx} & -\dfrac{c}{I_{yy}}L_{Cx} \end{bmatrix} \begin{bmatrix} i_{AD} \\ i_{BD} \\ i_{CD} \end{bmatrix}, \quad (4.65)$$

$$Y_2 = \begin{bmatrix} 1 & 0 & 0 & 0 & 0 & 0 \\ 0 & 1 & 0 & 0 & 0 & 0 \\ 0 & 0 & 1 & 0 & 0 & 0 \end{bmatrix} \begin{bmatrix} z \\ s \\ t \\ p \\ q \\ w \end{bmatrix}, \quad (4.66)$$

Here in the vertical mode, three laser distance sensors can only measure the displacement. That's the reason why the C matrix in the vertical mode is not an identity matrix. Similar to Eq. (4.61) Y_2 is used here to denote the outputs of laser distance sensors in the vertical mode. Attention must be paid that in the state-space form, the inputs are actually lateral currents $[i_{AQ}, i_{BQ}, i_{CQ}]^T$ and quadratic currents $[i_{AD}, i_{BD}, i_{CD}]^T$ instead of the physical phase current. As discussed earlier, this DQ decomposition is basically a feedback linearization approach for the original nonlinear system. As a result, whenever a MIMO controller gives an output (input to the model), the current conversion from i_Q and i_D to phase current i_A, i_B, and i_C is needed to get the real phase current inputs for each planar motor.

4.6   Sensor Equations

As mentioned in Chapter III, three laser interferometer sensors measure the displacement $(x, y, \text{ and } \phi)$ and velocity $(h, u, \text{ and } v)$ in the horizontal mode. Since laser interferometers only

measure the distance and velocity between the sensors and the stick mirrors, mathematical conversion must be needed to convert those sensors' measurement into the coordinates of the positioner.
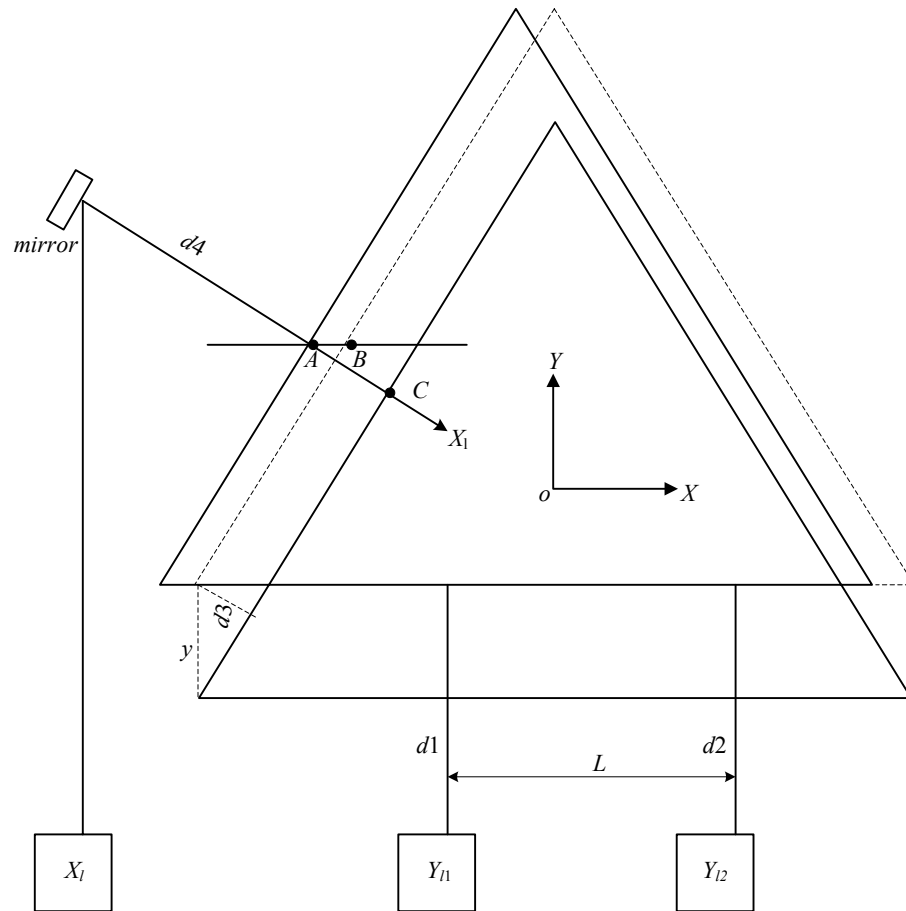
Fig. 4-8 Diagram illustrating metrology principle of laser interferometers

Fig. 4-8 illustrated the metrology principle of those laser interferometer sensors. By programming, the laser interferometers Y_{l1} and Y_{l2} in the y-direction are set to measure the displacement in the y-axis and rotation angle about the z-axis. Basically, sensor Y_{l1} are assigned to measure the displacement in the y-direction and Y_{l2} are set to measure the difference of

readings between Y_{l1} and Y_{l2}. And sensor X_l is set to measure the distance between the mirror and positioner. Those measurements can be represented in symbols labeled in Fig. 4-8 as following

$$Y_{l1} = d1, \tag{4.67}$$

$$Y_{l2} = d2 - d1, \tag{4.68}$$

$$X_l = d4, \tag{4.69}$$

In the initial position, all the laser interferometers will be set to be zero. In other words, those laser interferometer sensors will only measure any relative displacement and rotational angles compared to the initial point. So the displacement in the y-axis is the reading from sensor Y_{l1}. And rotational angle about the z-axis can be calculated.

$$y = Y_{l1}, \tag{4.70}$$

$$\tan \phi = \frac{d2 - d1}{L} = \frac{Y_{l2}}{L}, \tag{4.71}$$

Since the rotation angle about the z-axis is quite small (less than 10^{-4} radian), $\tan \phi \approx \phi$. So the rotational angle about the z-axis can be directly calculated by Eq. (4.71)

$$\phi = \frac{Y_{l2}}{L}, \tag{4.72}$$

It can be noticed that there is an angle of 30° between the X_l axis and the x-axis. As a result, there will be much more considerations when the reading of sensor X_l is converted to the *XOY* coordinate system.

Fig. 4-8 illustrated the movement process of the stage from one position to another position. The positioner first moved y meters in the $+y$-axis (the dash line configuration is the positioner after the $+y$-axis movement). Then it moved from point B to A in the $-x$-axis. The whole process, the positioner moved l_{BA} in the $-x$-axis. Whereas the displacement in the X_l axis is $-l_{CA}$. That's because the movement in the $+y$-axis makes another displacement $-d3$ in the X_l axis.

In order to get the right displacement in the x-axis, the extra displacement $-d3$ introduced by y

must be excluded from $-l_{CA}$. Since the positioner is an equilateral triangle, the displacement in

the x-axis can be calculated as follows.

$$x = -l_{BA} = (-l_{CA} + d3)/\cos 30 = (X_l + y \sin 30°)/\cos 30°,$$ (4.73)

After replacing y in Eq. (4.73) with Y_{l1}, the displacement in the x-axis can be expressed

as

$$x = \frac{X_l}{\cos 30°} + Y_{l1} \tan 30°,$$ (4.74)

The corresponding velocity equations can be easily got by differentiating those

displacement sensor equations. From those sensor equations of (4.70), (4.72), and (4.74), the

transformation matrix of both displacement and velocity can be generalized as

$$\begin{bmatrix} x \\ y \\ \phi \\ h \\ u \\ v \end{bmatrix} = \begin{bmatrix} \dfrac{1}{\cos 30°} & \tan 30° & 0 & 0 & 0 & 0 \\ 0 & 1 & 0 & 0 & 0 & 0 \\ 0 & 0 & \dfrac{1}{L} & 0 & 0 & 0 \\ 0 & 0 & 0 & \dfrac{1}{\cos 30°} & \tan 30° & 0 \\ 0 & 0 & 0 & 0 & 1 & 0 \\ 0 & 0 & 0 & 0 & 0 & \dfrac{1}{L} \end{bmatrix} \begin{bmatrix} X_l \\ Y_{l1} \\ Y_{l2} \\ V_l \\ V_{l1} \\ V_{l2} \end{bmatrix},$$ (4.75)

Where V_l, V_{l1}, and V_{l2} are the velocity readings from laser interferometer sensors X_l, Y_{l1},

and Y_{l2} respectively. Those above horizontal mode sensor equations were derived by considering

displacement in the x- and y-axis. The effects (when the positioner has a rotational angle about

the z-axis, the reading of both X_l and Y_{l1} will be changed.) to those displacements generated by

the rotation about the z-axis are trivial compared since the angle is less than 10^{-4} radian.

In the vertical mode, sensor equations are also necessary to convert the sensors' readings

into the coordinates for the mass center point o. Those laser distance sensors can only give the

displacement information, so only displacement sensor equations are needed. The main idea to

derive those sensor equations is considering any contribution from the motion to the displacement. Fig. 4-9 showed the position of each laser sensors in the platen.
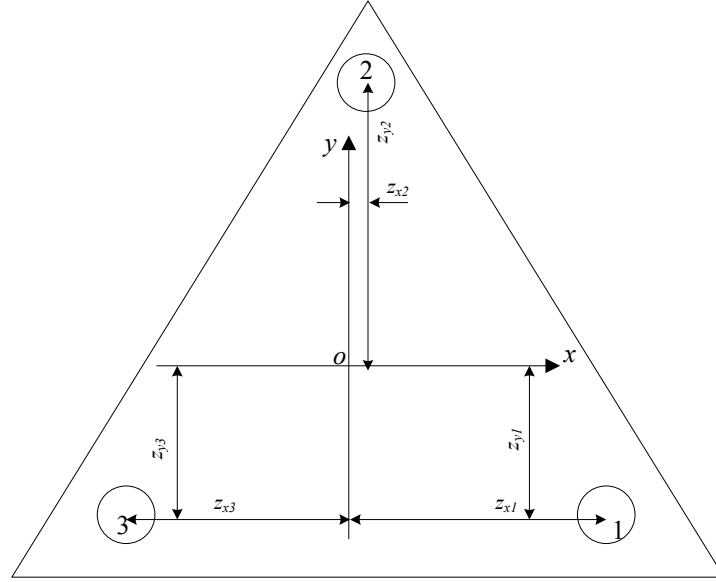
Fig. 4-9 Position of laser distance sensors (top view)

The relationship between the reading of each sensor and the displacement in the vertical mode is developed as follows.

$$\begin{bmatrix} z_1 \\ z_2 \\ z_3 \end{bmatrix} = \begin{bmatrix} -z_{y1} & -z_{x1} & 1 \\ z_{y2} & -z_{x2} & 1 \\ -z_{y3} & z_{x3} & 1 \end{bmatrix} \begin{bmatrix} \theta \\ \varphi \\ z \end{bmatrix},$$ (4.76)

Table 4.2 presented the values of geometric parameters in Fig. 4-9. After plugging those values into the Eq. (4.76) and inversing the coefficient matrix, it can be got the sensor transformation equations:

$$\begin{bmatrix} \theta \\ \varphi \\ z \end{bmatrix} = \begin{bmatrix} -2.410 & 4.600 & -2.190 \\ -3.946 & 0.127 & 3.818 \\ 0.315 & 0.289 & 0.410 \end{bmatrix} \begin{bmatrix} z_1 \\ z_2 \\ z_3 \end{bmatrix},$$ (4.77)

The above equation is the sensor equation in the vertical mode. Equations (4.75) and (4.77) make it possible to extract the velocity and displacement information about the mass center of the positioner from the six laser sensors.

Table 4.2 Values of length variables in Fig. 4-9

Variable	Value (mm)	Variable	Value (mm)
z_{y1}	58.9	z_{x1}	141.1
z_{y2}	155.1	z_{x2}	18.3
z_{y3}	66.0	z_{x3}	116.7

CHAPTER V

CONTROL SYSTEM DESIGN AND IMPLEMENTATION

In Chapter IV, both the decoupled (six different models in all directions) and state-space models of the system were developed. Based on those two models, there are two different methodologies to design the control system. One is classical SISO controller design. The other is MIMO controller design. In this chapter, SISO control design approache is discussed. The objective of the controller design is to make the positioning resolution as high as possible and to achieve high acceleration in motion. Experimental results are presented in this chapter to evaluate the designed controllers.

5.1   Initial Working Position of the System

The positoner can not start to work from anywhere in the base plate. There are some restrictions for the initial working position of the system. From the electromagnetic analysis discussed in previous chapters, it can be seen that the selection of initial working position is based on the stability in that position. The force Eq. (4.9) presented in Chapter IV is also developed based on the initial position. As a result, choosing the right initial working position is the first step to make the positioner to be under control.

The diagram (Fig. 4-2) of *DQ* decomposition presented in the last chapter illustrated the way to set the initial working position for the positioner. The detailed initial position is presented in Fig. 5-1.
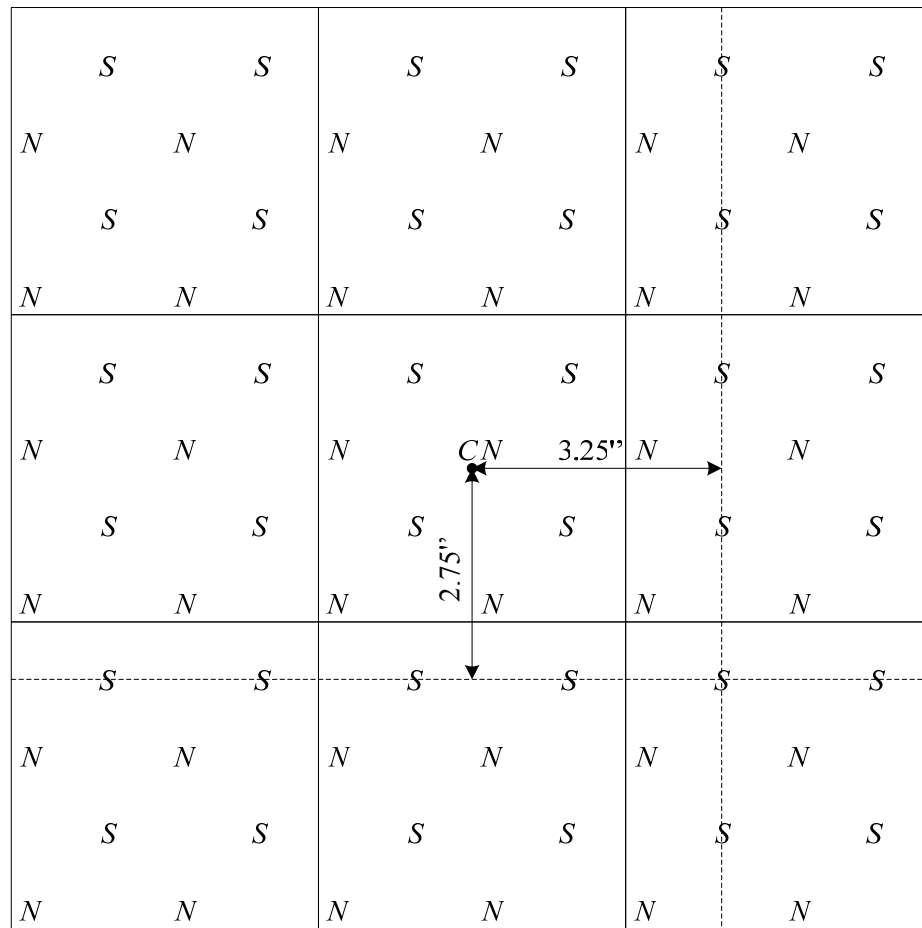
Fig. 5-1 Diagram of initial working position of the positioner

Since the magnet matrix and planar motor have a pitch of 2 inches, each possible initial position is 2 inches away in the *x-y* plane. The initial position is chosen to make the positioner have the full travel range in the horizontal mode. Since the distance of all the three planar motors is fixed, one of the planar motors (motor *B*) is marked with an identification point for the positioner. Then the position determined in the base plate is also marked. Each time, the positioner will begin to work from where the two points matched. With all the three laser interferometers in their measuring range, this matching points method can guarantee that each time the positioner work from the right initial position.

If all the three air bearings are on from the beginning, it will be very difficult to hold the positioner in the initial position because of the non-friction between the positioner and the base plate. As a result, to maintain the positioner in the initial working point at the beginning, the air bearings are off. When the controller is enabled, those air bearings will be on manually by the operator. Since when the air bearings are off, there is friction between the positioner and the base plate, the model developed in Chapter IV is incorrect for this case. However, if the controller is designed to have enough robustness, it should handle both the two cases. Next section, the controller design process will be discussed.

5.2   Sampling Rate and Discretization

Since the whole system is controlled by the DSP, the continuous signal has to be converted into discrete signal by sampling the original signal. The sampling rate is an important parameter in digital-signal-processing and digital-control-system design. There are many references [84−86] discussing on how to determine the sampling rate in digital control system design. The Nyquist frequency criterion is widely used in digital signal processing to avoid aliasing in frequency domain. However, in digital control system design, the sampling frequency is set to be as high as possible. There are several reasons to do that.

(1)   Reduce phase lag due to the time-delay effect of the sample-and-holder. The average delay by the sample-and-holder is $T_s/2$ on average.

(2)   If the sampling rate is fast enough, the dynamics of the discrete-time system can be emulated the continuous-time counterpart.

A sampling rate of at least 20 times greater than the system bandwidth is a rule of thumb in digital control system design [86]. Based on the hardware setup, the sampling frequency is determined to be 5 kHz. It is a challenge for the real-time control design since it has only 200 μs

to go through all its routine. All the time-consuming operations such as snapping data, displaying, and so on must be out of the real-time control routine which can be seen from the program flow chart in Fig. 2-23 of Chapter II.

There are a few ways to convert a continuous time system into a discrete time system by choosing different numerical approximation methods. Methods such as zero order hold (ZOH), pole-zero matching, and bilinear approximation (Tustin) are widely used in discretizing continuous time system [86]. Here the matched pole-zero (MPZ) method is selected as the discretize method. The function "c2d" in MATLAB is used to get the digital controller from the continuous one. The drawback of the MPZ method is that the bandwidth of the discrete-time system would be a slightly different from the original one. The trial-and-error adjustments of the gain in the discrete-time controller are necessary to make the digital system have the same design specifications as the continuous one.

5.3 SISO Controller Design

5.3.1 Lateral Mode Control

Eqs. (5.1), (5.2), and (5.3) showed three detailed models in the x-, y-, and ψ -direction respectively by plugging m and I_{zz} in the transfer functions developed in Chapter IV (Eqs. (4.37)−(4.39)).

$$\frac{x(s)}{f_x(s)} = \frac{1}{5.91s^2},$$

(5.1)

$$\frac{y(s)}{f_y(s)} = \frac{1}{5.91s^2},$$

(5.2)

$$\frac{\phi(s)}{M_{oz}(s)} = \frac{1}{0.054s^2},$$

(5.3)

Based on the model, three individual SISO controllers can be designed for each axis. In this design approach, the nonlinearity of magnet force equation can be properly eliminated by directly considering the transfer function from input magnet force to output displacement. In each sampling period, when the controller calculated a desired value of controlling force, Eq. (4.9) will immediately be applied to calculate the physical phase current for each planar motor.

A continuous time lead-lag compensator is first designed in the *x*-direction by using MATLAB root-locus routines. The closed-loop control structure is shown in Fig. 5-2. The controller *D* (*s*) is designed as shown in Eq. (5.4).
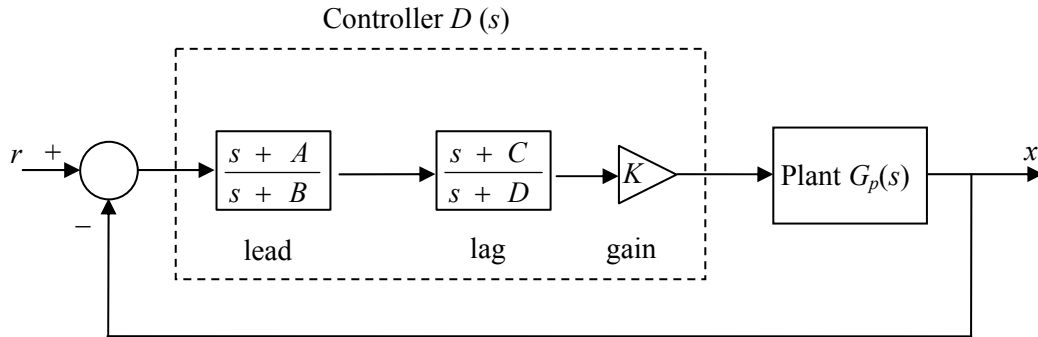
Fig. 5-2 Continuous time lead-lag compensator in the *x*-direction

$$D(s) = 9.0244 \times 10^5 \, \frac{(s + 55.6904)(s + 10)}{s(s + 1134.2247)}, \tag{5.4}$$

From Eq. (5.4), it can be noticed there is a pure integrator in the controller. Since the positioner is modeled as a pure mass in the horizontal mode, there are already two poles in the origin which should have enough power to eliminate the steady-state error due to the step input. It seems it is redundant to add another integrator in the controller to eliminate the steady-state error. However, experimental results proved that adding a pure integrator in the controller is extremely important to eliminate the steady-state error. The reason is that the positioner may not

behave completely modeled as a pure mass due to the inevitable disturbances brought by the stiff air pipe and the umbilical signal cable attached on the positioner. Fig. 5-3 showed the phase margin of 57.7° at a crossover frequency of 21 Hz.
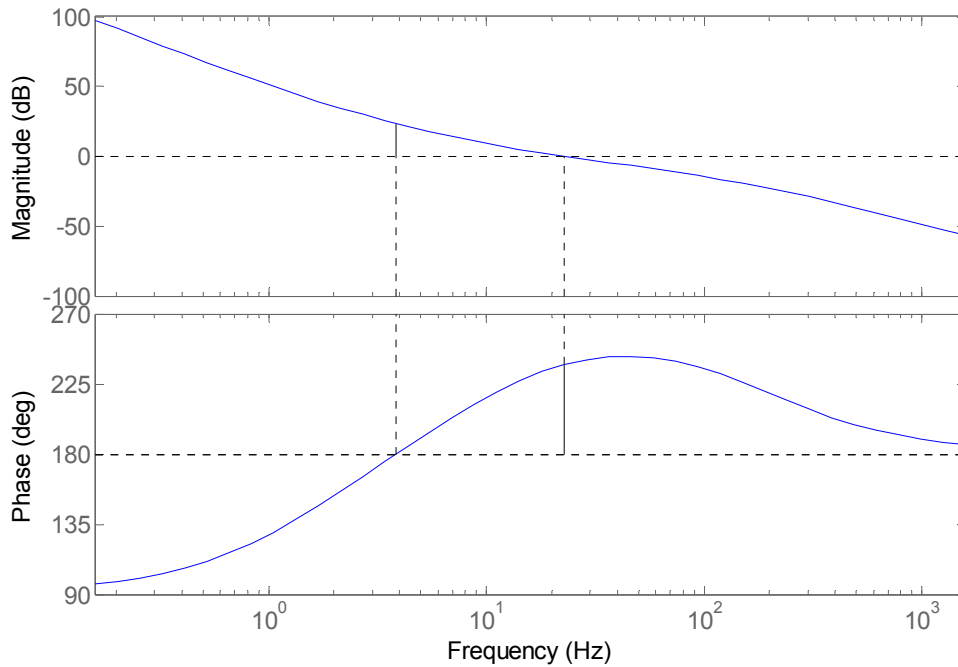
Fig. 5-3 Loop transmission in the *x*-direction

The model in the *y*-direction is exactly the same as that in the *x*-direction. So the same controller can be also used in the *y*-direction. The same design methodology can be used in the ψ-direction. The continuous time lead-lag compensator is designed as Eq. (5.5).

$$D(s) = 1.4481 \times 10^4 \frac{(s + 55.6904)(s + 10)}{s(s + 1134.2247)}, \tag{5.5}$$

The phase margin is designed to be 62.7° at a crossover frequency of 38 Hz, which can be seen from loop transfer function bode plot in the Fig. 5-4.
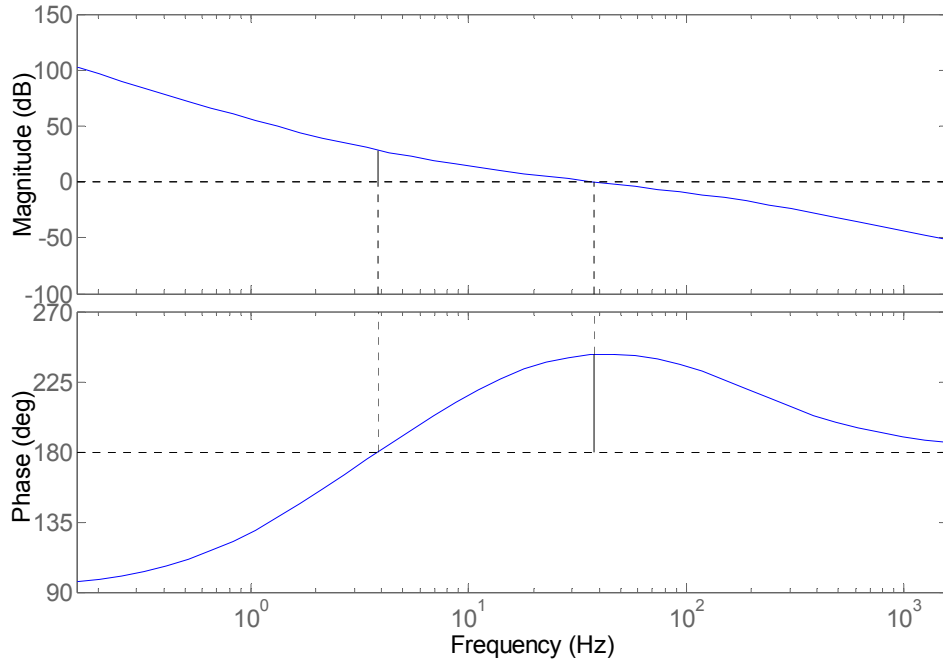
Fig. 5-4 Loop transmission in the ψ-direction

The corresponding digital controllers in the horizontal mode can be obtained from the MATLAB as following. It can be seen that the poles and zeros in the digital controller all have 5 digits. The purpose of that is to reduce the error from the discretization as small as possible.

$$D_{x,y}(z) = 7.4 \times 10^5 \frac{(z-0.9903)(z-0.9979)}{(z-0.7970)(z-1)}, \qquad (5.6)$$

$$D_{\phi}(z) = 13062.95 \frac{(z-0.9903)(z-0.9979)}{(z-0.7970)(z-1)}, \qquad (5.7)$$

Since the three air bearings will suspend the positioner in the vertical mode, the three controllers in the horizontal mode will first be functional to control the position in the lateral plane. Then the vertical mode controllers will work to control the motion in that plane. The following subsection discusses the design process of controllers in the vertical mode.

5.3.2   Vertical Mode Control

The models in the vertical mode are presented in the following equations with the parameters obtained previously.

$$\frac{z(s)}{f_z(s)} = \frac{1}{5.91s^2 + 1000000},$$ (5.8)

$$\frac{\theta(s)}{M_{ox}(s)} = \frac{1}{0.033s^2 + 11152},$$ (5.9)

$$\frac{\varphi(s)}{M_{oy}(s)} = \frac{1}{0.025s^2 + 11653},$$ (5.10)

Since the existence of large spring constants in the models, it can be expected that there will be significant resonance. For example, the resonance frequency of about 100 Hz in the φ-axis can be clearly seen in the Fig. 5-5.

In this case, since the resonant frequency is as high as 100 Hz, if the bandwidth of the controller is higher than 100 Hz, the system will go unstable due to the saturation of the actuators. But if the bandwidth of the loop transfer function is less than 100 Hz, the resonant dynamics will make the dynamics of the closed-loop system very slow. In order to control the system well in the vertical mode with the resonance at 100 Hz, a minor-loop control system was developed as shown in Fig. 5-6.

In the minor loop, a controller D (s) is designed in the feedback path. It is used to modify the dynamics of the original plant. The D (s) is designed in such a way that the closed-loop modified system (inside the dashed box) has better dynamic properties mitigating the air-bearing
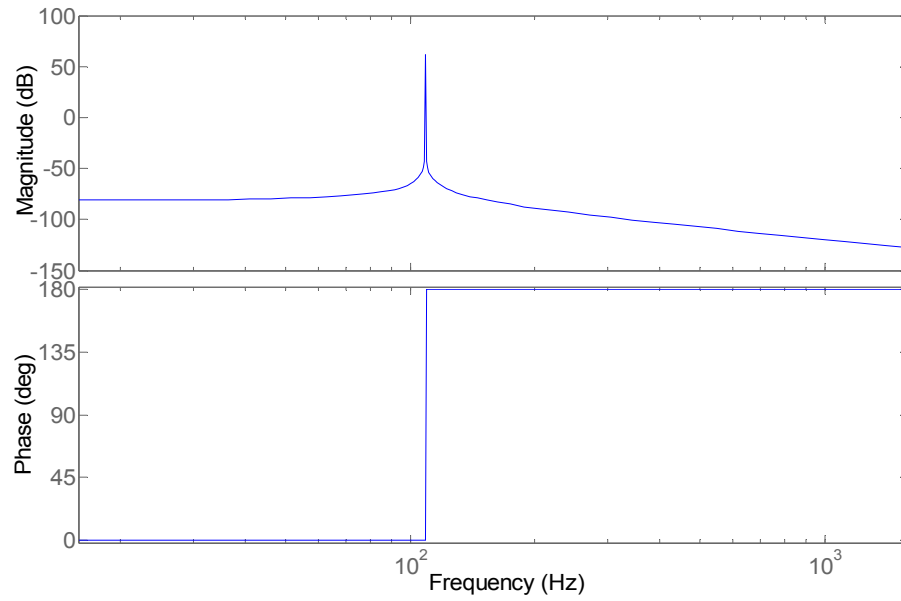
Fig. 5-5 Bode plot of dynamics in the φ-axis
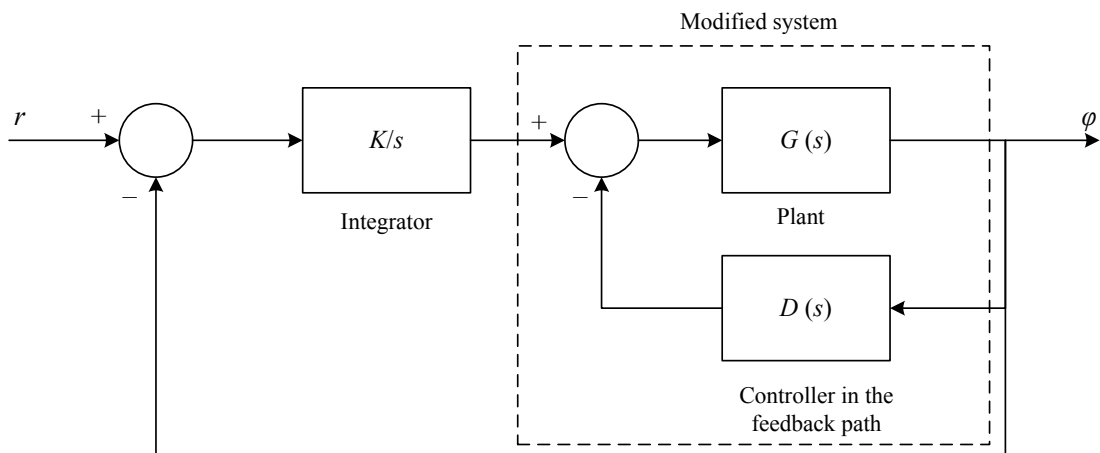
Fig. 5-6 Control structure in the vertical mode

resonance. After that, an integrator in the outer loop is designed to control the new modified system.

The controller D (s) in the φ-direction is designed as shown in Eq. (5.11). And the transfer function of the modified system is presented in the Eq. (5.12). It can be seen that the controller D (s) brought some damping into the new modified system. The Bode plot of the modified system $G_2(s)$ is shown in the Fig. 5-7.

$$D_\varphi(s) = \frac{12.5s}{0.0012s + 1},$$ (5.11)

$$G_2(s) = \frac{G(s)}{1 + D_\varphi(s)G(s)} = \frac{0.0012s + 1}{(0.025s^2 + 11653)(0.0012s + 1) + 12.5s},$$ (5.12)
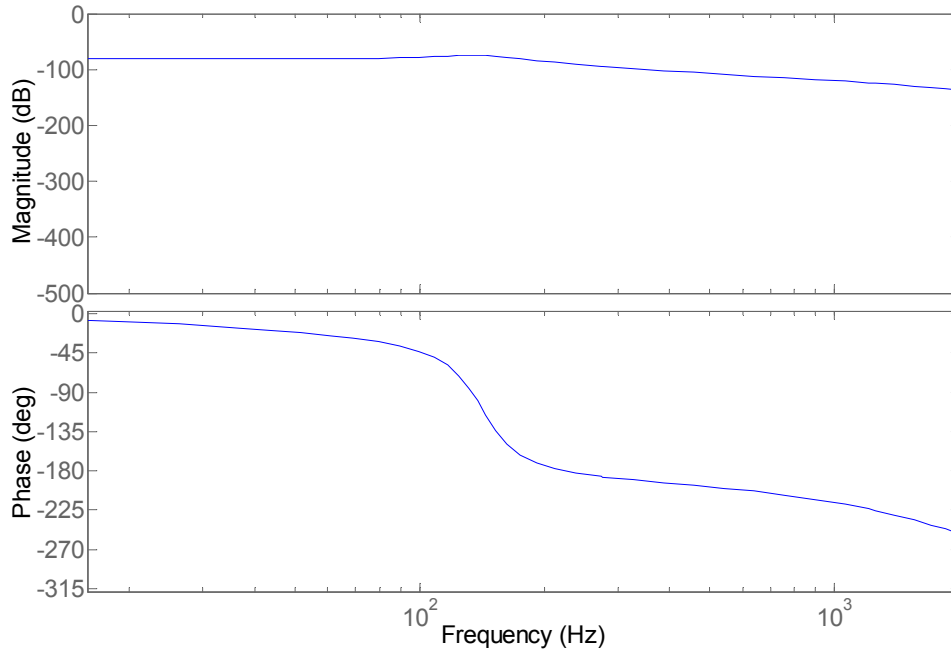
Fig. 5-7 Bode plot of the modified system in the φ-direction

It can be seen from the Fig. 5-7 that there is no resonant peak near 100 Hz any more. Based on this new system, the gain of the integrator in the outer loop can be determined by designing appropriate phase and gain margins for the system.

$$K_\varphi = 5 \times 10^5 \text{ N/rad-s},$$ (5.13)

With the gain K and controller $D_\varphi (s)$ determined, the bode plot of the loop transfer function can be got. Fig. 5-8 shows the phase margin is 87.06˚ with a crossover frequency of 6.8 Hz. The controller design of controllers in the φ-direction is completed.
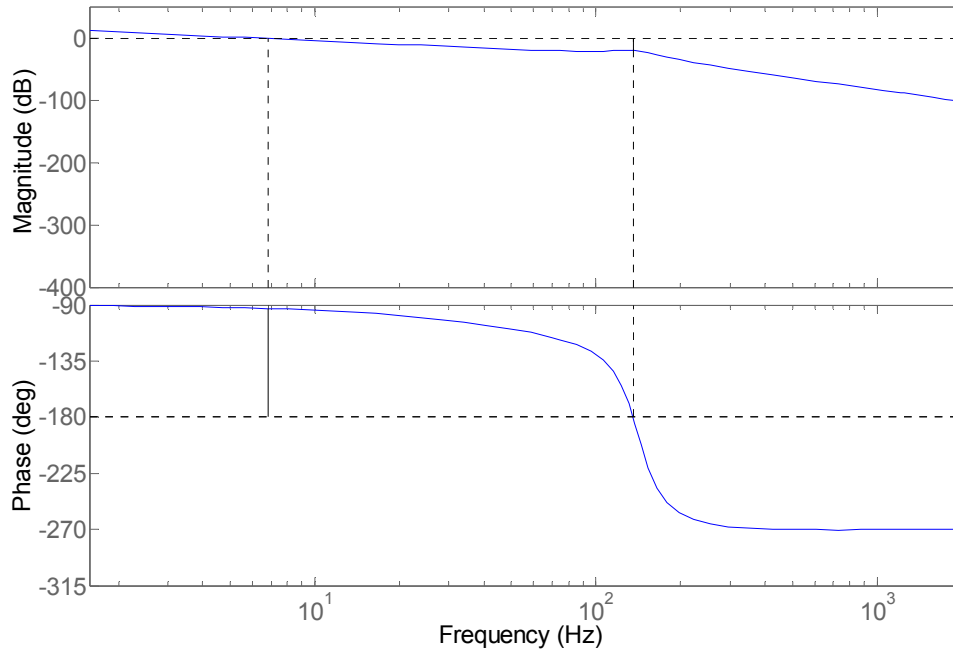
Fig. 5-8 Bode plot of loop transmission in the φ-direction

Since the transfer function in the θ-direction is almost the same as that in the φ-direction, the controller developed above can be also used in the θ-direction too. The crossover frequency and phase margin in the θ-direction should be similar to those parameters in the φ-direction. Similar methodology can be used to design the controller for the z-direction. The continuous time controller designed for the z-direction is shown in the Eqs. (5.14) and (5.15). Fig. 5-9 shows the controller achieved a phase margin of 80.65˚ with a crossover frequency of 7.90 Hz.

$$K_z = 5 \times 10^7 \, \text{N/rad-s}, \tag{5.14}$$

$$D_z(s) = \frac{3000s}{0.001s + 1}, \tag{5.15}$$
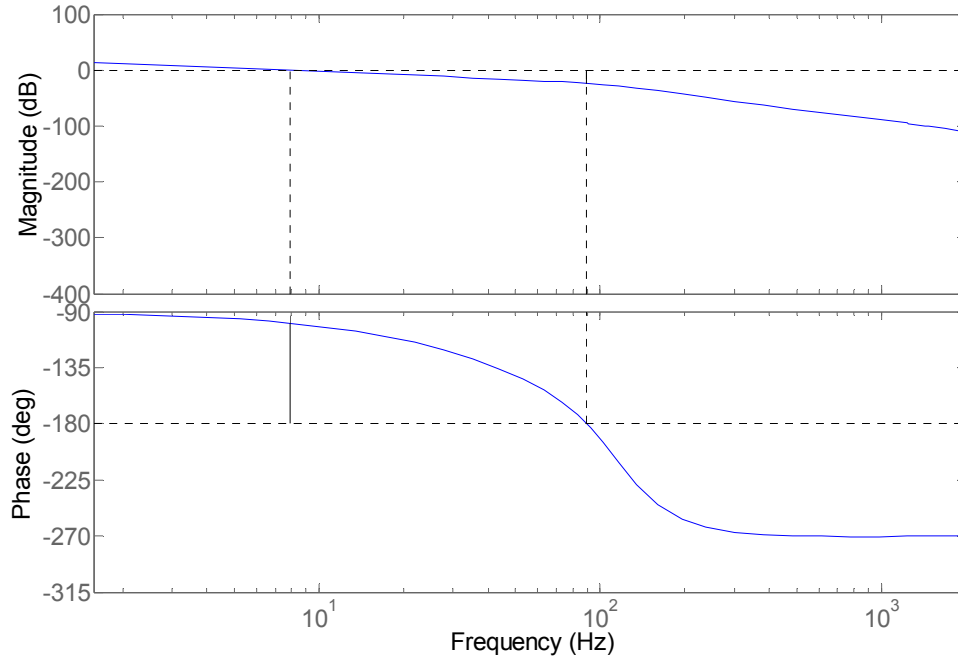
Fig. 5-9 Bode plot of loop transmission in the *z*-direction

The corresponding digital controllers in the vertical mode are shown in the following equations.

$$K_z(z) = 10^4 \, N/m \cdot s, D_z(z) = 3 \times 10^6 \, \frac{z-1}{z-0.8187} \, , \tag{5.16}$$

$$K_{\theta,\varphi}(z) = 10^2 \, N/rad \cdot s, D_z(z) = 1.083 \times 10^4 \, \frac{z-1}{z-0.8465} \, , \tag{5.17}$$

The controllers in all the six axes have been designed. The positioner is first placed in the initial position. Then the three horizontal controllers are enabled with all the three bearings off. After that, the air bearings are turned on manually. Since the positioner is levitated by the air, the distance of the positioner and the base plate would change. After resetting the three laser distance sensors in the vertical mode, the three vertical controllers are enabled. Then, the positioner is fully controlled in all six axes.

5.4   Experimental Results

After the digital controllers were implemented, the positioner was tested for its positioning capability in all six axes. For a stage to satisfy the requirements of precision manufacturing, the positioner should have a nanoscale positioning resolution, fast response, and an extended travel range. In addition, the capability of generating any two-dimensional trajectory is also necessary for such a positioner to be used in wafer inspection. The multi-DOF positioner presented herein has the potential to satisfy all these requirements. Several experimental results are presented in this section to demonstrate its applicability in future semiconductor manufacturing and factory automation. Those experiments include basic microscale and nanoscale step response, nano-positioning capabilities, acceleration capabilities, and generation of typical wafer-stage movement in semiconductor manufacturing. In this section, the experimental results are presented and analyzed.

5.4.1   Step Responses

10-μm step responses were taken in the x- and y-directions. At the same time, the perturbation to the other five axes were also recorded and shown in Fig. 5-10 and Fig. 5-11. The rise time is less than 3 ms, and the settling time is less than 150 ms without steady-state error in x and y. The more oscillatory behavior in the x-direction is believed to originate from the fact that motor C generates a perturbation torque. Although motors A and B would compensate for this torque, it might not have been completely canceled due to modeling errors. The perturbations to other axes demonstrated that there is dynamics coupling in all the axes. To show the dynamic performances in other axes, the step responses of 5 μm in z, 10 μrad in θ, φ, and ψ are also shown in Figs. 5-12, 5-13, 5-14, and 5-15, respectively.

The rise times of vertical step responses are a little longer than those in horizontal step responses because of the damped dynamics of the three aerostatic bearings. The low-frequency (at about 10 Hz) disturbance in ψ is believed to be generated by the umbilical cables and air pipes connected to the positioner.

Fig. 5-16 demonstrated the capability of nano positioning in the x-direction. There exists a 60-nm peak-to-peak (10 nm rms) position noise in the system. The fast Fourier transform (FFT) shows the dominant noise frequency is about 100 Hz. Both the noise generated by the three aerostatic bearings and the external disturbance transmitted through the umbilical cables are believed to contribute to the position noise. Fig. 5-17 presented sub-micron positioning capability of the positioner in the z-, θ-, φ-, and ψ-axis, respectively. These experimental results demonstrate the integrated positoner presented herein possesses the potential to satisfy the requirement of semiconductor manufacturing.
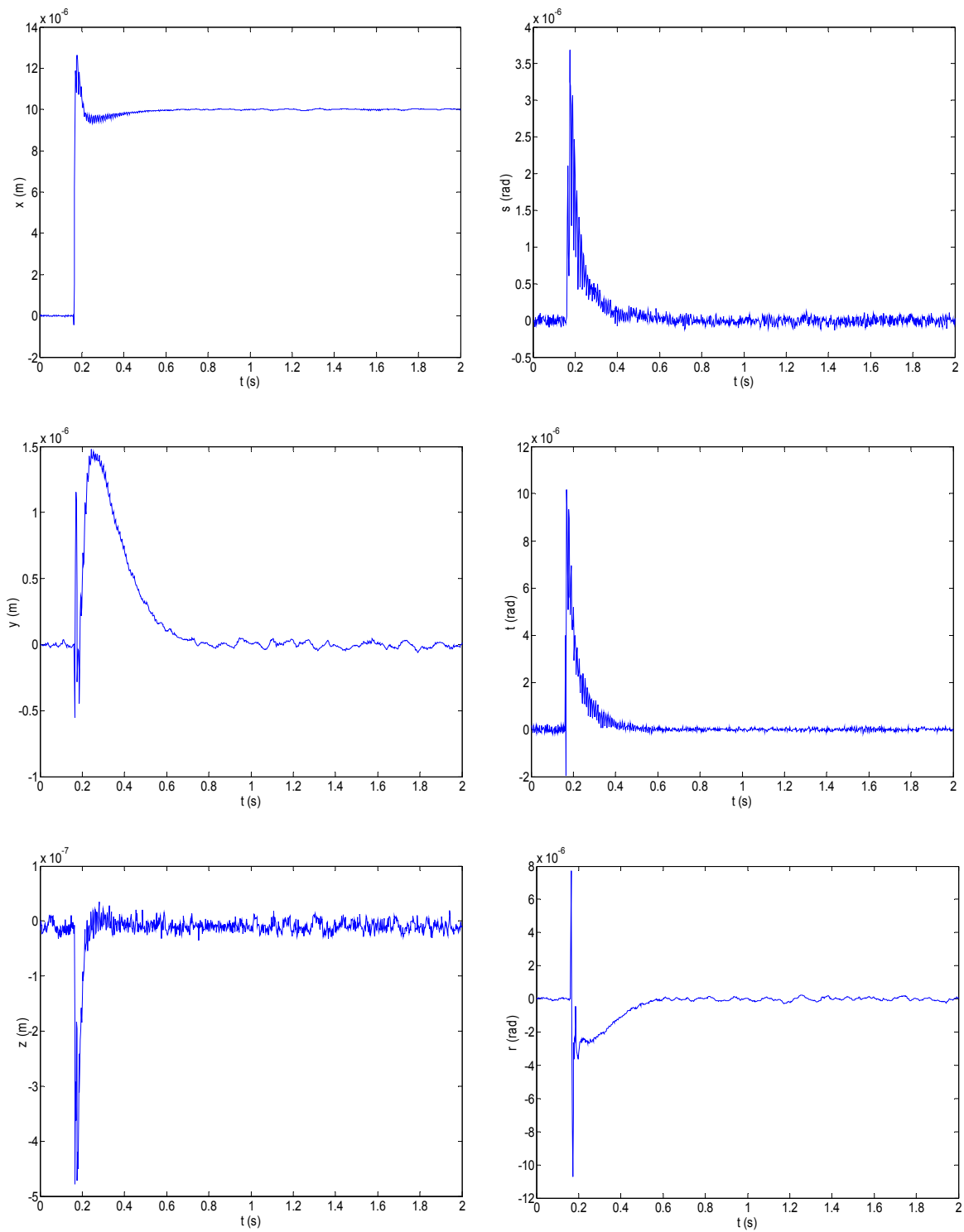
Fig. 5-10 10-μm step response in *x* with perturbation in other axes
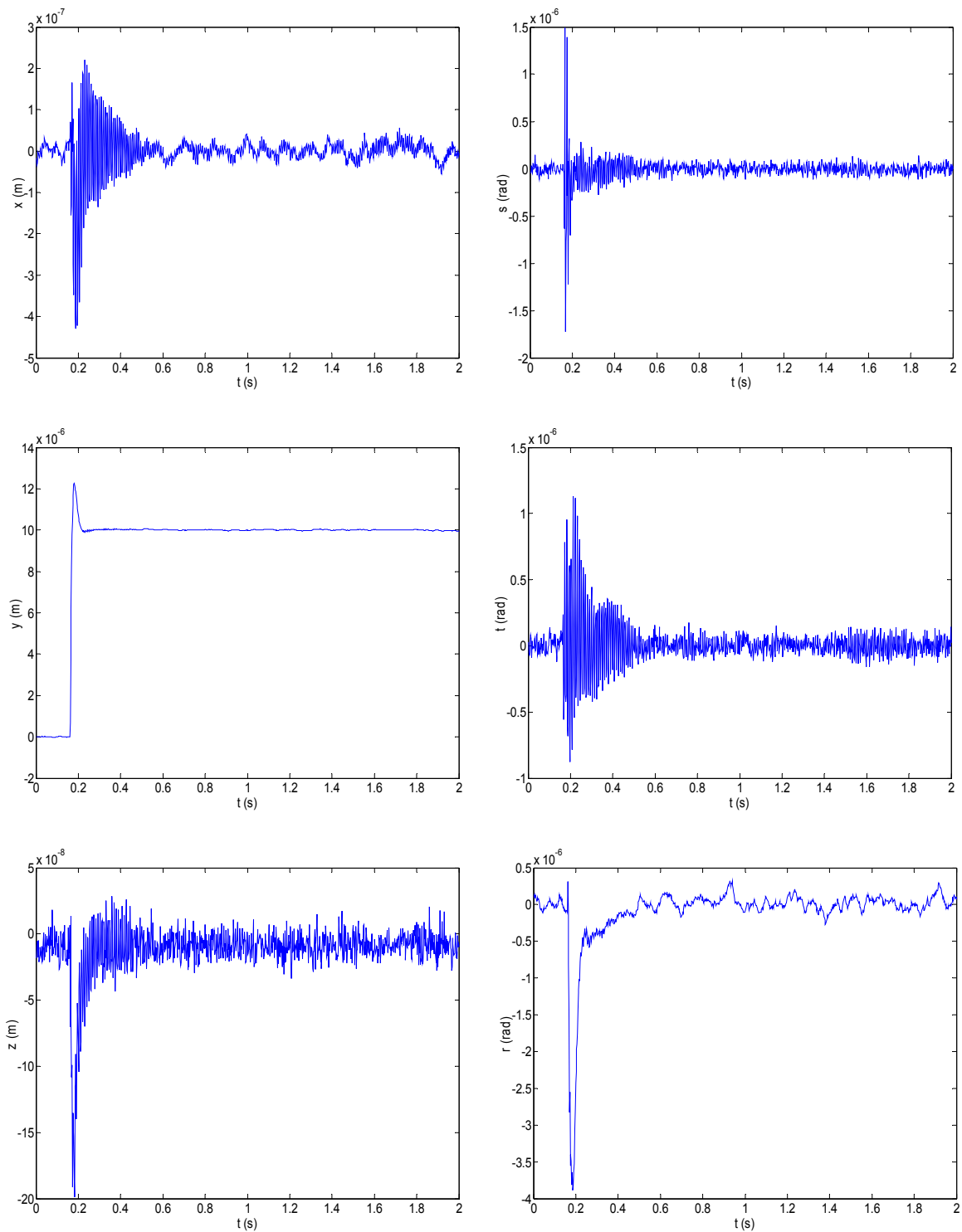
Fig. 5-11   10-μm step response in *y* with perturbation in other axes
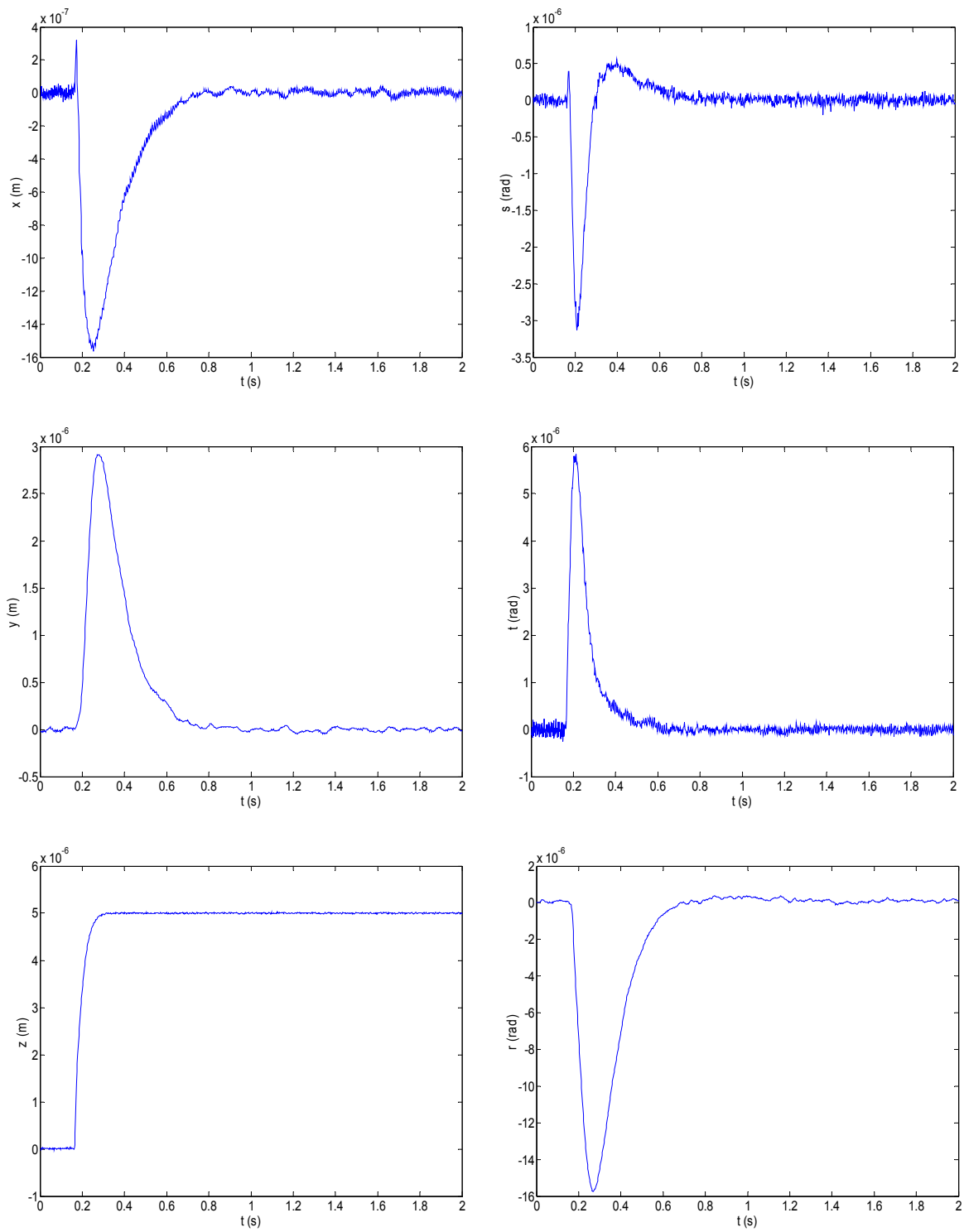
Fig. 5-12 5-μm step response in *z* with perturbation in other axes
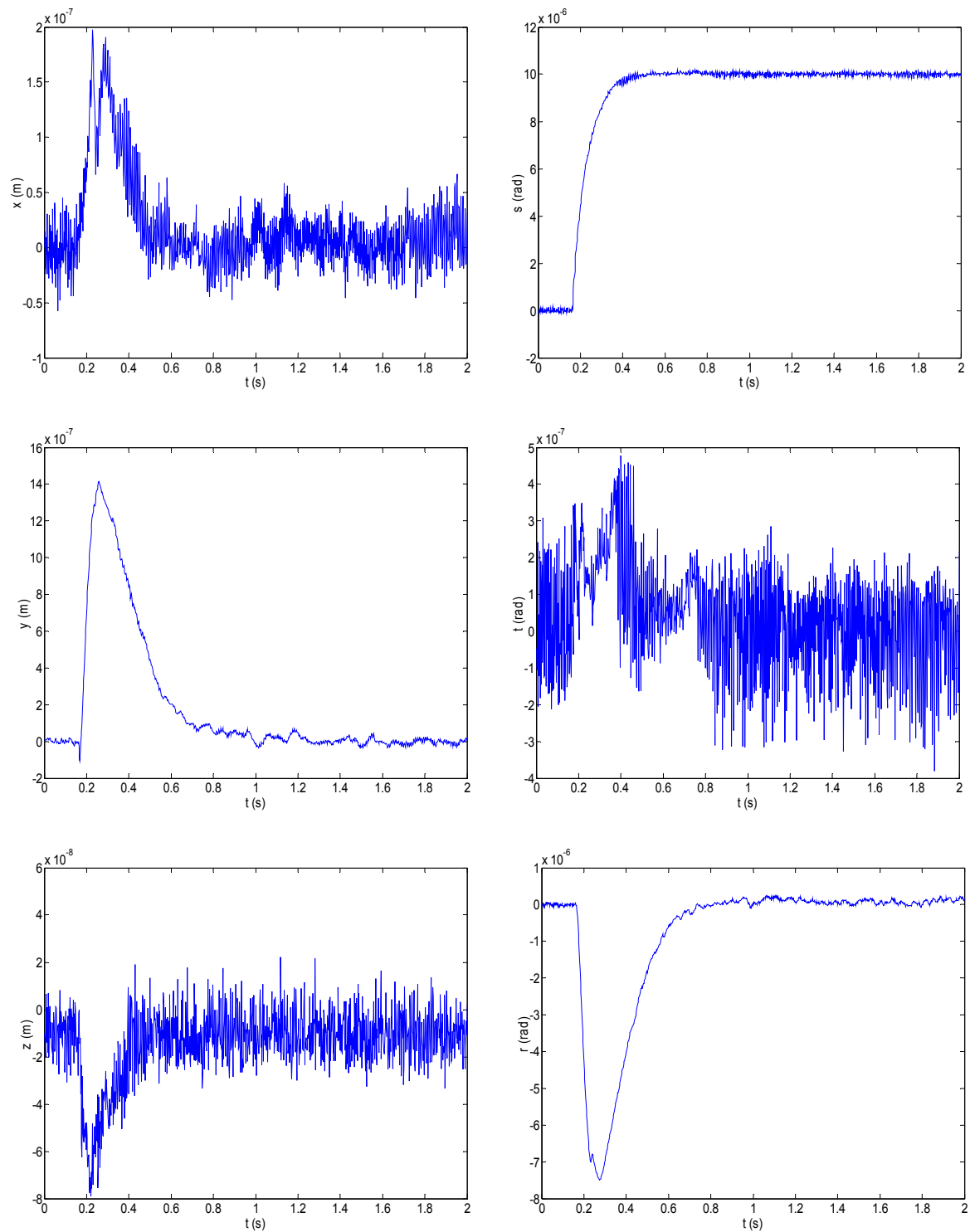
Fig. 5-13 10-μrad in θ with perturbation in other axes
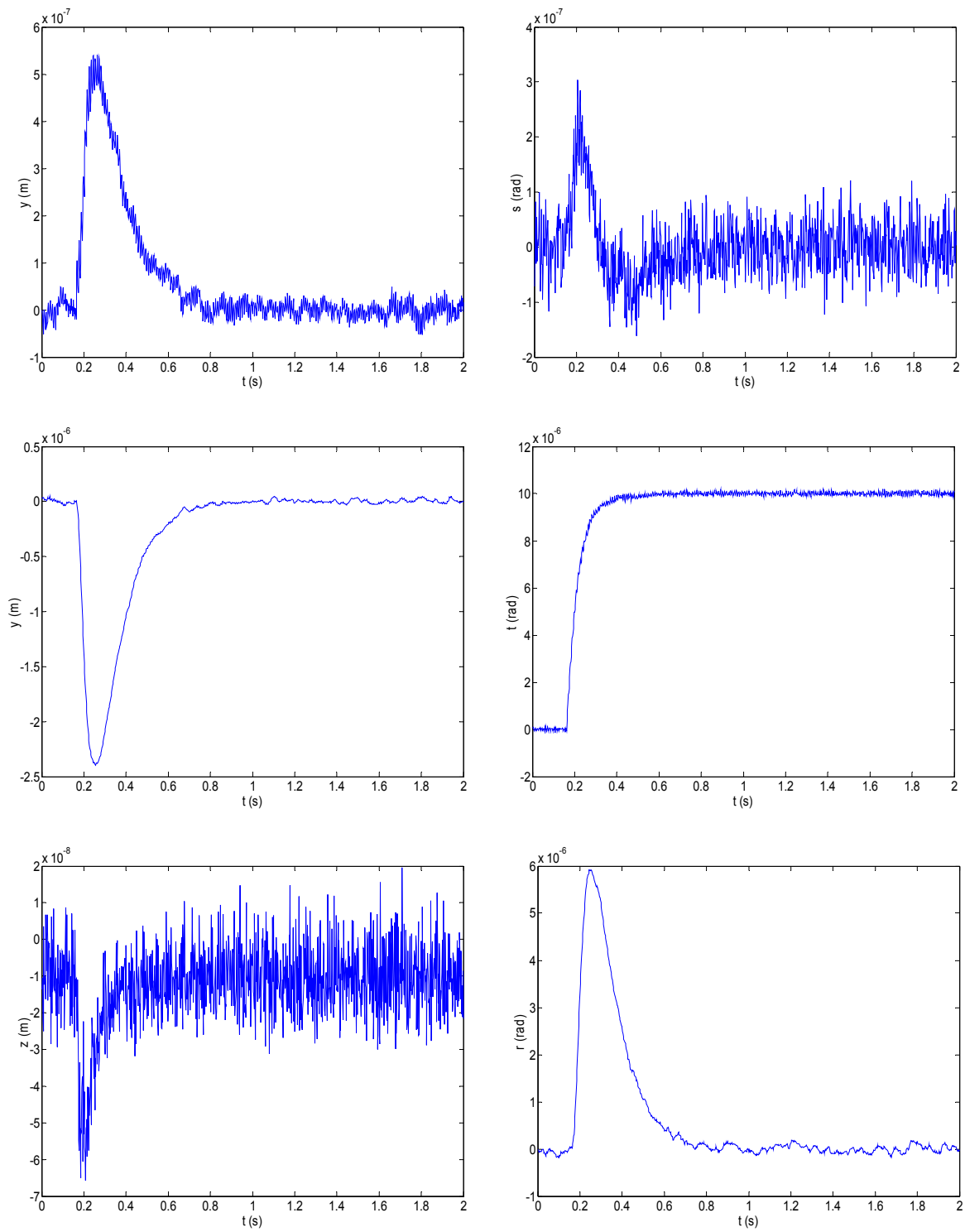
Fig. 5-14 10-μrad in φ with perturbation in other axes
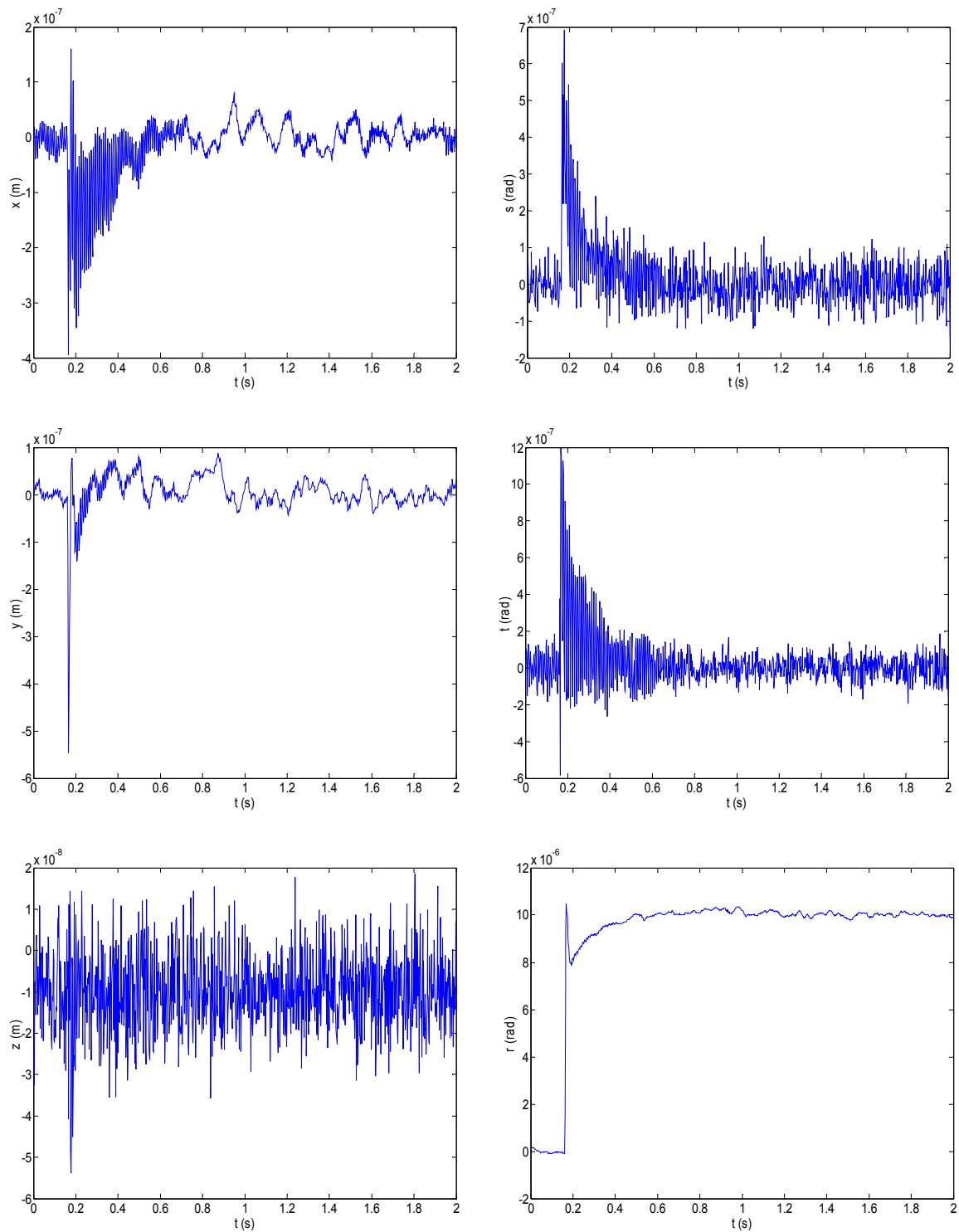
Fig. 5-15 10-µrad in ψ with perturbation in other axes
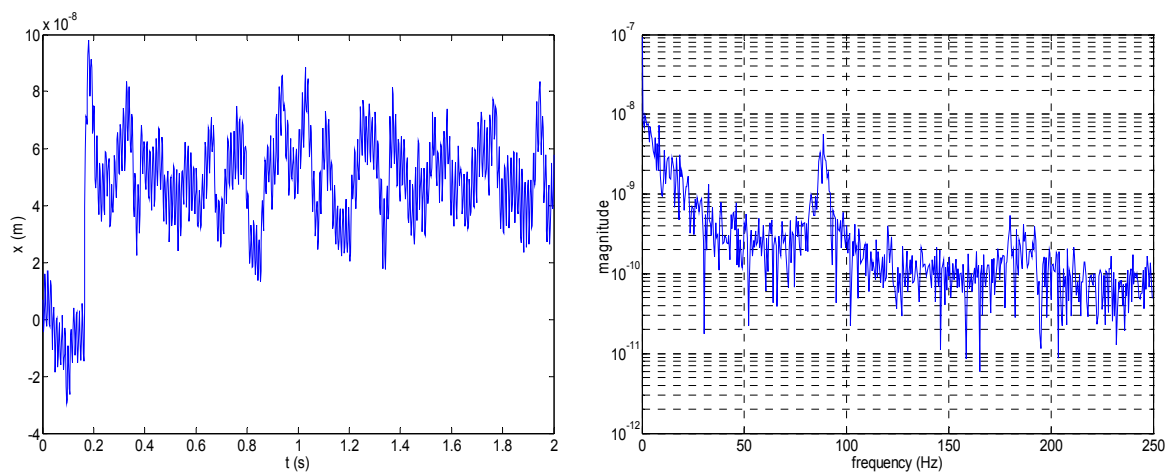
Fig. 5-16 50-μm step responses and FFT in *x*
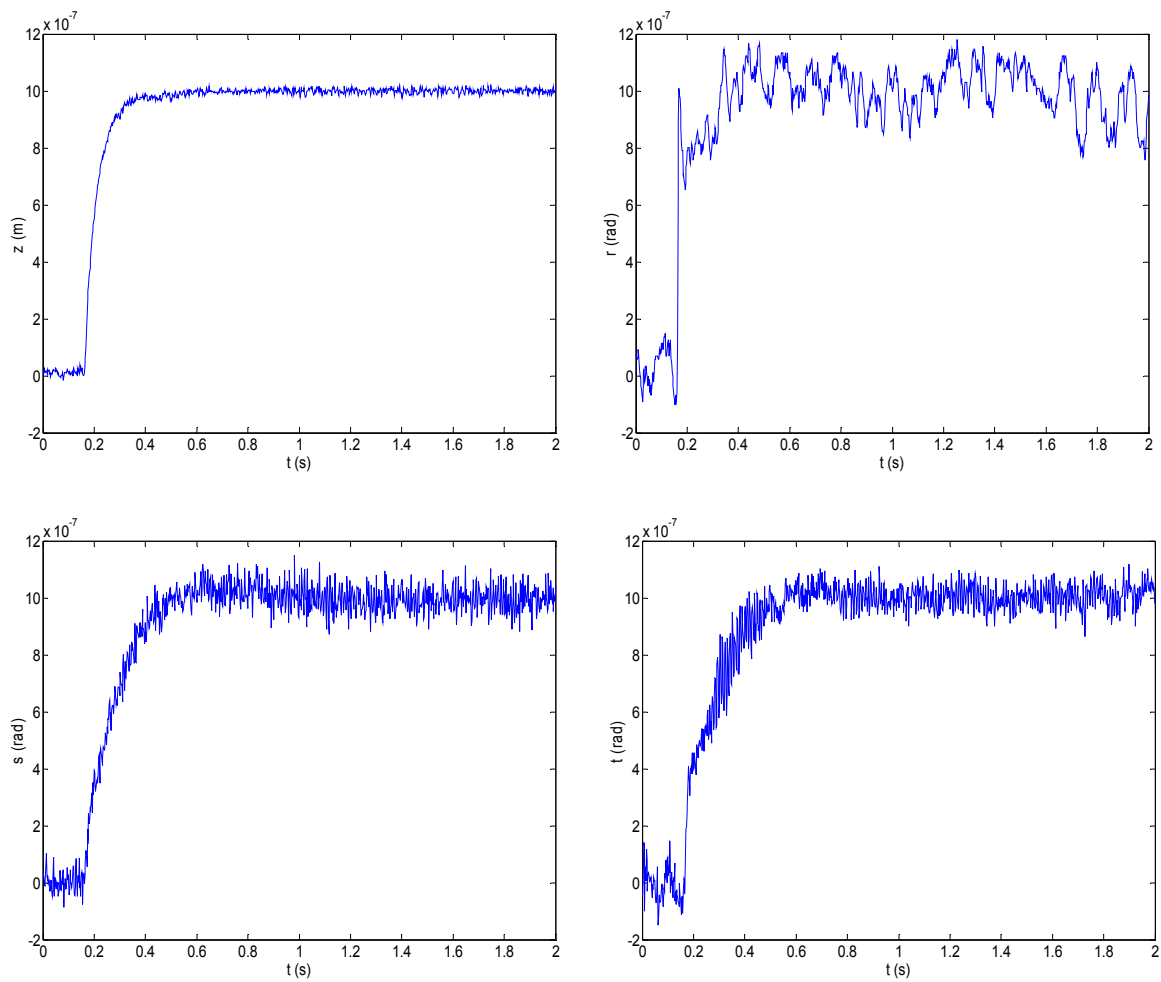
Fig. 5-17 1-μm in z and 1-μrad in ψ, θ, and φ respectively

5.4.2   Planar Scanning Motion

Planar scanning motion is a typical motion used in precision engineering such as microlithography, inspection, and optical machinery [87−89]. Several experimental results are presented to demonstrate the scanning capability of the positioner both in centimeter scale and in micrometer scale.

Fig. 5-18 (a) and (b) showed the positoner have a planar travel range of 16 cm both in x and y. And the scanning velocity is 5 mm/s. The travel range is limited by the length of stick mirrors and number of pitches in the magnet matrix. As a result, the travel range can be easily extended by adding more magnets in the base plate and using longer stick mirrors. Fig. 5-18 (c) and (d) demonstrated that the positioner has the capability of following both curved and straight-line long-range trajectories in the x-y plane. The angular velocity is 0.5 rad/s in the circle and the linear velocity was 5 mm/s in the double triangle.

Figs. 5-19, 5-20, and 5-21 show that the positioner can precisely follow any micro-scale trajectory in the x-y plane. From the tracking errors shown in Fig. 5-19 (b) and Fig. 5-21 (a) and (b), it can be seen that the position errors in following those trajectories are less than 30 nm rms. Fig. 5-20 (b) showed the frequency domain analysis of the positioning noise in the system. These experimental results demonstrated that the positioner has the capability of 1D and 2D precision positioning.
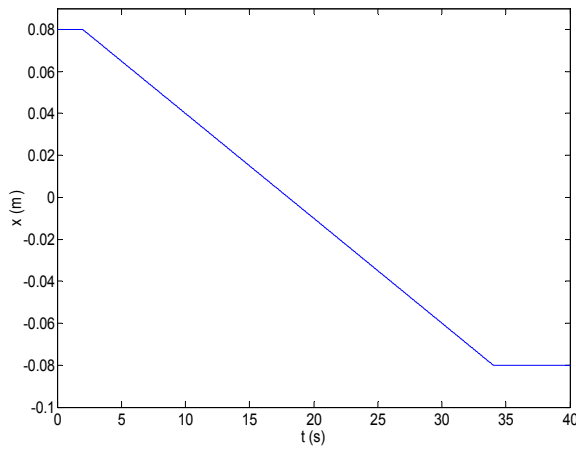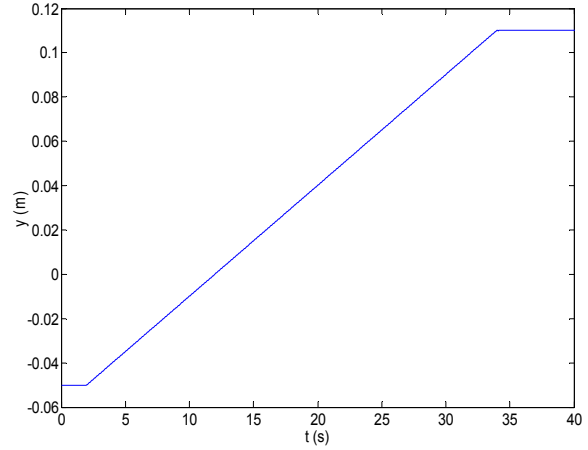
(a)   (b)
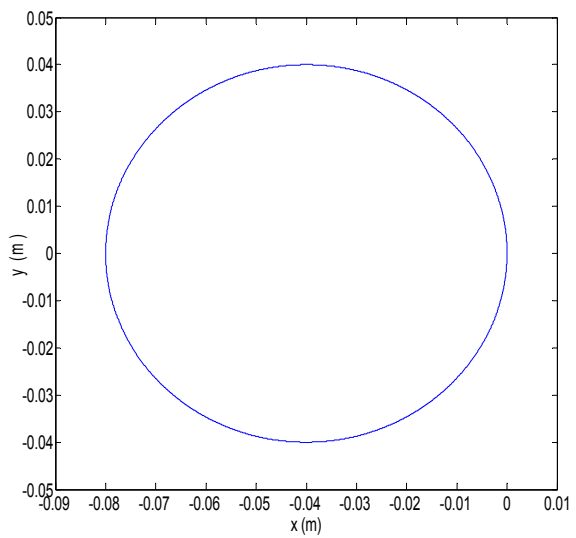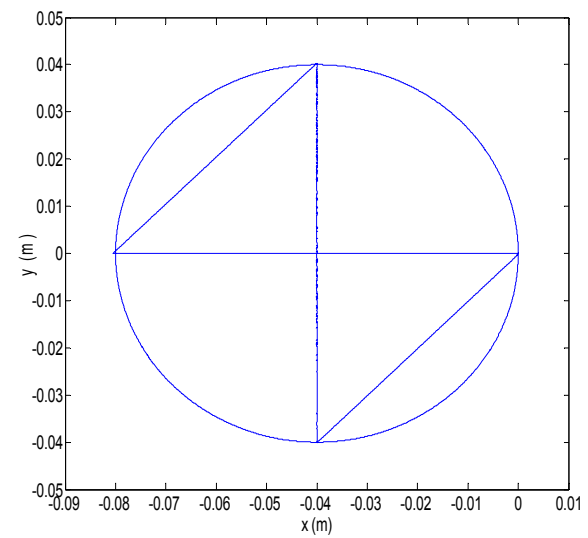
(c)   (d)

Fig. 5-18   160-mm travel range in both (*a*) *x* and (*b*) *y*. Capability of following planar trajectories of (*c*) a circle of 8-cm in diameter and (*d*) a circle and double-triangle combination.

(a)

(b)
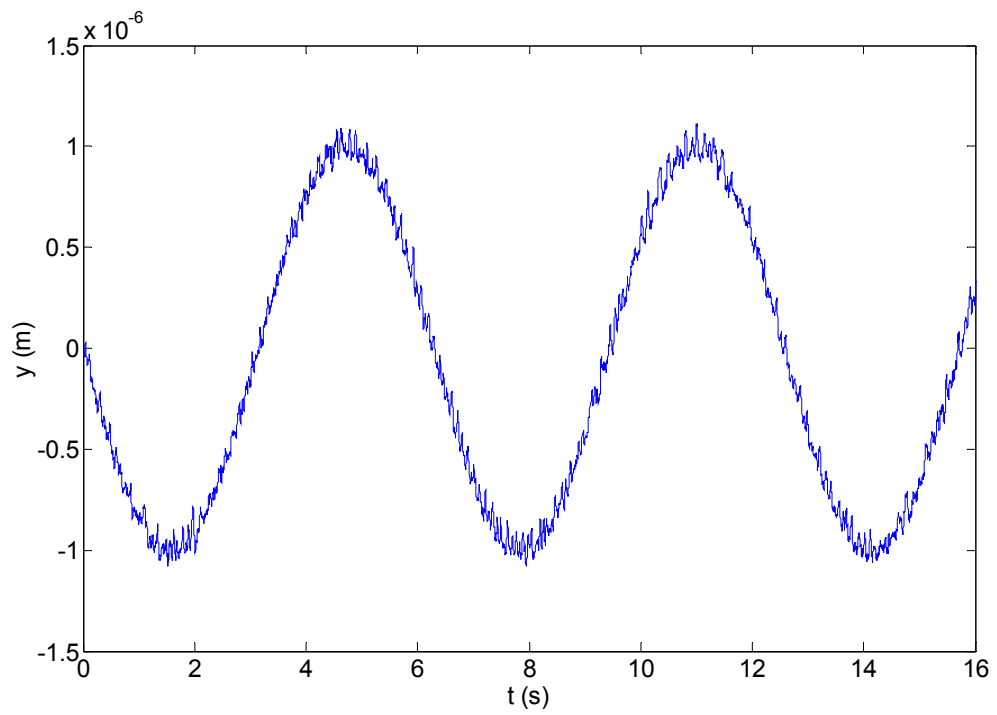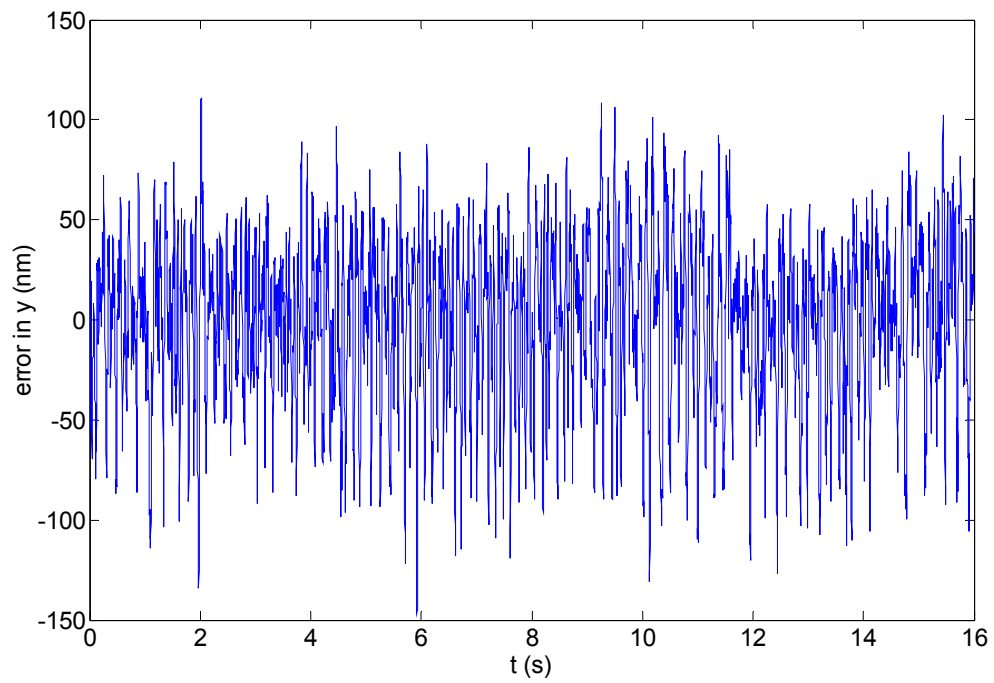
Fig. 5-19 (*a*) 1-µm amplitude sinusoidal motion and (*b*) the tracking error in *y*
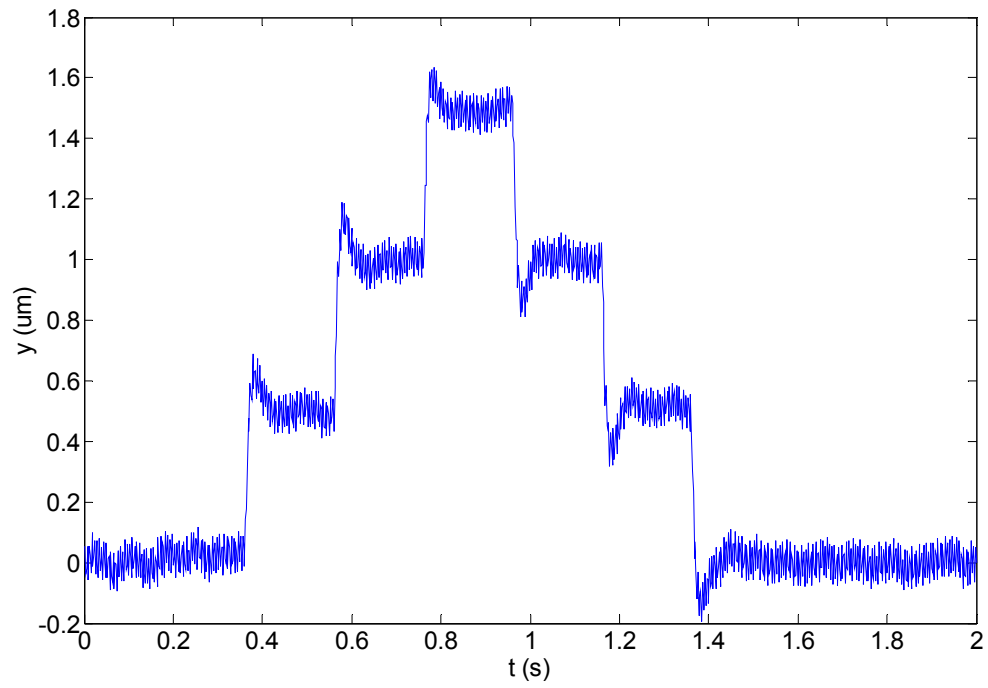
Fig. 5-20 500-nm stair case in *y*
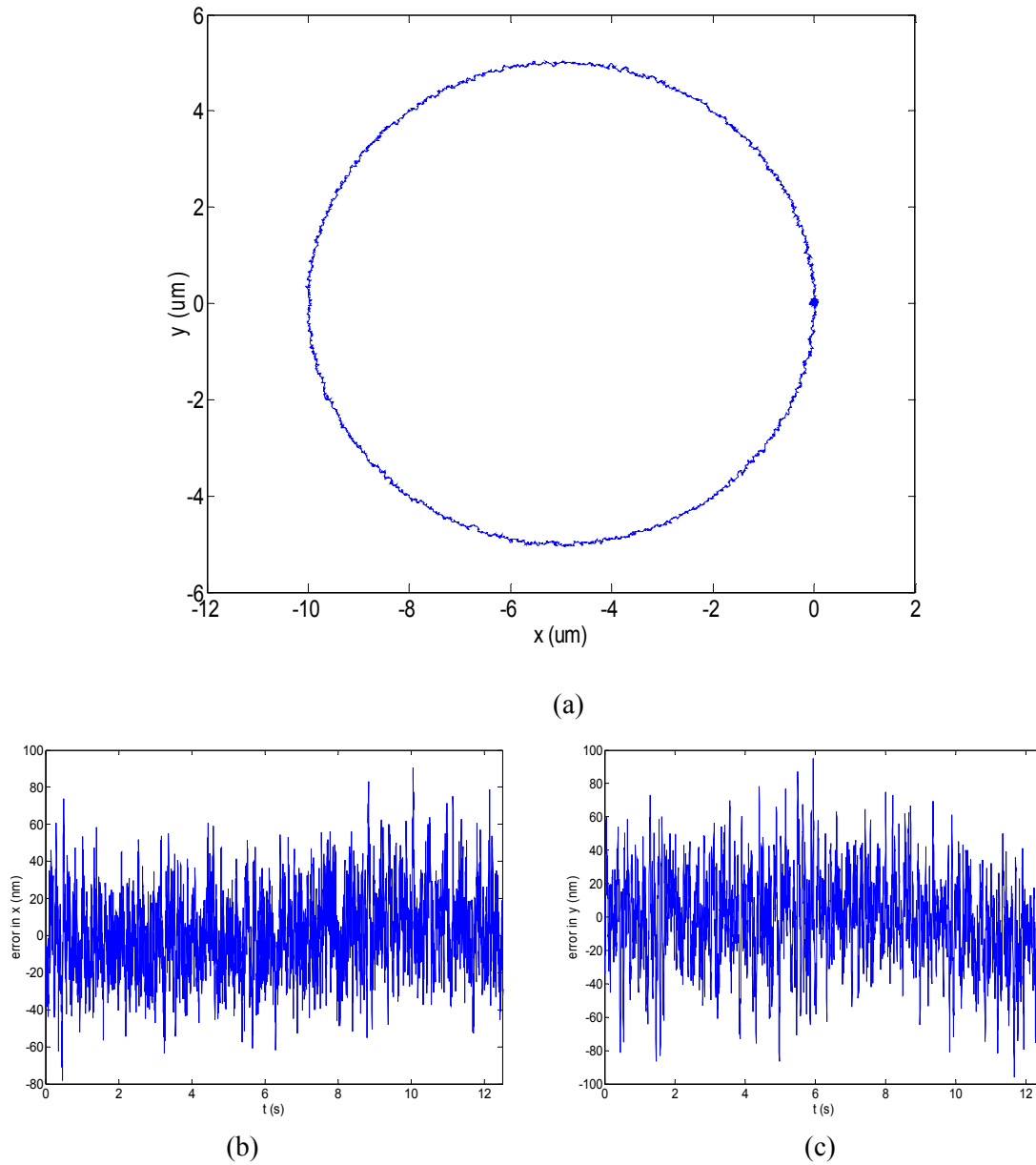
Fig. 5-21 (*a*) 5-μm radius circle in the *x-y* plane with the positioning error in (*b*) *x* and (*c*) *y*.

5.4.3   High-Speed Motion

This 6-DOF positioner is currently capable of generating the maximum velocity of 0.5 m/s with the maximum 5-m/s^2 acceleration in the *y*-direction. Fig. 5-22 (a) shows the stage

moved back and forth with a range of 140 mm in y. The platen first moved in the positive y-direction at the maximum acceleration of about ½ g (5 m/s^2). When the velocity reached 0.5 m/s, the platen stopped accelerating and moved at this constant velocity. After 0.18 s, the platen started to decelerate at 5 m/s^2 until its velocity reached zero. After resting at the position of 140 mm for a while, the stage moved back to its original position in the same way as it moved forth. Fig. 5-22 (b) shows the corresponding velocity profile. A 10% overshoot in velocity is visible at the end of abrupt velocity changes. The 0.5 m/s maximum velocity is limited by the laser interferometers not by the technology.

In the photolithographic process of chip fabrication, a wafer stage carries a silicon wafer from one die sit to another to repeat the exposure to the laser beam. These step-and-repeat aligners (steppers) have dominated in IC fabrication since late 1980s [90−91]. The positioner herein can simulate the similar step-and-repeat motion, which is used in semiconductor manufacturing. Fig. 5-23 presents a sample step-and-repeat motion profile both in position and velocity. Here, 2 cm was chosen as a typical die size.

Fig. 5-23 (a) is the displacement trajectory of the whole process in the x-y plane. The positioner started from point A at the origin of its coordinate system with an acceleration of 4 m/s^2 in the positive y-direction. After its velocity reached 0.2 m/s, it moved for 50 ms at this velocity. Then it decelerated at the acceleration of −4 m/s^2. After 50 ms the velocity was reduced to 0 m/s. Then one 2-cm step was completed. This 2-cm step was repeated three times in the positive y-direction until the positioner reached point B. Then the positioner moved with a constant velocity of −5 mm/s (This can be seen in Fig. 5-23 (b)) in the x-direction until it reached point C. After that, the positioner moved back from C to D at the same way as that from A to B, yet in the opposite direction. The same motion was repeated in the rest of the trajectory from D to H. When the positioner reached point H, it began to move back to the origin point A in the x-

direction. In parts (b), (c) and (d), only the first typical 12 s experimental results was presented to enhance the resolution of the subplots. The rest of the trajectories are similar to those plots.

Those experimental results demonstrated that the positioner can generate any similar typical motions to those generated by the wafer stage used in semiconductor manufacturing, such as step-and-scan, step-repeat-and-scan, and so on [92]. Therefore, the positioner presented herein has the potential to be used in the high precision manufacturing industry. All the demonstrations codes are attached in the Appendix B.
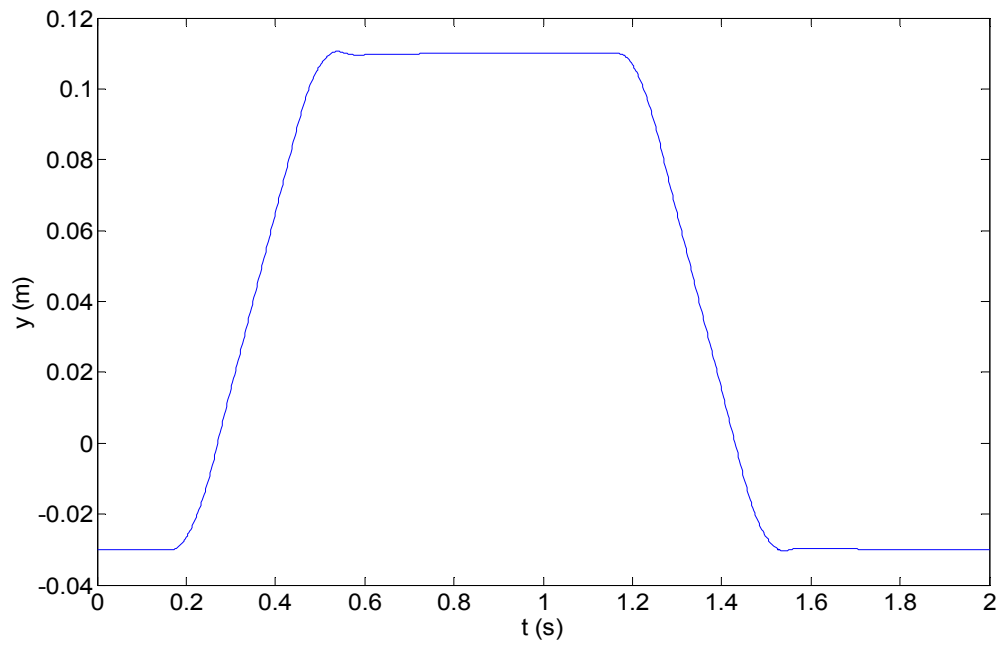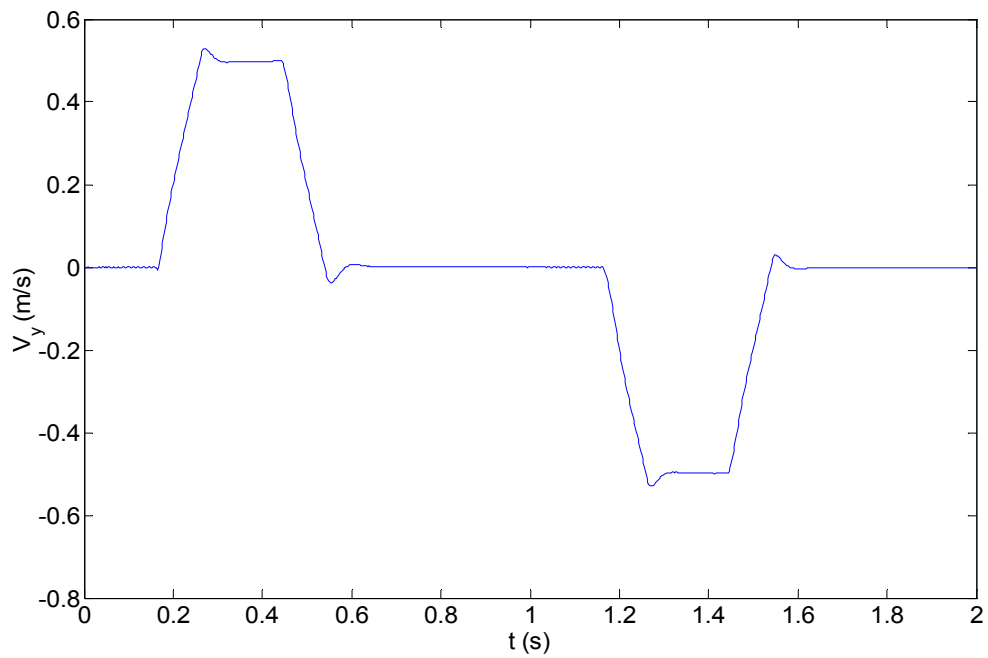
Fig. 5-22 (*a*) Displacement and (*b*) velocity profiles in *y* with 0.5-m/s maximum velocity and 5-m/s^2 maximum acceleration.
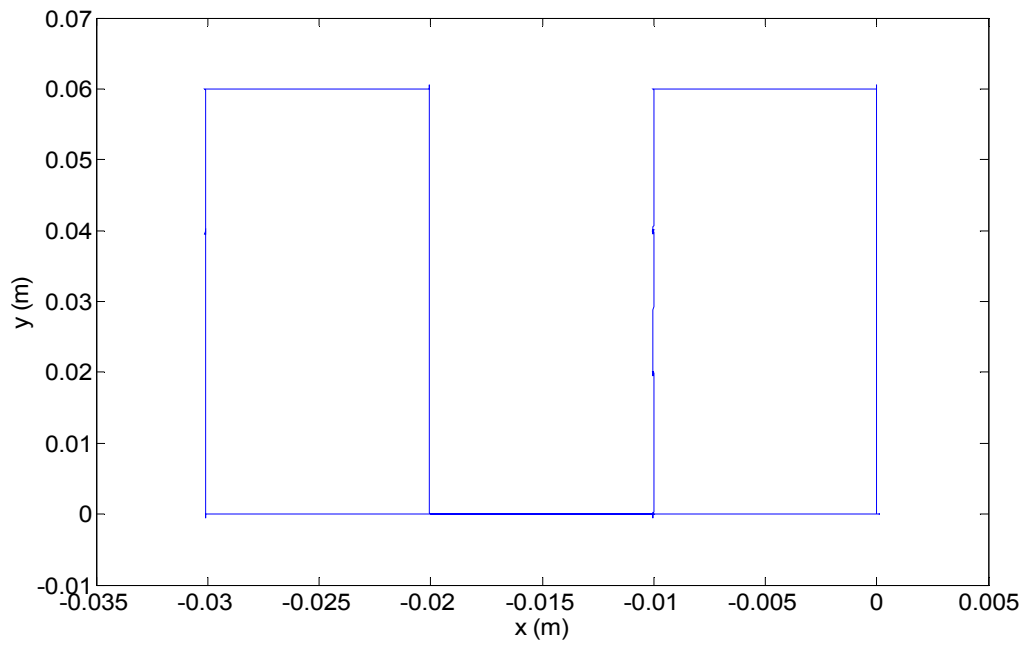
(a)
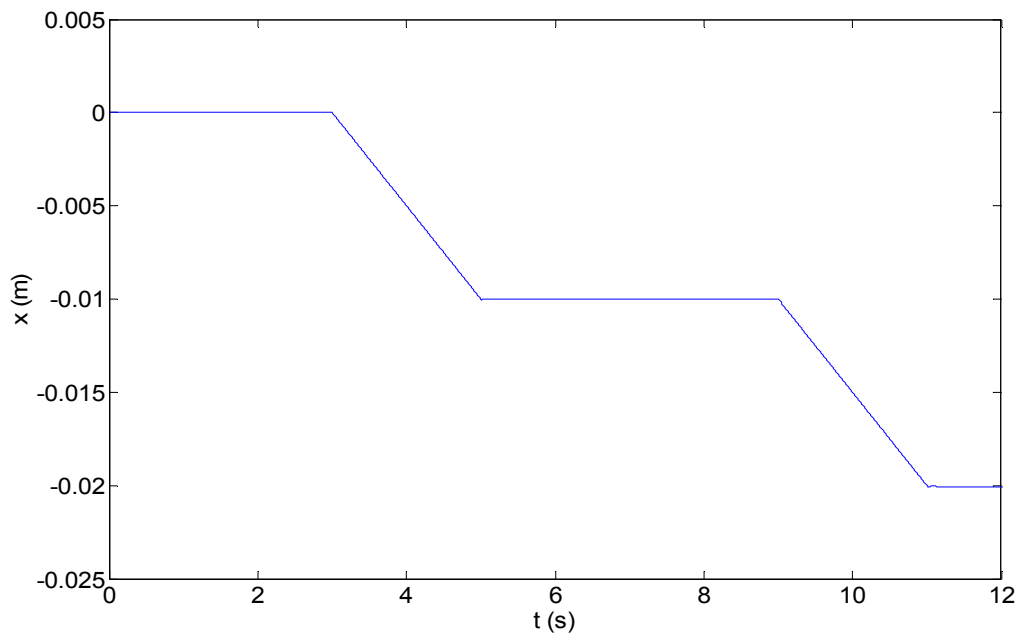
(b)

Fig. 5-23 (*a*) Experimental motion profile of a 2-cm step-and-repeat motion in the *y*-direction traversed by the platen. Position trajectory in (*b*) the *x*-direction and (*c*) the *y*-direction. (*d*) velocity profile in the *y*-direction.
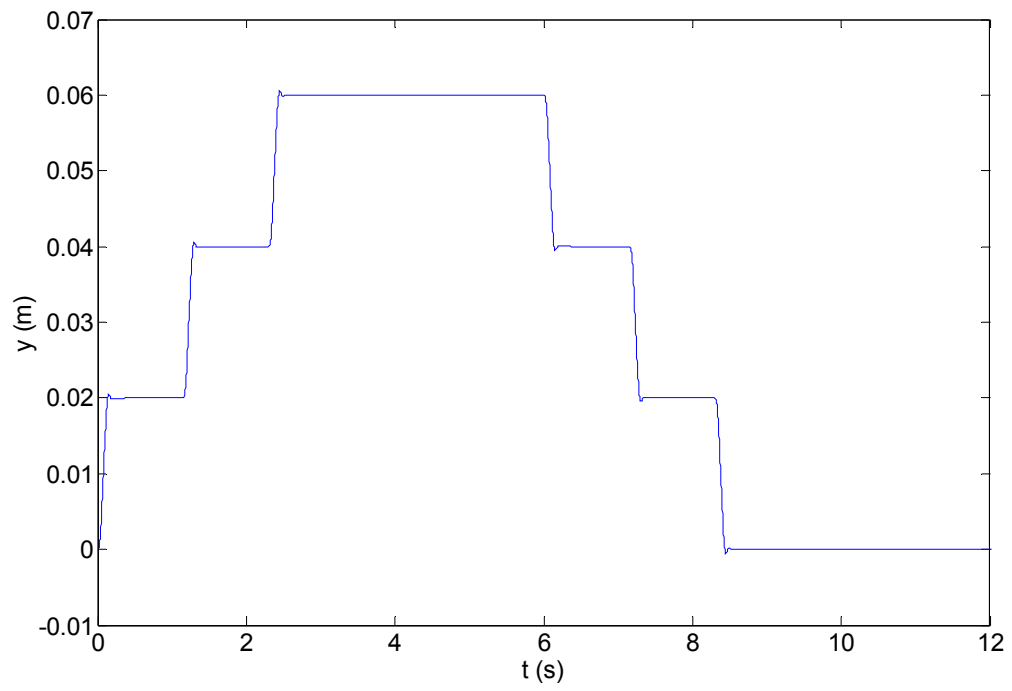
(c)
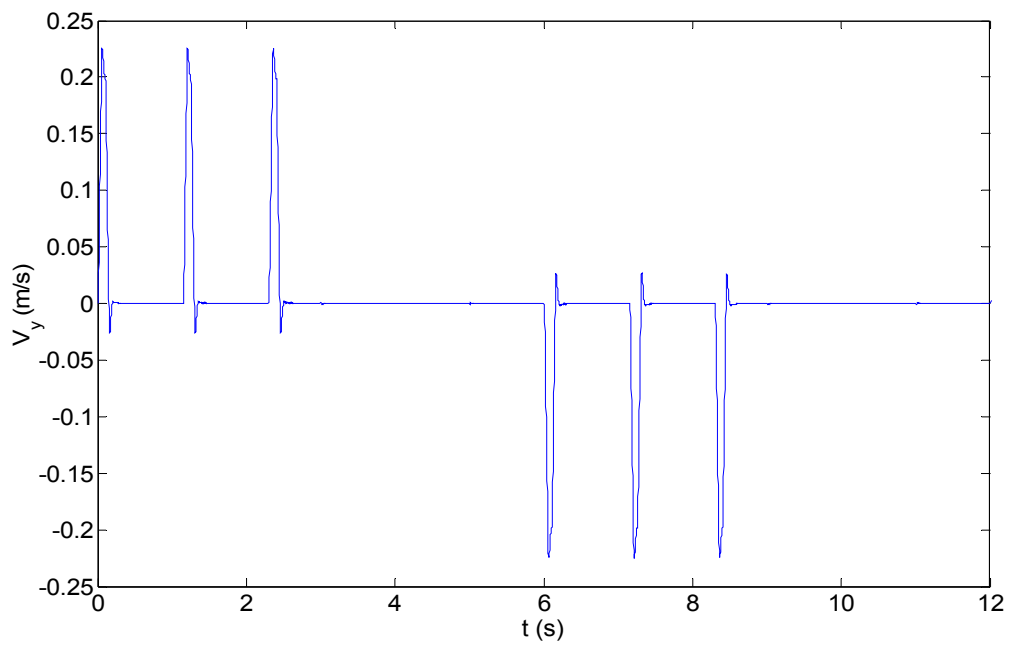
(d)

Fig. 5-23 continued

CHAPTER VI

MULTIVARIABLE CONTROL SYSTEM DESIGN AND

IMPLEMENTATION

This multi-dimensional positioner is a multi-inputs and multi-outputs (MIMO) system. The model of this system was developed in Chapter V. Compared with the SISO control system design, the MIMO one will focus on the dynamics of the whole system instead of the dynamics in each axis [93]. In this chapter, several multivariable controllers are designed and implemented. The design process of integrator augmented linear quadratic regulation (LQR), and integrator augmented linear quadratic Gaussian (LQG) control methodologies are discussed. Experimental results are also presented in this chapter.

6.1   Linear Quadratic Regulation (LQR) Control in the Horizontal Mode

By plugging corresponding values into the Eqs. (5.60) and (5.61), the state space model of the system in the horizontal mode can be represented in Eqs. (6.1) and (6.2).

$$
\begin{bmatrix} \dot{x} \\ \dot{y} \\ \dot{r} \\ \dot{h} \\ \dot{u} \\ \dot{v} \end{bmatrix} = \begin{bmatrix} 0 & 0 & 0 & 1 & 0 & 0 \\ 0 & 0 & 0 & 0 & 1 & 0 \\ 0 & 0 & 0 & 0 & 0 & 1 \\ 0 & 0 & 0 & 0 & 0 & 0 \\ 0 & 0 & 0 & 0 & 0 & 0 \\ 0 & 0 & 0 & 0 & 0 & 0 \end{bmatrix} \begin{bmatrix} x \\ y \\ r \\ h \\ u \\ v \end{bmatrix} + \begin{bmatrix} 0 & 0 & 0 \\ 0 & 0 & 0 \\ 0 & 0 & 0 \\ 0 & 0 & 3.4095 \\ 3.4095 & 3.4095 & 0 \\ -18.562 & 19.672 & 0 \end{bmatrix} \begin{bmatrix} i_{AQ} \\ i_{BQ} \\ i_{CQ} \end{bmatrix}, \tag{6.1}
$$

$$Y_1 = \begin{bmatrix} 1 & 0 & 0 & 0 & 0 & 0 \\ 0 & 1 & 0 & 0 & 0 & 0 \\ 0 & 0 & 1 & 0 & 0 & 0 \\ 0 & 0 & 0 & 1 & 0 & 0 \\ 0 & 0 & 0 & 0 & 1 & 0 \\ 0 & 0 & 0 & 0 & 0 & 1 \end{bmatrix} \begin{bmatrix} x \\ y \\ r \\ h \\ u \\ v \end{bmatrix}, \tag{6.2}$$

The above horizontal dynamic system can be presented as Eq. (6.3), where x is the state vector and u is the input vector.

$$\dot{x}(t) = Ax(t) + Bu(t), \tag{6.3}$$

The LQR problem, where all the sates were known, was the deterministic initial value problem: with non-zero initial state x (0), find the input signal u (t) which took the system to the zero state ($x = 0$) in an optimal manner, i.e. by minimizing the deterministic cost [94]

$$J_r = \int_0^\infty (x(t)^T Qx(t) + u(t)^T Ru(t))dt, \tag{6.4}$$

The optimal solution (for any initial state) is u (t) $= - K_r\, x$ (t), where

$$K_r = R^{-1}B^T P, \tag{6.5}$$

And $P = P^T \geq 0$ was the unique positive semi-definite solution of the algebraic Riccati equation

$$A^T P + PA - PBR^{-1}B^T P + Q = 0, \tag{6.6}$$

Where Q and R are constant weighting matrix needed to be designed to penalize some state variables (or inputs) more than others to meet dynamic requirements. It is necessary that Q be positive semidefinite, and R be positive definite [95]. LQR is an optimal full state-feedback pole placement approach. It provides an optimal way to place the eigenvalues of the multivariable system by designing appropriate Q and R matrix in Eqs. (6.5) and (6.6).

Since the LQ controller is a regulator, it will regulate the output of the system to be zero. In order to make the postioner track non-zero command, the error dynamical model of the system is needed for the LQ servo design. The error can be defined as following

$$\Delta x = x - x^*, \tag{6.7}$$

$$\Delta y = y - y^*, \tag{6.8}$$

$$\Delta r = r - r^*, \tag{6.9}$$

$$\Delta u = u - u^*, \tag{6.10}$$

Where the variables with an asterisk denoted are the final values of the corresponding state. Since the final values of the state are constant values, the derivative of those values will be zero. As a result, the following equations can be got.

$$\Delta \dot{x}(t) = A\Delta x(t) + B\Delta u(t), \tag{6.11}$$

$$\Delta y(t) = C\Delta x(t), \tag{6.12}$$

Here the A, B, and C matrix are the same as the original system. As a result, if the LQR controller is designed based on the error dynamics in Eqs. (6.11) and (6.12), the positioning system can track the input reference. So the control law will be

$$\Delta u(t) = -K_r \Delta x(t), \tag{6.13}$$

where K_r is the optimal solution for the Riccati Eq. (6.6) by designing Q and R matrix. Since the input to the system is u not Δu, from Eq. (6.10) it can be known that input to the system should be

$$u = \Delta u + u^*, \tag{6.14}$$

Once the system is in steady state, the steady-state input u^* will be zero, which can be seen from Eq. (6.1) by letting left hand side of the equation to be zero. Therefore, the Eq. (6.14) can be simplified as

$$u = -K_r \Delta x(t),\qquad(6.15)$$

Now it is ready to design the LQR servo for the system. Q = diag ([10000, 10000, 10000, 1, 1, 1]), R = diag ([1, 1, 1]) were found to be the most appropriate matrices for the system. In order to get better positioning performance, the Q matrices is selected in such a way that penalizes displacement states x, y, and r much more than the velocity states. The gain matrix is computed as shown in Eq. (6.16). The corresponding closed-loop system dynamics $\Delta \dot{x}(t) = (A - BK_r)\Delta x(t)$ is presented in Eq. (6.17).

$$\begin{bmatrix} i_{AQ} \\ i_{BQ} \\ i_{CQ} \end{bmatrix} = -\begin{bmatrix} 0 & 72.431 & -68.948 & 0 & 4.735 & -2.012 \\ 0 & 68.948 & 72.431 & 0 & 4.481 & 2.085 \\ 100.000 & 0 & 0 & 7.724 & 0 & 0 \end{bmatrix} \begin{bmatrix} \Delta x \\ \Delta y \\ \Delta r \\ \Delta h \\ \Delta u \\ \Delta v \end{bmatrix}, \qquad (6.16)$$

$$\begin{bmatrix} \Delta \dot{x} \\ \Delta \dot{y} \\ \Delta \dot{r} \\ \Delta \dot{h} \\ \Delta \dot{u} \\ \Delta \dot{v} \end{bmatrix} = \begin{bmatrix} 0 & 0 & 0 & 1 & 0 & 0 \\ 0 & 0 & 0 & 0 & 1 & 0 \\ 0 & 0 & 0 & 0 & 0 & 1 \\ -340.950 & 0 & 0 & -26.335 & 0 & 0 \\ 0 & -482.030 & -11.875 & 0 & -31.420 & -0.251 \\ 0 & -11.875 & -2704.700 & 0 & -25.080 & -78.363 \end{bmatrix} \begin{bmatrix} \Delta x \\ \Delta y \\ \Delta r \\ \Delta h \\ \Delta u \\ \Delta v \end{bmatrix},$$

$$(6.17)$$

The closed-loop poles are placed at $-13.167 \pm 12.945i$, $-39.182 \pm 34.198i$, and $-15.710 \pm 15.335i$. So the system is stabilized by the controller. Since the controller is to be implemented digitally in a 320C40 digital signal processor, the control gain matrix should be in a discrete time domain. The function 'lqrd' is found in Matlab to get the discrete time domain gain matrix as shown in Eq. (6.18).

$$K_{rd} = \begin{bmatrix} 0 & 72.205 & -68.412 & 0 & 4.727 & -2.003 \\ 0 & 68.730 & 71.864 & 0 & 4.473 & 2.076 \\ 99.737 & 0 & 0 & 7.714 & 0 & 0 \end{bmatrix}, \qquad (6.18)$$

The continuous time state-space form model of the system can be converted into discrete-time form by the function 'c2d' in Matlab. Then in each sampling time period, the control current output to the system can be calculated by Eq. (6.16) with K_{rd} as the gain matrix. The experimental results are shown in Fig. 6-1 after implementing the controller into the system in the horizontal mode.

(a)

(b)

(c)

(d)
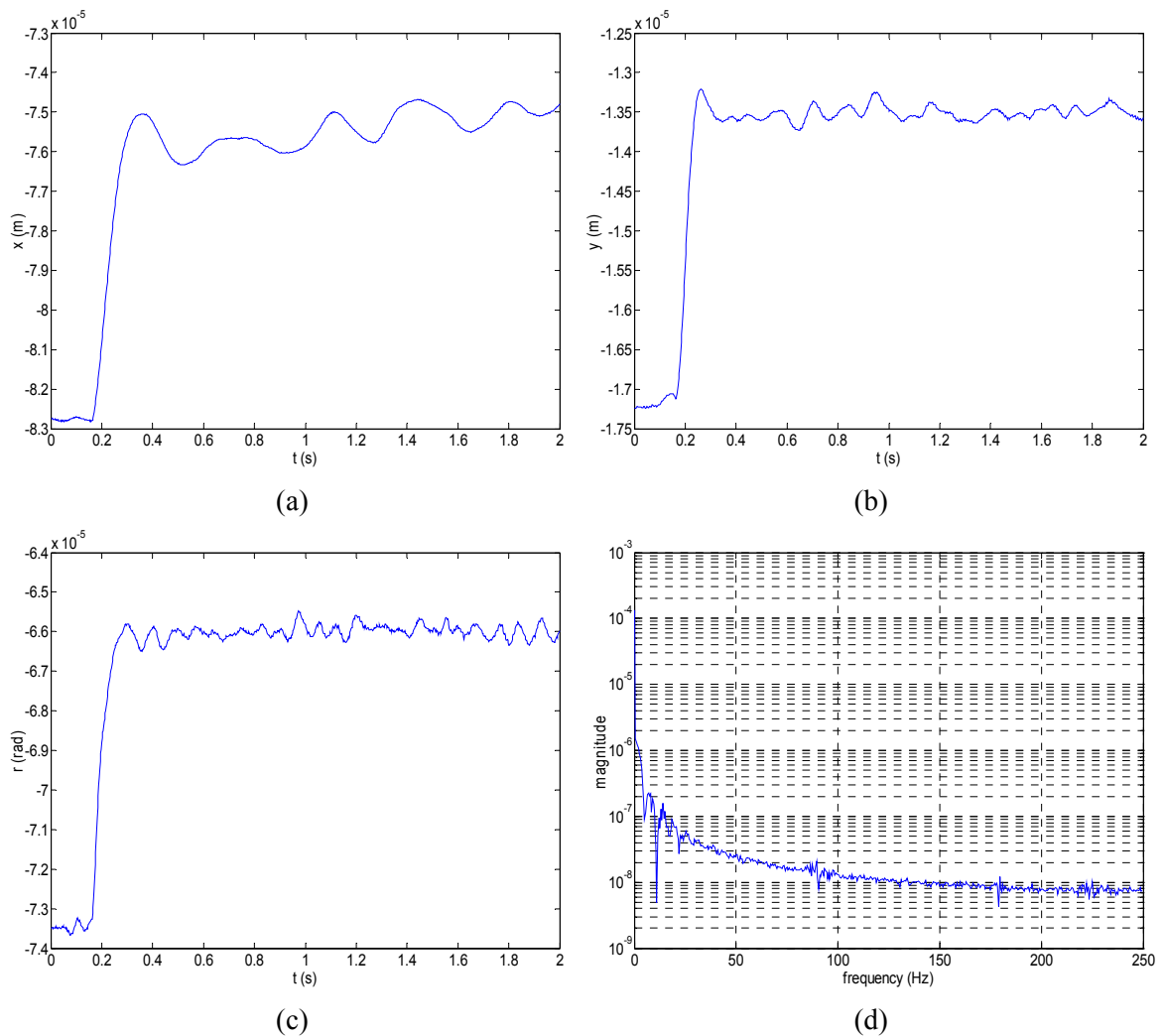
Fig. 6-1 10-μm step response in (*a*) *x*, (*b*) *y*. 10-μrad step response in (*c*) *r*. (*d*) FFT of (*c*)

From those experimental results, it is noticed with interest that there are steady-state errors in those step responses: about 2 μm steady state error in *x*, 6 μm in *y*, and 2 μrad in *r*. It was because the traditional LQR regulator does not have integrator which also can be seen from the closed-loop poles of the system. Thus, it is necessary to augment plant with integrator before applying the LQR method. The augmented control structure is shown as follows:
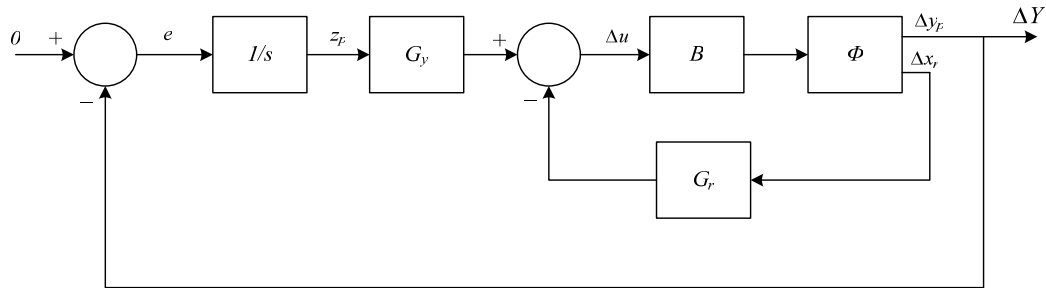
Fig. 6-2 Integrator augmented LQR servo

The methodology is to isolate the plant output vector Δy_p as the top component of plant state vector x_p, such that

$$\Delta \dot{x}_p = A_p \Delta x_p + B_p \Delta u_p,$$
$$\Delta y_p = C_p \Delta x_p \qquad (6.19)$$

Then add new state vector z_p, which is the integrators states. The dynamics of these new states are:

$$\dot{z}_p = \Delta y_p = C_p \Delta x_p, \qquad (6.20)$$

Now with Eqs. (6.19) and (6.20), the dynamics of the augmented system can be obtained

$$\begin{bmatrix} \Delta \dot{x}_p \\ \dot{z}_p \end{bmatrix} = \begin{bmatrix} A_p & 0 \\ C_p & 0 \end{bmatrix} \begin{bmatrix} \Delta x_p \\ z_p \end{bmatrix} + \begin{bmatrix} B_p \\ 0 \end{bmatrix} \Delta u_p, \qquad (6.21)$$

$$\Delta y_p = \begin{bmatrix} C_p & 0 \end{bmatrix} \begin{bmatrix} \Delta x_p \\ z_p \end{bmatrix}, \qquad (6.22)$$

Because in a precision positioning system, usually the positioning resolution is the most important specification, in order to reduce the steady-state errors in position, it is necessary to add only three pure integrators in those outputs. As a result, the augmented system should have nine states altogether. The elements of the A, B, and C matrix are calculated as follows:

$$
\begin{bmatrix} \Delta\dot{x} \\ \Delta\dot{y} \\ \Delta\dot{r} \\ \Delta\dot{h} \\ \Delta\dot{u} \\ \Delta\dot{v} \\ \dot{z}_1 \\ \dot{z}_2 \\ \dot{z}_3 \end{bmatrix} = \begin{bmatrix} 0 & 0 & 0 & 1 & 0 & 0 & 0 & 0 & 0 \\ 0 & 0 & 0 & 0 & 1 & 0 & 0 & 0 & 0 \\ 0 & 0 & 0 & 0 & 0 & 1 & 0 & 0 & 0 \\ 0 & 0 & 0 & 0 & 0 & 0 & 0 & 0 & 0 \\ 0 & 0 & 0 & 0 & 0 & 0 & 0 & 0 & 0 \\ 0 & 0 & 0 & 0 & 0 & 0 & 0 & 0 & 0 \\ 1 & 0 & 0 & 0 & 0 & 0 & 0 & 0 & 0 \\ 0 & 1 & 0 & 0 & 0 & 0 & 0 & 0 & 0 \\ 0 & 0 & 1 & 0 & 0 & 0 & 0 & 0 & 0 \end{bmatrix} \begin{bmatrix} \Delta x \\ \Delta y \\ \Delta r \\ \Delta h \\ \Delta u \\ \Delta v \\ z_1 \\ z_2 \\ z_3 \end{bmatrix} + \begin{bmatrix} 0 & 0 & 0 \\ 0 & 0 & 0 \\ 0 & 0 & 0 \\ 0 & 0 & 3.410 \\ 3.410 & 3.410 & 0 \\ -18.562 & 19.672 & 0 \\ 0 & 0 & 0 \\ 0 & 0 & 0 \\ 0 & 0 & 0 \end{bmatrix} \begin{bmatrix} \Delta i_{AQ} \\ \Delta i_{BQ} \\ \Delta i_{CQ} \end{bmatrix}, \quad (6.23)
$$

$$
\Delta y_p = \begin{bmatrix} 1 & 0 & 0 & 0 & 0 & 0 & 0 & 0 & 0 \\ 0 & 1 & 0 & 0 & 0 & 0 & 0 & 0 & 0 \\ 0 & 0 & 1 & 0 & 0 & 0 & 0 & 0 & 0 \end{bmatrix} \begin{bmatrix} \Delta x \\ \Delta y \\ \Delta r \\ \Delta h \\ \Delta u \\ \Delta v \\ z_1 \\ z_2 \\ z_3 \end{bmatrix}, \quad (6.24)
$$

It can be expected that in the steady state $\dot{z}_1$, $\dot{z}_2$, and $\dot{z}_3$ will be zero, so Δx, Δy, and Δr will become zero in the steady state. This will eliminate the steady state error in the previous LQR design. To emphasize the effect of integrators, the Q matrix is chosen as $Q = \text{diag}$ ($[10^4, 10^4, 10^5, 1, 1, 1, 10^8, 10^8, 10^{10}]$). It is a fact from experiment that if the weight of integrators is not significant enough, the effect of integrator will be so small or even trivial that they cannot eliminate the steady-state errors. The R matrix is a 3 by 3 identity matrix. The corresponding gain matrix K_r is computed by Matlab as shown in Eq. (6.25).

$$K_r = \begin{bmatrix} 0 & 408.9 & -1021.3 & 0 & 11.13 & -7.28 & 0 & 7269.6 & -68668 \\ 0 & 385.9 & 1078.1 & 0 & 10.51 & 7.60 & 0 & 6866.8 & 72696 \\ 628.0 & 0 & 0 & 19.22 & 0 & 0 & 10000 & 0 & 0 \end{bmatrix}, \quad (6.25)$$

The closed-loop poles are placed at $-74.556 \pm 119.95i$, $-16.808 \pm 28.034i$, and $-19.047 \pm 31.430i$, 135.60, 31.912, and 35.685. The corresponding discrete-time gain matrix is shown in Eq. (6.26). After the implementation, the experiment results are presented in Fig. 6-3.

$$K_{rd} = \begin{bmatrix} 0 & 406.6 & -999.4 & 0 & 11.09 & -7.18 & 0.00026 & 7216.2 & -66741 \\ 0 & 383.8 & 1054.9 & 0 & 10.47 & 7.49 & 0.00026 & 6816.2 & 70654 \\ 624.8 & 0 & 0 & 19.16 & 0 & 0 & 9934.7 & -0.00038 & -0.00013 \end{bmatrix},$$

$$(6.26)$$

Compared with the experimental results shown in Fig. 6-1, the results with integrators augmented LQR controller have successfully eliminated the steady-state errors in the horizontal mode. Furthermore, the positioning noise is much lower than that in Fig. 6-1. Experimental experience shows that the more weights given to those displacement states, the smoother the steady state. However, if the weights are too large, the actuator may get saturated and the system may go unstable. Fig. 6-3 (d) shows the FFT of the system when it is under LQR control. It shows that there is no dominant noise frequency existing in the system.
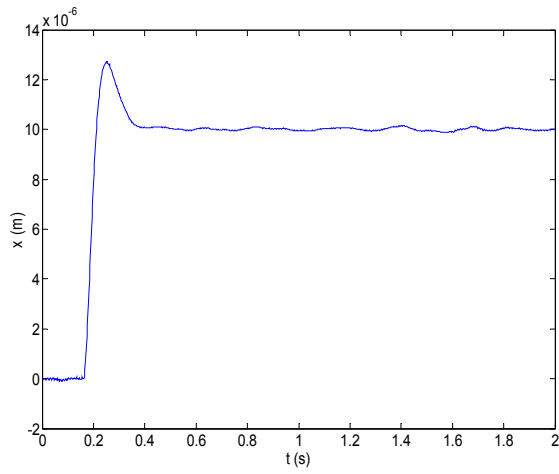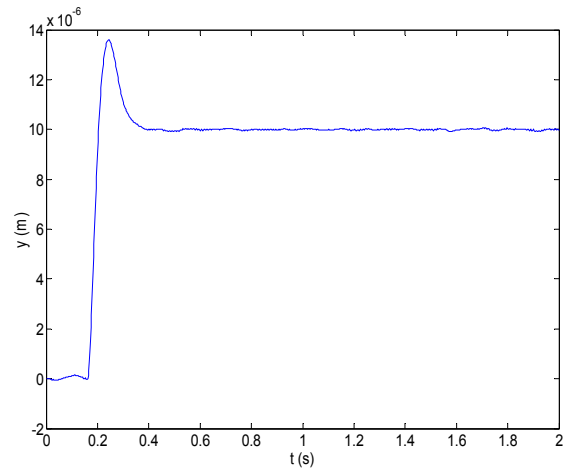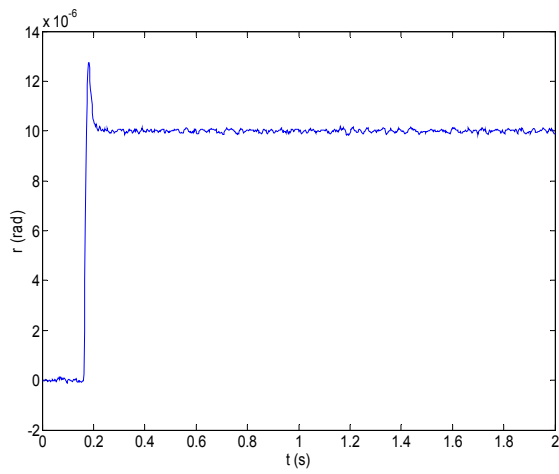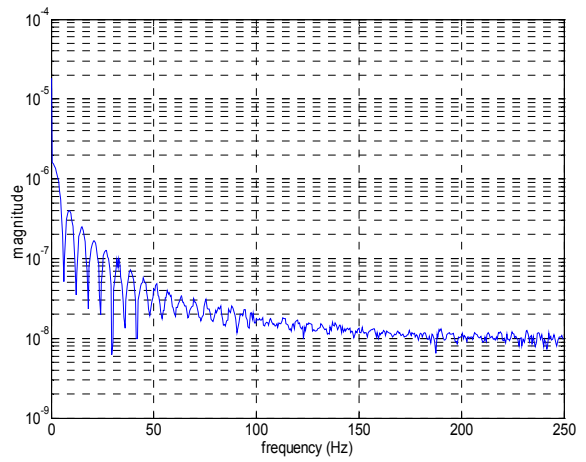
Fig. 6-3 10-μm step response in (*a*) *x*, (*b*) *y*. 10-μrad step response in (*c*) *r*. (d) FFT of (*c*)

6.2 Observer/State-Feedback Control in the Vertical Mode

Eqs. (6.27) and (6.28) are the state-space model of the system in the vertical mode. Unlike the outputs in the horizontal mode, the outputs in the vertical mode are only displacements. In other words, the states in the vertical mode are not completely available. The implementation of state feedback requires the complete states. As a result, an observer is needed to reconstruct the unknown state variables. It is well known, if (A, B) is controllable and (A, C) is observable, it is possible to design an observer/state-feedback controller for the system. An observer is itself a linear system whose task is to accept as inputs the original system's (i. e., the plant's) input and output signals, and produce as its output an estimate of the plant's state vector. This state estimates asymptotically track the actual states. In this way, the output of the observer, rather than the true state, can be used to compute state feedback.

$$\begin{bmatrix} \dot{z} \\ \dot{s} \\ \dot{t} \\ \dot{p} \\ \dot{q} \\ \dot{w} \end{bmatrix} = \begin{bmatrix} 0 & 0 & 0 & 1 & 0 & 0 \\ 0 & 0 & 0 & 0 & 1 & 0 \\ 0 & 0 & 0 & 0 & 0 & 1 \\ -169205 & 0 & 0 & 0 & 0 & 0 \\ 0 & -337939 & 0 & 0 & 0 & 0 \\ 0 & 0 & -466120 & 0 & 0 & 0 \end{bmatrix} \begin{bmatrix} z \\ s \\ t \\ p \\ q \\ w \end{bmatrix} + \begin{bmatrix} 0 & 0 & 0 \\ 0 & 0 & 0 \\ 0 & 0 & 0 \\ 3.4095 & 3.4095 & 3.4095 \\ -27.383 & -27.383 & 51.474 \\ 40.094 & -42.492 & 0 \end{bmatrix} \begin{bmatrix} i_{AD} \\ i_{BD} \\ i_{CD} \end{bmatrix}, \quad (6.27)$$

$$Y = \begin{bmatrix} 1 & 0 & 0 & 0 & 0 & 0 \\ 0 & 1 & 0 & 0 & 0 & 0 \\ 0 & 0 & 1 & 0 & 0 & 0 \end{bmatrix} \begin{bmatrix} z \\ s \\ t \\ p \\ q \\ w \end{bmatrix}, \quad (6.28)$$

Fig. 6-4 shows that the observer tracks the output of the plant and the output error drives the observer. It is possible to regard the observer as having the same basic structure as the plant, but with the additional input $y - \hat{y}$:

$$\dot{\hat{x}} = A\hat{x} + Bu + L(y - \hat{y})$$
$$\hat{y} = C\hat{x} + Du \qquad , \qquad (6.29)$$

The dynamics of error between x and $\hat{x}$ by estimating can be written as the following

$$e = x - \hat{x}, \qquad (6.30)$$

$$\dot{e} = \dot{x} - \dot{\hat{x}} = (A - LC)e, \qquad (6.31)$$
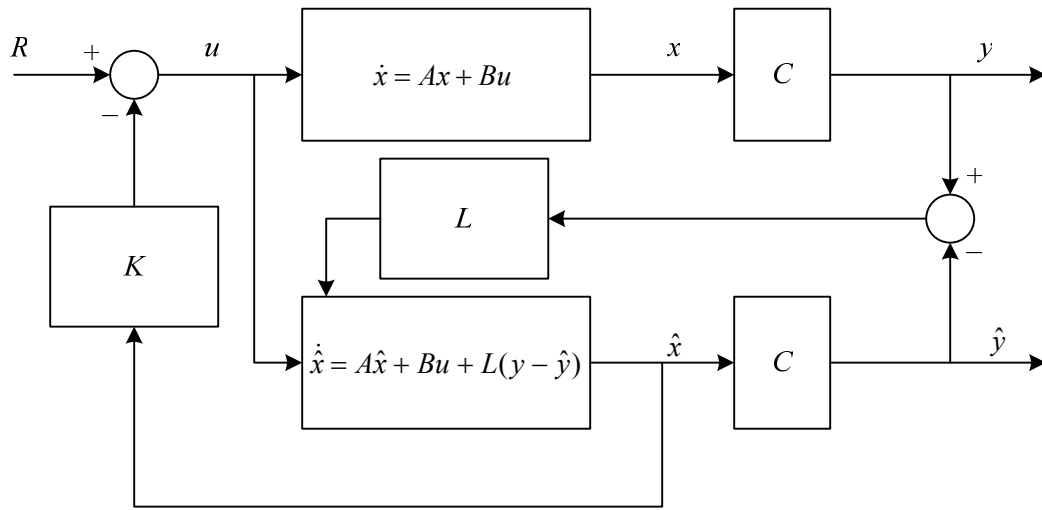
Fig. 6-4 Structure of observer/state-feedback controller [96]

Since (A, C) is observable, it is possible to design the gain matrix L in such a way that the eigenvalues of Eq. (6.31) can be placed in the left half plane. Therefore, the estimated states $\hat{x}$ will asymptotically converge to the original states x. Thus x can be replaced by $\hat{x}$ in the state feedback methodology $u = -K\hat{x}$. The closed-loop dynamics of the system can be shown as following.

$$\begin{bmatrix} \dot{x} \\ \dot{\hat{x}} \end{bmatrix} = \begin{bmatrix} A & -BK \\ LC & A - BK - LC \end{bmatrix} \begin{bmatrix} x \\ \hat{x} \end{bmatrix}, \qquad (6.32)$$

$$Y = Cx, \qquad (6.33)$$

$$\begin{bmatrix} A & -BK \\ LC & A-BK-LC \end{bmatrix} \rightarrow \begin{bmatrix} A-BK & -BK \\ A-BK & A-BK-LC \end{bmatrix} \rightarrow \begin{bmatrix} A-BK & -BK \\ 0 & A-LC \end{bmatrix}, \quad (6.34)$$

Matrices in (6.34) show the matrix manipulation process of the closed-loop A matrix in

Eq. (6.32). The last matrix in (6.34) indicates that the eigenvalues of the composite system are

the union of the eigenvalues of a system with matrix $A-LC$ and those of a system with matrix.

It means the control system can be designed by using the separation principle. It can be seen that

if (A, B) is controllable and (A, C) is observable, by designing appropriate control gain matrix K

and observer gain matrix L, the close-loop poles (eigenvalues) can be placed anywhere in the s

plane such that some desired dynamic performance of the system is satisfied. Fortunately, the

system is both controllable and observable, so it is possible to use above observer/state-feedback

controller in the system. However, because the sensors can directly provide the value of

displacement in the vertical direction to the controller, it will be inefficient to implement the full

order (all states) observer into the system. Instead, if only the unknown states are estimated, it

will make the structure of controller more compact and save much more computing time for the

DSP. The reduced-order observer can be derived as follows.

$$\begin{bmatrix} \dot{x}_1 \\ \dot{x}_2 \end{bmatrix} = \begin{bmatrix} A_{11} & A_{12} \\ A_{21} & A_{22} \end{bmatrix} \begin{bmatrix} x_1 \\ x_2 \end{bmatrix} + \begin{bmatrix} B_1 \\ B_2 \end{bmatrix} u, \quad (6.35)$$

$$Y = \begin{bmatrix} I & 0 \end{bmatrix} \begin{bmatrix} x_1 \\ x_2 \end{bmatrix} + Du, \quad (6.36)$$

Here, the system states are divided into measurable states x_1 and unknown states x_2.

Since the value of measurable states can be got directly from the outputs of the system, these

states can be treated as known signals. So the Eq. (6.35) can be rewritten as:

$$\begin{aligned} A_{12}x_2 &= \dot{x}_1 - A_{11}x_1 - B_1 u \\ \dot{x}_2 &= A_{22}x_2 + \begin{bmatrix} B_2 u + A_{21}x_1 \end{bmatrix}, \end{aligned} \quad (6.37)$$

Then, by defining those known signals as shown in Eq. (6.38), Eq. (6.37) can be rewritten in a

form as shown in Eq. (6.39).

$$\overset{\Delta}{\bar{u}} = A_{21}x_1 + B_2 u$$
$$\overset{\Delta}{\bar{y}} = \dot{x}_1 - A_{11}x_1 - B_1 u$$

$$\text{(6.38)}$$

$$\dot{x}_2 = A_{22}x_2 + \bar{u}$$
$$\bar{y} = A_{12}x_2$$

$$\text{(6.39)}$$

Eq. (6.39) can be regarded as a new system consisting of the unknown states. An

observer for the unknown states then can be designed based on this new system.

$$\dot{\hat{x}}_2 = A_{22}\hat{x}_2 + \bar{u} + L(\bar{y} - \hat{\bar{y}}) = A_{22}\hat{x}_2 + \bar{u} + L(\bar{y} - A_{12}\hat{x}_2) = (A_{22} - LA_{12})\hat{x}_2 + \bar{u} + L\bar{y}, \quad \text{(6.40)}$$

It can be seen that $\bar{y}$ is dependent on $\dot{x}_1$ (which can be seen from Eq. (6.38)), and the value of

$\dot{x}_1$ cannot be directly obtained from the sensor. As a result, a change of variable $z = \hat{x}_2 - Lx_1$ is

necessary to be introduced. If the state vector $\dot{z}$ instead of $\dot{\hat{x}}_2$ is used, the state equation for the

observer in (6.39) will be simplified as:

$$\dot{z} = \dot{\hat{x}}_2 - L\dot{x}_1 = (A_{22} - LA_{12})\hat{x}_2 + \bar{u} + L\bar{y} - L\dot{x}_1 = (A_{22} - LA_{12})\hat{x}_2 + \bar{u} - L(A_{11}x_1 + B_1 u)$$

$$= (A_{22} - LA_{12})z + [(A_{22} - LA_{12})L + A_{21} - LA_{11}]x_1 + (B_2 - LB_1)u, \quad \text{(6.41)}$$

The state-feedback control law $u = -k_1 x_1 - k_2 \hat{x}_2$, will be changed into:

$$u = -k_1 x_1 - k_2 z - k_2 Lx_1 = -(k_1 + k_2 L)x_1 - k_2 z, \quad \text{(6.42)}$$

$$\begin{bmatrix} \dot{x}_1 \\ \dot{x}_2 \\ \dot{z} \end{bmatrix} = \begin{bmatrix} A_{11} - B_1 k_1 - B_1 k_2 L & A_{12} & -B_1 k_2 \\ A_{21} - B_2 k_1 - B_2 k_2 L & A_{22} & -B_2 k_2 \\ (A_{22} - LA_{12})L + A_{21} - LA_{11} - (B_2 - LB_1)(k_1 + k_2 L) & 0 & A_{22} - LA_{12} - B_2 k_2 + LB_1 k_2 \end{bmatrix} \begin{bmatrix} x_1 \\ x_2 \\ z \end{bmatrix},$$

$$\text{(6.43)}$$

$$Y = \begin{bmatrix} I & 0 & 0 \end{bmatrix} \begin{bmatrix} x_1 \\ x_2 \\ z \end{bmatrix}, \quad \text{(6.44)}$$

So the closed-loop dynamics of the new introduced system is presented in Eq. (6.43) and (6.44). It can be seen from Eq. (6.43) that the ordinary differential equation (ODE) of introduced state z consists of only x_1 and z itself. Here, x_1 is known (directly measured from sensors) and the coefficient constant matrix is also known, so z can be calculated by integration during each sampling time if the initial value of z is given. Once z is available, by applying the control law presented in Eq. (6.42), the dynamics of the system can be controlled to satisfy the desired requirements. By some mathematical manipulations, the A matrix in Eq. (6.43) can be changed into the following format:

$$\begin{bmatrix} A_{11} - B_1 k_1 & A_{12} - B_1 k_2 & -B_1 k_2 \\ A_{21} - B_2 k_1 & A_{22} - B_2 k_2 & -B_2 k_2 \\ 0 & 0 & A_{22} - L A_{12} \end{bmatrix} = \begin{bmatrix} A - BK & -Bk_2 \\ 0 & A_{22} - L A_{12} \end{bmatrix}, \qquad (6.45)$$

Where, $A = \begin{bmatrix} A_{11} & A_{12} \\ A_{21} & A_{22} \end{bmatrix}$, $B = \begin{bmatrix} B_1 \\ B_2 \end{bmatrix}$, and $K = \begin{bmatrix} k_1 & k_2 \end{bmatrix}$. The Eq. (6.45) demonstrated that the separation principle can be also used in the design of reduced order observer control system. So the controller gain K can be designed independently of the observer gain L. Furthermore, if (A, B) is controllable and (A_{22}, A_{12}) is observable, the eigenvalues of observer and controller can be placed anywhere by designing appropriate gain matrices. It can be noticed that there are no integrators in the controller and the plant, so there will be steady state error existing in the closed-loop system. Using the same methodology as that used in the LQR design, three integrators for the displacement can be introduced into the original system. The integrator augmented system in the vertical mode is shown in Eqs. (6.46) and (6.47).

$$
\begin{bmatrix}
\Delta\dot{z} \\
\Delta\dot{s} \\
\Delta\dot{t} \\
\dot{z}_4 \\
\dot{z}_5 \\
\dot{z}_6 \\
\Delta\dot{p} \\
\Delta\dot{q} \\
\Delta\dot{w}
\end{bmatrix}
=
\begin{bmatrix}
0 & 0 & 0 & 0 & 0 & 0 & 1 & 0 & 0 \\
0 & 0 & 0 & 0 & 0 & 0 & 0 & 1 & 0 \\
0 & 0 & 0 & 0 & 0 & 0 & 0 & 0 & 1 \\
1 & 0 & 0 & 0 & 0 & 0 & 0 & 0 & 0 \\
0 & 1 & 0 & 0 & 0 & 0 & 0 & 0 & 0 \\
0 & 0 & 1 & 0 & 0 & 0 & 0 & 0 & 0 \\
-169205 & 0 & 0 & 0 & 0 & 0 & 0 & 0 & 0 \\
0 & -337940 & 0 & 0 & 0 & 0 & 0 & 0 & 0 \\
0 & 0 & -466120 & 0 & 0 & 0 & 0 & 0 & 0
\end{bmatrix}
\begin{bmatrix}
\Delta z \\
\Delta s \\
\Delta t \\
z_4 \\
z_5 \\
z_6 \\
\Delta p \\
\Delta q \\
\Delta w
\end{bmatrix}
+
\begin{bmatrix}
0 & 0 & 0 \\
0 & 0 & 0 \\
0 & 0 & 0 \\
0 & 0 & 0 \\
0 & 0 & 0 \\
0 & 0 & 0 \\
3.410 & 3.410 & 3.410 \\
-27.383 & -27.383 & 51.474 \\
40.094 & -42.492 & 0
\end{bmatrix}
\begin{bmatrix}
\Delta i_{AD} \\
\Delta i_{BD} \\
\Delta i_{CD}
\end{bmatrix},
$$

$$(6.46)$$

$$
\Delta y_p =
\begin{bmatrix}
1 & 0 & 0 & 0 & 0 & 0 & 0 & 0 & 0 \\
0 & 1 & 0 & 0 & 0 & 0 & 0 & 0 & 0 \\
0 & 0 & 1 & 0 & 0 & 0 & 0 & 0 & 0
\end{bmatrix}
\begin{bmatrix}
\Delta z \\
\Delta s \\
\Delta t \\
z_4 \\
z_5 \\
z_6 \\
\Delta p \\
\Delta q \\
\Delta w
\end{bmatrix},
$$

$$(6.47)$$

Here, the integrator states (z_4, z_5, and z_6) and the displacement states (Δz, Δs, and Δt) are grouped together as the known states x_1 and the other velocity states (Δp, Δq, and Δw) are grouped together as the unknown states x_2. Therefore the A matrix in Eq. (6.46) can be divided into some sub-matrix as shown in Eqs. (6.48) and (6.49). The corresponding B_1 and B_2 are shown in Eq. (6.50).

$$
A_{11} =
\begin{bmatrix}
0 & 0 & 0 & 0 & 0 & 0 \\
0 & 0 & 0 & 0 & 0 & 0 \\
0 & 0 & 0 & 0 & 0 & 0 \\
1 & 0 & 0 & 0 & 0 & 0 \\
0 & 1 & 0 & 0 & 0 & 0 \\
0 & 0 & 1 & 0 & 0 & 0
\end{bmatrix},\
A_{12} =
\begin{bmatrix}
1 & 0 & 0 \\
0 & 1 & 0 \\
0 & 0 & 1 \\
0 & 0 & 0 \\
0 & 0 & 0 \\
0 & 0 & 0
\end{bmatrix},
$$

$$(6.48)$$

$$A_{21} = \begin{bmatrix} -169205 & 0 & 0 & 0 & 0 & 0 \\ 0 & -337940 & 0 & 0 & 0 & 0 \\ 0 & 0 & -466120 & 0 & 0 & 0 \end{bmatrix}, \ A_{22} = \begin{bmatrix} 0 & 0 & 0 \\ 0 & 0 & 0 \\ 0 & 0 & 0 \end{bmatrix}, \quad (6.49)$$

$$B_1 = \begin{bmatrix} 0 & 0 & 0 \\ 0 & 0 & 0 \\ 0 & 0 & 0 \\ 0 & 0 & 0 \\ 0 & 0 & 0 \\ 0 & 0 & 0 \end{bmatrix}, \ B_2 = \begin{bmatrix} 3410 & 3410 & 3410 \\ -27.383 & -27.383 & 51.474 \\ 40.094 & -42.492 & 0 \end{bmatrix}, \quad (6.50)$$

It can be verified from the above matrices that (A, B) is stabilizable and (A_{11}, A_{12}) is detectable. In order to implement the controller into the system, the continuous time model 6.46 is discretelized at the sampling frequency of 5 kHz using Matlab. After that, the poles of controller are selected in the z domain as: 0.984, 0.97, 0.986, 0.976, 0.988, 0.99, 0.96, 0.962, and 0.964. And the poles of observer are: 0.851, 0.852, and 0.855. When selecting the locations of poles, it would make little sense if the closed-loop plant eigenvalues are "faster" than the observer eigenvalues. If that were the case, the plant would "outrun" the observer. In order to make the observer states converge to the plant state faster than the plant states converge to zero, a workable rule of thumb is to place the observer eigenvalues two to five times farther left on the complex plane than the closed-loop plant eigenvalues [94]. That is the reason why the poles of observer and controller are selected as those values shown above. Based on those selected poles, the corresponding gain matrices are designed to be as follows.

$$K = \begin{bmatrix} -12841 & 688.02 & -4939.5 & 128300 & -73730 & 22873 & 33.231 & -7.1149 & 4.9051 \\ -12174 & 728.71 & 5293.4 & 118700 & -65749 & -12708 & 31.097 & -6397.3 & -3.1094 \\ -13541 & -5006.2 & 169.91 & 119620 & -46052 & 5062.2 & 33.285 & -0.7562 & 0.8726 \end{bmatrix}$$
$$(6.51)$$

$$L = \begin{bmatrix} 708.89 & 0 & 0 & 0.0709 & 0 & 0 \\ 0 & 707.84 & 0 & 0 & 0.0708 & 0 \\ 0 & 0 & 700.64 & 0 & 0 & 0.0702 \end{bmatrix}, \quad (6.52)$$

Once the gain matrices K and L are available, the control law based on the delta system: $\Delta u = -(k_1 + k_2 L) x_1 - k_2 z$ can be updated in each sampling period. x_1 can be obtained from the sensors and integrators and z can be calculated from its ODE in Eq. (6.43). So the control inputs to the original system can be got from formula (6.14). Here, special attention must be paid to calculate control inputs u. The u^* is a non-zero value in the vertical direction control which can be calculated using the Eq. (6.53). Plugging Eqs. (6.53) and (6.42) into Eq. (6.14), the final control law to the system is presented in Eq. (6.54).

$$u^* = -\text{pinv}(B)AX^*, \tag{6.53}$$

$$u = -(k_1 + k_2 L)x_1 - k_2 z - \text{pinv}(B)AX^*, \tag{6.54}$$

Where X^* denotes the final values of the states in the vertical mode and "pinv" means pseudo-inverse of the B matrix. The initial values for calculating z and integrator states are set to be zero. After implementing the control law into the system, the step response of closed-loop system is shown in Fig. 6-5. Those step responses have slow rise and settling time. The main reason for that is the locations of poles in observer and controller were determined arbitrarily. Unlike the LQR method used before, the poles location are only determined to make the system stable. The nonlinearity of the dynamics of those air bearings are also counted as another reason for the dynamic performance in the vertical mode.
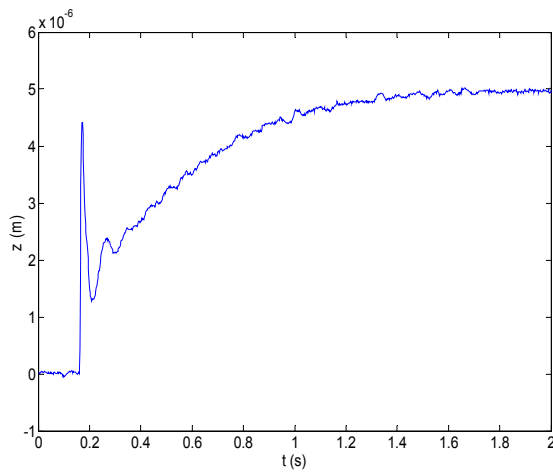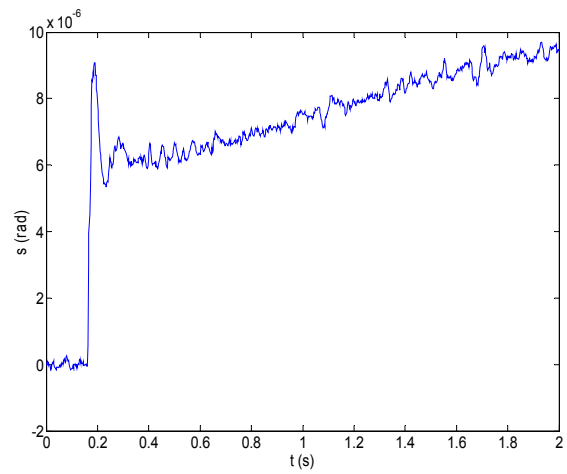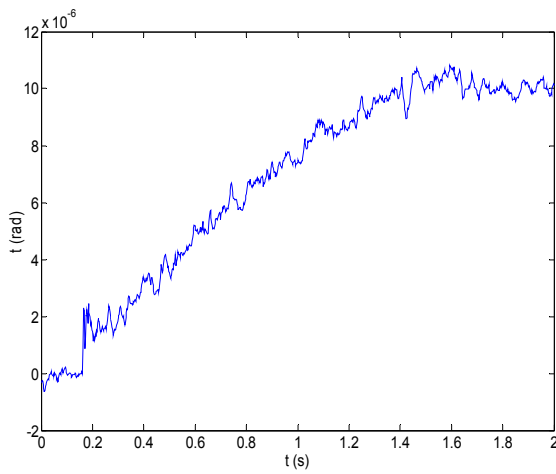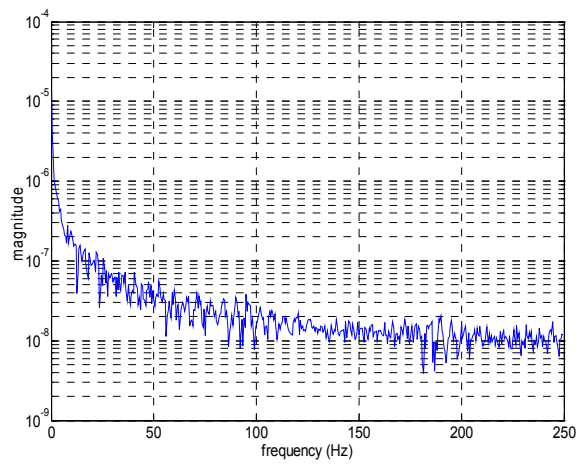
Fig. 6-5 5-μm step response in (*a*) *z*, 10-μrad step response in (*b*) *s*, and (*c*) *t*. (*d*) FFT of (*c*)

6.3   Linear Quadratic Gaussian (LQG) Control in the Vertical Mode

LQG control methodology is a combined optimal state estimation and optimal state feedback control. Compared with the estimator/state feedback algorithm, LQG uses a Kalman filter as the state estimator and LQR design for the state feedback. So in the design of LQG control, two Riccati equations have to be solved. Due to its optimization in control effort, LQG control is widely used in multivariable control industry such as rocket maneuvering.

There are two assumptions in LQG control design. First is that the plant dynamics is linear and known. Second is that the measurement noise and disturbance signals (process noise) are stochastic with known statistical properties [97]. That is, the plant model can be presented as follows.

$$\dot{x}(t) = Ax(t) + Bu(t) + L\zeta(t), \tag{6.55}$$

$$y(t) = Cx(t) + \theta(t), \tag{6.56}$$

Where, the A, B, L, and C are constant matrix. And $\zeta(t)$ is assumed to be the stationary, white Gaussian disturbance (process noise). It has the following properties.

$$E\{\zeta(t)\} = 0, \tag{6.57}$$

$$\text{Cov}\{\zeta(t), \zeta(t)\} = \Psi\delta(t - \tau), \tag{6.58}$$

$$\Psi = \Psi^T > 0, \tag{6.59}$$

Similarly, $\theta(t)$ is also assumed to be stationary, white Gaussian noise coming from the measurement inputs. So its expectation and covariance have the following properties.

$$E\{\theta(t)\} = 0, \tag{5.60}$$

$$\text{Cov}\{\theta(t), \theta(t)\} = \Theta\delta(t - \tau), \tag{5.61}$$

$$\Theta = \Theta^T > 0, \tag{5.62}$$

Where $E\{\cdot\}$ is the expectation operator and $\delta(t-\tau)$ is a delta function [98].

Furthermore, if (A, L) is controllable and (A, C) is observable, then a Kalman filter can be designed as the following equations. And the optimal choice of H, which minimizes $E\{[x - \hat{x}]^T [x - \hat{x}]\}$, is given by Eq. (6.64).

$$\dot{\hat{x}} = A\hat{x} + Bu + H(y - C\hat{x}),$$ (6.63)

$$H = \Sigma C^T \Theta^{-1},$$ (6.64)

Where $\Sigma = \Sigma^T \geq 0$ is the unique positive-semidefinite solution of a filter algebraic Ricatti equation (FARE):

$$A\Sigma + \Sigma A^T + L\Psi L^T - \Sigma C^T \Theta^{-1} C\Sigma = 0,$$ (6.65)

Then an LQ state feedback is implemented through the Kalman filter designed above, such that an optimal control law $u(t) = -K\hat{x}(t)$ (K is optimally determined by the control algebraic Ricatti equation) can be derived to minimize

$$J = E\left\{ \lim_{T \to \infty} \frac{1}{T} \int_0^T [x^T Q x + u^T R u] dt \right\},$$ (6.66)

$$K = R^{-1} B^T P,$$ (6.67)

Similarly, the P is the unique positive-semidefinite solution of the control algebraic Riccati equation (CARE):

$$A^T P + PA - PBR^{-1} B^T P + Q = 0,$$ (6.68)

Those equations further verified that the LQG control methodology is actually the combination of a Kalman filter and a LQR control law. The control structure of LQG is shown in Fig. 6-6 as following:
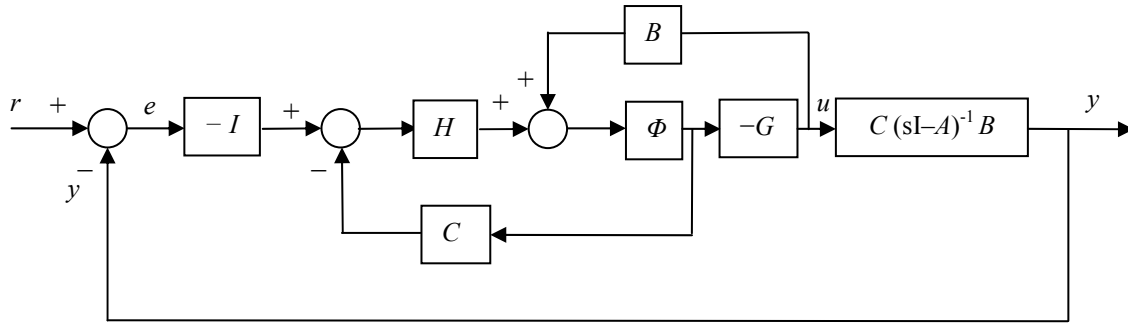
Fig. 6-6 Control structure of LQG controller [99]

LQG is introduced into the control system design in the vertical direction for the expectation that the LQG algorithm can optimize the pole location both for the observer and for the controller to get a better dynamic performance in that direction. Because the Kalman filter is actually an optimal observer for the system, the same design methodology for reduced order observer can be applied to design a reduced order LQG controller as well. To eliminate the steady state error, three integrators are also needed to be implemented in the original plant whose dynamics are shown in Eqs. (6.46) and (6.47). Based on previous analysis, the LQG controller will be designed based on the subsystem which is shown through Eqs. (6.48) to (6.50).

There are three inputs Δi_{AD}, Δi_{BD}, and Δi_{CD} and three outputs z, s, and t. Covariance of the noise in the output is experimentally determined to be on the order of 10^{-6} m^2. Assume the noise disturbance came from each inputs is in the same order as that in output channels. So at the input and output ends, the input noise disturbance and output measurement noise can be characterized as following.

$$L = \begin{bmatrix} 1 \\ 1 \\ 1 \end{bmatrix}, \ \Psi = 10^{-6}\,\text{m}^2, \tag{6.69}$$

$$\Theta = \begin{bmatrix} 10^{-6} & 0 & 0 \\ 0 & 10^{-6} & 0 \\ 0 & 0 & 10^{-6} \end{bmatrix} m^2, \tag{6.70}$$

With those values, it is ready to design the LQG controller. It can be checked that (A, B) is stabilizable and (A_{11}, A_{12}) is detectable. So in the LQR state feedback controller design, the Q and R matrix can be selected as:

$$Q = \text{diag} ([1e4\ 1e3\ 1e3\ 1e10\ 1e9\ 1e9\ 1e2\ 1e2\ 1e2]), \tag{6.71}$$

$$R = \begin{bmatrix} 1 & 0 & 0 \\ 0 & 1 & 0 \\ 0 & 0 & 1 \end{bmatrix}, \tag{6.72}$$

From the designed Q matrix, it can be seen that those displacement states z, s, and t and integrator states z_4, z_5, z_6 are penalized much more than those velocity states. The positioning resolution can be improved and steady-state error can be removed. To emphasize the importance of the integrators, their weights are chosen more than 5 times higher order than those of the displacement states. That is because the experimental data showed that if the weights of the integrators are very small the purpose of integrating will be dramatically reduced or even trivial. As a result, steady state error can not be efficiently removed. The gain matrix K of the digital LQR controller can be then designed by Matlab which is shown as following.

$$K = \begin{bmatrix} -67.94 & 104.09 & -291.90 & 57517 & -12628 & 20786 & 6.08 & 4.07 & 6.55 \\ -118.85 & 109.70 & 282.82 & 55498 & -12267 & -21425 & 5.91 & -3.95 & -6.86 \\ -45.04 & -216.03 & 4.34 & 59054 & 23886 & -52.75 & 6.27 & 7.57 & -0.064 \end{bmatrix}, \tag{6.73}$$

As it is discussed in Eq. (6.42), the sub gain matrix k_1 and k_2 can be extracted from K matrix as following:

$$k_1 = \begin{bmatrix} -67.94 & 104.09 & -291.90 & 57517 & -12628 & 20786 \\ -118.85 & 109.70 & 282.82 & 55498 & -12267 & -21425 \\ -45.04 & -216.03 & 4.34 & 59054 & 23886 & -52.75 \end{bmatrix}, \tag{6.74}$$

$$k_2 = \begin{bmatrix} 6.08 & 4.07 & 6.55 \\ 5.91 & -3.95 & -6.86 \\ 6.27 & 7.57 & -0.064 \end{bmatrix}, \tag{6.75}$$

Because the states of integrator can be obtained by integrating in each sampling period, these states are regarded as known states. Thus they are grouped together with these displacement states as known states and the dimension of k_1 is 3 by 6 as shown in Eq. (6.74).

With the noise covariance matrics determined in Eqs. (6.69) and (6.70), it is easy to use Matlab to design the Kalman filter. Caution must be paid in the design of reduced order Kalman filter that similar to the reduced order observer design, A_{22} and A_{12} should be used as the A and C matrices. The filter gain matrix H of the digital Kalman filter is presented as following:

$$H = \begin{bmatrix} 9977.4 & 0.0001 & 0.0001 & 0.998 & 0 & 0 \\ 0.0001 & 9954.9 & 0.0001 & 0 & 0.997 & 0 \\ 0.0001 & 0.0001 & 9937.8 & 0 & 0 & 0.995 \end{bmatrix}, \tag{6.76}$$

The control law to the original plant is shown in Eq. (6.77). Similarly, the introduced new states z can be updated by integrating its ODE equation in Eq. (6.43). The A and B matrices are the same matrices as shown in Eq. (6.46). And X^* is the desired value of the outputs in the vertical mode.

$$u = -(k_1 + k_2 H)x_1 - k_2 z - \mathrm{pinv}(B)AX^*, \tag{6.77}$$

The LQG implemented experimental step response is shown in Fig. 6-7. From those results, it can be seen that there are some vibrations in all the three vertical axes. This was because of the modeling error of the disturbance noise. And unlike the minor loop controller used in SISO control, the LQG controller can not modify the resonant dynamics of the positioner in the vertical mode. Thus those dynamics from the air bearings degraded the dynamic performance in the vertical mode.
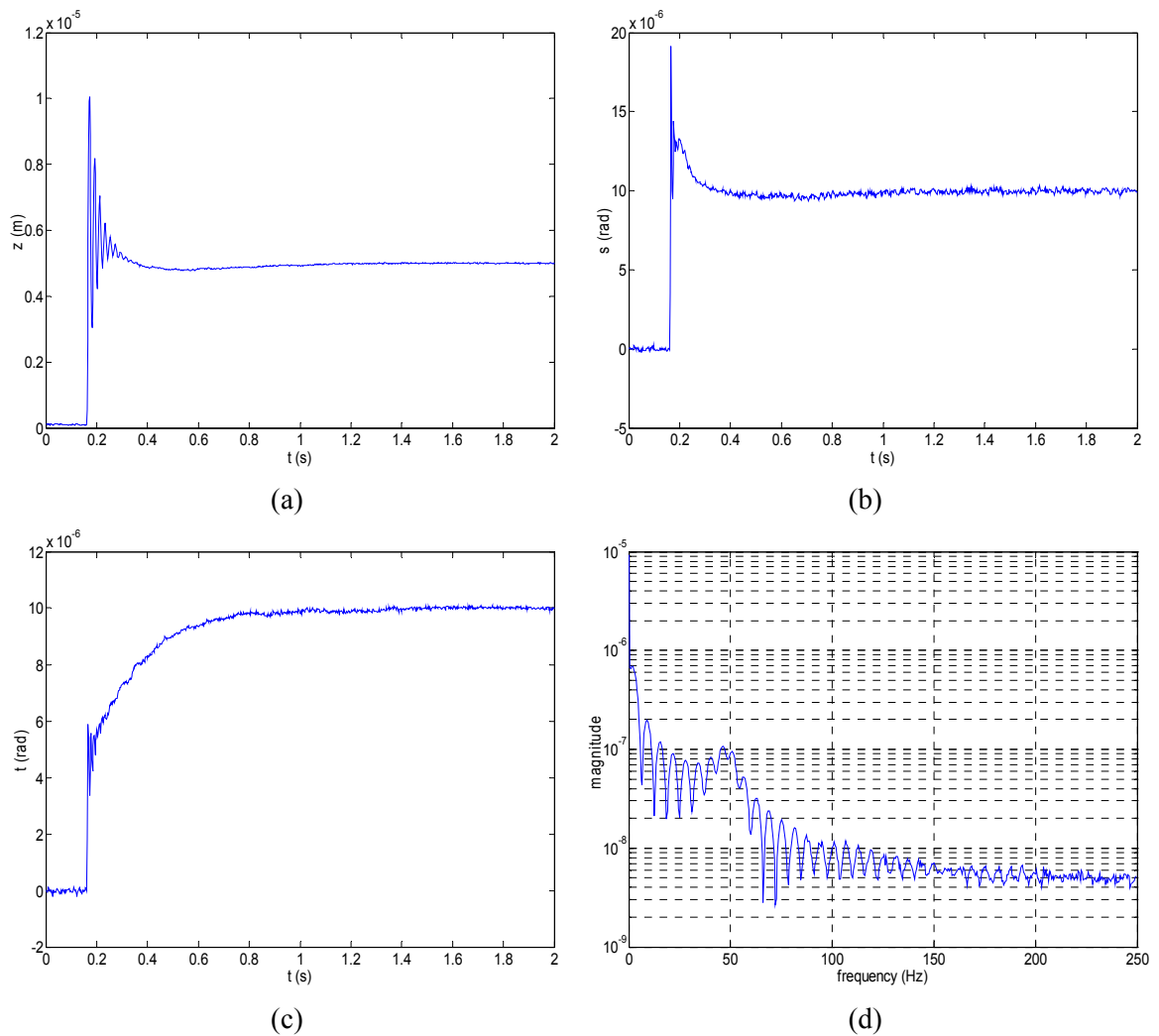
Fig. 6-7 (*a*) 5-µm step response in *z*, 10-µrad step response in (*b*) *θ* and (*c*) *φ* with integrator augmented reduced order LQG controller, and (*d*) FFT of (*a*).

CHAPTER VII

CONCLUSIONS AND SUGGESTIONS FOR FUTURE WORK

In this final chapter, the contributions and achievements of this thesis are discussed. To make this prototype postioner have wider applications in precision engineering, several suggestions about the incremental improvements of this positioner are also given in this chapter.

7.1   Conclusions

A high-precision multi-dimensional positioning system consisting of a novel concentrated-field magnet matrix based on Halbach magnet arrays and a triangular single-moving platen was designed, fabricated, assembled and tested. The actuators for the positioner are three 3-phase planar levitation motors, which exhibit no cogging force. Each of these actuators can generate vertical as well as lateral forces. This high precision multi-dimensional positioner can generate all the required small motions for optical focusing and alignments as well as large planar motions for wafer positioning. Since the positioner is levitated by three aerostatic bearings and the mass of the positioner is only 5.91 kg, the power consumption of the system is small. Furthermore, no lubrications are required for the system since there is no mechanical contact between the moving part and the stationary base plate. The positioning system generates zero wear particles, so the system is suitable for clean-room environment. Because no power transmission mechanism such as ball screws is used in the system, the positioning system has a fast dynamic response without any backlash. The system is controlled by a DSP. Therefore the positioning resolution of the system is primarily dependent on the fundamental limits of metrology and controls.

Compared with other positioning systems which have either crossed-axes structure or gantry configuration, this single-moving compact positioner has plenty of advantages for the high-precision motion-control applications. This compact moving system has a simpler mechanical structure which yields fast and simple dynamics. Thus the positioner developed in this thesis is a competitive candidate for the innovation in product throughput in industry.

This thesis illustrated the whole design process of the high-precision multidimensional postioner from the electromagnetic concept to the final advanced control system design. In the mechatronics design part of the system, the thesis dealt with the fundamental design and fabrication considerations of the concentrated magnet matrix base plate and the novel 3-phase planar motors. The working principle of how the positioning system achieves 6-DOF motions was also fully illustrated. A comprehensive dynamics analysis of the system was included and both the decoupled dynamics model and the coupled dynamics model were derived in the thesis. The electrical system design includes anti-aliasing filter design, power amplifier design, and driving circuits design.

This positioning system is controlled by a TMS320C40 DSP. The sampling rate of the system is 5 kHz. Digital lead-lag compensators were designed to control the horizontal motions with a bandwidth of 38 Hz. By implementing a controller in a minor feedback loop, the aerostatic-bearing resonance in the vertical axes was successfully reduced. This high precision multidimensional positioner was tested successfully. After being implemented these digital feedback controllers, the positioner achieved a position resolution of 20 nm with a position noise of 10 nm rms in both x and y, and a submicrometer resolution in other axes. The positioning error in tracking a 1-μm sinusoidal wave and a 5-μm radius circle was less than 30 nm rms, which demonstrated the positioner's 1D and 2D nanoscale positioning capabilities.

The design process and experimental results of advanced multivariable control were fully explored in this thesis. A digital LQR controller was designed and implemented in the horizontal mode control. To reduce the steady-state error, integrators were also designed. Comparative experimental results demonstrated the LQR controller with integrators could achieve good dynamic performance, such as reducing the rise time and settling time, in horizontal mode without steady-state error. Both the input disturbance noise and output measure noise are analyzed and identified in the thesis. To save the computation time for the DSP, a reduced-order digital LQG controller with integrators was designed and implemented. Compared to the traditional observer/state-feedback controller, the LQG controller successfully achieved a better dynamic performance and higher positioning resolution in the vertical mode.

Several experiments were performed to evaluate the potential application of this positioner in semiconductor manufacturing. This prototype positioner has a planar travel range of 160×160 mm, which can be easily extended by adding more magnets to the magnet matrix. It currently exhibits 0.5-m/s maximum speed at an acceleration of 5 m/s^2. The large arbitrary planar-motion generation capability of this positioning stage was demonstrated by following large 2D motion profiles such as a 4-cm-radius circle combined with a double triangle. These extended-range tracking capabilities make this prototype positioner qualified to be used as a wafer inspection stage. The 2-cm step-and-repeat motion with an acceleration of 4 m/s^2 generated by the positioner and the step-and-scan motion indicate that it has the potential to be used as a wafer stepper in semiconductor factory automation.

In conclusion, this thesis presented a novel high precision multidimensional positioning system and successfully demonstrated its potential applications in precision engineering. The basic idea and control methodology in this thesis hopefully can be applied to any other future design and development of high-precision positioning systems.

7.2   Suggestions for Future Work

In order to further improve the positioning resolution and dynamic performance of the positioner, several considerations in mechanical and electrical design should be taken in developing the next generation positioner.

- Other materials such as ceramics can be better than Delrin for the platen in terms of the structural stiffness, which will have less deformation and can yield higher natural resonant frequency.

- The measuring range of the laser distance sensor in the vertical axis should be significantly improved. Laser interferometer can be a good replacement for its higher resolution and longer measuring range.

- The mechanical design of mirror and sensor mounts should be more elaborately developed. How to mount the stick mirrors parallel to the edge of the platen and to make the vertical sensors strictly perpendicular to the base plate are two of the most important issues in assembly.

- System identification should be performed to be applied to further refine the dynamic model of the system due to the umbilical signal and power cables and stiff air pipes connected to the platen.

.

REFERENCES

[1] C. Bauer, A. Bugacov, B. E. Koel, A. Madhukar, N. Montoya, T. R. Ramachandran, A. A. G. Requicha, R. Resch, and P. Will, "Nanoparticle manipulation by mechanical pushing: underlying phenomena and real-time monitoring," *Nanotechnology*, vol. 9, no. 4, pp. 360−364, December 1999.

[2] R. M. Talor, II, "The Nanomanipulator: A virtual-reality interface to a scanning tunneling microscope," Ph.D. dissertation, University of North Carolina at Chapel Hill, May 1994.

[3] M. F. Yu, M. J. Dyer, H. W. Rohrs, X. K. Lu, K. D. Ausman, J. V. Her, and R. S. Ruoff, "Three-dimensional manipulation of carbon nanotubes under a scanning electron microscope," *Nanotechnology*, vol. 10, no. 3, pp. 244−252, September 1999.

[4] C. H. Baskin, "Challenges in 300-mm wafer assembly," *Solid State Technology*, vol. 40, no. 7, pp. 131−140, July 1997.

[5] ——, "Semiconductor manufacturing technician skill standards," Maricopa Community College District, Tempe, Arizona.

[6] M. Quirk and J. Serda, *Semiconductor Manufacturing Technology*. Upper Saddle River, NJ: Prentice-Hall, 2001.

[7] Semiconductor Industry Association, "Semiconductor industry association 2004 annual report," http://www.sia-online.org/downloads/SIA_AR_2004.pdf, accessed on April 26, 2005.

[8] R. A. de Callafon and P. M. J. Van den Hof, "Multivariable feedback relevant system identification of a wafer stepper system," *IEEE Transactions on Control System Technology*, vol. 9, no. 2, pp. 381−382, March 2001.

[9] G. Van Engelen and A. G. Bouwer, "Two-step positioning device using Lorentz forces and a static gas bearing," U.S. Patent 5 120 034, June 9, 1992.

[10] S. Sakino, E. Osanai, M. Negishi, M. Horikoshi, M. Inoue, and K. Ono, "Movement guiding mechanism," U.S. Patent 5 040 431, August 20, 1991.

[11] S. Wittekoek and A. G. Bouwer, "Displacement device, particularly for the photolithographic treament of a substrate," U.S. Patent 4 655 594, April 7, 1987.

[12] W. Leonhard, *Control of Electrical Drives*. New York: Springer-Verlag, 1996.

[13] ——, *MicroPositioning, NanoPositioning, NanoAutomation*. Tustin, CA: Physik Instrumente (PI), 2001.

[14] A. E. Braun, "Nanotechnology: genesis of semiconductor's future," *Semiconductor International*, vol. 27, no. 12, pp. 45−52, November 2004.

[15] U. Schaff, "Pushy motors [piezoelectric motors]," *IEEE Review*, vol. 41, no. 3, pp. 105−108, May 1995.

[16] Piezo Systems, Inc, "Introduction to piezo transducers," http:// Piezo Systems - piezo actuators & transducers.htm, accessed on April 13, 2005.

[17] D. Newton, E. Garcia, and G.C. Horner, "A linear piezoelectric motor," *Smart Material and Structure*, no.6, pp. 295−304, 1997.

[18] R. Thibadeau, "Tutorial on the rotary or swing arm voice coil actuator used on modern hard disk (disc) drives," http://yuan.ecom.cmu.edu/rotaryvoicecoil/, accessed on April 13, 2005.

[19] M. Koizumi, "An integral equation method for analysis of three-dimensional magneto-dynamics with moving objects," *IEEE Transactions on Magnetics*, vol. 29, no. 2, pp. 1516−1517, March 1993.

[20] H. Numasato and M. Tomizuka, "Settling control and performance of a dual-actuator system for hard disk drives," *IEEE/ASME Transactions on Mechatronics*, vol. 8, no. 4, pp. 431−433, December 2003.

[21] D. A. Horsley, D. Hernandez, R. Horowitz, A. K. Packard, and A. P. Pisano, "Closed-loop control of a micofabricated actuator for dual-stage hard disk drive servo systems," In *IEEE Proceedings of the American Control Conference*, 1998, vol. 5, pp.3028−3032.

[22] T. Hirano, L. S. Fan, W. Y. Lee, J. Hong, W. Imaino, S. Pattanaik, S. Chan, P. Webb, R. Horowitz, S. Aggarwal, and D. A. Horsley, "High-bandwidth high-accuracy rotary microactuators for magnetic hard disk drive tracking servos," *IEEE/ASME Transactions on Mechatronics.*, vol.3, no. 3, pp. 156–165, September 1998.

[23] D. Hernandez, S. Park, R. Horowitz, and A. K. Packard, "Dual-stage track-following servo design for hard disk drives," in *Proceedings of American Control Conference*, 1999, vol. 6, pp. 4116–4121.

[24] S. J. Schorceck and W. C. Messner, "On controller design for linear time-invariant dual-input single-output systems," in *Proceedings of American Control Conference*, 1999, vol. 6, pp. 4122–4126.

[25] X. Hu, W. Guo, T. Huang, and B. M. Chen, "Discrete-time LQG/LTR dual-stage controller design and implementation for high track density hdds," in *Proceedings of American Control Conference*, 1999, vol. 6, pp. 4111–4115.

[26] J. Ding, M. Tomizuka, and H. Numasato, "Design and robustness analysis of dual stage servo system," in *Proceedings of American Control Conference*, 2000, vol. 4, pp. 2605–2609.

[27] Y. Li and R. Horowitz, "Analysis and self-tuning control of dual stage servos with MEMS micro-actuators," in *Proceedings of American Control Conference*, 2000, vol. 4, pp. 2627–2632.

[28] K. Mori, T. Munemoto, H. Otsuki, Y. Yamaguchi, and K. Akagi, "A dual-stage magnetic disk drive actuator using a piezoelectric drive for a high track density," *IEEE Transactions on Magnetics*, vol. 27, no. 6, pp. 5298–5300, November 1991.

[29] R. B. Evans, J. S. Griesbach, and W. C. Messner, "Piezoelectric microactuator for dual stage control," *IEEE Transactions on Magnetics*, vol. 35, no. 2, pp. 977–982, March 1999.

[30] S. Koganezawa, Y. Uematsu, T. Yamada, H. Nakano, J. Inoue, and T. Suzuki, "Dual-stage actuator system for magnetic disk drives using a shear piezoelectric microactuator," *IEEE Transactions on Magnetics*, vol. 35, no. 2, pp. 988–992, March 1999.

[31] I. Naniwa, S. Nakamura, S. Saegusa, and K. Sato, "Low voltage driven piggy-back actuator of hard disk drives," in *Proceedings of IEEE International Micro Electro Mechanical Systems Conference*, 1999, pp. 49–52.

[32] J. Cao, Y. Zhu, J. Wang, W. Yin, and G. Duan, "Analysis and comparison of two-dimensional permanent-magnet arrays for planar motor," *IEEE Transactions on Magnetics*, vol. 40, no. 6, pp. 3490−3491, November 2004.

[33] H.-S. Cho, C.-H. Im, and H.-K. Jung, "Magnetic field analysis of 2-D permanent magnet array for planar motor," *IEEE Transactions on Magnetics*, vol. 37, no. 5, pp. 3762–3766, September 2001.

[34] H.-S. Cho and H.-K. Jung, "Analysis and design of synchronous permanent-magnet planar motors," *IEEE Transactions on Energy Conversion*, vol. 17, no. 4, pp. 492–499, December 2002.

[35] H.-S Cho and H.-K. Jung, "Effect of coil position and width on back-EMF constant of permanent magnet planar motors," in *Proceedings of International Electric Machines and Drives Conference*, 2001, pp. 430–435.

[36] T. Ueta, B. Yuan, and T.-C. Teng, "Moving magnet type planar motor control," U.S. Patent Application Publication 0 102 722, June 5, 2003.

[37] T. Ueta and B. Yuan, "Moving coil type planar motor control," U.S. Patent Application Publication 0 102 721, June 5, 2003.

[38] J. K. Rough, "Electric motor drive system," U.S. Patent 4 187 453, February 5, 1980.

[39] W.-C. Gan and N. C. Cheung, "Development and control of a low-cost linear variable-reluctance motor for precision manufacturing automation," *IEEE/ASME Transactions on Mechatronics*, vol. 8, no. 3, pp. 326–333, September 2003.

[40] T. J. E. Miller, *Switched Reluctance Motor and Their Control*. New York: Oxford University Press, 1993.

[41] P. C. Kjaer, J. J. Gribble, and T. J. E. Miller, "High-grade control of switched reluctance machines," *IEEE Transactions on Industry Applications*, vol. 33, no. 6, pp. 1585–1593, November/December 1997.

[42] B. S. Lee, H. K. Bae, P. Vijayraghvan, and R. Krishnan, "Design of a linear switched reluctance machine," *IEEE Transactions on Industry Applications*, vol. 36, no. 6, pp. 1571−1580, November/December 2000.

[43] I. Boldea and S. A. Nasar, *Linear Electric Actuators and Generators*. Cambridge, U.K.: Cambridge University Press, 1997.

[44] B. A. Swayer, "Magnetic positioning device," U. S. Patent 3 376 578, April 2, 1968.

[45] T. Asakawa, "Two dimensional precise positioning devices for use in a semiconductor apparatus," U.S. Patent 4 535 278, August 13, 1985.

[46] D. Ebihara and M. Watada, "Study of a basic structure of surface actuator," *IEEE Transactions on Magnetics*, vol. 25, no. 5, pp. 3916–3918, September 1989.

[47] J. D. Buckley, D. N. Galburt, and C. Karatzas, "Step-and-scan lithography using reduction optics," *Journal of Vacuum Science and Technology, B*, vol. 6, no. 7, pp. 1607−1612, November/December 1989.

[48] V. Fernandez, G. Reyne, and O. Cugat, "Prospective FEM modeling of induction planar micromotors," *IEEE Transactions on Magnetics*, vol. 35, no. 3, May 1999.

[49] H. Guckel, T. R. Christenson, K. J. Skrobis, T. S. Jung, J. Klein, K. V. Hartojo, "A first functional current excited planar rotational magnetic micromotor," in *IEEE Proceedings of MEMS*, 1993, pp. 7−11.

[50] K.-P. Kamper, W. Ehrfeld, B. Hagemann, H. Lehr, A. Schirling, C. Thurigen, and T. Wittig, "Electromagnetic permanent magnet micromotor with integrated micro gear box," in *Proceedings of 5th International Conference on New Actuators*, Bremen, Germany, 1996, pp. 429−432.

[51] O. Cugat, V. Fermandez, D. Roy, J. Delamare, and G. Reyne, "Miniature permanent magnet bearings: application to planar micromotors," in *Proceedings of Congress Mechatronics,* Besancon, France, 1996, pp. 624−626.

[52] C. H. Ahn, Y. J. Kim, and M. G. Allen, "A planar variable reluctance magnetic micromotor with fully integrated stator and coils," *Journal of Microelectromechanical Systems*, vol. 2, no. 4, pp. 165−173, December 1993.

[53] W. E. Hinds and B. Nocito, "The Sawyer linear motor," in *Proceedings of 2nd Symposium on Incremental Motion Control Systems and Devices*, 1973, pp. W-1−W-10.

[54] E. R. Pelta, "Two axis Sawyer motor," in *Proceedings of the 12th Annual IEEE Industrial Electronics Society Conference*, 1986, pp. 3−8.

[55] P. Krishnamurthy and F. Khorrami, "Robust adaptive control of Sawyer motors without current measurements," *IEEE/ASME Transactions on Mechatronics*, vol. 9, no. 4, pp. 689–690, December 2004.

[56] H. Melkote, F. Khorrami, and J. Ish-Shalom, "Closed-loop control of a three degree-of-freedom ultra accurate linear stepper motor," in *Proceedings of IEEE Conference on Control Applications*, 1997, pp. 639–644.

[57] H. Melkote and F. Khorrami, "Closed-loop control of a base xy stage with rotational degree-of-freedom for a high-speed ultra-accurate manufacturing system," in *Proceedings of IEEE International Conference on Robotics and Automation*, 1999, pp. 1812–1817.

[58] A. E. Quaid and A. A. Rizzi, "Robust and efficient motion planning for a planar robot using hybrid control," in *Proceedings of IEEE International Conference on Robotics and Automation*, 2000, pp. 4021–4026.

[59] A. E. Quaid and R. L. Hollis, "3-dof closed-loop control for planar linear motors," in *Proceedings of IEEE International Conference on Robotics and Automation*, 1998, pp. 2488–2493.

[60] H. Melkote and F. Khorrami, "Output feedback control of a three degree-of-freedom linear stepper motor with position measurements only," in *Proceedings of American Control Conference*, 1999, pp. 2531–2535.

[61] P. Krishnamurthy and F. Khorrami, "TriM: ultra-accurate high-speed six degree-of-freedom manipulator using linear motors," in *Proceedings of the 2003 IEEE/RSJ International Conference Intelligent Robots and Systems*, 2003, pp. 3306–3307.

[62] ——, *Northern Magnetics Linear Motor Technology Manual*, Saalburgstr, Germany: Normag GmbH, 1998.

[63] Megamation, "Electronic industry," http://www.megamation.com/hm_frame.htm, accessed on April 13, 2005.

[64] W. E. Hinds, "Single plane orthogonally movable drive system," U. S. Patent 4 654 571, March 31, 1987.

[65] Chitayat, "Two-axis motor with high density magnetic platen," U. S. Patent 5 777 402, July 7, 1998.

[66] T. Asakawa, "Two dimensional positioning devices," U. S. Patent 4 626 749, December 2, 1986.

[67] H.-S. Cho, C.-H. Im, and H.-K. Jung, "Magnetic field analysis of 2-D permanent magnet array for planar motor," *IEEE Transactions on Magnetics*, vol. 37, no. 5, pp. 3762−3763, September 2001.

[68] D. L. Trumper, W.-J. Kim, and M. E. Williams, "Magnetic arrays," U. S. Patent 5 631 618, May 20, 1997.

[69] K. Halbach, "Design of permanent multipole magnets with oriented rare earth cobalt material," *Nuclear Instruments and Methods*, vol. 169, no. 1, pp. 1−10, 1980.

[70] M. Marinescu and N. Marinescu, "New concept of permanent magnet excitation for electrical machines analytical and numerical computation," *IEEE Transactions on Magnetics*, vol. 28, no. 2, pp. 1390−1393, 1992.

[71] M. G. Abele, H. Rusinek, and F. Bertora, "Field computation in permanent magnets," *IEEE Transactions on Magnetics*, vol. 28, no. 1, pp. 931−934, 1992.

[72] H. A. Leupold, E. Potenziani II, and M. G. Abelle, "Novel magnet structure for free-electron lasers," *Journal of Applied Physics*, vol. 67, no. 9, pp. 4653−4655, May 1990.

[73] D. L. Trumper, W.-J. Kim, and M. E. Williams, "Design and analysis framework for permanent-magnet machines," *IEEE Transactions on Industry Applications*, vol. 32, no. 2, pp. 371−379, March/April 1996.

[74] W.-J. Kim, "High-precision planar magnetic levitation," Ph.D. dissertation, Massachusetts Institute of Technology, Cambridge, MA, June 1997.

[75] Z. Q. Zhu and D. Howe, "Instantaneous magnetic field distribution in brushless permanent magnet DC motors, part I: open-circuit field," *IEEE Transactions on Magnetics*, vol. 29, no. 1, pp. 124−135, January 1993.

[76] A. E. Fitzgerald, C. Kingsley, Jr., and S. Umans, *Electric Machinery*. Boston, MA: McGraw-Hill, 2003.

[77] W.-J. Kim and D. L. Trumper, "Force ripple in surface-wound permanent- magnet linear motors," in *Proceedings of IEEE International Magnetics Conference*, 1996, FE-03.

[78] W.-J. Kim, D. L. Trumper, and J. H. Lang, "Modeling and vector control of planar levitator," *IEEE Transactions on Industry Applications*, vol. 34, no. 6, pp. 1254−1262, 1998.

[79] X. Z. Liu, G. C. Verghese, J. H. Lang, and M. K. Önder, "Generalizing the Blondel-Park transformation of electrical machines: necessary and sufficient conditions," *IEEE Transactions on Circuits and Systems*, vol. 36, no. 8, pp. 1058−1067, August 1989.

[80] A. Blondel, *Synchronous Motor and Converters*. Boston, MA: McGraw-Hill, 1913.

[81] R. H. Park, "Two-reaction theory of synchronous machines, generalized method of analysis−Part I," *Transactions AIEE*, vol. 48, pp. 716−730, 1929.

[82] J. H. Ginsberg, *Advanced Engineering Dynamics*. Cambridge, U.K.: Cambridge University Press, 1998.

[83] L. Ljung, *System Identification: Theory for the User*. Upper Saddle River, NJ: Prentice-Hall, 1999.

[84] J. G. Proakis and D. G. Manolakis, *Digital Signal Processing*. Upper Saddle River, NJ: Prentice-Hall, 1996.

[85] D. B. Stewart and M. Moy, "An engineering approach to determining sampling rates for switches and sensors in real-time systems," in *Proceedings of the 3rd IEEE International Conference on Electronics, Circuits, and Systems*, 1996, pp. 671−675.

[86] G. F. Franklin, J. D. Powell, and M. L. Workman, *Digital Control of Dynamic Systems*. Reading, MA: Addison-Wesley, 1990.

[87] Y. Egshira, K. Kosaka, S. Takada, T. Iwabuchi, T. Baba, S. Moriyama, T. Harada, K. Nagamoto, A. Nakada, H. Kubota, and T. Ohmi, "0.69 nm resolution ultrasonic motor for large stroke precision stage," in *Proceedings of the 2001 1st IEEE conference on nanotechnology*, 2001, pp. 397−402.

[88] M. L. Holmes, R. Hocken, and D. Trumper, "The long range scanning stage: a novel platform for scanned probe microscopy," *Precision Engineering*, vol. 24, no. 3, pp. 191−209, July 2000.

[89] W.-J. Kim and D. L. Trumper, "High precision magnetic levitation stage for photolithography," *Precision Engineering*, vol. 22, no. 2, pp. 66−77, April 1998.

[90] C. Sparkes, L. Thompson, and P. Bischoff, "Integrated solutions Inc.: XLS wafer steppers—deep UV for production environments," *Solid State Technology*, vol. 38, no. 9, pp. 90−91, September 1995.

[91] W. Arnold, "Is a scanner better than a stepper?" *Solid State Technology*, vol. 40, no. 3, pp. 77, March 1997.

[92] H. Levison and W. Arnold, "Optical lithography," *Microlithography, Micromachining and Microfabrication*, vol. 1, pp. 69, ed. R. Rai-Choudhury, Bellingham, WA: SPIE, 1997.

[93] X. Shan, S.-K. Kuo, J. Zhang, and C.-H. Menq, "Ultra precision motion control of a multiple degrees of freedom magnetic suspension stage," *IEEE/ASME Transactions on Mechatronics*, vol. 7, pp. 67−78, March 2002.

[94] S. Skogestad and I. Postlethwaite, *Multivariable Feedback Control Analysis and Design*. New York, NY: John Wiley & Sons, 1996.

[95] J. S. Bay, *Fundamentals of Linear State Space Systems*. Boston, MA: WCB/McGraw-Hill, 1999.

[96] University of Michigan, "Control tutorials for Matlab," http://www.engin.umich.edu/group/ctm/, accessed on April 13, 2005.

[97] L. Dai, "Filtering and LQG problems for discrete-time stochastic singular system," *IEEE Transactions on Automatic Control*, vol. 34, no. 10, pp. 1105−1108, October 1989.

[98] P. S. Maybeck, *Stochastic Models, Estimation, and Control*. New York: Academic Press, 1979.

[99] S. Jayasuriya, "MEEN 652—multivariable control system design," *Lecture Notes*. Texas A&M University, College Station, March 2003.

APPENDIX A

DRAWINGS OF THE DESIGNED PARTS [After Bhat]

This is the bottom surface of the base plate

R.125 at the 4 corners of the pocket
R.125 at 4 corners of the pocket
R.125 at 4 corners of the pocket

Note
1: Pockets of depth 0.75 inch

Reference Point from where all the tap holes are specified

Texas A&M Mechatronics Lab
Phone: 979-862-9010

Title:
Base Plate

	NAME	DATE
DRAWN	Nikhil B	July 23
CHECKED		
ENG APPR.		
MFG APPR.		
Q.A.		
COMMENTS:		

# of parts: 1

DIMENSIONS ARE IN INCHES
TOLERANCES:
FRACTIONAL±
ANGULAR: MACH± BEND ±
TWO PLACE DECIMAL ±
THREE PLACE DECIMAL ±0.005

MATERIAL   Delrin

FINISH   ---

DO NOT SCALE DRAWING

PROPRIETARY AND CONFIDENTIAL
THE INFORMATION CONTAINED IN THIS
DRAWING IS THE SOLE PROPERTY OF
<INSERT COMPANY NAME HERE>. ANY
REPRODUCTION IN PART OR AS A WHOLE
WITHOUT THE WRITTEN PERMISSION OF
<INSERT COMPANY NAME HERE> IS
PROHIBITED.

SIZE Drawing No:1
A

SCALE:1:5   SHEET:1 of 4

REV.

This is the bottom surface of the base plate

Note

3: Pocket of depth 0.550

③

1.613

2.005

6.838

7.159

7.841

12.155

3 Ø.614 holes

.197

1.894

5.688

10.319

Reference Point from
where all the tap holes
are specified

(1.000)

DIMENSIONS ARE IN INCHES TOLERANCES: FRACTIONAL± ANGULAR: MACH± BEND ± TWO PLACE DECIMAL ± THREE PLACE DECIMAL ±0.005				Texas A&M Mechatronics Lab	
				Phone: 979-862-8010	
		DRAWN	NAME Nikhil B	DATE JULY 22	Title:
		CHECKED			Base Plate
		ENG APPR.			
		MFG APPR.			
MATERIAL	Delrin	Q.A.			
		COMMENTS:			SIZE DWG. NO. 1 REV.
FINISH	--	# of parts: 1			A
PROPRIETARY AND CONFIDENTIAL THE INFORMATION CONTAINED IN THIS DRAWING IS THE SOLE PROPERTY OF <INSERT COMPANY NAME HERE>. ANY REPRODUCTION IN PART OR AS A WHOLE WITHOUT THE WRITTEN PERMISSION OF <INSERT COMPANY NAME HERE> IS PROHIBITED.		DO NOT SCALE DRAWING			SCALE:1:5 SHEET :3 OF 4

168

.256
.197

(.118)

.256

.256

.394

4.134

(.081)

3.858

.350±.001

(.256)

.547

.394

(.118)

Ø.114 at 4 places

.394

1.213±.001

2.000

4.134

.256

.118

PROPRIETARY AND CONFIDENTIAL

THE INFORMATION CONTAINED IN THIS DRAWING IS THE SOLE PROPERTY OF <INSERT COMPANY NAME HERE>. ANY REPRODUCTION IN PART OR AS A WHOLE WITHOUT THE WRITTEN PERMISSION OF <INSERT COMPANY NAME HERE> IS PROHIBITED.

DIMENSIONS ARE IN INCHES
TOLERANCES:
FRACTIONAL±
ANGULAR: MACH± BEND ±
TWO PLACE DECIMAL ±
THREE PLACE DECIMAL ±0.005

MATERIAL   Delrin

FINISH   --

DO NOT SCALE DRAWING

	NAME	DATE
DRAWN	Nikhil B	July 23
CHECKED		
ENG APPR.		
MFG APPR.		
Q.A.		
COMMENTS:		

# of parts: 3

Texas A&M Mechatronics Lab
Phone: 979-862-8010

Title:
Coil Core

SIZE A   DWG. NO. 2   REV.

SCALE:1:1   SHEET 1 OF 1

(.2181)

(.8996)

(.9449)

(.5669)

(Ø .9449)

(Ø .5000)

(Ø .5669)

(Ø .1181 at 120 degrees)

Texas A&M Mechatronics Lab
Phone: 979-862-8010

Title:

Air Bearing Holder

	NAME	DATE
DRAWN	Sean E.	May 31
CHECKED		
ENG APPR.		
MFG APPR.		
Q.A.		
COMMENTS:		

# of parts: 2

DIMENSIONS ARE IN INCHES
TOLERANCES:
FRACTIONAL±
ANGULAR: MACH±   BEND ±
TWO PLACE DECIMAL   ±
THREE PLACE DECIMAL ±

MATERIAL   Al

FINISH   --

DO NOT SCALE DRAWING

PROPRIETARY AND CONFIDENTIAL
THE INFORMATION CONTAINED IN THIS
DRAWING IS THE SOLE PROPERTY OF
<INSERT COMPANY NAME HERE>. ANY
REPRODUCTION IN PART OR AS A WHOLE
WITHOUT THE WRITTEN PERMISSION OF
<INSERT COMPANY NAME HERE> IS
PROHIBITED.

SIZE **A**   DWG. NO.

REV.

SCALE:2:1   SHEET 1 OF 1

3 holes of ⌀.088 at 120°

⌀1.063

⌀.732

1.019

.631±.001

.276

⌀.811

.427

.358

.167

.286

⌀.551

.453

⌀.614±.001

.069

.153

.591

.056

3 4-40 tap holes at 120°

REVISIONS

ZONE	REV.	DESCRIPTION	DATE	APPROVED

	NAME	DATE
DRAWN	Nikhil B	
CHECKED		
ENG APPR.		
MFG APPR.		
Q.A.		
COMMENTS:		

Texas A&M Mechatronics Lab

Sensor Mount bottom

SIZE A	DWG. NO.3	REV.
SCALE:2:1	WEIGHT:	SHEET 1 OF 1

DIMENSIONS ARE IN INCHES
TOLERANCES:
FRACTIONAL±
ANGULAR: MACH± BEND ±
TWO PLACE DECIMAL ±
THREE PLACE DECIMAL ±0.005

MATERIAL
Delrin

FINISH

# of parts:3

NEXT ASSY	USED ON
APPLICATION	

DO NOT SCALE DRAWING

Sensor mount top

Texas A&M Mechatronics Lab

3 4-40 tap holes at 120°

(.062)

(.118)

(∅1.063)

(∅.315)

(.236)

(.167)

(.427)

.358

(.286)

3 Clearance Holes of ∅0.088 at 120°

(.453)

(∅.551)

(.069)

REVISIONS

ZONE	REV.	DESCRIPTION	DATE	APPROVED

DIMENSIONS ARE IN INCHES
TOLERANCES:
FRACTIONAL±
ANGULAR: MACH± BEND ±
TWO PLACE DECIMAL ±
THREE PLACE DECIMAL ±0.005

MATERIAL Delrin

FINISH

		NAME	DATE
DRAWN	Nikhil B		
CHECKED			
ENG APPR.			
MFG APPR.			
Q.A.			
COMMENTS:			

Parts:3

SIZE A   DWG. NO.5

SCALE:2:1   WEIGHT: SHEET 1 OF 1

REV.

NEXT ASSY   USED ON

APPLICATION   DO NOT SCALE DRAWING

PROPRIETARY AND CONFIDENTIAL
THE INFORMATION CONTAINED IN THIS
DRAWING IS THE SOLE PROPERTY OF
<INSERT COMPANY NAME HERE>. ANY
REPRODUCTION IN PART OR AS A WHOLE
WITHOUT THE WRITTEN PERMISSION OF
<INSERT COMPANY NAME HERE> IS
PROHIBITED.

3 4-40 tap holes at 120°

(.062)

(.118)

(Ø1.063)

(Ø.315)

(.236)

(.167)

(.427)

.358

3 Clearance Holes of Ø0.088 at 120°

(.286)

(Ø.551)

(.453)

(.069)

		REVISIONS		
ZONE	REV.	DESCRIPTION	DATE	APPROVED

DIMENSIONS ARE IN INCHES
TOLERANCES:
FRACTIONAL±
ANGULAR: MACH±   BEND ±
TWO PLACE DECIMAL   ±
THREE PLACE DECIMAL   ±0.005

MATERIAL Delrin

FINISH   --

	NAME	DATE
DRAWN	Nikhil B	
CHECKED		
ENG APPR.		
MFG APPR.		
Q.A.		
COMMENTS:		

NEXT ASSY   USED ON

APPLICATION   DO NOT SCALE DRAWING

Parts:3

Texas A&M Mechatronics Lab

Sensor mount top

SIZE DWG. NO.5   REV.
A
SCALE:2:1   WEIGHT: SHEET 1 OF 1

APPENDIX B

REAL-TIME CONTROL C CODES

Lead-Lag Control Routine:

```c
#include "dsp.h"
#include "math.h"
void c_int01()
{
unsigned long D1reading;
long ADreading;
float z_mea;
int     i,j;
tr_low();
D1reading=*(unsigned long *) AD_FIFO_D1;
*(unsigned long int *) 0xb0300003=0x0041;
    raw_x_pos=(*(long int *)0xb0300048 << 16) & 0xffff0000;
    raw_y1_pos=(*(long int *)0xb0310048 << 16) & 0xffff0000;
    raw_y2_pos=(*(long int *)0xb0320048 << 16) & 0xffff0000;
    raw_x_vel=(*(long int *)0xb030004e << 16) & 0xffff0000;
    raw_y1_vel=(*(long int *)0xb031004e << 16) & 0xffff0000;
    raw_y2_vel=(*(long int *)0xb032004e << 16) & 0xffff0000;

    tr_high();
    raw_x_pos|=((*(long int *)0xb0300048 >> 16) & 0x0000ffff);
    raw_y1_pos|=((*(long int *)0xb0310048 >> 16) & 0x0000ffff);
    raw_y2_pos|=((*(long int *)0xb0320048 >> 16) & 0x0000ffff);
    raw_x_vel|=((*(long int *)0xb030004e >> 16) & 0x0000ffff);
    raw_y1_vel|=((*(long int *)0xb031004e >> 16) & 0x0000ffff);
    raw_y2_vel|=((*(long int *)0xb032004e >> 16) & 0x0000ffff);

    x_pos=raw_x_pos*6.1815119987e-10;
```

```
   y1_pos=raw_y1_pos*6.1815119987e-10;
   y2_pos=raw_y2_pos*6.1815119987e-10;


x_vel=raw_x_vel*3.77292037e-7;
y1_vel=raw_y1_vel*3.77292037e-7;
y2_vel=raw_y2_vel*3.77292037e-7;


tr_high();
ADreading=(*(unsigned long int *)AD_FIFO_A1>>16) & 0xffff;
If (ADreading & 0x8000)
ADreading = ADreading | 0xffff0000;
z_pos1=50e-6+ADreading*1.55389559450e-9;     /* 5/0x7fff*1.018e-5=1.55389559450e-9 */
z_pos1 = z_pos1-z_pos10;
v1=ADreading*1.525925473799859614856410 4129154e-4;  /*voltage*/


ADreading=((*(unsigned long int *)AD_FIFO_B1>>16) & 0xffff);
if(ADreading & 0x8000)
ADreading = ADreading | 0xffff0000;
z_pos2=50e-6+ADreading*1.52898344068e-9;     /* 5/0x7fff*1.002e-5=1.52898344068e-9*/
z_pos2 = z_pos2-z_pos20;
v2=ADreading*1.525925473799859614856410 4129154e-4; /*voltage*/


ADreading=((*(unsigned long int *)AD_FIFO_C1>>16) & 0xffff);
if(ADreading & 0x8000)
ADreading = ADreading | 0xffff0000;
z_pos3=50e-6+ADreading*1.53823132440e-9;     /* 5/0x7fff*5e-5=? */
z_pos3 = z_pos3-z_pos30;
v3=ADreading*1.525925473799859614856410 4129154e-4;  /*voltage output--+-3.8v  out  of
range*/
tr_low();


yr=y1_pos;
```

```
xr=0.5773502692*y1_pos+1.1547005384*x_pos;
zr=0.3015*z_pos1+0.2889*z_pos2+0.4097*z_pos3;
rr=18.532*y2_pos;        /*17.8571 18.532*/
sr=z_pos1*-2.4097+z_pos2*4.6+z_pos3*-2.1903;
tr=z_pos1*-3.9455+z_pos2*0.1274+z_pos3*3.8182;

ur=y1_vel;                          /*velocity*/
hr=0.5773502692*y1_vel+1.1547005384*x_vel;
vr=18.532*y2_vel;
cos_x=cos(123.25*xr);
cos_y=cos(123.25*yr);
sin_x=sin(123.25*xr);
sin_y=sin(123.25*yr);

if(demo_enable==1)
{
   t+=0.0002;
   switch(time_count)
   {
     case 1:
      {
      if(yr>=3e-2)
       demo_enable=0;
      if(t>=0.0004)
       {
        t=0;
      /*  yc+=2e-6;*/
        yc+=2e-6;
        xc=0;
       }
       break;
      }
```

```
case -1:
{
 if(yr<=-11e-2)
  demo_enable=0;
 if(t>=0.0002)
  {
   t=0;
   yc-=1e-6;
   xc=0.0; /*1.154700538e-6;*/
  }
  break;
}
case 2:
{
 if(xr<=-11e-2)      /*-11e*/
  demo_enable=0;
 if(t>=0.0004)
  {
   t=0;
  /*  yc-=1e-6;*/
   xc-=2e-6;
  }
  break;
}
case -2:
{
 if(xr>=3e-2)
  demo_enable=0;
 if(t>=0.0004)
  {
   t=0;
  /* yc=0;*/
```

```
   xc+=2e-6;
 }
 break;
}
case 3:
{
if(step>6.28)
 demo_enable=0;
if(t>=0.0004)
 {
 t=0;
 step+=2e-4;
 if(step<6.28)
  {
  xc=-3e-2*(1-cos(step));
  yc=3e-2*sin(step);
  }
 }
 break;
}
case 4:
{
 if(xr<=0)
 demo_enable=0;
 if(t>=0.0004)
  {
   t=0;
  /* yc=0;*/
   xc-=2e-6;
  }
 break;
}
```

```
      case -5:
      {
      if(t>3)
       {
        demo_enable=0;
       }
      if(t<=0.1) yc=0.03-2.5*t*t;
      else if(t>0.1&&t<=0.28) yc=0.005-0.5*(t-0.1);
      else if(t>0.28&&t<=0.38) yc=-0.085-0.5*(t-0.28)+2.5*(t-0.28)*(t-0.28);
/*      if(t<=0.1) yc=0.03-3*t*t;
      else if(t>0.1&&t<=0.22) yc=-0.6*(t-0.1);
      else if(t>0.22&&t<=0.32) yc=-0.072-0.6*(t-0.22)+3*(t-0.22)*(t-0.22); */
 /*      if(t<=0.1) yc=0.03-3.5*t*t;
      else if(t>0.1&&t<=0.2) yc=-0.005-0.7*(t-0.1);
      else if(t>0.2&&t<=0.3) yc=-0.075-0.7*(t-0.2)+3.5*(t-0.2)*(t-0.2);
     if(t<=0.2) yc=0.03-1*t*t;
      else if(t>0.2&&t<=0.35) yc=-0.01-0.4*(t-0.2);
      else if(t>0.35&&t<=0.55) yc=-0.07-0.4*(t-0.35)+(t-0.35)*(t-0.35);*/
      break;
      }
      case 5:
      {
      if(t>3)
       {
        demo_enable=0;
       }
      if(t<=0.02) yc=0.5*t*t;
      else if(t>0.02&&t<=1.5) yc=0.0002+0.02*(t-0.02);
      else if(t>1.5&&t<=1.52) yc=0.0298+0.02*(t-1.5)-0.5*(t-1.5)*(t-1.5);
     /* if(t<=0.1) yc=1*t*t;
      if(t>0.1&&t<0.2) yc=0.01+0.3*(t-0.1);*/
      break;
```

```
        }
        case 6:
        {
        if(t>3)
         {
         demo_enable=0;
         }
/*      if(t<=0.1) xc=0.03-t*t;
        else if(t>0.1&&t<=0.5) xc=0.02-0.2*(t-0.1);
        else if(t>0.5&&t<=0.6) xc=-0.06-0.2*(t-0.5)+(t-0.5)*(t-0.5);
        if(t<=0.1) xc=0.03-2*t*t;
        else if(t>0.1&&t<=0.25) xc=0.01-0.4*(t-0.1);
        else if(t>0.25&&t<=0.35) xc=-0.05-0.4*(t-0.25)+2*(t-0.25)*(t-0.25); 4 m/s*s */
        if(t<=0.1) xc=0.03-1.5*t*t;
        else if(t>0.1&&t<=0.3) xc=0.015-0.3*(t-0.1);
        else if(t>0.3&&t<=0.4) xc=-0.045-0.3*(t-0.3)+1.5*(t-0.3)*(t-0.3);
        break;
        }
        case 7:
        {
        if(t>0.02&&t<=15)
         {
          xc-=1e-6;
         }
        if(t>17.02&&t<=32)
         {
         xc+=1e-6;
         yc-=1e-6;
         }
        if(t>34.02&&t<=49)
         {
         xc-=1e-6;
```

```
      }
     if(t>51.02&&t<=66)
      {
       xc+=1e-6;
       yc+=1e-6;
      }
     if(t>66)
      {
       demo_enable=0;
       t=0;
      }
      break;
     }
    case 8:
     {
      if(t>5)
      {
/*       demo_enable=0; */
       t=0;
      }
/*     if(t<=0.2) yc=-0.11+0.5*t*t;
     else if(t>0.2&&t<=0.7) yc=-0.09+0.2*(t-0.2);
     else if(t>0.7&&t<=0.9) yc=0.01+0.2*(t-0.7)-0.5*(t-0.7)*(t-0.7);


     else if(t>2&&t<=2.2) yc=0.03-0.5*(t-2)*(t-2);
     else if(t>2.2&&t<=2.7) yc=0.01-0.2*(t-2.2);
     else if(t>2.7&&t<=2.9) yc=-0.09-0.2*(t-2.7)+0.5*(t-2.7)*(t-2.7); */


     if(t<=0.1) yc=0.03-2.5*t*t;
     else if(t>0.1&&t<=0.28) yc=0.005-0.5*(t-0.1);
     else if(t>0.28&&t<=0.38) yc=-0.085-0.5*(t-0.28)+2.5*(t-0.28)*(t-0.28);
```

```
        else if(t>1&&t<=1.1) yc=-0.11+2.5*(t-1)*(t-1);
        else if(t>1.1&&t<=1.28) yc=-0.085+0.5*(t-1.1);
        else if(t>1.28&&t<=1.38) yc=0.005+0.5*(t-1.28)-2.5*(t-1.28)*(t-1.28);


        break;
     }
          }
}


/* controller */
if (controller_flag == 1)
{
er0x=xc-xr;
er0y=yc-yr;
er0r=rc-rr;


/*u0x=1.68592*u1x-0.68592*u2x+2226100*(er0x-1.95924*er1x+0.95938*er2x);*/
/*u0x=1.753*u1x-0.753*u2x+2630000*(er0x-1.987*er1x+0.987*er2x);*/ /*good*/
/*u0x=1.488*u1x-0.488*u2x+4000000*(er0x-1.995*er1x+0.995*er2x);*/
/*u0x=1.868*u1x-0.868*u2x+744000*(er0x-1.993*er1x+0.99302*er2x);*/    /*ok 25hz*/
u0x=1.797*u1x-0.797*u2x+740000*(er0x-1.9882*er1x+0.98822*er2x);   /*21hz,pm=50*/
/*u0x=1.683*u1x-0.683*u2x+2320000*(er0x-1.993*er1x+0.993*er2x);*/
/*u0y=1.68592*u1y-0.68592*u2y+2226100*(er0y-1.95924*er1y+0.95938*er2y);*/
/*u0y=1.753*u1y-0.753*u2y+2630000*(er0y-1.987*er1y+0.987*er2y);*/
/*u0y=1.868*u1y-0.868*u2y+744000*(er0y-1.993*er1y+0.993*er2y);*/    /*ok 25hz*/
u0y=1.797*u1y-0.797*u2y+740000*(er0y-1.9882*er1y+0.98822*er2y); /*21hz,pm=50*/
/*u0r=1.68592*u1r-0.68592*u2r+39809*(er0r-1.95924*er1r+0.95938*er2r); */
/*u0r=1.753*u1r-0.753*u2r+24300*(er0r-1.987*er1r+0.987*er2r);*/
/*u0r=1.7530*u1r-0.7530*u2r+24200*(er0r-1.986*er1r+0.986024*er2r); /*good 56hz*/
/*u0r=1.7977*u1r-0.7977*u2r+18688*(er0r-1.9749*er1r+0.9749*er2r);*/   /*ok*/
/*u0r=1.607*u1r-0.607*u2r+58900*(er0r-1.986*er1r+0.9860*er2r);*/
u0r=1.797*u1r-0.797*u2r+13062.95*(er0r-1.9882*er1r+0.98822*er2r); /*38hz,pm=62 good!!*/
```

```
/*u0r=1.86781*u1r-0.86781*u2r+5910*(er0r-1.99106*er1r+0.99107*er2r); /*26hz,pm=60.4*/
/*u0r=1.5156*u1r-0.5156*u2r+15929.83*(er0r-1.9882*er1r+0.9882*er2r); /*21hz,pm=61.8*/
/*u0r=1.5156*u1r-0.5156*u2r+13300*(er0r-1.9757*er1r+0.9757*er2r);*/      /*21hz,pm=45*/


/*fA=-0.8477*u0x+0.5*u0y-10.01*u0r;          /*0.1 -0.8477*u0x 0.7477*/
/*fB=0.8477*u0x+0.5*u0y+10.01*u0r;           /*-0.1 0.8477*u0x -0.7477*/
/*fC=u0x;*/
fA=-0.82273*u0x+0.51452*u0y-9.75956*u0r;         /*-0.82273*/
fB=0.82273*u0x+0.48548*u0y+9.75956*u0r;
fC=u0x;
/*fA=0;
fB=0;
fC=0;*/


if(z_control==33)
{
er0z=zc-zr;
er0s=sc-sr;
er0t=tc-tr;
z0er=zc-zr;
z0r=zr;
z0cer=z1cer+10000*z0er;
z0cr=0.8187*z1cr+3000000*(z0r-z1r);          /*2.5e6 almost good*/
u0z=z0cer-z0cr;

s0er=sc-sr;
s0r=sr;
s0cer=s1cer+100*s0er;
s0cr=0.8465*s1cr+10830*(s0r-s1r);          /*10830 is good*/
u0s=s0cer-s0cr-0.022*u0y;    /*-0.022*u0y*/

t0er=tc-tr;
```

```
t0r=tr;
t0cer=t1cer+100*t0er;
t0cr=0.8465*t1cr+10830*(t0r-t1r);          /*10830 is good*/
u0t=t0cer-t0cr+0.022*u0x;    /*+0.022*u0x*/


/*u0z=1.797*u1z-0.797*u2z+740000*(er0z-1.9882*er1z+0.9882*er2z);*/   /*740000*/
/*u0z=1.6827*u1z-0.6827*u2z+650000*(er0z-1.992800*er1z+0.992811*er2z); very slow*/
/*u0z=1.6037*u1z-0.6037*u2z+4360000*(er0z-1.9875*er1z+0.98752*er2z);   /*less than 5s*/
/*u0z=1.6041*u1z-0.6041*u2z+17400000*(er0z-1.9875*er1z+0.98752*er2z);   doesn't   work!
frequency is too high!*/
/*u0s=1.6859*u1s-0.6859*u2s+7000*(er0s-1.9654*er1s+0.965517*er2s);
/*u0s=1.6827*u1s-0.6827*u2s+12300*(er0s-1.9928*er1s+0.99281*er2s); /*bad*/
/*u0t=1.6859*u1t-0.6859*u2t+7000*(er0t-1.9654*er1t+0.965517*er2t);
/*u0t=1.6827*u1t-0.6827*u2t+14860.16*(er0t-1.9928*er1t+0.99281*er2t); bad*/
/*u0t=0.1;*/
/*u0s=0;
u0t=0;  */


/*u0s=-0.022*(fA+fB);
u0t=-0.022*fC;*/
/*u0z=0; */
/*u0t=0.022*u0x;*/
/*u0z=0;*/
/*u0z=0;
u0s=0;*/


/*fZA=0.32637*u0z-3.87159*u0s+10.01*u0t;
fZB=0.32637*u0z-3.87159*u0s-10.01*u0t;
fZC=0.34726*u0z+7.74317*u0s;*/


fZA=0.34024*u0z-3.88602*u0s+9.75956*u0t;
fZB=0.31251*u0z-3.85715*u0s-9.75956*u0t;
```

```
fZC=0.34725*u0z+7.74316*u0s;
/*fZA=-2;
fZB=-2;*/
/*fZC=1;*/
i_Ad=fZA*f2ih;      /*-2 0.079116*/
i_Bd=fZB*f2ih;
i_Cd=fZC*f2ih;
}
if(z_control==0)
{

i_Ad=0;      /*-2 0.079116*/
i_Bd=0;
i_Cd=0;
}

i_Aq=fA*f2ih;
i_Bq=fB*f2ih;
i_Cq=fC*f2ih;

i_Aa=cos_y*i_Aq-sin_y*i_Ad;
i_Ba=cos_y*i_Bq-sin_y*i_Bd;
i_Ca=cos_x*i_Cq-sin_x*i_Cd;
i_Ab=sin_y*i_Aq+cos_y*i_Ad;
i_Bb=sin_y*i_Bq+cos_y*i_Bd;
i_Cb=sin_x*i_Cq+cos_x*i_Cd;



current_A[0][0]=i_Aa;
current_A[1][0]=0.5*i_Aa+0.8660254037844*i_Ab;
current_A[2][0]=-0.5*i_Aa+0.8660254037844*i_Ab;
```

```
current_B[0][0]=i_Ba;
current_B[1][0]=0.5*i_Ba+0.8660254037844*i_Bb;
current_B[2][0]=-0.5*i_Ba+0.8660254037844*i_Bb;
current_C[0][0]=i_Ca;
current_C[1][0]=0.5*i_Ca+0.8660254037844*i_Cb;
current_C[2][0]=-0.5*i_Ca+0.8660254037844*i_Cb;

for(j=0;j<3;j++)
{
        v[0][j]=0x800+0xfff*current_A[j][0]/(-2.6); /*(20*0.13)*/
        v[1][j]=0x800+0xfff*current_B[j][0]/(-2.6);
        v[2][j]=0x800+0xfff*current_C[j][0]/(-2.6);
}
}
 tr_low();
if(flag_d2a==1)
{
for(i=2;i>=0;i--)        /*i=0;i<3;i++*/
        for(j=0;j<3;j++)
                *(unsigned int *) DAC_DATA_Reg=v[i][j];
for(i=0;i<7;i++)
        *(unsigned int *) DAC_DATA_Reg=0x800;
}
if ((snap_begin==1)&&(snap_enable=1))
{
int_count++;
}
z1cer=z0cer;
z1r=z0r;
z1cr=z0cr;
s1cer=s0cer;
s1r=s0r;
```

```
s1cr=s0cr;
t1cer=t0cer;
t1r=t0r;
t1cr=t0cr;
u2z=u1z;
u1z=u0z;
er2z=er1z;
er1z=er0z;
u2s=u1s;
u1s=u0s;
er2s=er1s;
er1s=er0s;
u2t=u1t;
u1t=u0t;
er2t=er1t;
er1t=er0t;
u2x=u1x;
u1x=u0x;
er2x=er1x;
er1x=er0x;
u2y=u1y;
u1y=u0y;
er2y=er1y;
er1y=er0y;
u2r=u1r;
u1r=u0r;
er2r=er1r;
er1r=er0r;
display=1;
MX_Int_Clr= 0x20000029;
*(unsigned int *)MX_Int_Clr=0x0;
}
```

LQR, LQG Control Routine:

```
#include "dsp.h"
#include "math.h"

void c_int01()
{
unsigned long D1reading;
long ADreading;
float z_mea;
int      i,j;

tr_low();
D1reading=*(unsigned long *)AD_FIFO_D1;
*(unsigned long int *)0xb0300003=0x0041;
    raw_x_pos=(*(long int *)0xb0300048 << 16) & 0xffff0000;
    raw_y1_pos=(*(long int *)0xb0310048 << 16) & 0xffff0000;
    raw_y2_pos=(*(long int *)0xb0320048 << 16) & 0xffff0000;

    raw_x_vel=(*(long int *)0xb030004e << 16) & 0xffff0000;
    raw_y1_vel=(*(long int *)0xb031004e << 16) & 0xffff0000;
    raw_y2_vel=(*(long int *)0xb032004e << 16) & 0xffff0000;

    tr_high();
    raw_x_pos|=((*(long int *)0xb0300048 >> 16) & 0x0000ffff);
    raw_y1_pos|=((*(long int *)0xb0310048 >> 16) & 0x0000ffff);
    raw_y2_pos|=((*(long int *)0xb0320048 >> 16) & 0x0000ffff);

    raw_x_vel|=((*(long int *)0xb030004e >> 16) & 0x0000ffff);
    raw_y1_vel|=((*(long int *)0xb031004e >> 16) & 0x0000ffff);
    raw_y2_vel|=((*(long int *)0xb032004e >> 16) & 0x0000ffff);

    x_pos=raw_x_pos*6.1815119987e-10;
```

```
  y1_pos=raw_y1_pos*6.1815119987e-10;
  y2_pos=raw_y2_pos*6.1815119987e-10;


  x_vel=raw_x_vel*3.77292037e-7;
      y1_vel=raw_y1_vel*3.77292037e-7;
  y2_vel=raw_y2_vel*3.77292037e-7;


tr_high();
ADreading=(*(unsigned long int *)AD_FIFO_A1>>16) & 0xffff;
if(ADreading & 0x8000)
ADreading = ADreading | 0xffff0000;
z_pos1=50e-6+ADreading*1.55389559450e-9;    /* 5/0x7fff*1.018e-5=1.55389559450e-9 */
                /*5/0x7fff=1.52592547379985961485641041291154e-4*/
z_pos1 = z_pos1-z_pos10;
v1=ADreading*1.52592547379985961485641041291154e-4;  /*voltage*/


ADreading=((*(unsigned long int *)AD_FIFO_B1>>16) & 0xffff);
if(ADreading & 0x8000)
ADreading = ADreading | 0xffff0000;
z_pos2=50e-6+ADreading*1.52898344068e-9;    /* 5/0x7fff*1.002e-5=1.52898344068e-9*/
z_pos2 = z_pos2-z_pos20;
v2=ADreading*1.52592547379985961485641041291154e-4; /*voltage*/


ADreading=((*(unsigned long int *)AD_FIFO_C1>>16) & 0xffff);
if(ADreading & 0x8000)
ADreading = ADreading | 0xffff0000;
z_pos3=50e-6+ADreading*1.53823132440e-9;    /* 5/0x7fff*5e-5=? */
z_pos3 = z_pos3-z_pos30;
v3=ADreading*1.52592547379985961485641041291154e-4;  /*voltage output--+-3.8v  out  of
range*/
tr_low();
```

```
yr=y1_pos;
xr=0.5773502692*y1_pos+1.1547005384*x_pos;
zr=0.3015*z_pos1+0.2889*z_pos2+0.4097*z_pos3;


rr=18.532*y2_pos;        /*17.8571 18.532*/
sr=z_pos1*-2.4097+z_pos2*4.6+z_pos3*-2.1903;
tr=z_pos1*-3.9455+z_pos2*0.1274+z_pos3*3.8182;


ur=y1_vel;                          /*velocity*/
hr=0.5773502692*y1_vel+1.1547005384*x_vel;
vr=18.532*y2_vel;

cos_x=cos(123.25*xr);
cos_y=cos(123.25*yr);
sin_x=sin(123.25*xr);
sin_y=sin(123.25*yr);

/* controller */
if (controller_flag == 1)

{
er0x=-xc+xr;
er0y=-yc+yr;
er0r=-rc+rr;
u0x=u1x+0.0002*er0x;
u0y=u1y+0.0002*er0y;
u0r=u1r+0.0002*er0r;


if(z_control==33)
```

```
{
er0z=-zc+zr;
er0s=-sc+sr;
er0t=-tc+tr;
ier1z=ier0z+0.0002*er0z;
ier1s=ier0s+0.0002*er0s;
ier1t=ier0t+0.0002*er0t;


p1_est=-1.5358e+002*er0z   +8.6627e+000*er0s   -1.5145e+000*er0t   -2.3202e+002*ier0z
+1.1741e+002*ier0s -9.6360e+000*ier0t +7.9323e-001*p0_est +9.0292e-003*q0_est -1.6885e-
003*w0_est;
q1_est= 8.5637e+000*er0z  -1.5590e+002*er0s  +7.2816e-001*er0t  +1.1242e+002*ier0z  -
2.6866e+002*ier0s +3.2960e+000*ier0t +8.9410e-003*p0_est +7.9061e-001*q0_est +7.8903e-
004*w0_est;
w1_est=-1.9017e+000*er0z   +2.3896e+000*er0s   -1.5510e+002*er0t   -1.8611e+001*ier0z
+3.0098e+001*ier0s -2.7013e+002*ier0t -2.0414e-003*p0_est +2.4911e-003*q0_est +7.9005e-
001*w0_est;


i_Ad=-1.0716e+004*er0z   +4.3482e+003*er0s   +1.5028e+003*er0t   -1.2830e+005*ier0z
+7.3730e+004*ier0s   -2.2873e+004*ier0t   -3.3231e+001*p0_est   +7.1149e+000*q0_est   -
4.9051e+000*w0_est;
i_Bd=-9.8701e+003*er0z   +3.7995e+003*er0s   -3.1148e+003*er0t   -1.1870e+005*ier0z
+6.5749e+004*ier0s    +1.2708e+004*ier0t    -3.1097e+001*p0_est    +6.3973e+000*q0_est
+3.1094e+000*w0_est;
i_Cd=-1.0054e+004*er0z   +5.5414e+003*er0s   -7.8126e+002*er0t   -1.1962e+005*ier0z
+4.6052e+004*ier0s -5.0623e+003*ier0t -3.3285e+001*p0_est +7.5616e-001*q0_est -8.7256e-
001*w0_est;


i_Ad=i_Ad+1.6667e+004*zc -2.2049e+003*sc +5.6441e+003*tc;
i_Bd=i_Bd+1.5727e+004*zc -2.0805e+003*sc -5.6441e+003*tc;
i_Cd=i_Cd+1.7233e+004*zc +4.2854e+003*sc -1.6315e-012*tc;
}
```

```
if(z_control==0)

{


i_Ad=0;      /*-2 0.079116*/
i_Bd=0;
i_Cd=0;
}



i_Aq=-0.000*er0x-406.615*er0y+999.400*er0r-0.0000*hr-11.092*ur+7.179*vr-0.00026*u0x-
7216.238*u0y+66741.495*u0r;
i_Bq=0.000*er0x-383.792*er0y-1054.923*er0r+0.0000*hr-10.467*ur-7.494*vr-0.00026*u0x-
6816.245*u0y-70654.791*u0r;
i_Cq=-624.896*er0x-0.0000*er0y+0.0000*er0r-19.156*hr-0.0000*ur+0.0000*vr-
9934.686*u0x+0.00038*u0y+0.00013*u0r; /*Q=diag(1e4 1e4 1e5 1 1 1 1e8 1e8 1e10)*/


i_Aa=cos_y*i_Aq-sin_y*i_Ad;
i_Ba=cos_y*i_Bq-sin_y*i_Bd;
i_Ca=cos_x*i_Cq-sin_x*i_Cd;
i_Ab=sin_y*i_Aq+cos_y*i_Ad;
i_Bb=sin_y*i_Bq+cos_y*i_Bd;
i_Cb=sin_x*i_Cq+cos_x*i_Cd;



current_A[0][0]=i_Aa;
current_A[1][0]=0.5*i_Aa+0.8660254037844*i_Ab;
current_A[2][0]=-0.5*i_Aa+0.8660254037844*i_Ab;
current_B[0][0]=i_Ba;
current_B[1][0]=0.5*i_Ba+0.8660254037844*i_Bb;
current_B[2][0]=-0.5*i_Ba+0.8660254037844*i_Bb;
current_C[0][0]=i_Ca;
```

```
current_C[1][0]=0.5*i_Ca+0.8660254037844*i_Cb;
current_C[2][0]=-0.5*i_Ca+0.8660254037844*i_Cb;


for(j=0;j<3;j++)
{
        v[0][j]=0x800+0xfff*current_A[j][0]/(-2.6); /*(20*0.13)*/
        v[1][j]=0x800+0xfff*current_B[j][0]/(-2.6);
        v[2][j]=0x800+0xfff*current_C[j][0]/(-2.6);
}
}
tr_low();


if(flag_d2a==1)
{
for(i=2;i>=0;i--)        /*i=0;i<3;i++*/
        for(j=0;j<3;j++)
                *(unsigned int *) DAC_DATA_Reg=v[i][j];
for(i=0;i<7;i++)
        *(unsigned int *) DAC_DATA_Reg=0x800;
}



if ((snap_begin==1)&&(snap_enable=1))
{
int_count++;
}


er0z_est=er1z_est;
er0s_est=er1s_est;
er0t_est=er1t_est;
p0_est=p1_est;
q0_est=q1_est;
```

```
w0_est=w1_est;
ier0z=ier1z;
ier0s=ier1s;
ier0t=ier1t;


u2z=u1z;
u1z=u0z;
er2z=er1z;
er1z=er0z;
u2s=u1s;
u1s=u0s;
er2s=er1s;
er1s=er0s;
u2t=u1t;
u1t=u0t;
er2t=er1t;
er1t=er0t;


u2x=u1x;
u1x=u0x;
er2x=er1x;
er1x=er0x;


u2y=u1y;
u1y=u0y;
er2y=er1y;
er1y=er0y;


u2r=u1r;
u1r=u0r;
er2r=er1r;
er1r=er0r;
```

```
display=1;
MX_Int_Clr= 0x20000029;
*(unsigned int *)MX_Int_Clr=0x0;
}
```

APPENDIX C

MATLAB CODES

LQR Design:

```
%integrator+lqr for horizontal plane
clear all;
A=[0 0 0 1 0 0 0 0 0;
   0 0 0 0 1 0 0 0 0;
   0 0 0 0 0 1 0 0 0;
   0 0 0 0 0 0 0 0 0;
   0 0 0 0 0 0 0 0 0;
   0 0 0 0 0 0 0 0 0;
   1 0 0 0 0 0 0 0 0;
   0 1 0 0 0 0 0 0 0;
   0 0 1 0 0 0 0 0 0;]
B=[0 0 0;
   0 0 0;
   0 0 0;
   0 0 3.4095;
   3.4095 3.4095 0;
   -18.5621 19.6720 0;
   0 0 0;
   0 0 0;
   0 0 0;]
C=[1 0 0 0 0 0 0 0 0;
   0 1 0 0 0 0 0 0 0;
   0 0 1 0 0 0 0 0 0];
co=ctrb(A,B);
unco=length(A)-rank(co)

Q=diag([1e4,1e4,1e5,1,1,1,1e8,1e8,1e10]); %1e4,1e5
```

```
R=diag([1,1,1]);
x0=[-10e-6;-20e-6;-30e-6;0;0;0;0;0;0];
yd=[10e-6;20e-6;10e-6];
[k,s,e]=LQR(A,B,Q,R);
k
[kd,sd,ed]=lqrd(A,B,Q,R,0.0002);
kd
A_c=A-B*k;
sys_c=ss(A_c,[],C,[]);
[y,t,x]=initial(sys_c,x0);
y=ones(size(y))*diag(yd)+y;
figure(1);plot(t,y);
```

LQG Design:

```
clear all;
m=5.91;
Ixx=0.033;
Iyy=0.025;
kz=1e6;
ks=11152;
kt=11653;
lay=0.0448462;
lby=0.0448462;
lcy=0.0843;
lax=0.0497445;
lbx=0.0527191;
lcx=0.0012968;
lcx=0;
con=20.15;

A_c=[0   0   0   0   0   0   1   0   0;
```

```
0    0    0    0    0    0    0    1    0;
0    0    0    0    0    0    0    0    1;
1    0    0    0    0    0    0    0    0;
0    1    0    0    0    0    0    0    0;
0    0    1    0    0    0    0    0    0;
-kz/m 0    0    0    0    0    0    0    0;
0 -ks/Ixx  0    0    0    0    0    0    0;
0    0 -kt/Iyy 0    0    0    0    0    0;];
B_c=[0              0              0;
     0              0              0;
     0              0              0;
     0              0              0;
     0              0              0;
     0              0              0;
     con/m          con/m          con/m;
     -con*lay/Ixx   -con*lby/Ixx   con*lcy/Ixx;
     con*lax/Iyy    -con*lbx/Iyy       0];

C_c=[1 0 0 0 0 0 0 0 0;
     0 1 0 0 0 0 0 0 0;
     0 0 1 0 0 0 0 0 0];

%Q=diag([1e4 1e3 1e3 1e11 1e9 1e9 1e2 1e2 1e2]); %xyz24-*.13
%Q=diag([1e4 1e3 1e3 1e15 1e8 1e8 1e2 1e2 1e2]); %unstable
Q=diag([1e4 1e3 1e3 1e10 1e9 1e10 1e2 1e1 2e1]);%IMECE2004 xyz29-*.25
%Q=diag([1e4 1e3 1e3 1e10 1e9 1e9 1e2 1e2 1e2]);
R=eye(3);

psi=1e-6;
thida=1e-6*eye(6);
L=[1 1 1]';
```

```
sys_c=ss(A_c,B_c,C_c,0);
sys_d=c2d(sys_c,0.0002);
[A_d,B_d,C_d,D_d,E_d,Ts]=dssdata(sys_d);

A11=A_d(1:6,1:6); A12=A_d(1:6,7:9); A21=A_d(7:9,1:6); A22=A_d(7:9,7:9);
B1=B_d(1:6,1:3);B2=B_d(7:9,1:3);

ob=obsv(A22,A12);
unob=length(A22)-rank(ob)
co=ctrb(A_d,B_d);
unco=length(A_d)-rank(co)

Kc_d=lqrd(A_c,B_c,Q,R,0.0002);
kc2=lqr(A_c,B_c,Q,R)

k1=Kc_d(1:3,1:6); k2=Kc_d(1:3,7:9);
% k=-Kc_d
sys_temp=ss(A22,L,A12,0);
[kest,H,P]=kalman(sys_temp,psi,thida);
H_d=H;

% A_new=[A_d -B_d*Kc_d;H_d*C_d A_d-B_d*Kc_d-H_d*C_d];
A_new=[A11-B1*k1 A12    -B1*k2;
    A21-B2*k1 A22    -B2*k2;
    A21-B2*k1 H_d*A12 A22-H_d*A12-B2*k2];

C_new=eye(12);
sys_new=dss(A_new,[],C_new,[],eye(12),Ts);

conx=(A22-H_d*A12)*H_d+A21-H_d*A11-(B2-H_d*B1)*(k1+k2*H_d);
conz=(A22-H_d*A12-B2*k2+H_d*B1*k2);
conxz=[conx conz]
```

```
outputx=-k1-k2*H_d;
outputz=-k2;
outputxz=[outputx outputz]
ku=-pinv(B_d)*A_d

x0=[5e-6 10e-6 20e-6 0 0 0 0 0 0 0 0 0]';
[y,t]=initial(sys_new,x0,[0:0.0002:0.1]);
figure(22);
subplot(2,2,1);
plot(t,y(:,7),'-',t,y(:,10),'--');
xlabel('t (s)');ylabel('z-dot direction (m/s)');
subplot(2,2,2);
plot(t,y(:,8),'-',t,y(:,11),'--');
xlabel('t (s)');ylabel('s-dot (rad/s)');
subplot(2,2,3);
plot(t,y(:,9),'-',t,y(:,12),'--');
xlabel('t (s)');ylabel('t-dot (rad/s)');
subplot(2,2,4);
plot(t,y(:,1),'-',t,y(:,2),'--',t,y(:,3),'+');
xlabel('t (s)');ylabel('z, s, t-direction');
```

VITA

TIEJUN HU

Education

Texas A&M University, College Station, Texas. 2002−2005, Doctor of Philosophy in Mechanical Engineering. Dissertation advisor: Won-jong Kim

Tsinghua University, Beijing, China. 1999−2002, Master of Science in Mechanical Engineering. Thesis advisor: Dianfang He

Tsinghua University, Beijing China. 1995−1999, Bachelor of Science in Mechanical Engineering. Thesis advisor: Dianfang He

Permanent Address

E'Nan High School
Xian Ning, 437100
Hu Bei Province, China